PICOSECOND PUMP DISPERSION MANAGEMENT AND JITTER STABILIZATION IN A PETAWATT-SCALE FEW-CYCLE OPCPA SYSTEM

SANDRO KLINGEBIEL

München, 2013

PICOSECOND PUMP DISPERSION MANAGEMENT AND JITTER STABILIZATION IN A PETAWATT-SCALE FEW-CYCLE OPCPA SYSTEM

SANDRO KLINGEBIEL

Dissertation der Fakultät für Physik
der Ludwig-Maximilians-Universität München

Vorgelegt von
Sandro Klingebiel
aus Heilbad Heiligenstadt

München, 30.04.2013

ERSTGUTACHTER:	Prof. Dr. Stefan Karsch
ZWEITGUTACHTER:	Prof. Dr. Malte C. Kaluza
DATUM DER MÜNDLICHEN PRÜFUNG:	15.07.2013

ABSTRACT

The petawatt field synthesizer (PFS) is a high-power optical parametric chirped-pulse amplification (OPCPA) system under development, which aims at generating few-cycle pulses with high energies of several Joule. The availability of light pulses with these unique parameters will enable an efficient generation of even shorter attosecond pulses with significantly higher photon flux than achievable today [1]. Not only the real-time observation, but also the control of charge transfer in molecular systems will become feasible for the first time [2].

The technique for realizing the ambitious PFS specifications is short-pulse pumped OPCPA in mm-thin crystals. The reduced crystal thickness allows for ultra-broadband amplification. The pump-pulse duration is reduced to a picosecond—compared to 100 ps to nanosecond pump-pulse duration in conventional high power OPCPA systems. The shortened pulse duration facilitates higher pump intensities whereby an efficient amplification in the mm-thin crystals is achieved.

The demonstration of this novel scheme in the PFS project will allow its use in the extreme light infrastructure (ELI)[3]—a pan-European high-power laser project. Based on the PFS technology for the front end, the ELI will generate exawatt peak-power pulses and therefore facilitate the study of laser-matter interaction in an unprecedented intensity range [4].

This work describes the CPA-aspects of a suitable chirped pulse amplification (CPA) pump laser for the PFS OPCPA system. The diode-pumped Yb:YAG amplifiers up to an energy of 300 mJ (at 1030 nm) are presented in combination with the dispersion management. The application of spectral-amplitude shaping in conjunction with an Yb:glass amplifier with broader bandwidth than Yb:YAG enables an unprecedented bandwidth of 3.5 nm in the Yb:YAG amplifier at this energy level. Simulations show that a similar bandwidth can be maintained for the full amplifier system. The pulses with 200 mJ could be compressed to 900 fs, close to the transform limit. Later changes in the stretcher increase the bandwidth more and compression down to 740 fs is demonstrated. To date, these are the highest peak power pulses generated in Yb:YAG. For the application as OPCPA pump, the so generated pulses are frequency doubled in a DKDP crystal.

Another key aspect of this work is the synchronization of the OPCPA pump and signal pulses. In spite of optical synchronization of both pulses, a large timing fluctuation between these pulses is measured at the first OPCPA stage. The high accuracy jitter measurement setup and a series of measurements, which showed that the stretcher/compressor setup is the main source of jitter, are presented. Theoretical investigations yield that the optical delay in a compressor is orders of magnitude more sensitive to angle changes compared to free space propagation. This makes the stretcher and compressor extremely sensitive for timing jitter caused by turbulent air or mechanical instabilities. This novel insight helped us to significantly reduce the jitter to 100 fs and to demonstrate the feasibility of the PFS concept with first broad-band OPCPA experiments.

ZUSAMMENFASSUNG

Das PFS OPCPA System befindet sich zurzeit im Aufbau und zielt darauf ab, ultrakurze Lichtpulse mit wenigen optischen Zyklen und einigen Joule Pulsenergie zu erzeugen. Wenn Lichtpulse mit diesen einzigartigen Parametern verfügbar werden, können kürzere Attosekundenpulse mit höherer Effizienz und deutlich höherem Photonenfluss als bisher generiert werden [1]. Die Anwendung der so erzeugten Attosekundenpulse könnte erstmalig die Beobachtung in Echtzeit und die Kontrolle von Ladungsübergängen in Molekularen Systemen ermöglichen [2].

Die Technik, um die PFS Spezifikationen zu erreichen ist OPCPA mit mm dünnen Kristallen, gepumpt mit kurzen Pulsen. Die reduzierte Kristalldicke ermöglicht ultra-breitbandige Verstärkung. Die Pumppulsdauer ist dabei auf eine Pikosekunde reduziert, im Vergleich zu 100 ps bis Nanosekunden Pulsdauer in konventionellen Hochleistungs-OPCPA Systemen. Dies ermöglicht höhere Pumpintensitäten, wodurch eine effiziente Verstärkung in den kurzen Kristallen gewährleistet wird.

Die Demonstration dieses neuartigen Verstärkungsschemas innerhalb des PFS Projektes erlaubt dessen Nutzung in ELI[3]—einem gesamt-europäische Laser Projekt. Basierend auf der PFS-Technologie für das Frontend wird ELI Lichtpulse mit Exawatt Spitzenleistung generieren, wodurch Laser-Materie-Wechselwirkung in einem bis dahin unerreichten Intensitätsbereich untersucht werden kann [4].

Diese Arbeit beschreibt die Entwicklung eines geeigneten CPA Pumplasers für das PFS OPCPA-System. Die diodengepumpten YB:YAG Verstärker bis zu einer Energie von 300 mJ (bei 1030 nm) werden in Kombination mit dem Dispersionsmanagement präsentiert. Die Anwendung von spektralem Amplitudenformen in Verbindung mit einem breitbandigen Verstärker ermöglicht eine bis dahin unerreichte Bandbreite von 3.5 nm in Yb:YAG bei diesem Energieniveau. Simulationen zeigen, dass ähnliche Bandbreiten für das vollständige Verstärkersystem erreicht werden können. Die Pulse mit 200 mJ wurden auf 900 fs (nah am Transformlimit) komprimiert. Spätere Veränderungen im Strecker führen zu einer vergrößerten Bandbreite, wodurch eine Kompression auf 740 fs ermöglicht wurde. Aktuell ist dies die höchste Pulsspitzenleistung, die je in Yb:YAG generiert wurde. Für die Anwendung als OPCPA Pumpe werden die so generierten Pulse in einem DKDP Kristall frequenzverdoppelt.

Ein weiterer Schwerpunkt dieser Arbeit ist die Synchronisation der OPCPA Pump- und Signalpulse. Trotz optischer Synchronisation beider Pulse wurde eine große zeitliche Schwankung zwischen diesen Pulsen am Ort der ersten OPCPA Stufe gemessen. Der Messaufbau wird vorgestellt und eine Reihe von Messungen zeigt, dass der Strecker/Kompressor des Pumplasers die Hauptursache der zeitlichen Schwankungen von einigen hundert Femtosekunden ist. Theoretische Untersuchungen ergeben, dass der Strecker und Kompressor extrem sensitiv sind für zeitliche Schwankungen, die durch Turbulenzen in Luft oder durch instabile mechanische Komponenten hervorgerufen werden können. Diese neue Einsicht hat geholfen, diese Schwankungen auf 100 fs zu reduzieren und die Machbarkeit des PFS Konzeptes mit ersten breitbandigen OPCPA Experimenten zu demonstrieren.

CONTENTS

LIST OF FIGURES

LIST OF TABLES

ACRONYMS

ASE amplified spontaneous emission

CEO carrier-envelope offset

CPA chirped pulse amplification

DKDP deuterated potassium dihydrogen phosphate

ELI extreme light infrastructure

FOD forth order dispersion

FWHM full width at half maximum

GD group delay

GDD group delay dispersion

HCF hollow-core fiber

HWP half-wave plate

LBO lithium triborate

MPQ Max-Planck-Institut für Quantenoptik

OPA optical parametric amplification

OPCPA optical parametric chirped-pulse amplification

PCF photonic-crystal fiber

PFS petawatt field synthesizer

SFG sum-frequency generation

SHG second-harmonic generation

SLM spatial light modulator

TFP thin-film polarizer

TOD third order dispersion

1 MOTIVATION

1.1 OVERVIEW OF THE HISTORY OF HIGH POWER LASERS

In 1917, Einstein introduced the concept of stimulated emission; the interaction of a photon with an excited atom or molecule which causes the emission of a second photon with the same frequency, phase and direction [5, 6]. With this finding the foundation for the laser was laid—recalling that the acronym LASER stands for "Light Amplification by Stimulated Emission of Radiation".

Before the first laser was developed, stimulated emission was observed in the microwave spectral range. In 1958 Schawlow and Townes published a key theoretical paper suggesting masers in the infrared and optical frequency region [7]. Only two years later, in 1960, Maiman demonstrated the first laser [8]. In 1964, the invention of the laser was rewarded with the Nobel Prize in physics. At this point, the huge potential for technical applications had already been recognized. In the presentation speech of the Nobel Prize it has been stated, "The invention of the laser has provided us with a powerful new tool for research in many fields, the exploitation of which has only just started." [9]

The first laser was operating in a quasi-continuous wave regime, pumped by flash lamps. Nevertheless, high power densities—which are inaccessible otherwise—can be obtained in short laser pulses. In this regime the laser opens new possibilities for studying the nonlinear interaction of light and matter. A further increase in intensity gives rise to ever new physical phenomena and processes which can be studied. Thus, increasing the laser peak power and intensity has been one of the most important challenges for laser science and technology since the invention of the laser.

1.1.1 *Peak power and intensity*

Historically, increasing the peak intensity has been achieved by developing methods to shorten the pulse duration. Q-switching [10, 11] and mode-locking techniques [12, 13] (developed in the 60s-70s) helped to continuously reduce the pulse length from nanosecond down to few-ten femtoseconds in the following decade [14]. In this way, the peak power was pushed to the Megawatt and Gigawatt range and the intensity reaches beyond $10^{13}\,\mathrm{W/cm^2}$ up to $10^{18}\,\mathrm{W/cm^2}$, respectively. Along with this increase of intensity, new physical phenomena could be studied at certain intermediate intensity levels. At intensities around $10^{10}\,\mathrm{W/cm^2}$, the electric field of the laser becomes comparable to intra-atomic fields and the response of the atom to the applied laser field becomes dependent non-linearly on the laser intensity. Thus, the discovery of basic nonlinear optic phenomena such as harmonic generation [15], nonlinear Raman [16] and Brillouin scattering [17], 4-wave mixing [18, 19] or self-focusing [20, 21] was enabled.

The latter phenomena is based on the optical Kerr effect, which makes the refractive index of a medium linearly dependent on the light intensity [22]. In most materials, the refractive index becomes larger in the areas where the intensity is higher, usually at the center of a beam. This creates a focusing density profile, which potentially leads to medium damage [23]. This effect slowed down further progress in increasing the laser peak power in the 80s and increasing the beam size seemed to be the only way to overcome the self-focusing intensity limit at that time, which made high power lasers bulky and expensive.

The major breakthrough was achieved in the late 80s, when Strickland and Mourou introduced CPA [24, 25]. In CPA a short laser pulse is expanded to a nanosecond pulse duration before amplification. In this way, the peak power and hence the intensity are drastically reduced and significant amplification is possible well below the amplifier damage threshold. Subsequently, the pulses are compressed back to the original pulse width with drastically increased peak power and intensity. In order to handle these high intensities, transmission through material usually has to be avoided or minimized in the compressor.

The stretching and compression is provided by introduction of a frequency dependent delay. The expanded pulse is therefore chirped (has a varying frequency over time). There are many different stretcher compressor designs using the dispersion of gratings [26, 27, 28], prisms [29, 30, 31], grisms [32] (a combination of grating and prism), high-dispersive mirrors [33, 34] and bulk material [35, 36].

The application of CPA enabled an increase in the peak intensity of laser systems by several orders of magnitude over the last decades. When the laser intensity is increased above certain thresholds, different physical phenomena are relevant. Above $10^{12}\,\mathrm{W/cm^2}$ the laser immediately ionizes all atoms and creates a plasma [37]. At $10^{18}\,\mathrm{W/cm^2}$, laser-matter interaction is governed by the electron relativistic behavior and novel effects occur [38, 39] like: X-ray generation, γ-ray generation, relativistic self-focusing, high-harmonic generation, electron and proton acceleration as well as neutron and positron production. This is the limit of current high power laser systems with few 100 TW up to PW peak power. Nevertheless, there are also large scale laser projects like ELI [3] which aim at further increasing the intensities to $10^{25}\,\mathrm{W/cm^2}$ in order to enter a regime of ultra-relativistic physics, where the relativistic behavior of protons creates positrons, pions, muons and neutrinos, as well as high energy photons [40, 4].

1.2 PETAWATT PEAK POWER LASER SYSTEMS

PW level peak power amplification with 660 J of pulse energy at 440 fs pulse duration was first obtained in 1996 at the Lawrence Livermore National Laboratories using neodymium glass [41, 42]. Similar systems were later developed at the Rutherford Appleton Laboratory (670 J, 500 fs) [43] and Osaka University (420 J, 470 fs) [44]. All these systems are large scale facilities and have a very low repetition rate in the range of 1 shot per hour. The reason for the low repetition rate is the applied flash-lamp pumping. This pumping technique is not very efficient and stores an enormous amount of heat in the system, which has to be dissipated before the next pumping cycle.

Another branch of high peak power lasers is based on Ti:sapphire. This material is almost ideal for CPA lasers, because it supports the largest bandwidth and has excellent mechanical and thermal properties. A 0.85 PW CPA system (28 J, 33 fs) was reported in Japan [45]. Lately the repetition rate could be increased to 0.1 Hz (30 J, 30 fs) [46]. One limitation of Ti:sapphire lies in the short lifetime of the upper laser level (3 μs), which makes laser pumping necessary. Thus, high energy, high repetition rate Ti:sapphire lasers rely on the development of high energy, high repetition rate pump lasers. Nd:YAG lasers with an output energy of ca. 14 J at 532 nm and 5 Hz repetition rate are commercially available at present. Higher energies can be delivered at lower repetition rate or on a single shot basis.

The scaling of these PW systems in repetition rate is achieved amongst others when the thermal load is minimized. This can be accomplished with more efficient pumping techniques in the laser (or in the pump laser for Ti:sapphire). The most promising candidate is laser-diode-pumping which has many advantages over flash-lamp pumping. Besides the higher wall plug efficiency, the compactness and higher brightness, the emission of the diodes can be matched to the absorption bands of the laser material. This dramatically increases the optical to optical efficiency and reduces the thermal load compared to flash lamps, where only a small spectral portion of the white light can be absorbed and the remaining energy is stored as heat in the system. Despite the advantages, the use of laser-diode pumps was limited to low power applications in the past—mainly due to the relatively high price. Recent progress in the development of high power diode lasers arrays [47] opened a broad range of applications. The increased request has allowed for volume production and a significant cost reduction over the last decades. Nowadays, the price reached a value where the design of high power diode pumped solid state lasers becomes reasonable and scalable diode pumped solid state lasers are developed [48].

The reduction of the pulse duration has been the most successful way to increase the peak power in the past. Thus, further shortening of the pulse duration seems the natural way for further peak power scaling. Nevertheless, conventional CPA systems, as described above, suffer from the limited gain bandwidth of the amplifier material. This limits the shortest achievable pulse length. Existing techniques for spectral broadening subsequent to amplification [49] are limited to relatively low pulse energy. Therefore, an ultra-broadband amplification mechanism is needed in order to produce ultra-short high-power pulses, which will be described in the next section.

1.3 OPTICAL PARAMETRIC AMPLIFICATION

Optical parametric amplification OPA [50] is a nonlinear χ^2 process describing the interaction of three waves at different wavelengths: The pump wave with the highest intensity and the lowest wavelength transfers energy to the signal wave. At the same time an idler wave is generated at the difference frequency, so the energy between the three waves is conserved. For an efficient energy transfer, phase matching must be accomplished in order to also fulfill momentum conservation. For uni-axial birefringent media, phase matching can be achieved by angle tuning. In a noncollinear situation an angle is introduced between the pump and the signal beam. Tuning

of this noncollinear angle and the angle between the pump and crystal axis allows achieving broadband phase matching in the OPA crystal and the amplified signal can support few-cycle pulse widths [51, 52]. In combination with the CPA technique, the OPCPA enables the generation of high-power few-cycle pulses [53].

Apart from the much higher bandwidth, OPCPA is superior to conventional laser amplification in a number of additional aspects.

A. In the conventional laser process energy is stored in exited atoms or molecules. After extraction of the energy by the seed pulse, the energy difference between pump and seed photons ("quantum defect") is stored as heat in the laser material, making the thermal management one of the key design issues of high average power lasers. The OPCPA process is instantaneous: energy is transferred directly from the pump to the seed and the energy difference is emitted as idler photons. Given the crystal is transparent for all three waves, the OPCPA process is inherently free of heat generation in the crystals and therefore suitable for high average power applications.

B. In conventional lasers the pump pulse is commonly much longer than the stretched laser pulse and creates an inversion in the laser medium during most of its duration. Amplified spontaneous emission ASE originating from the inverted medium creates a pedestal around the main pulse, limiting the pulse contrast. The pump and stretched signal beam have comparable pulse length in optical parametric amplification (OPA) and parametric fluorescence is also limited to this short time window. This creates an immense potential for improvement of the pulse contrast if short pump pulses are applied.

C. In OPCPA amplifiers a much higher single-pass gain can be achieved compared to conventional lasers. Thus a chain of several single-pass OPCPA stages can substitute a chain of rather complicated multi-pass laser amplifiers, making the setup more simple and compact.

These features make the OPCPA scheme attractive and first high power amplification was shown in [54] (120 fs, 3 J) or [55] (84 fs, 35 J). Several large scale laser systems which are currently in the development phase are fully based on OPCPA [56] (30 fs, 30 J) or at least mixed OPCPA with conventional power amplifiers [57] (150 fs, 200 J), [58] (15 fs, 150 J). The probably most important project is the pan-European ELI project involving more than 40 research institutions from 13 European countries [3] (200 PW in several beams of 20 fs, 200 J).

1.4 THE PETAWATT FIELD SYNTHESIZER- PFS

The main drive for the development of the PFS system is attosecond physics [59, 2]. The potential of this relatively young field of physics could be dramatically enhanced, if current limitations in photon flux and photon energy can be overcome. This would afford a different mechanism for attosecond pulse generation- high harmonic generation from solid surfaces [60]. In theory, this process has much higher conversion efficiency than currently achievable and is scalable with laser intensity.

In order to exploit its full potential, few-cycle pulses with highly relativistic intensity are required, which would allow this technique to extend the photon energy of attosecond pulses to the extreme ultraviolet and soft-X-ray regime [1]. At the same time the flux is expected to increase by several orders of magnitude, enabling attosecond pump/attosecond probe spectroscopy. Therefore real-time observation and control of charge transfer in molecular systems will become feasible for the first time.

The PFS is a petawatt OPCPA system, currently developed at the Max-Planck-Institut für Quantenoptik (MPQ). The goal of this system is to produce few-cycle pulses with several joule of energy, ideally 5 fs with 5 J (1 petawatt peak power). This system will rely on the OPCPA technique described above and combine ultra-broadband amplification with PW-scale peak power. This combination has not been reached so far and will give the PFS an outstanding position in the current field of petawatt class laser systems.

1.4.1 *PFS strategy*

The PFS design is based purely on OPCPA technology in order to achieve the ambitious goals and to combine high energy amplification of several Joules energy with few-cycle, few-femtosecond pulse durations. The design of this OPCPA system is therefore challenging in many aspects:

HIGH ENERGY The extraction of several Joules of energy requires large apertures on the order of 10 cm due to the optical damage threshold of the surface or coating. In most existing broad-band OPA systems the nonlinear medium used for amplification is BBO or LBO due to the extraordinarily large phasematching bandwidth they can support [61]. Current technology does not allow for BBO or LBO to be grown in the sizes required for the Joule-level pulses targeted by PFS. The only useful crystal available with large enough apertures are the more narrow-band KDP and the deuterated KDP (deuterated potassium dihydrogen phosphate (DKDP)) [62].

In high average-power applications, absorption can cause crystal heating (which influences the phase matching) or even damage of the crystal. Therefore the crystal must be transparent for the whole bandwidth of both, the broad-band signal and idler. The DKDP has a larger transmission window than KDP and is therefore chosen as amplifier crystal in the PFS OPCPA design.

ULTRA-BROAD BAND OPCPA In noncollinear OPA, the additional degree of freedom (the noncollinear angle) helps to achieve approximate phase matching for a large spectral range. The bandwidth depends on the remaining phase mismatch and therefore on the crystal thickness. This fundamental principle of OPA can be used to design few-cycle OPCPA systems simply by reducing the crystal thickness. The drawback of this kind of scaling is that the gain will be reduced as well. Nevertheless, since the OPA gain depends on the pump intensity, this effect can be compensated when the pump intensity is increased simultaneously.

High power OPCPA systems are normally working with ns−100 ps pulse duration and are designed for intensities close to the damage threshold in order to maximize

the gain. The only way to increase the intensity further is to choose a shorter pulse length. The damage fluence scales with the square root of the pulse length (τ) [63]. Thus, the damage intensity threshold—fluence divided by time—scales as $1/\sqrt{\tau}$ and is therefore increased for a reduced τ. For pulses shorter than 10 ps this scaling is even more beneficial.

In the PFS, mm-thin DKDP crystals will be applied together with a 1 ps pulse duration in order to achieve the ultra-broadband amplification with significant gain per amplifier stage. The seed bandwidth is given by the pump wavelength of 515 nm and phase matching and coves the range of $700 - 1400$ nm. [64] In this case (close to the degenerate case) the idler covers a wavelength range of $820 - 1950$ nm.

A direct consequence of the short pump pulse length is the small stretching factor for the seed pulses, which allows the use of a simple and high throughput compressor consisting of bulk material and/or chirped mirrors. The most important advantage is that the fluorescence is limited to the 1 ps pump time, which results in superior pulse contrast outside this time window, which is a requirement for many high intensity experiments.

However, the pump and seed pulses need to be synchronized on a timescale much shorter than the pulse duration in order to provide a stable amplification. This principle is inherent in OPA, but becomes especially severe for the short picosecond pulse duration in our approach. Therefore, the signal and the pump pulses are optically synchronized by deriving them from the same master oscillator.

PUMP LASER As described above, the requirements for the pump laser for this new approach are far from trivial. Following the PFS rationale, in order to achieve the goal of 5 fs pulses with several Joules energy, a pump laser delivering 4 beams with 1 ps, 5 J at 515 nm is required. Such a laser is not commercially available and the design and development of this pump laser constitutes one of the main challenges of the PFS project. The pump laser is planned at 10 Hz repetition rate and is based on CPA in diode-pumped Yb:YAG and subsequent frequency doubling. This thesis treats compression and dispersion management aspects of this pump laser. The unique combination of bandwidth engineering in natively narrow-band Yb:YAG, and a large stretching factor to keep the damage fluence low enough makes this a particularly challenging task.

As the OPCPA system is designed for 1 ps pulses, synchronization between pump and seed pulses to less than 100 fs is a crucial issue. The characterization of the synchronization and a theoretical model for additional timing jitter occurring in the system will be discussed in detail in this thesis.

1.5 THESIS OUTLINE

After the general introduction and the motivation for the PFS system in this chapter, the properties of short light pulses are described in Chapter 2. The spatial characteristics and propagation of Gaussian beams are presented in addition to the propagation of short pulses in dispersive media and spatio-temporal couplings. Subsequently, the PFS OPCPA system is described in detail: In Chapter 3 special focus lies on the design of the OPCPA stages and the generation of the seed pulses for

the OPCPA signal and the pump laser. Chapter 4 is dedicated to the pump laser. The amplifiers of the pump laser chain are briefly described in separate sections. Gain narrowing is simulated and the technique of spectral shaping for preserving the bandwidth is introduced. The experimental results for the amplification of spectrally shaped pulses are compared to simulations. The main focus of this chapter lies on the dispersion management. The stretcher and compressor design is presented in combination with ray-tracing analysis. A detailed discussion of aberrations and alignment sensitivity is given.

The main results of this thesis are presented in the experiments part (Part iii). In Chapter 5, the compression of the 3.5 nm broad amplified spectrum to sub-picosecond level is presented. Followed by modifications in the dispersion management, which lead to an even broader bandwidth and a shortened compressed pulse duration on the order of 700 fs. Finally, a redesigned compressor in combination with a vacuum chamber is proposed and will be installed in the future.

In Chapter 6, fluctuations in the arrival time of the signal and pump pulse in the OPCPA are investigated. After the description of the measurement setup, different timing measurements are presented. From these measurements the stretcher/compressor setup is identified as main source for timing jitter. Based on these measurements, in Section 6.3 a novel theory for path-length differences caused by angle changes in a compressor setup is developed. This theory helps to improve the timing jitter significantly: Systematic jitter measurements in combination with beam pointing measurements are described, which resulted in changes of the grating mount in the stretcher and the installation of a new air-tight stretcher box. The implementation of a compressor vacuum chamber will further reduce the timing fluctuations in future. An active stabilization is applied to remove slow fluctuations and to stabilize the timing to 100 fs. This improved jitter level enabled first OPCPA experiments, which are summarized briefly.

Part I

THEORY

2

DESCRIPTION OF LASER PULSES

The electric field of a light pulse is described as a vector and can be a complicated function of space and time in general. In order to simplify things, it is often useful to consider only one component of the field. The so called scalar approximation [65] is equivalent to considering linear polarized light and is therefore justified for many applications. As for all light waves this electric field has to satisfy the wave equation, which can be derived directly from Maxwell's equations (i.e. [66]):

$$\nabla^2 E - \frac{n^2}{c^2}\frac{\partial^2 E}{\partial^2 t^2} = 0. \tag{2.1}$$

This is the wave equation for a linear, homogeneous and isotropic medium with refractive index n. The real wave function, with physical meaning, can be expressed as a sum of a complex function and its conjugate complex function. Often, the complex conjugate is left out during calculations for convenience and all calculations are performed with the complex wavefunction instead [67]:

$$E(\bar{r},t) = a(z,t)U(\bar{r})exp(-i\phi(t)), \tag{2.2}$$

where $\phi(t) = \omega_0 t$ is the temporal phase and $a(z,t)$ and $U(\bar{r})$ are the longitudinal and transverse envelope, respectively. The real wave function with physical meaning can be easily obtained as real part of this complex wave function.

This ansatz assumes that the pulse propagates in z-direction with the carrier frequency $\nu_0 = \omega_0/2\pi$. In order to gain a better understanding, in Section 2.1 the spatial characteristics of laser beams are discussed separately while the temporal characteristics are neglected. Thereafter, in Section 2.2 the temporal description of short pulses will be introduced, neglecting the spatial shape of the pulse. Subsequently, spatio-temporal couplings up to the first order are discussed in Section 2.3.

2.1 SPATIAL CHARACTERISTICS OF LASER BEAMS- GAUSSIAN BEAMS

Neglecting the longitudinal envelope in Equation 2.2 i.e $a(z,t) = 1$, the complex wavefunction rewrites as

$$E(\bar{r},t) = U(\bar{r})exp(-i\omega_0 t). \tag{2.3}$$

The separation of variables in this ansatz can be utilized to yield a time-independent equation by substituting this ansatz in the wave equation (Equation 2.1) one obtains

$$(\nabla^2 + k^2)U(\bar{r}) = 0, \tag{2.4}$$

the so called Helmholtz equation [68], where $k = n\,\omega_0/c = 2\pi\, n/\lambda_0$ is the wavenumber.

Following for example Saleh [67], a wavefront is considered to be paraxial when its wavefront normals are paraxial rays. This can be achieved when $U(\bar{r})$ is expressed as a plane wave with a slowly varying amplitude $F(\bar{r})$.

$$U(\bar{r}) = F(\bar{r})exp(ikz) \tag{2.5}$$

The variation of $F(r)$ has to be small on the length of a wavelength in order to approximately maintain the paraxial character of the plane wave. This constraint can be written as $\Delta F << F$ within a distance $\Delta z = \lambda$. For small quantities it can be written $\Delta F/\Delta z = \partial F/\partial z$. By replacing ΔF with F and Δz with λ, it follows that $\frac{\partial F}{\partial z} << kF$ and $\frac{\partial^2 F}{\partial z^2} << k^2 F$. Applying this to Equation 2.4 and neglecting $\frac{\partial^2 F}{\partial z^2}$ in comparison with $\frac{\partial F}{\partial z}$, one obtains the paraxial Helmholtz equation

$$\nabla_T^2 F + 2ik\frac{\partial F}{\partial z} = 0, \tag{2.6}$$

where $\nabla_T^2 = \frac{\partial^2}{\partial x^2} + \frac{\partial^2}{\partial y^2}$ is the transverse Laplacian operator. The most important solution to this paraxial Helmholtz equation is the Gaussian beam which is also the suitable model to describe the propagation of ideal laser beams [68]:

$$F(\bar{r}) = \frac{F_0}{q(z)}\, exp\left(-ik\frac{x^2+y^2}{2q(z)}\right), \tag{2.7}$$

where $q(z) = z + iz_0$ and the parameter z_0 is known as Rayleigh length.

2.1.1 *Properties of Gaussian beams*

The Properties of such Gaussian beams are described in various textbooks, and this section is based on [69, 68, 70]. Defining two new parameters $R(z)$ and $w(z)$ one can rewrite $1/q(z)$

$$\frac{1}{q(z)} = \frac{1}{R(z)} - i\frac{\lambda}{\pi w^2(z)}. \tag{2.8}$$

Using this expression and $\rho^2 = x^2 + y^2$, the complex amplitude $U(\bar{r})$ of the Gaussian beam takes the form:

$$U(\bar{r}) = F_0\frac{w_0}{w(z)}\, exp\left(-\frac{\rho^2}{w^2(z)}\right)\, exp\left(-ikz - ik\frac{\rho^2}{2R(z)} + i\zeta\right), \tag{2.9}$$

where $w(z)$ is the beam width, $R(z)$ is the wavefront radius of curvature and $\zeta(z)$ is the Gouy phase. These functions are plotted in Figure 2.1 and explained in more detail in the following.

$$w(z) = w_0\sqrt{1+\left(\frac{z}{z_0}\right)^2} \tag{2.10}$$

$$R(z) = z\left[1+\left(\frac{z_0}{z}\right)^2\right] \tag{2.11}$$

$$\zeta(z) = arctan\frac{z}{z_0} \tag{2.12}$$

$$w_0 = \sqrt{\frac{\lambda z_0}{\pi}} \tag{2.13}$$

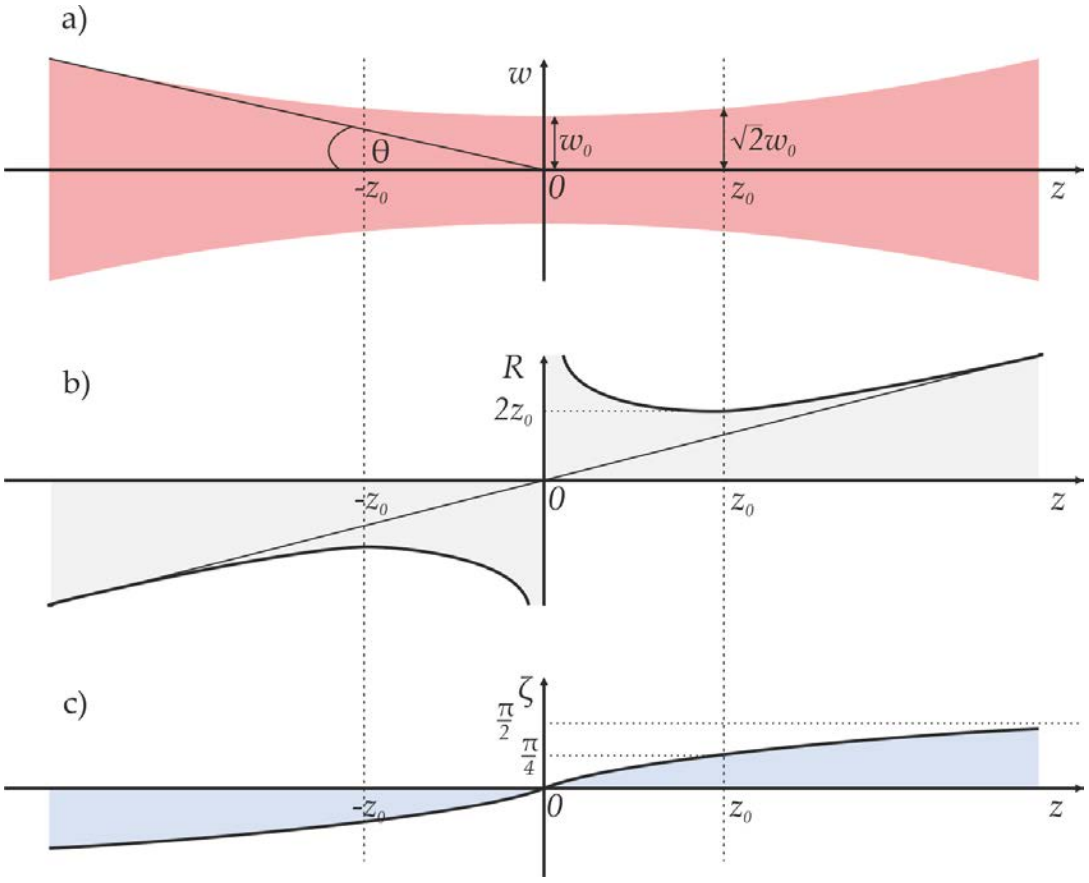

Figure 2.1: a) shows the change of the beam radius w with propagation distance z. Starting from the minimum w_0 at $z = 0$ the beam increases to $\sqrt{2}\,w_0$ at the Rayleigh length z_0. For large z the radius increases linearly with θ. In b) The dependence of the wavefront radius of curvature R on the distance z is shown. At $z = 0$ the wavefront is plane, at z_0 the curvature takes its minimum and converges asymptotically to the wavefront curvature of a spherical wave (shown as linear curve). Graph c) illustrates the Gouy phase ζ which shifts the wavefront of a Gaussian beam compared to a plane wavefront by $\frac{\pi}{2}$ for large z.

BEAM WIDTH Equation 2.10 describes how the beam radius is changing when the beam is propagating in z-direction. Obviously, $w(z)$ takes its minimum value w_0 at $z = 0$, called beam waist. For $z = z_0$ (Rayleigh range) the beam size is increased to $w(z_0) = \sqrt{2}w_0$ leading to a reduction of the intensity by a factor of 2. The double Rayleigh range $2\,z_0$ is often called the confocal parameter or depth of focus because the increase of the beam size is moderate in this range. For values $z >> z_0$ the first term in Eq.2.10 can be neglected and w shows a linear dependence of z with a half-opening angle of θ.

$$w(z >> z_0) = \frac{w_0}{z_0} z = tan(\theta)\, z \tag{2.14}$$

WAVEFRONT RADIUS OF CURVATURE Equation 2.11 describes how the wavefront radius of curvature changes when the beam propagates in z-direction. At $z = 0$ (waist position) the curvature is infinite corresponding to a plane wavefront. It decreases to a minimum value of $2\,z_0$ at $z = z_0$ and increases again for larger z. For $z >> z_0$, the first term in Eq.2.11 is negligible and $R(z) = z$, which describes the wavefront curvature of a spherical wave.

GOUY PHASE As described in the previous paragraph, the wavefront changes from planar at the focus position to spherical for large distances. The Gouy phase (Eq.2.12) introduces a phase shift with increasing z. For large z the phase front on the optical axis is advanced by $\frac{\pi}{2}$ compared to a plane wave with the same origin leading to an effectively increased local phase velocity.

2.1.2 *Gaussian beam propagation through optical systems*

A commonly method applied for the propagation through optical systems in paraxial ray optics is the ABCD matrix formalism. It is outlined in e.g. [71], and the following paragraph is based on that treatment. An optical ray is fully described by its distance x and angle α to the optical axis. A general paraxial optical system is characterized by its effect on an incoming ray with arbitrary x and α. The interaction of a ray with an optical system can then be written in Matrix form:

$$\begin{pmatrix} x_2 \\ \alpha_2 \end{pmatrix} = \begin{pmatrix} A & B \\ C & D \end{pmatrix} \begin{pmatrix} x_1 \\ \alpha_1 \end{pmatrix} \tag{2.15}$$

Since the displacements and angles are assumed to be small, the matrix elements can be expressed as partial derivatives of the output parameters corresponding to the input parameters. For example $A = \partial x_{out}/\partial x_{in}$ and $D = \partial \alpha_{out}/\partial \alpha_{in}$ are the spatial and angular magnification, respectively. $C = \partial \alpha_{out}/\partial x_{in}$ is the refraction power of the system. If $B = 0$, it follows that $x_{out} = A\ x_{in}$ and the system is of imaging type. Matrices for many optical components are known and an optical system consisting of many different components can be described as matrix multiplications of the corresponding component matrices. For example the matrix for free space propagation over distance d and for a thin lens are $F = \begin{pmatrix} 1 & d \\ 0 & 1 \end{pmatrix}$ and $L = \begin{pmatrix} 1 & 0 \\ -\frac{1}{f} & 1 \end{pmatrix}$, respectively.

In [72] it is shown that the propagation of a Gaussian beam through a paraxial optical system described by an ABCD matrix can be calculated with a generalized Huygens' integral. As a result, a Gaussian beam at the output plane is obtained but with a transformed q-parameter

$$\frac{1}{q_2} = \frac{C\,q_1 + D}{A\,q_1 + B}. \tag{2.16}$$

With this transformation law it is possible to extend the well-established ABCD matrix formalism to Gaussian beams. As a simple example the propagation of a Gaussian beam through a thin lens is considered. The incident beam has its waist w_0 at the start position and, as follows from Equation 2.8, is fully characterized by the complex expression $q_1 = i\frac{\pi\, w_0^2}{\lambda}$. The beam propagates the distance f to the lens, then is transmitted through the lens and propagates again over a distance f to the back focal plane. The matrix for this system can be obtained by the matrix multiplication $F \cdot L \cdot F$, with $d = f$. The result is the system matrix

$$\begin{pmatrix} 0 & f \\ -\frac{1}{f} & 0 \end{pmatrix} \tag{2.17}$$

Together with Equation 2.16 one obtains:

$$\frac{1}{q_2} = -\frac{1}{f^2}\, q_1 = i\frac{\pi w_0^2}{\lambda f^2} \tag{2.18}$$

Here, the function $1/q_2$ has no real part. A vanishing the real part in Eq.2.8 means $R = \infty$. A plane wavefront is present in the waist of a laser beam only. Therefore, the first result of the ABCD analysis of the system is that the laser waist is exactly at the back focal plane if the incident laser beam has its waist in the front focal plane of the focusing lens. This is a special feature of Gaussian beams and it should be noted that the system is not imaging in the classical sense (i.e. $B \neq 0$). Comparison of the imaginary part of Eq.2.18 with Eq.2.8 results in the relation for the focused beam radius w_2:

$$w_2 = \frac{\lambda}{\pi}\frac{f}{w_0} \tag{2.19}$$

Different cases are included in this example: When $f << z_0$, the input waist is large and the beam is collimated. In this case the radius of curvature stays infinite for the propagation to the lens. The lens changes R to $-f$ (according to the well-known law: $1/R_{out} = 1/R_{in} - 1/f$) and produces a small waist at the back focal length. This scenario is equivalent to the illumination of a lens with a parallel bundle in ray optics.

If $f = z_0$, the radius of curvature is $2f$ at the lens position. The effect of the lens is a change of R to $-2f$ and the propagation to the back focal length is symmetric. According to 2.19, the waist in the output plane is identical to the waist in the input plane for this special case.

When $f >> z_0$, the propagation is inverse to the case with $f << z_0$: the input waist is small and $R = f$ after propagation to the lens. The lens changes R to ∞ and produces a large waist in the back focal plane.

As example a focal length of $f = 100\,\text{mm}$ is considered with light of $\lambda = 1030\,\text{nm}$. For an input beam with $w_0 = 10\,\text{mm}$, the Rayleigh length is $z_0 = 305\,\text{m}$ ($f << z_0$) and the output waist w_2 is $3.3\,\mu\text{m}$ small. The case $f = z_0$ is valid for an input waist of $w_0 = 181\,\mu\text{m}$ and the output waist has the same size as the input. As example for the $f >> z_0$ case, a $w_0 = 10\,\mu\text{m}$ waist with $z_0 = 305\,\mu\text{m}$ can be considered, which is converted to a $w_2 = 3.3\,\text{mm}$ waist at the output.

This example shows the power of the ABCD matrix formalism for the propagation through optical systems. The formalism can also be used for more complex systems and is especially important for analyzing resonator cavities and modes [73]. The matrix for a full cavity round trip is obtained by multiplying the matrices for all individual components in the cavity including free-space propagation matrices. The constraint for a stable cavity eigensolution (mode) is that the laser beam is reproduced after a full round trip i.e. $1/q_1 = 1/q_2$ in Equation 2.16. Rearranging of this equation leads to a quadratic equation which can be solved by [73]:

$$\frac{1}{q_{1/2}} = \frac{A-D}{2B} \pm \sqrt{\left(\frac{A-D}{4B}\right)^2 + \frac{C}{B}} \tag{2.20}$$

In order to find a statement for the stability of a certain eigensolution, a calculation with a small perturbation of the mode can be performed [74]. As a result the mode is considered to be stable when:

$$-1 < \frac{A+D}{2} < 1 \tag{2.21}$$

If there are asymmetries in the system like tilted curved mirrors or uncollimated beams on Brewster windows, the calculation has to be performed separately on the meridional (plane which contains the chief ray and the optical axis) and sagittal plane (perpendicular to the meridional plane). For example, a tilted curved mirror with the radius of curvature R will have a modified curvature $R_m = R\,cos(\theta)$ and $R_s = R/cos(\theta)$ in the meridional and sagittal plane, respectively.

2.2 PROPAGATION OF SHORT LASER PULSES IN DISPERSIVE MEDIA

This section is based on the book by Trebino [65]. In this section, the transverse envelope of the electric field (Equation 2.2) is ignored and the temporal dependence of the pulse is again written as a complex field in order to facilitate the calculations:

$$\tilde{E}(t) = \sqrt{I(t)}e^{-i\phi(t)}e^{i\omega_0 t} = E(t)\,e^{i\omega_0 t}, \tag{2.22}$$

where $I(t)$ and $\phi(t)$ are the time-dependent intensity and phase of the pulse. These quantities can be separated from the $e^{-i\omega_0 t}$ term—an oscillation with the carrier frequency ω_0.

This term shifts the center of the spectrum from zero to ω_0, as can be seen by performing the Fourier transform from time to frequency domain:

$$E(\omega) = \int dt\,\tilde{E}(t)e^{-i\omega t} = \int dt \sqrt{I(t)}e^{i\phi(t)}\,e^{-i(\omega-\omega_0)t} \tag{2.23}$$

The $e^{-i\omega_0 t}$ term is often omitted when describing pulses in the time domain (because especially for long pulses with a large number of optical cycles it does not make sense to plot the fast oscillations) but at the same time the spectrum is still centered around ω_0 which would correspond to the full field in Eq.2.22. This is an inconsistency one has to keep in mind.

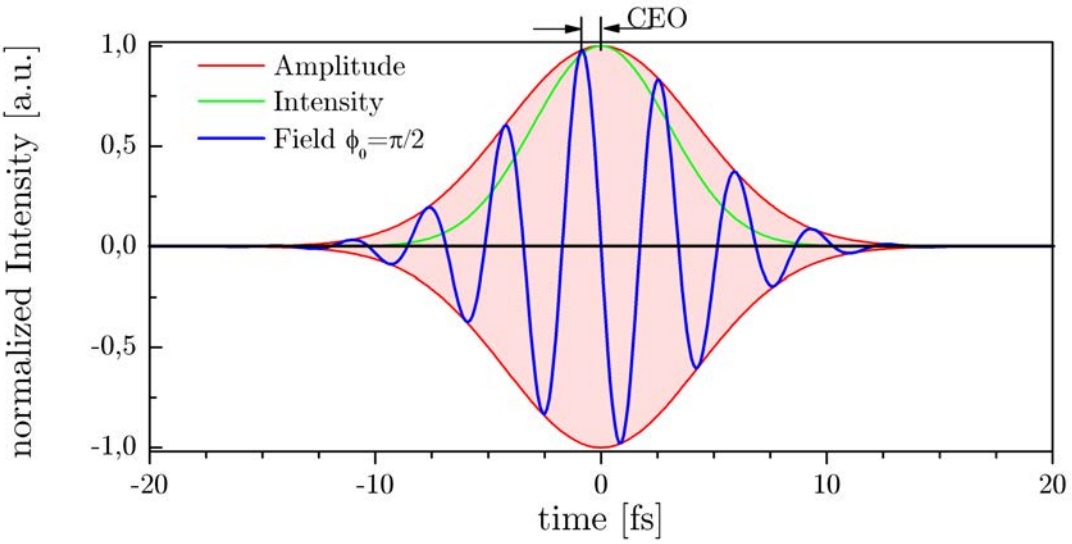

Figure 2.2: Representation of an ultra-short (Gaussian) laser pulse with $\lambda_0 = 1030nm$ and 10 fs pulse length (FWHM). The electric field (blue) has a CEO phase of $\pi/2$. The intensity (green) of a Gaussian pulse is factor $\sqrt{2}$ shorter than the envelope (red).

Figure 2.2 illustrates the intensity, the envelope (i.e. $\sqrt{I(t)}$ term) and the complete field for a few cycle pulse.

As in the time domain, an intensity and phase function can be defined in the frequency domain.

$$E(\omega) = \sqrt{S(\omega)}\, e^{i\varphi(\omega)} \tag{2.24}$$

The quantity $S(\omega)$ is the measurable spectrum and $\varphi(\omega)$ is the spectral phase. When a pulse propagates through a medium with length L, the spectral phase is changed due to the dispersion of the medium (the frequency dependent refractive index $n(\omega)$). Also, constant or frequency-dependent absorption $\alpha(\omega)$ will change the spectrum.

$$S_{out}(\omega) = S_{in}(\omega) e^{-\alpha(\omega)L} \tag{2.25}$$

$$\varphi_{out}(\omega) = \varphi_{in}(\omega) + i\, n(\omega) \frac{\omega}{c} L \tag{2.26}$$

Absorption (or the frequency-dependent gain- in the case of laser amplification) can alter the spectrum but more importantly change the phase. For an approximate

mathematical description, it is common to write the temporal and the spectral phase as Taylor series expanded around $t = 0$ and $\omega = \omega_0$, respectively

$$\phi(t) = \phi_0 + \phi_1 t + \frac{\phi_2}{2} t^2 + \dots \tag{2.27}$$

$$\varphi(\omega) = \varphi_0 + (\omega - \omega_0)\varphi_1 + (\omega - \omega_0)^2 \frac{\varphi_2}{2} + \dots, \tag{2.28}$$

where the index stands for the n-th derivative carried out at the expansion point. The advantage is that higher orders are usually less pronounced and can be neglected. Additionally, it is possible to look at the effects of the different orders separately. It can be shown [65] that the instantaneous angular frequency is

$$\omega_{inst} = \omega_0 - d\phi/dt. \tag{2.29}$$

A direct consequence is for example that the zeroth order temporal phase does not change the frequency. In the following, the meaning of the individual orders of the temporal and spectral phase (i.e. Equation 2.27 and 2.28) are discussed in detail.

2.2.1 *The zeroth-order phase- CEO phase*

The constant terms in Eqs. 2.27 and 2.28 are identical, i.e. $\phi_0(t) = \varphi_0(\omega)$. The reason is the linear character of the Fourier transform. The zeroth-order phase is often called carrier-envelope-offset phase (CEO phase) and describes the relative offset of the maximum of the electric field compared to the maximum of the envelope as depicted in Figure 2.2. The CEO phase is very important for ultra-short pulses with few optical cycles, because the peak electric field can vary drastically with the CEO phase. For longer pulses this effect is minor and the CEO phase is often neglected in this case.

2.2.2 *First-order phase*

In Equation 2.23 it was already discussed that a linear temporal phase term ($\omega_0 t$) results in a spectral shift. The analog behavior is observed for a linear spectral phase φ_1 which results in a temporal shift. Hence, φ_1 is also called group delay (GD).

2.2.3 *Second order phase- linear chirp*

The second order temporal phase (a non-zero value of ϕ_2) is the lowest order term which creates a variation of the instantaneous frequency over time. Considering a pulse with Gaussian amplitude and quadratic temporal phase $\phi(t) = -bt^2$, one obtains [65]:

$$E(t) = E_0\, e^{-at^2}\, e^{ibt^2} = E_0\, e^{-(a-ib)t^2}, \tag{2.30}$$

where E_0 is a constant and b is the chirp parameter. The Fourier transform of this field is (see Section A.4):

$$E(\omega) = \frac{E_0\sqrt{\pi}}{\sqrt{a - ib}}\, exp\left[-\frac{\omega^2}{4(a - ib)}\right] \tag{2.31}$$

Separating this in spectrum and phase, a Gaussian spectrum and a quadratic spectral phase are obtained.

$$S(\omega) = \frac{E_0^2 \pi}{\sqrt{a^2+b^2}} exp\left[-\frac{a\omega^2}{2(a^2+b^2)}\right] \tag{2.32}$$

$$\varphi(\omega) = \frac{b}{(a^2+b^2)}\omega^2 \tag{2.33}$$

As a result, a Gaussian amplitude in time corresponds to a Gaussian amplitude in the frequency domain and a quadratic phase $\phi(t)$ corresponds to a quadratic spectral phase $\varphi(\omega)$. The second order spectral phase is also called group delay dispersion (GDD).

Propagation through materials usually causes positive linear chirp (positive GDD). This means, the high frequency components will move to the rear of the pulse and the low frequency components will lead.

2.2.4 *Higher order phase- TOD, FOD*

Material or dispersive elements (chirped mirrors, gratings, prisms) introduce higher order spectral phase, as well. Often φ_3 or third order dispersion (TOD) and φ_4 or forth order dispersion (FOD) are also considered. Usually one talks about the spectral phase, because the spectrum is easily measurable and thus a full description of the pulse can be given. Contrastingly, it is more difficult to measure the intensity vs. time to achieve the same in the time domain.

In Figure 2.3 the effects of the different dispersion terms are shown. In order to gain a feeling for the magnitude of relevant dispersion in the PFS pump laser, the calculations are carried out for pulses with $\lambda_0 = 1030\,\text{nm}$ and $\tau = 1\,\text{ps}$, roughly corresponding to the ones produced by the PFS pump laser described in Chapter 4. Figure 2.3(b)-(d) show the magnitude of the GDD, TOD, or FOD which increase the initial full width at half maximum (FWHM) pulse length by 10%.

The effect of the different orders of dispersion on the pulse shape is more pronounced on a logarithmic scale (see right side in Fig.2.3). While GDD and FOD broaden the pulse symmetrically, TOD introduces prepulses (or postpulses depending on the sign of φ_3). Generally higher order phase terms decrease the peak intensity and the pulse contrast: energy from the main peak is transferred to the wings.

In a real world application of a CPA system it is difficult to compensate all higher orders exactly. If designed and set up properly, the compressor can completely cancel out the dispersion of the stretcher (as will be discussed in Chapter 4), but the material dispersion of the laser chain (air, transmission optics, amplifier media etc.) usually prevents full dispersion compensation.

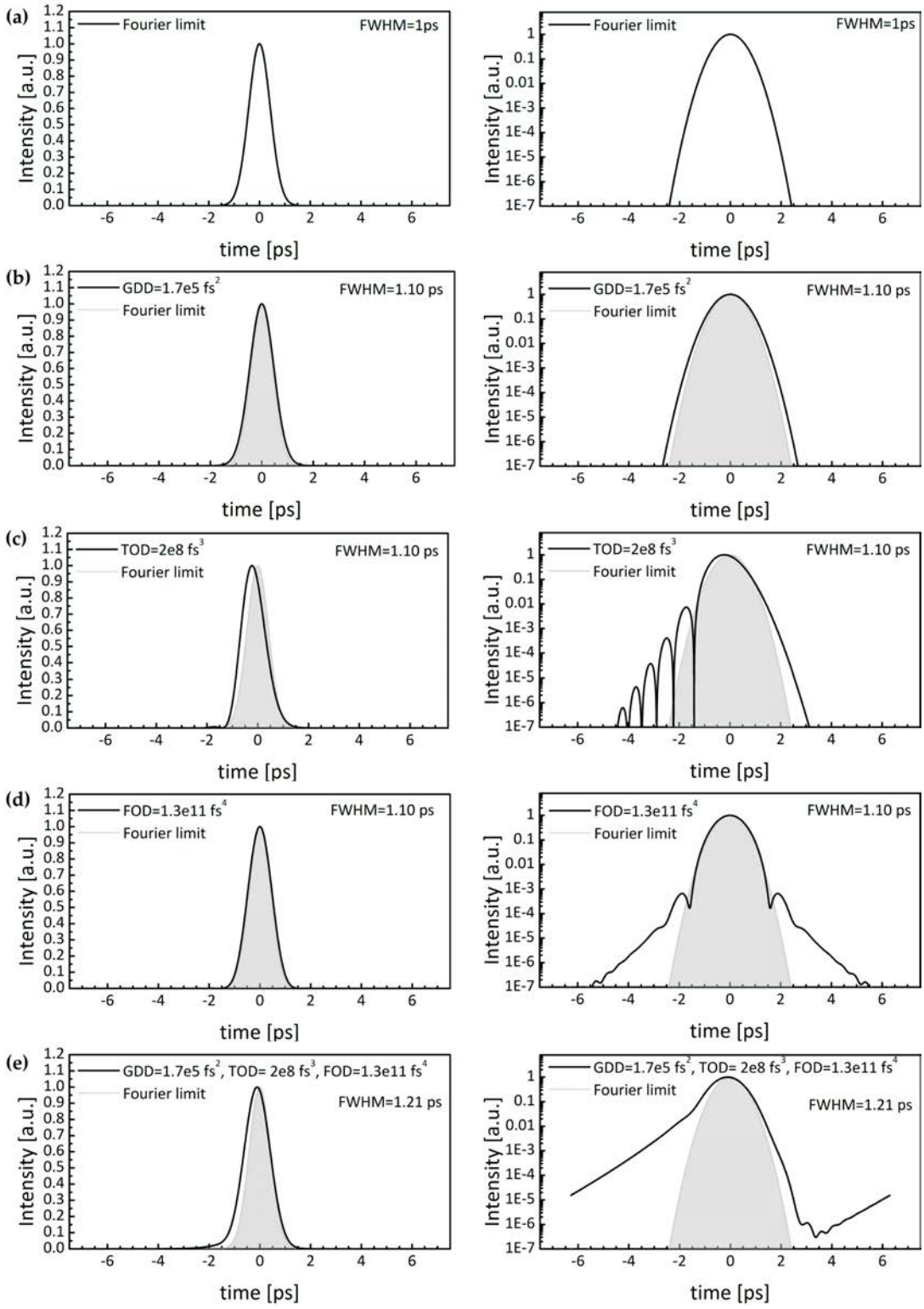

Figure 2.3: Comparison of different dispersion terms. A Gaussian-intensity pulse with constant phase $\varphi = 0$ (a), GDD= $1.7e5\,\mathrm{fs}^2$ (b), TOD= $2e8\,\mathrm{fs}^3$ (c), FOD= $1.3e11\,\mathrm{fs}^4$ (d), and with all phase terms from b-d combined (e) are shown on a linear scale (left) and on a logarithmic scale (right). The individual phase terms are chosen in a way to increase the FWHM by 10%. The effect of the different phase terms on the pulse wings are more pronounced on the logarithmic scale.

With the two degrees of freedom in the compressor (angle and grating separation) it is in principle possible to correct up to third order exactly but the higher orders can be large for this case. In order to get a feeling which order of magnitude in the different dispersion orders is tolerable, some example values are combined in Table 2.1.

increase in τ_{FWHM}	GDD [fs^2]	TOD [fs^3]	FOD [fs^4]
10%	$1.7 \cdot 10^5$		
10%		$2 \cdot 10^8$	
10%			$1.3 \cdot 10^{11}$
20%	$1.7 \cdot 10^5$	$2 \cdot 10^8$	$1.3 \cdot 10^{11}$
$< 0.1\%$	$1.7 \cdot 10^4$		
$< 0.1\%$		$2 \cdot 10^7$	
$< 0.1\%$			$1.3 \cdot 10^{10}$
$< 0.4\%$	$1.7 \cdot 10^4$	$2 \cdot 10^7$	$1.3 \cdot 10^{10}$

Table 2.1: Effect of different dispersion orders on the FWHM pulse length of a 1 ps pulse at 1030 nm.

The different dispersion orders from Fig.2.3 which still enable compression to 10% above the Fourier limit are summarized in the upper part of Table 2.1. As seen in the right hand side of Figure 2.3, these values for the dispersion terms distort the temporal wings a lot and reduce the pulse contrast significantly. In the lower part of Table 2.1 it is suggested that a factor 10 less dispersion will already be so close to perfect compression, that it cannot be distinguished by a pulse length measurement. These values for the dispersion terms have also a minor influence on the contrast, as shown in Figure 2.4.

Here, the contrast for a pulse with Gaussian spectrum and flat phase is compared to a pulse with identical spectrum, but with a phase consisting of the dispersion terms from the last row of Table 2.1. It shows that this phase does not significantly change the pulse contrast. Therefore, it can be concluded that it is enough to compensate the dispersion terms to the mentioned order of magnitude (last row of Table 2.1) to compress the narrow-band PFS pump pulses at 1030 nm to 1 ps.

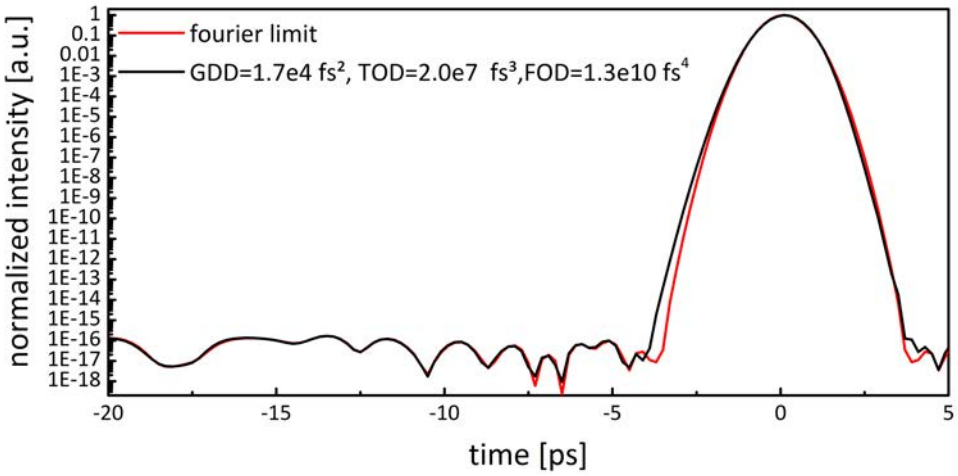

Figure 2.4: Comparison of the contrast for a Fourier-limited pulse and a pulse with the dispersion terms from the last row of Table 2.1. The remaining noise level on the order of 10^{-16} is caused by the numerical calculation on a discrete spectrum on a truncated wavelength range.

2.2.5 *The time-bandwidth product*

A direct consequence of the Fourier principle is that the widths in the time domain $\Delta\tau$ and in the frequency domain $\Delta\omega$ are related (this can also be seen in Eqs.2.30 and2.32). In order to synthesize a short pulse from individual monochromatic waves, a broad spectrum of wavelengths is needed. This fact is usually expressed as time-bandwidth product $\Delta\tau\Delta\omega$. It can be shown [75] that for any spectrum the shortest pulse (and also the smallest time-bandwidth product) occurs for a flat temporal phase.

$$\Delta\tau\,\Delta\omega \geq \mathcal{O}(1) \tag{2.34}$$

The exact form of Equation 2.34 depends on the shape of the pulse envelope and on the definition of the width. For example the FWHM time-bandwidth product for a Gaussian and sech^2 temporal profile are 2.77 and 1.98, respectively.

2.3 SPATIO-TEMPORAL COUPLING

In the previous sections, the spatial and temporal dependencies of the electric field were discussed separately. This formalism implies that the spatial dependence of a pulse is completely separable from its time or frequency dependence. However, especially for the generation of ultra-short pulses spatio-temporal couplings are used in stretcher and compressor setups.

Considering a typical compressor setup several of such couplings are involved. A dispersive element (prism or grating) introduces angular dispersion (coupling of spatial frequency and frequency) and at the same time pulse-front tilt (the arrival time of the intensity maximum varies over the transverse direction). Propagation of an angularly dispersed beam introduces spatial chirp (frequency varies over position). These effects are used to create different optical paths for different wavelength

and therefore the necessary different delay (temporal chirp). A second identical and parallel dispersive element removes the angular dispersion but the spatial chirp remains. In order to remove the unwanted spatial chirp, two more dispersive elements (or a retro reflector) are necessary. If these dispersive elements are not exactly parallel, some spatio-temporal coupling will remain. A pulse with strong distortions of this kind will be useless for certain applications. Therefore it is important to mathematically describe these couplings. Following the line of [76], a general theory for first order spatio-temporal distortions is presented for Gaussian pulses in space and time.

2.3.1 *Matrix formalism for combined temporal and spatial effects*

Kostenbauder [77] extended the previously mentioned matrix formalism (see Section 2.1.2) to 4x4 matrices in order to treat temporal and spatial dependencies of pulses at the same time. The propagation matrix (or Kostenbauder matrix) has the form:

$$\begin{pmatrix} x_{out} \\ \alpha_{out} \\ t_{out} \\ \nu_{out} \end{pmatrix} = \begin{pmatrix} A & B & 0 & E \\ C & D & 0 & F \\ G & H & 1 & I \\ 0 & 0 & 0 & 1 \end{pmatrix} \begin{pmatrix} x_{in} \\ \alpha_{in} \\ t_{in} \\ \nu_{in} \end{pmatrix}, \tag{2.35}$$

where t is the time (group delay) and ν is the frequency. The matrix elements A, B, C, D are the same as previously mentioned for 2×2 matrices. The other elements are again the partial derivatives of the output parameters with respect to the input parameters. For example $E = \partial x_{out}/\partial \nu_{in}$ describes, how the output position depends on the frequency and therefore corresponds to a spatial chirp. $F = \partial \alpha_{out}/\partial \nu_{in}$ describes angular dispersion and $I = \partial t_{out}/\partial \nu_{in}$ is the system GDD. In the static systems considered here, the position, angle and frequency do not depend on the timing and the frequency stays constant during propagation. Therefore, several matrix elements are zero. As simple example propagation in a dispersive medium is expressed by the following matrix.

$$\begin{pmatrix} x_{in} + L/n\,\alpha_{in} \\ \alpha_{in} \\ t_{in} + 2\,\pi\,\varphi_2\,\nu_{in} \\ \nu_{in} \end{pmatrix} = \begin{pmatrix} 1 & L/n & 0 & 0 \\ 0 & 1 & 0 & 0 \\ 0 & 0 & 1 & 2\pi\varphi_2 \\ 0 & 0 & 0 & 1 \end{pmatrix} \begin{pmatrix} x_{in} \\ \alpha_{in} \\ t_{in} \\ \nu_{in} \end{pmatrix} \tag{2.36}$$

The only new term here is the GDD with a factor of 2π, since these matrices are defined for ν instead of ω. The angle and frequency stay the same and the position varies in the usual way. The group delay becomes frequency dependent and changes with $\omega_{in}\,\varphi_2$ and the pulse is therefore chirped. Matrices for many components like gratings and prisms are known [77] and complex systems can be described as matrix multiplication. At this point the propagation of rays through optical systems can be treated. Analogous to Section 2.1.2, an extension of this formalism for Gaussian beams [77] will be discussed in the following section.

2.3.2 *Extended matrix formalism for Gaussian pulses*

A Gaussian pulse in space and time (without coupling terms) can be written in the usual way:

$$E(x,t) \propto exp\left[-i\frac{\pi}{\lambda}\left(\frac{x^2}{q_x}-\frac{t^2}{q_t}\right)\right], \tag{2.37}$$

with the complex q-parameters:

$$\frac{1}{q_x} = \frac{1}{R(z)} - i\frac{\lambda}{\pi\, w^2(z)} \tag{2.38}$$

$$\frac{1}{q_t} = \frac{\lambda}{\pi}\left(\beta + \frac{i}{\tau^2}\right), \tag{2.39}$$

where R is the radius of curvature of the wavefront, w is the beam radius, β is the chirp parameter and τ is the pulse length. In order to introduce coupling terms (i.e. terms proportional to x and t) and to use the 4×4 matrices, the electric field is written in a more generalized form with a Q matrix [77]:

$$E(x,t) \propto exp\left[-i\frac{\pi}{\lambda}\left\{\begin{pmatrix} x \\ -t \end{pmatrix}^T Q^{-1} \begin{pmatrix} x \\ t \end{pmatrix}\right\}\right] \tag{2.40}$$

$$= exp\left[-i\frac{\pi}{\lambda}\left\{Q_{11}^{-1}\,x^2 + 2Q_{12}^{-1}\,xt - Q_{22}^{-1}\,t^2\right\}\right] \tag{2.41}$$

In this notation, Q^{-1} means the inverse of the matrix Q with the matrix elements Q_{ij}^{-1} of the inverse matrix and the constraint $Q_{12}^{-1} = -Q_{21}^{-1}$ [77]. It is obvious that $Q_{11}^{-1} = 1/q_x$ and $Q_{22}^{-1} = 1/q_t$. For a Gaussian beam without coupling, the matrix Q is therefore

$$Q = \begin{pmatrix} q_x & 0 \\ 0 & q_t \end{pmatrix} \tag{2.42}$$

The propagation of such an Gaussian beam through the system described by a Kostenbauder-matrix (Equation 2.35) can be calculated with a generalized transformation law [77] with a similar form as Eq.2.16:

$$Q_{out} = \left[\begin{pmatrix} A & 0 \\ G & 1 \end{pmatrix} Q_{in} + \begin{pmatrix} B & \frac{E}{\lambda} \\ H & \frac{I}{\lambda} \end{pmatrix}\right] \cdot \left[\begin{pmatrix} C & 0 \\ 0 & 0 \end{pmatrix} Q_{in} + \begin{pmatrix} D & \frac{F}{\lambda} \\ 0 & 1 \end{pmatrix}\right]^{-1} \tag{2.43}$$

As an example, a grating can be described with the system matrix M:

$$M = \begin{pmatrix} 1/\alpha & 0 & 0 & 0 \\ 0 & \alpha & 0 & \lambda\gamma \\ \gamma/\alpha & 0 & 1 & 0 \\ 0 & 0 & 0 & 1 \end{pmatrix}, \tag{2.44}$$

where $\alpha = cos\theta_i / cos\theta_d$ and $\gamma = (sin\theta_i + sin\theta_d)/(c\, cos\theta_d)$ with the diffraction angle θ_d and the incidence angle θ_i. The transformation law (Equation 2.43) can then be written:

$$Q_{out} = \begin{pmatrix} 1/\alpha & 0 \\ \gamma/\alpha & 1 \end{pmatrix} Q_{in} \cdot \begin{pmatrix} \alpha & \gamma \\ 0 & 1 \end{pmatrix}^{-1} \tag{2.45}$$

$$Q_{out}^{-1} = \begin{pmatrix} \alpha & \gamma \\ 0 & 1 \end{pmatrix} \cdot \left[\begin{pmatrix} 1/\alpha & 0 \\ \gamma/\alpha & 1 \end{pmatrix} Q_{in} \right]^{-1} \tag{2.46}$$

In absence of couplings for the input beam (i.e. Q_{in} equals Q from Equation 2.42) it follows:

$$Q_{out}^{-1} = \begin{pmatrix} \alpha & \gamma \\ 0 & 1 \end{pmatrix} \cdot \begin{pmatrix} q_x/\alpha & 0 \\ \gamma\, q_x/\alpha & q_t \end{pmatrix}^{-1} \tag{2.47}$$

$$= \begin{pmatrix} \alpha & \gamma \\ 0 & 1 \end{pmatrix} \cdot \begin{pmatrix} \alpha/q_x & 0 \\ -\gamma/q_t & 1/q_t \end{pmatrix} \tag{2.48}$$

$$= \begin{pmatrix} \alpha^2/q_x - \gamma^2/q_t & \gamma/q_t \\ -\gamma/q_t & 1/q_t \end{pmatrix} \tag{2.49}$$

The first element to discuss is the off-diagonal element Q_{12}^{-1}, which describes the coupling term. This term is complex in general and with the definition of the field (Equation 2.41), the real part causes a space and time dependent phase (Wave-front rotation) whereas the imaginary part yields a position-time coupling in the Intensity. The latter one is called pulse front tilt (PFT).

$$PFT = \frac{Im\{Q_{12}^{-1}\}}{Im\{Q_{22}^{-1}\}} = \gamma = \frac{sin\theta_i + sin\theta_d}{c\, cos\theta_d} = \frac{\partial\theta}{\partial\lambda}\, \lambda/c \tag{2.50}$$

Here, the fact was used that the parameter γ is actually the angular dispersion for a grating [78] (obtained by differentiation of the grating equation) multiplied by λ/c, where c is the speed of light. The pulse front tilt angle (ψ) i.e. the angle between the pulse front and the phase front can be expressed as $tan\psi = PFT \cdot c$:

$$tan\psi = \lambda\, \frac{\partial\theta}{\partial\lambda}, \tag{2.51}$$

which is the well-known connection between pulse front tilt and angular dispersion as derived for example by Hebling [79].

The diagonal elements of Equation 2.49 Q_{11}^{-1} and Q_{22}^{-1} represent $1/q_x^{out}$ and $1/q_t^{out}$, respectively. It can be seen that $1/q_t$ is not altered by the diffraction off the grating i.e. that the pulse length and chirp stay constant. Nevertheless, the spatial properties are changed as $1/q_x^{out} = \alpha^2/q_x - \gamma^2/q_t$. Comparison with Equation 2.38 shows $1/w_{out}^2 = \alpha^2/w_{in}^2 + \gamma^2/\tau^2$ and $1/R_{out} = \alpha^2/R_{in}^2 + \gamma^2\, \lambda\, \beta/\pi$.

It should be noted that the situation becomes much more complicated when propagation after the grating is considered. Nevertheless, it is possible with this formalism to calculate the propagation of Gaussian beams for very general systems. The

space time coupling is included so that pulse-front tilt and the so called wave front rotation can be calculated. The latter coupling is not commonly known and is difficult to measure (since it is a phase distortion) but other well-known couplings like spatial dispersion and angular dispersion were not calculated so far.

Akturk [76] presents a very general theory for first order spatio-temporal couplings. This theory is summarized in Section A.5 and reveals all possible couplings and the connections between them. For example, the useful relation:

$$PFT \propto SPC \times FCH + AGD, \tag{2.52}$$

can be obtained, which means in words that there are two different sources of a pulse-front tilt: Firstly, an angular chirp (as already discussed in Section 2.3.2) and secondly a combination of spatial chirp and frequency chirp (or temporal chirp). The latter was also described in [76]. In the application of a pulse compressor this means that the pulse front tilt introduced by a residual angular chirp could be canceled out by a certain combination of spatial and temporal chirp.

The conclusion of this theory is that there exist 8 different coupling terms (of first order), from which two have to be measured. The rest is not independent and can be calculated from these by Fourier transforms. In general 6 quantities have to be measured (from which two are coupling terms); all others can be calculated from these.

In [76] it is suggested to use the following quantities: The beam spot size, the wavefront curvature, the temporal pulse width, the temporal chirp, the pulse front tilt (which are all in the (x,t) domain) and the spatial chirp (x, ω). This selection is made, because measurement techniques exist for all these quantities: the beam size can be measured with a CCD camera, and the wavefront for example with a Shack-Hartman sensor [80]. FROG [65], GRENOUILLE [81] or SPIDER [82] are common techniques to measure the temporal pulse width and phase. The pulse front tilt can be measured with an inverted field autocorrelator [83], by spectrally resolved interferometry [84] or again with the GRENOUILLE [85]. The spectral chirp can be measured with an imaging spectrometer [86]. It is also useful to measure the spectral bandwidth in order to normalize the different quantities.

2.4 DISPERSION MANAGEMENT- STRETCHER AND COMPRESSOR

The CPA technique is a requirement for high-power short-pulse lasers. The pulses are temporally stretched before amplification in order to avoid high intensities and nonlinear effects in the material during amplification. Subsequent to the amplification, the pulses are compressed back to the minimum pulse length and thus reach high intensities inside the compressor. The ideal compressor therefore consists of reflective components only and transmission through material is avoided.

As the perhaps most widely-used compressor, a typical Treacy-type compressor setup is shown in Figure 2.5. The compressor consists of two parallel gratings with identical line density and a folding mirror. The diffraction off the first grating disperses the beam, after the second grating all wavelengths propagate parallel but are spatially separated. The fold mirror sends the beam back through the whole setup and in the exiting beam all wavelength are overlapping again. (Instead of a fold

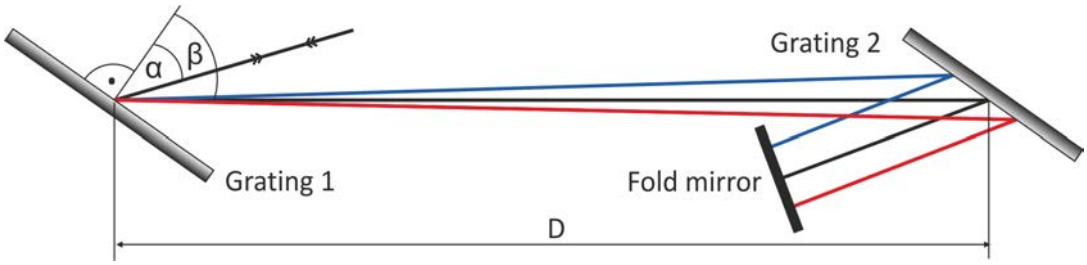

Figure 2.5: Sketch of a Treacy-type grating compressor [26] with reflection gratings. The beam path for an angle of incidence α and a refraction angle $\beta(\lambda)$ is drawn for different wavelengths.

mirror, two more gratings can be used, alternatively) This kind of pulse compressor was first studied by Treacy [26]. The spectral phase (relative to the center frequency ω_0) of a complete round trip in such a system can be written as:

$$\varphi(\omega) = 2\frac{\omega}{c} D\, cos(\beta_0 - \beta(\omega)), \tag{2.53}$$

where D is the Grating separation, c is the speed of light and β_0 and β are the diffraction angles for the center frequency and general frequencies. The grating equation relates the angle of incidence α, the wavelength λ and the refraction angle β for the refraction on a grating with a line density N at the m-th diffraction order.

$$sin(\alpha) + sin(\beta) = mN\lambda \tag{2.54}$$

Equation 2.53 and Equation 2.54 can be used to obtain analytical expressions for the dispersion orders [87] for GDD, TOD and FOD.

$$\varphi_2 = \frac{-2D\,\lambda^3\,N^2}{2\pi\,c^2\,cos^2\,\beta_0} \tag{2.55}$$

$$\varphi_3 = \frac{6D\,\lambda^4\,N^2}{4\pi^2\,c^3\,cos^2\,\beta_0}\left(1 + \frac{\lambda\,N\,sin\,\beta_0}{cos^2\,\beta_0}\right) \tag{2.56}$$

$$\varphi_4 = \frac{-6D\,\lambda^5\,N^2}{8\pi^3\,c^4\,cos^2\,\beta_0}\left[4\left(1 + \frac{\lambda\,N\,sin\,\beta_0}{cos^2\,\beta_0}\right)^2 + \left(\frac{\lambda\,N}{cos^2\,\beta_0}\right)^2\right] \tag{2.57}$$

The knowledge of the dispersion terms is important in order to optimize a compressor for a certain application. In general, the material of the laser chain and the stretcher should ideally have the same dispersion terms with the opposite sign as the compressor. In 1987, Martines [27] found a configuration including gratings and an imaging system, where the dispersion terms are the exact negative of a matching Treacy compressor. This concept is also illustrated in Figure 2.6.

The Martinez stretcher uses a 4f-imaging system together with two anti-parallel gratings. When the gratings are placed exactly in the focal planes, no net dispersion is introduced. The displacement of the gratings from the focal plane can introduce positive or negative dispersion- depending on the direction of the displacement. The version with positive dispersion is more relevant in praxis, since the Treacy compressor has negative dispersion. As shown in Figure 2.6, the gratings are placed inside the focal distance of the respective lenses. In this case, a virtual image of the

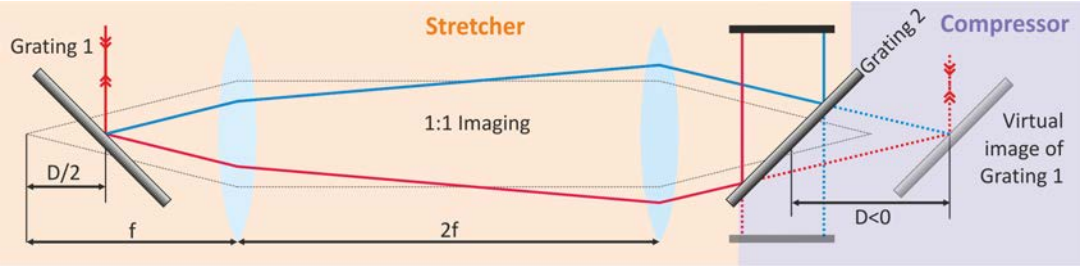

Figure 2.6: Principle setup of a Martinez stretcher [27]. Two anti-parallel gratings are used together with a 4f- imaging system. (The focal planes are connected by the dashed, gray lines.) The displacement of the gratings from the focal plane creates net dispersion. The virtual image of the first grating together with the second grating act as a Treacy compressor with negative grating separation and therefore produce the same dispersion as a matching Treacy compressor, but with opposite sign.

first grating is created. Since the distance to the focal point has to be equal for both gratings, in practice a folding mirror is placed at exactly the middle between the two lenses, which also saves one lens and one grating. The second grating together with the virtual image of the first grating is acting as a Treacy compressor- but with negative distance D. Consequently, the dispersion terms from Equation 2.55-2.57 will also have the opposite sign. The Treacy compressor and the Martinez stretcher are a perfect combination in a CPA system since their dispersion can cancel out exactly, apart from aberrations of the imaging telescope. In a real application the situation is more complex, since the material dispersion accumulated in the CPA chain can have a significant effect.

2.4.1 *Material dispersion*

The dispersion of a material $n(\omega)$ is usually expressed by a Sellmeier equation, e.g. of the following type:

$$n(\lambda) = \sqrt{1 + \sum_{i=1}^{3} \frac{A_i \cdot \lambda^2}{\lambda^2 - \lambda_i^2}} \tag{2.58}$$

The material constants A_i and λ_i^2 can be found in glass catalogs [88] or special optics books, i.e. [89]. The phase is given as $\varphi(\omega) = x/c \cdot \omega \cdot n(\omega)$ and can be differentiated analytically (with mathematical tools like Mathematica) in order to obtain the dispersion orders. In Table 2.2, the Sellmeier coefficients and the corresponding dispersion orders at 1030 nm are summarized for a path length of 1 cm in different materials.

From Table 2.1 it can be seen that a certain dispersion in the different orders can be tolerated without a significant effect on a 1 ps pulse at 1030 nm. These values are: $D_2 = 1.7 \cdot 10^4$ fs^2, $D_3 = 2.0 \cdot 10^7$ fs^3, $D_2 = 1.3 \cdot 10^{10}$ fs^4. Together with the dispersion values for 1 cm material from Table 2.2 it can be seen that the GDD value can be reached in less than 1 m material, whereas for the TOD and FOD more than 300 m or 300 km material would be necessary before the pulse is affected. Consequently,

	N BK7	Fused silica	YAG
A_1	1.03961212	0.6961663	2.28200
A_2	0.231792344	0.40792426	3.27644
A_3	1.01046945	0.8974794	0
$\lambda_1^2\,[\mu m^2]$	0.00600069867	0.00467914826	0.01185
$\lambda_2^2\,[\mu m^2]$	0.0200179144	0.0135120631	282.734
$\lambda_3^2\,[\mu m^2]$	103.560653	97.9340025	-
$D_2\ [fs^2]$	251	189	665
$D_3\ [fs^3]$	454	410	672
$D_4\ [fs^4]$	−504	−503	−429

Table 2.2: The Sellmeier coefficients A_i and λ_i^2 for a selection of materials were found in [89, 88]. The dispersion orders are computed at a center wavelength of 1030 nm, for 1 cm Material

the second order material dispersion has to be considered in the design for the dispersion management in a CPA system for 1 ps pulses at 1030 nm. In contrast, the higher order dispersion is negligible as long as the amount of material is kept below few hundreds of meters.

In the previous section, the grating stretcher and compressor were introduced in a very general and compact manner. The detailed layout and the design considerations for the PFS pump stretcher and compressor are presented in Chapter 4.

Part II

THE PFS SYSTEM

3

PFS LAYOUT

The PFS project was started with funding from the Max-Planck Society in 2006. Its aim is to build a light source for with few-cycle (5 fs) pulses and high pulse energies around 5 J in order to reach relativistic intensities [64]. As already mentioned in Chapter 1, the amplification of the broad bandwidth needed for few cycle pulses is achieved via OPCPA in thin crystals, pumped by high intensity picosecond pulses. The layout of the PFS system is sketched in Figure 3.1.

The PFS is a large scale OPCPA system which is based on new technologies in several of its aspects. Consequentially, the work in this project is divided in subfields (as indicated by different colors in Figure 3.1). An OPCPA system in general can in most cases be divided into three different fields of activity: the seed generation, the pump laser, and the OPCPA itself. These fields naturally divide the PFS project into several functional blocks.

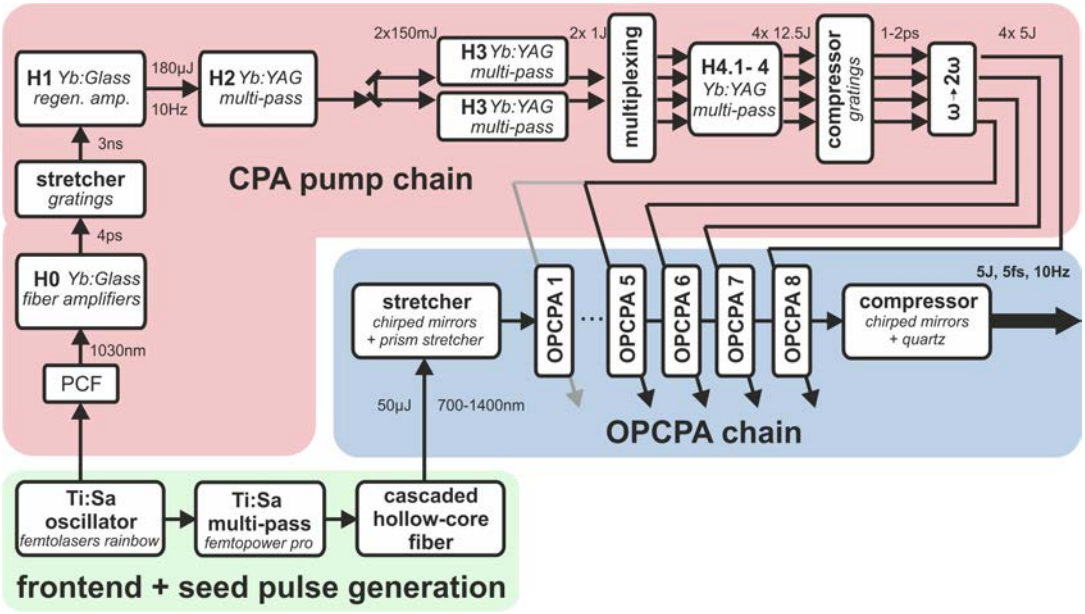

Figure 3.1: The broadband amplification is achieved in several OPCPA stages (blue box). The OPCPA seed is generated via a double stage hollow-core fiber pumped by a commercial Ti:sapphire oscillator and amplifier system (green box). The pump laser is a frequency doubled CPA amplifier chain based on Yb:YAG (red box). A detailed explanation can be found in the text. Adapted from [64]

These areas are the subject of work for a number of PhD students in addition to this work: The front end and seed generation was built by Izhar Ahmad [90] and is currently being developed further by Alexander Kessel. Christoph Skrobol is responsible for the modeling, building and optimization of the OPCPA stages.

The pump laser is developed by Christoph Wandt and myself and the first amplifier stages up to 300 mJ were developed in close collaboration. Additionally, Christoph

is developing and implementing the high energy amplifiers up to 10 J. The CPA principle has to be applied in the pump laser system in order to generate picosecond pulses at the necessary energies. The dispersion management in this system is also challenging, because it is difficult to stretch the narrow bandwidth of Yb:YAG to nanosecond pulse duration. One main part of this work has been the implementation of the stretcher/compressor system.

In the following, the different parts of the PFS layout are described in more detail. At first, the design of the OPCPA stages (from the design phase of the PFS project) will be presented, followed by a description of the front end and seed generation. The latter constitutes to be the major component of Izhar Ahmad's PhD-thesis [90] and is summarized here, in order to give a full description of the PFS system. The pump laser is described in more detail in a separate chapter.

3.1 DESIGN OF THE OPCPA CHAIN

As discussed in Section 1.4.1, the only feasible crystal choice for the last OPCPA stages is DKDP, due to the necessary apertures for high energy extraction. In the design phase of the PFS system, the amplification was simulated with a simple 1D model of the parametric amplification including pump depletion [64]. Eight OPCPA stages with thin (mm scale) DKDP crystals were modeled with 1 ps pump pulses at 515 nm. In the simulation the phase-matching angle and the noncollinear angle had a value of 37° and 0.91°, respectively. For these settings, broad bandwidth amplification is achieved in the range 700 − 1400 nm. The simulated spectra are presented in Figure 3.2 and the design parameters of the individual OPCPA stages are summarized in Table 3.1.

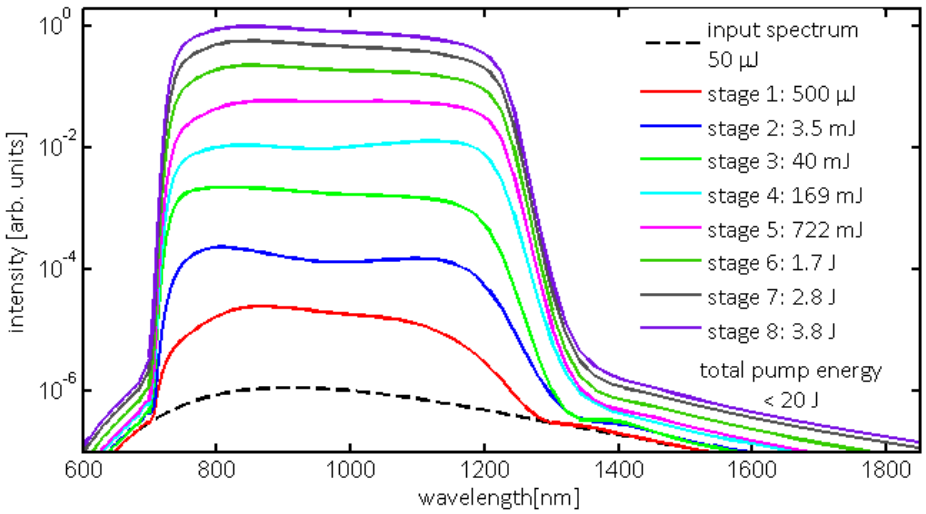

Figure 3.2: Simulated amplified spectra in eight consecutive OPCPA stages, based on DKDP pumped at 515 nm. The parameters used for the simulation are summarized in Table 3.1. Reprinted from [64]

These simulations suggest that pulses with an energy of 3.8 J can be generated with a Fourier-limited pulse duration of sub 5 fs and a total pump energy of 20 J.

This design was found in order to use 4 pump beams with identical energy, where the first pump beam is split in order to pump the first 5 stages. The last three stages are pumped with an identical pump energy of 5 J. The simulation predicts that the final stages are saturated and have a high efficiency of up to 20%.

OPCPA Stage	crystal thickness	beam size	pump energy	amplified energy
1	3.8 mm	1.5 mm	2.5 mJ	500 μJ
2	3.8 mm	5.0 mm	20 mJ	3.5 mJ
3	3.5 mm	1.4 cm	200 mJ	40 mJ
4	3.0 mm	6.5 cm	1 J	169 mJ
5	2.8 mm	9.0 cm	3 J	0.7 J
6	2.4 mm	9.0 cm	5 J	1.7 J
7	1.7 mm	9.0 cm	5 J	2.8 J
8	1.5 mm	10.0 cm	5 J	3.8 J

Table 3.1: Design parameters of the DKDP based OPCPA stages, based on 1D simulations with a phase-matching angle and the noncollinear angle of 37° and 0.91°, respectively.

Before the PFS was built, various aspects of the short-pulse OPCPA scheme, including the high gain when high pump intensities are used, the ultra-broadband amplification in noncollinear geometry, pulse-front matching between seed and pump pulses, compressibility of the pulses and their preserved focusability could be verified in a proof of principle experiment [91].

3.2 SEED PULSE GENERATION

In this section the front end and the seed generation of the PFS (green box in Figure 3.1) will be described in more detail. As depicted in Figure 3.3, the front end of the PFS system is a commercial CEO-phase stabilized Ti:sapphire oscillator (*Femtolasers Rainbow*) with 70 MHz repetition rate, 250 mW output power and a spectral range of 620 − 950 nm. The output of this oscillator is split in two parts in order to seed the pump chain and the OPCPA chain with synchronized pulses.

3.2.1 *OPCPA seed generation*

For the OPCPA seed generation, one part of the oscillator output is amplified up to 2 mJ in a commercial Ti:Sa CPA amplifier system (*Femtopower pro*). The stretcher of this system contains of a SF57 glass block and a programmable acousto-optical dispersive filter (*Dazzler, Fastlite*) in order to stretch the pulses to 10 ps and to fine-tune the spectral phase. The amplification is accomplished in a Ti:sapphire multi-pass amplifier, where the FWHM bandwidth is reduced from approximately 230 nm down to 60 nm due to gain narrowing. The subsequent compression to approximately 23 fs is done in a hybrid prism and high dispersive mirror compressor [92] (compare

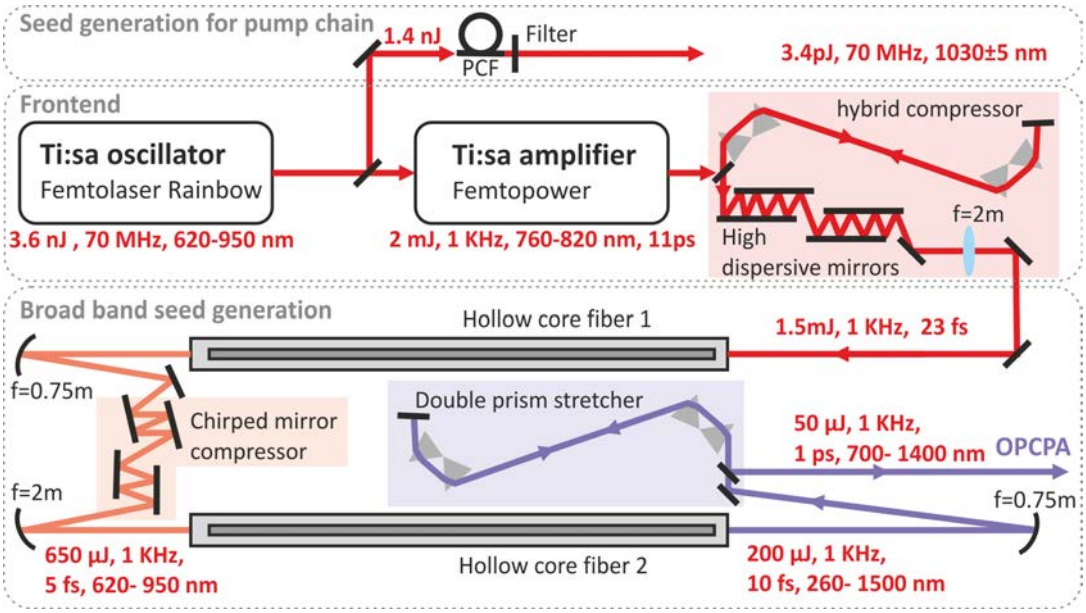

Figure 3.3: Detailed layout for the front end, the generation of the broadband seed pulses and the seed pulses for the pump laser chain. (Detailed description in [90].) PCF: photonic-crystal fiber

Figure 3.3 highlighted in red). This approach has the advantage that the pulse is not fully compressed in the last prism, which would cause self-phase modulation and spectral narrowing in high power systems. The output pulses of this amplifier have an energy of 1.5 mJ with 23 fs pulse length at 1 kHz repetition rate and are used to generate the broadband OPCPA seed. Since the bandwidth of the Ti:sapphire laser is insufficient for supporting 5 fs pulses that can be amplified further in the DKDP OPCPA chain, its output has to be dramatically broadened. Not only is the central wavelength of the OPCPA chain shifted to the infrared, but also its bandwidth amounts to one octave.

The generation of supercontinua spanning over multiple octaves has been shown with different cascaded broadening techniques based on nonlinear propagation of short pulses and intermediate compression [93, 94, 95]. Nevertheless, self-steepening caused by the slower phase velocity of the pulse maximum as compared with the weaker wings causes an abrupt slope of the pulse tail after some propagation [96]. This gives rise to a strong UV shift and thus, broadening to the UV has a considerable advantage over the infrared spectral region. In order to generate the seed pulses for the PFS system in the spectral region from $700 - 1400$ nm, different new broad band seed generation schemes were investigated and characterized [92]. The double hollow-core fiber (HCF) scheme turns out to be the most suitable approach for PFS [90].

The amplified 1.5 mJ pulses are focused into the first HCF filled with neon gas. An overall throughput of 650 μJ was obtained with the central mode containing more than 85% of the energy. The output spectrum of the first HCF is shown in Figure 3.4 in black. The pulses are compressed to 5 fs using negatively chirped mirrors (compare Figure 3.3, highlighted orange). These pulses are focused into the second HCF, filled with Ne. At the output of this double stage HCF setup, a total

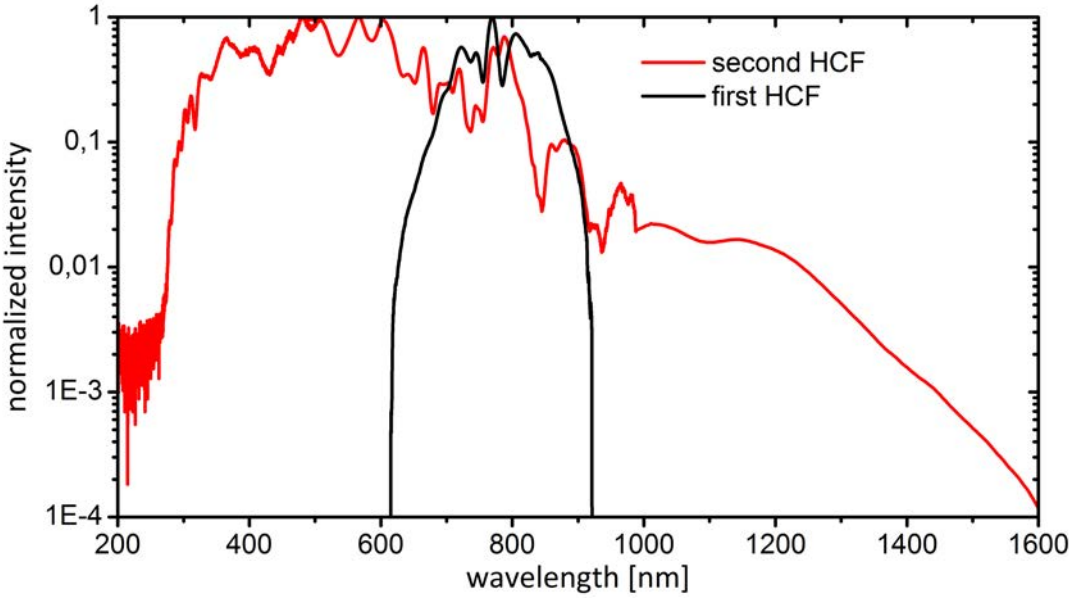

Figure 3.4: Broadband seed spectrum generated in the first hollow-core fiber (black) with 300 μm core, 1 m length filled with 1.5 bar of Neon. Output spectrum after the second HCF (red) with 250 μm core, 1 m length filled with 3.3 bar of Neon. Reprinted from [90]

energy of 200 μJ is obtained with a spectrum that spans over nearly three octaves (260 − 1500 nm), as depicted in Figure 3.4 in red. About 25% of the total energy is contained in the desired spectral range from 700 − 1400 nm. A more detailed description can be found in [90].

The generated broadband pulses have a pulse duration on the order of 10 fs. For the amplification in the OPCPA stages, these pulses have to be stretched to approximately the pump pulse length (i.e. 1 ps). This is achieved with a double prism stretcher utilizing fused silica prisms and a separation of ca. 10 cm (compare Figure 3.3 highlighted in violet). After the final amplification the pulses are compressed mainly by bulk material. In order to match the higher order dispersion, broadband chirped mirrors will also be designed and used in future.

3.2.2 *Seed generation for the pump laser chain*

The short pulse length in the OPCPA stages (1 ps) calls for a high accuracy in the timing synchronization of the pump and seed pulses. Therefore, the pump pulses and the seed pulses are derived from the same oscillator.

As indicated in Figure 3.3, a part from the master oscillator output (ca. 100 mW, 1.4 nJ) is split off with a broad-band beam splitter. The seed pulses at 1030 nm are generated via soliton self-frequency shift in a photonic-crystal fiber (PCF) [97, 98]. The input and output spectra of the PCF (*NL-PM-750, Crystal Fibre LTD*) are shown in Figure 3.5. The peak at 1030 nm in the output spectrum is strongly increased, compared to the input spectrum. An interference filter selects a Gaussian spectrum with a bandwidth of $\Delta\lambda = 10$ nm centered around 1030 nm, as indicated yellow in Figure 3.5. The filtered pulses have an energy 3.4 pJ and are further amplified in a

two-stage Yb-doped fiber amplifier. The fiber amplifier would allow amplification in a much larger bandwidth, but later the bandwidth is limited to ca. 4 nm in the stretcher. Therefore, it makes sense to limit the bandwidth before the fiber amplifier in order to optimize the amplification in the desired bandwidth range of 4 nm around 1030 nm.

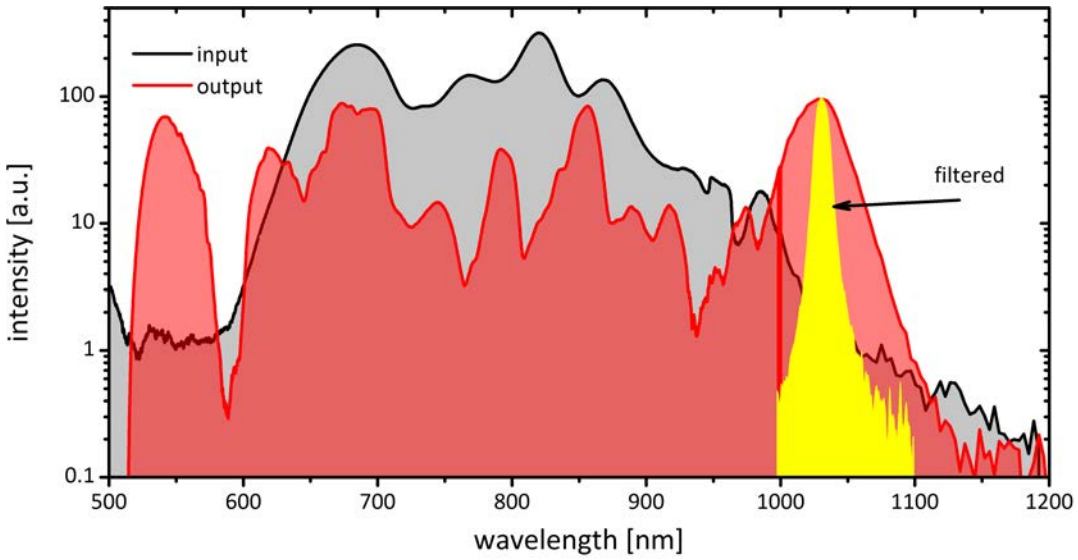

Figure 3.5: Generation of synchronized seed pulses at 1030 nm for the OPCPA pump laser chain, utilizing soliton self-frequency shift in a PCF. The output spectrum shows a peak at 1030 nm. The interference filter selects a bandwidth of 10 nm at 1030 nm for further use (yellow). Adapted from [90]

In this chapter, the PFS layout is introduced and based on this, the initial PFS OPCPA design is presented. The generation of broad-band seed pulses is summarized together with the generation of optically synchronized seed pulses for the pump laser chain. The following chapter will focus on the current status of the pump laser chain including the detailed description of its building blocks and the design considerations for the dispersion management.

4

PUMP LASER

The pump laser development is the key aspects of this thesis. The planned pump laser chain was highlighted in red in the PFS layout (Figure 3.1). In this chapter, the current status of the pump laser chain is presented. Its individual building blocks are illustrated in Figure 4.1 and will be discussed in detail.

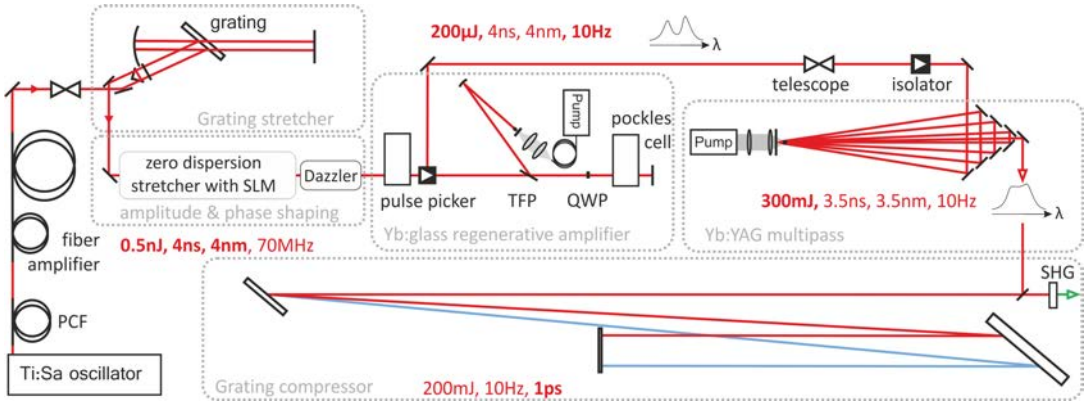

Figure 4.1: Detailed layout of the pump laser setup. The individual building blocks-the fiber amplifier, the stretcher, the regenerative amplifier, the multi-pass amplifier and the compressor are discussed in the following. PCF: photonic crystal fiber, SLM: spatial light modulator, TFP: thin film polarizer, QWP: quater wave plate, SHG: second harmonic generation. (modified from [99])

The main emphasis in this chapter lies on the dispersion management in the stretcher and compressor setup and the spectral amplitude shaping, which helps to suppress gain narrowing and allows for an unprecedented amplified bandwidth. The results of the amplification of shaped spectra and the corresponding compression results (Section 4.4 and Section 4.5.2) are published in [99], which is appended in Appendix A.5 as an electronic reprint with the permission of OSA.

4.1 DOUBLE-STAGE FIBER AMPLIFIER

The double-stage Yb-doped fiber amplifier was built by the Institute of Applied Physics of the Friedrich Schiller-Universität Jena. The first fiber amplifier consists of a single-mode, polarization-maintaining, Yb-doped fiber where the single-mode fiber-coupled pump diode with 180 mW at 980 nm is coupled via wavelength-division multiplexing.

The output of the first amplifier is spliced directly to the second stage and decoupled from back reflections with a fiber coupled Faraday isolator. The second amplifier consists of a 1.3 m fiber with 10 μm core directly spliced to the 30 cm long active double-clad fiber (20/125 μm). This amplifier is pumped by a free-space coupled 5 W diode laser. In this double stage amplifier, the input signal is amplified to

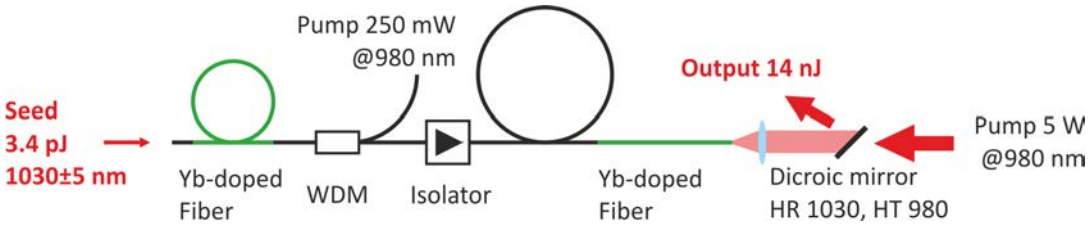

Figure 4.2: Layout of the double-stage Yb-doped fiber amplifier. The seed pulses generated from the Ti:sapphire front end are amplified to 14 nJ at 70 MHz repetition rate. This amplifier was built by the fiber laser group of the Friedrich-Schiller University, Jena.

1 W of output power- corresponding to 14 nJ pulse energy at the repetition rate of 70 MHz.

4.1.0.1 *Characterization of the seed pulses*

The fact that both fiber amplifiers are spliced together results in an unwanted side effect: The amplified spontaneous emission (ASE) of the first amplifier seeds the second amplifier. On the one hand, this limits the signal-to-noise ratio to 26 dB for the amplification of pulsed signals, because ASE builds up between the pulses. On the other hand, the output power is independent of the seeding level, because the ASE of the first amplifier can saturate the second amplifier.

Therefore, the usual way of measuring the output power to optimize the input coupling is not applicable in this case and a different measurement procedure is applied: the auto-correlation trace of the fiber amplifier output is measured with a second-order scanning autocorrelator (*APE GmbH, Berlin*). In this way one can distinguish the seeded and the unseeded case. A constant autocorrelation signal (no pulse) is observed for an unseeded amplifier, whereas the contrast of the autocorrelation signal can be optimized with the coupling of the signal to the first fiber (compare Figure 4.3).

Optimizing the input coupling means firstly so-called mode matching, where the input-beam waist—with a size matched to the fiber—is created at the fiber end facet with an appropriate telescope. Secondly, the beam has to hit the fiber at the correct position under the correct angle. The latter can be achieved with a direction and position scan with two mirrors (beam walk). For the best input-coupling, the peak of the autocorrelation signal is a factor 500 above the noise level, as depicted in Figure 4.3 on the left.

The measured autocorrelation trace has a FWHM of 4.8 ps. The factor for the conversion from autocorrelation width to pulse width can be obtained from the calculated Fourier-limited pulse duration and autocorrelation width. For the measured output spectrum (see Figure 4.3 right), this factor is 1.48. Together with the measured autocorrelation width this gives a FWHM pulse duration of 3.24 ps. This pulse duration is caused by the introduced dispersion from the two fiber amplifiers. (The Fourier limited pulse duration for our spectrum (FWHM= 10 nm at 1030 nm) would be approximately 150 fs.)

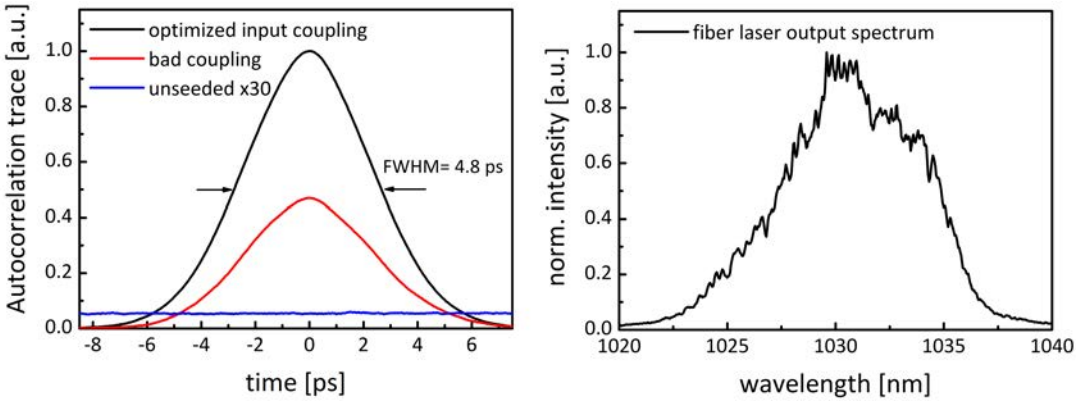

Figure 4.3: (Left) The measurement of the autocorrelation of the seed pulses after the double-stage Yb-doped fiber amplifier indicates a FWHM of 4.8 ps. The autocorrelation measurement is also used for optimization of the coupling to the fiber. Bad coupling (i.e. beam pointing or wrong mode size) cause a decreased contrast in the autocorrelation trace (red). If the amplifier is not seeded at all, a constant autocorrelation signal (blue) can be detected with a factor 500 lower signal compared to the optimized case. (Right) Spectrum after the double stage fiber amplifier.

As a summary, the fiber amplifier provides pulses with 14 nJ energy, 3.24 ps pulse duration at 1030 ± 5 nm, with 70 MHz repetition rate for further amplification in the pump laser chain.

4.2 THE STRETCHER

The next component in the pump laser chain is the stretcher, which stretches the pulse duration to few nanoseconds for damage-free amplification in the following amplifiers. The initial dispersion design was conducted by Izhar Ahmad during his work as PhD [90]. In this work, the detailed analysis of the spatio-temporal couplings and the effects of aberrations on the dispersion was performed with ray-tracing methods. Additionally, the stretcher and compressor setup were implemented in the laser (including the development of a reliable alignment procedure for both setups). Furthermore, an online monitoring for the laser beam alignment was established. These actions are crucial for a reliable and stable alignment of stretcher and compressor since the pulse compression depends strongly on the correct alignment of the input angles and the parallelism of the gratings.

The basic stretcher design was done before the amplifiers were built and therefore is based on some assumptions regarding the amplified bandwidth. The amplifier chain is based on Yb:YAG as gain material. Other sources (e.g. [100]) report that the amplified bandwidth can be expected to be $\Delta\lambda = 1.5$ nm at a center wavelength of 1030 nm for amplification in Yb:YAG at room temperature. The Fourier-limited FWHM pulse length τ_0 can be calculated for a Gaussian spectrum from the time bandwidth product as

$$\tau_0 = \frac{2\,ln2}{\pi\,c}\frac{\lambda_0^2}{\Delta\lambda}. \tag{4.1}$$

For $\Delta\lambda = 1.5$ nm at 1030 nm, it follows $\tau_0 = 1$ ps.

The amount of GDD which stretches a Gaussian transform-limited pulse to a desired pulse length τ can be calculated with formula 4.2 (in absence of higher order dispersion) [87].

$$GDD = \frac{\tau_0}{4ln2}\sqrt{\tau^2 - \tau_0^2} \tag{4.2}$$

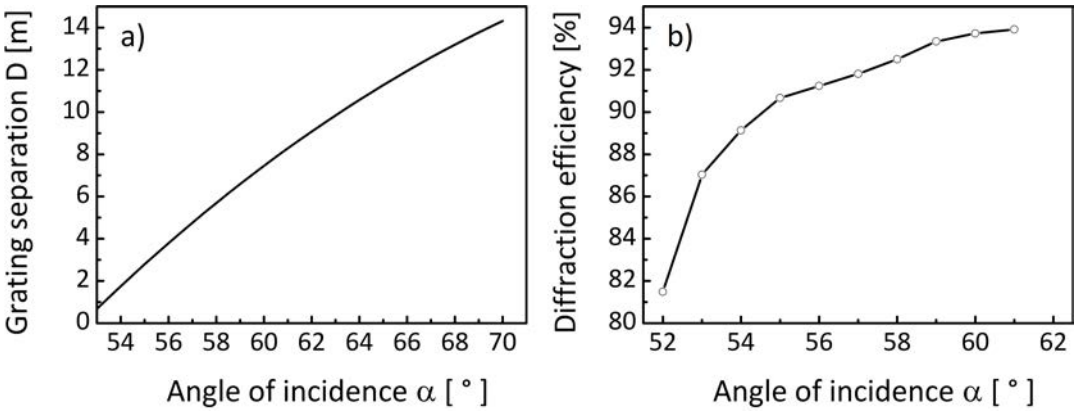

Figure 4.4: (a) The grating separation D is plotted as function of the angle of incidence α, for $N = 1740$ lines/mm, 1030 nm and a fixed $GDD = 6.14 \cdot 10^8$ fs^2. (b) shows the measured diffraction efficiency. Reprinted from [90]

The pulses should be stretched to few ns in the PFS pump laser, in order to avoid nonlinear effects. With the given parameters a chirp of $GDD = 6.14 \cdot 10^8$ fs^2 is needed to achieve the stretching to approximately two nanoseconds.

The gratings which are used in the stretcher (as well as in the compressor) have a line density of 1740 l/mm. Rearranging of Equation 2.55 gives a relation for the distance D in dependence of the diffraction angle β for a given φ_2 (or GDD). The grating equation (Equation 2.54) relates the angle of incidence α to the diffraction angle β. In Figure 4.4 (a) the grating separation D is plotted as a function of the incidence angle α for a constant target GDD of $6.14 \cdot 10^8$ fs^2.

Figure 4.4 helps to find a useful parameter range for the stretcher. The left plot indicates that smaller angles of incidence are beneficial for a compact stretcher and compressor design (i.e. small grating separation D). Unfortunately, the right plot dictates angles around 60° in order to maximize the diffraction efficiency. As a tradeoff between compactness and efficiency, an angle of incidence of $\alpha = 58.5°$ was chosen, according to $D = 6.14$ m grating separation.

4.2.1 *Stretcher layout and ray-tracing*

The stretcher design is based on the Martinez stretcher [27], which was briefly introduced in Section 2.4. In contrast to Figure 2.6 where two lenses are used as imaging system, here a spherical mirror in combination with a flat folding mirror are applied. This has the advantage that a single grating can be used with multiple reflections, as well. Since the grating separation for a single pass through the stretcher is quite large at 6.14 m, two complete round trips (i.e. 8 diffractions off the grating) are used in order to half the length of the stretcher setup.

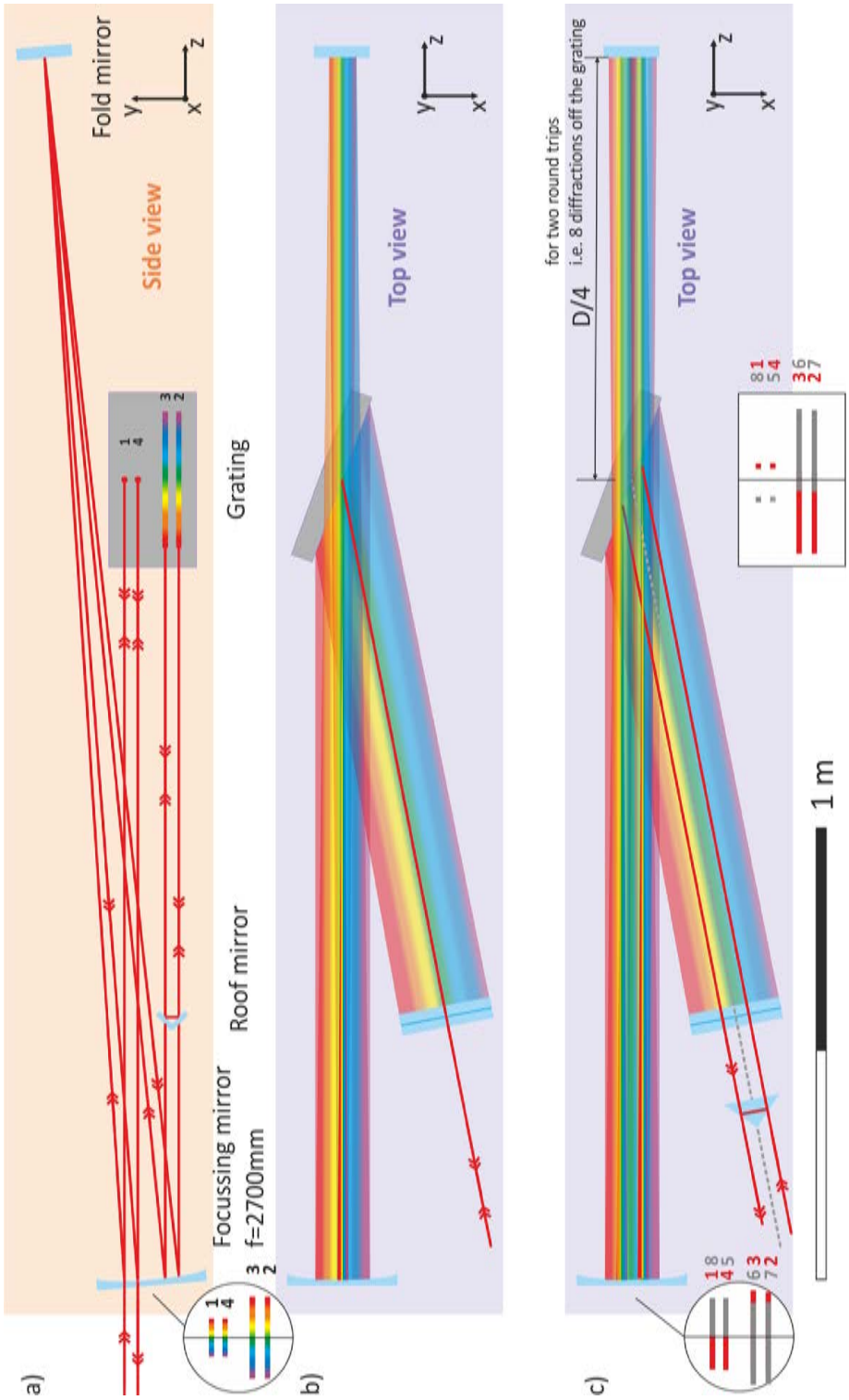

Figure 4.5: The beam path in the folded Martinez stretcher [27] is shown. (a) The side view for one complete round trip in the stretcher (i.e. 4 diffractions off the grating). (b) Same as (a) but top view. The beam positions and dispersion on the focusing mirror and on the grating are also illustrated for better understanding. (c) Shows the top view for two complete round trips (i.e. 8 diffractions off the grating). The input beam is offset from its initial input axis (dashed gray) and the output from the first round trip is offset horizontally by a prism in order to perform the second round trip.

The stretcher setup including the beam path is shown in Figure 4.5. Since the beam path is rather complicated, in (a) and (b) the side- and the top- view of the setup are shown for a single round trip. The position and the dispersion on the grating and on the focusing mirror are also illustrated with corresponding numbers.

The input beam is sent to the grating ($1740\,lines/mm$) at the uppermost position (1) at an angle of 58.5° from normal, parallel to the x-z plane. From there the beam is diffracted (and dispersed) at a center angle of 69.97° to the uppermost position (1) of the focusing mirror ($f = 2700\,\text{mm}$). The focusing mirror is tilted around the x-axis by 1.5° and sends the beam above the grating to the fold mirror. The fold mirror sends the beam back to the lowest position on the focusing mirror from where the beam goes back to the grating (2). From there the beam is diffracted parallel, but vertically offset to the input beam. At this position, the beam is spatially chirped—all wavelengths propagate parallel but are spatially separated, which can be compensated when the beam is send back through the whole stretcher setup. This is done by a vertical roof mirror, in order to separate the input and output beam in height. Up to now, one complete round trip in the stretcher is described.

Since a second round trip should be implemented, the output of the first round trip is retro-reflected horizontally by an additional prism, as shown in Figure 4.5 (c). The horizontal offset of the input from the center line (dashed gray in Figure 4.5 (d)) is introduced to make the beam path symmetric with respect to the optical axis.

For two round trips in the stretcher, the distance between grating and folding mirror is $D/4$, which is 1.535 m for the design GDD. Ray-tracing was used, in order to find the beam size inside the stretcher and to properly dimension the optical components. Additionally, ray-tracing helps to find an optimum focal length for the spherical mirror.

The design considerations start by choosing an appropriate beam size in the stretcher. The beam size should be small in order to minimize the needed aperture, but at the same time the Rayleigh length should be large enough to maintain the approximate beam size for propagation over few meters. As a compromise, $w = 1\,\text{mm}$ ($z_0 = 3\,\text{m}$) is chosen in this case, together with a vertical beam separation of 10 mm in order to avoid diffraction losses. Since there are 4 beams stacked in the stretcher, the highest beam should hit the focusing mirror 20 mm above its center in order to provide a symmetrical beam path.

After the vertical separation is set, the tip angle of the focusing mirror and the beam sizes are simulated via ray tracing with the software extension *Lambdaspect* for *Autodesk inventor*. Imaging with a spherical mirror is fraught with spherical aberration- the beams hitting the mirror off-center are focused more strongly than paraxial beams. When the spherical mirror is tilted, another aberration- so-called coma- appears: light from different positions on the mirror is focused on different positions in the tilt direction (height). These kinds of aberrations in the imaging system of a stretcher can introduce unwanted spatio-temporal couplings and deviations from the calculated dispersion. In order to minimize spatio-temporal couplings, the tip angle of the focusing mirror should be minimized. This angle can be minimized by using larger focal lengths in the imaging but this makes the setup impractically large. As a compromise, a focal length of $f = 2700\,\text{mm}$ for the focusing mirror is used according to a 1.5° vertical tilt angle for the focusing mirror. Aberrations cause

spatio-temporal couplings, which can change the dispersion of the setup. These effects are discussed in the following

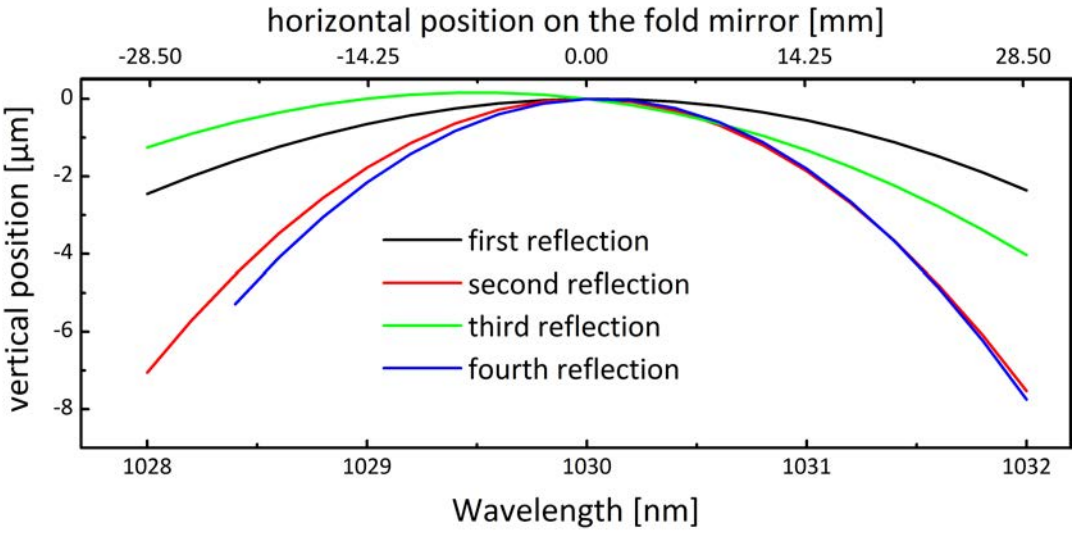

Figure 4.6: The effect of coma in the stretcher introduced by a 1.5° tilted spherical mirror ($f = 2700\,\text{mm}$) is shown. The spatial distribution of the wavelength on the folding mirror (in the focal plane) is shown for the tilt direction (vertical), for four reflections (i.e. two complete stretcher round-trips).

The effect of coma is shown in Figure 4.6. The wavelengths are dispersed in the horizontal dimension to approximately 57 mm on the folding mirror. Instead of a straight line, which would be expected for an aberration-free imaging, a bending in the vertical direction is observed due to coma. The vertical beam position on the folding mirror (in the focal plane) is shown as function of the wavelength for four reflections on the folding mirror (i.e. 2 complete compressor round-trips). The vertical spatial chirp on the folding mirror is on the order of 1 μm/nm for the first and third reflection and 4 μm/nm for the second and fourth reflection. The coma is more pronounced for the second and fourth reflection at the end mirror, because the beam is more dispersed at the corresponding reflections on the focusing mirror in these cases.

Figure 4.7 (a) shows the spatial chirp of the output beam after two complete round trips in the stretcher. The position of the fold mirror was varied in order to find the optimum position, which minimizes the horizontal spatial chirp. The resulting spatial chirp is on the order of 1 μm/nm and 3 μm/nm for the horizontal and vertical axes, respectively. In addition to that, there is a residual angular dispersion in the horizontal direction of 0.03 μrad/nm. The residual spatio-temporal couplings are much smaller than the beam diameter or divergence and can be neglected. Due to the narrow bandwidth in the PFS pump laser, the total displacement or angle difference for the extreme wavelengths is still small, whereas for systems operating with few tens of femtosecond pulses (or 100 nm bandwidth) these kind of aberrations become severe and have to be avoided. More complex aberration-free stretcher designs were developed for these cases [28]. Figure 4.7 (b) shows a dramatic increase in the horizontal spatial chirp when the folding mirror is displaced by 2 mm from the ideal position. The displacement of the fold mirror de-tunes the telescope from

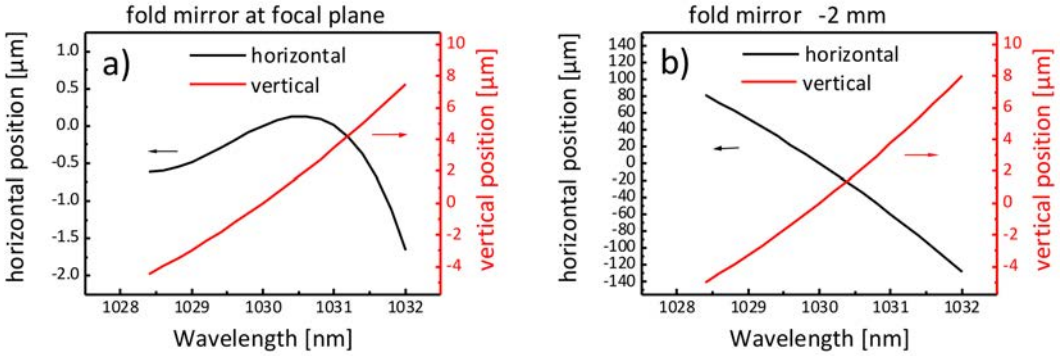

Figure 4.7: In (a), the spatial chirp at the stretcher output is shown for optimum alignment. The remaining spatio-temporal couplings arise from aberrations in the stretcher. (b) Shows the spatial chirp when the folding mirror is displaced by 2 mm from the focal plane.(Note the changed scale for the horizontal position)

exact 1:1 imaging and thus the virtual image of the grating is no longer parallel to the original. This shows the sensitivity for the alignment of the stretcher setup.

	Theory	Ray-tracing	Difference
GDD $[fs^2]$	$6.2226 \cdot 10^8$	$6.2227 \cdot 10^8$	$1 \cdot 10^4$
TOD $[fs^3]$	$-1.5684 \cdot 10^{10}$	$-1.5763 \cdot 10^{10}$	$8 \cdot 10^7$
FOD $[fs^4]$	$6.57552 \cdot 10^{11}$	$6.8301 \cdot 10^{11}$	$1.5 \cdot 10^{10}$

Table 4.1: Comparison of the dispersion terms for the stretcher from the ray-tracing with the dispersion obtained from Eqs. 2.55, 2.56, 2.57 using $\alpha = 58.5°$ and $D = 6.2255\,\text{m}$.

The effect of the aberrations on the dispersion is shown in Table 4.1, where the calculated values and the simulated values using ray-tracing are compared. The difference is caused by the aberrations and also represents the difference between the stretcher and the compressor dispersion. Therefore, these values can be compared to the values from Table 2.1, resulting in a good fit of the second and forth order dispersion terms between stretcher and compressor. In contrast, the difference in the third order will decrease the compression fidelity and increase the compressed pulse width by a few percent, if not compensated. This issue will be discussed in more detail in Section 4.6 where the compressor design is discussed.

In the following, the beam size in the stretcher and the size of optical components are discussed. In the stretcher, a grating with a size of $200\,x\,100\,\text{mm}$ is used. Ray-tracing shows that the size of 200 mm in the dispersion plane limits the spectrum to approximately $1028 - 1032\,\text{nm}$ for a stretcher with sufficient GDD. The horizontal spread of the spectral components between 1028 and 1032 nm on the different optics of the stretcher are summarized in Table 4.2. The values from Table 4.2 are the minimum optics size for 4 nm transmission of the stretcher. In the actual setup (compare Figure 4.8), larger optics are applied: the focusing mirror and the folding mirror have a size of 6 and 4 inch in diameter, respectively. The mirrors in the roof mirror have an aperture of 14 x 140 mm. The grating with 200 mm horizontal dimension is

Position	Reflection Nr.	Beam size [mm]	
Grating	1,4,5,8	2	
Focusing mirror	1,4,5,8	32	
Folding mirror	1-4	57	
Focusing mirror	2,3,6,7	92	
Grating	2,3,6,7	68	(199)
Roof mirror	1-4	98	

Table 4.2: Beam size in the dispersion direction for a wavelength range of $1028 - 1032$ nm on the different stretcher components. For the grating, the beam size projected on the grating surface (at 70°) is given in braces.

the limiting factor in our stretcher setup. Photographs of the individual components of the stretcher setup are shown in Figure 4.8.

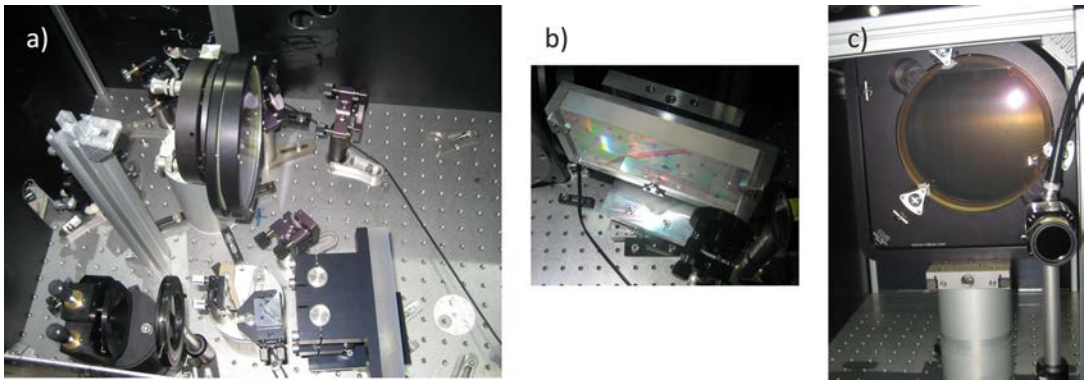

Figure 4.8: Photographs of the stretcher components. (a) The in-coupling mirror, the vertical roof mirror, the prism for the horizontal offset and the concave mirror are shown.(compare Figure 4.5) (b) shows the stretcher grating in the mount with three rotation degrees of freedom and a translation stage. In (c) the end-mirror is shown on a translation stage for exact tuning of the stretcher telescope magnification.

Generally, the spectral window of the stretcher could be increased by larger optics. Each additional 50 mm grating width increases the bandwidth by 1 nm. At approximately 7 nm the other optics start clipping and would have to be increased in dimension, too. A redesign of the stretcher would make sense if amplification experiments indicate a larger effective-gain bandwidth. In this case less dispersion would be needed in order to reach the same stretched pulse length, which could make both stretcher and compressor more compact. However, this does not seem to be the case with Yb:YAG as gain material but might be an option for one of the sesquioxides [101] or Yb:CaF2 [102, 103, 104].

4.2.2 *Stretcher alignment tolerances*

The crucial element for the alignment of the stretcher is the grating. The grating has to be aligned with very high accuracy in three rotational degrees of freedom. The rotation angles are defined in Figure 4.9, where the grating in its mount is shown.

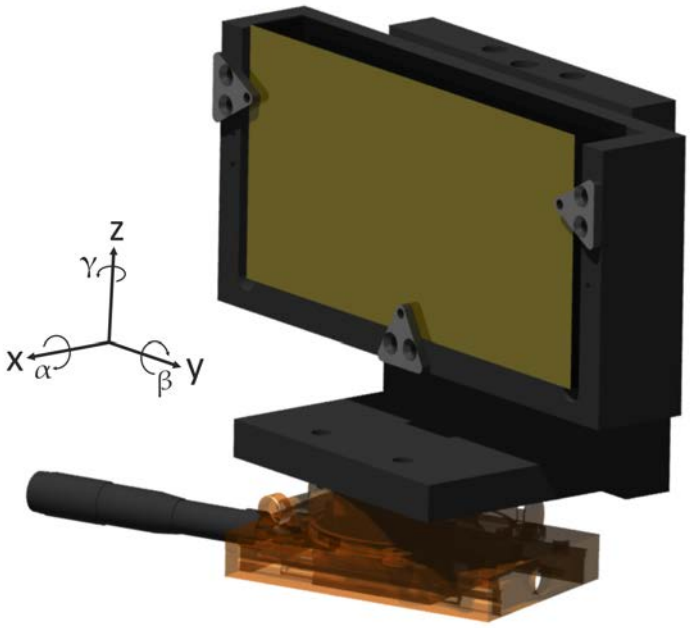

Figure 4.9: 3D model of the grating in its mount with ability of alignment in 3 rotation directions and one translation. The Rotation angles are defined in the axes plot.

The tilt angle γ is the angle of incidence for the input beam measured to the grating normal (58.5° in our case). The groove orientation and tip angles α and β should be zero in an ideal stretcher or compressor.

Minimizing of the angles α and β is usually done in an iterative alignment process. The first step is to align the angles γ and β perpendicular to the incoming beam by precisely retro-reflecting the zeroth order. Then γ is adjusted to retro-reflect the first or minus-first order, and α chosen such that the height of that reflex matches the incoming beam. If all axes are precisely orthogonal, this concludes the alignment process, otherwise an iterative procedure ensures a high accuracy. An angle accuracy of 50 μrad can be easily achieved in the lab and even higher accuracy is possible when advanced techniques are used [105, 106].

In Figure 4.10, the effect of angular misalignment of the tip (β) and the groove-orientation angle (α) are shown. The spatial chirp in the horizontal (and vertical) direction is increased but still small for angles of 200 μrad. For these angle deviations, the dispersion is not altered in a significant way. This analysis shows that the alignment of the tip (β) and groove-orientation (α) angles of the gratings in the stretcher (or compressor) is possible with high enough accuracy in the lab.

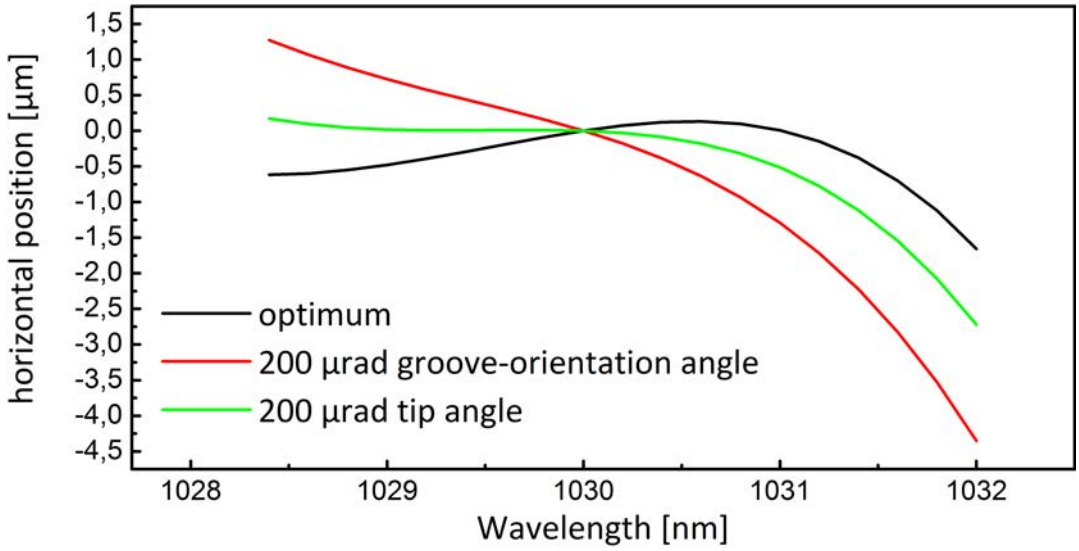

Figure 4.10: The effect of alignment errors for the tip and groove-orientation angle on the spatial chirp in the horizontal direction after the stretcher.

The measurement of the angle γ is done in two steps: Firstly, the angle is read from the scale of the respective rotation stage at the working position of the grating. Secondly, the grating is rotated to be normal to the input beam, so that the zeroth order is retro-reflected to the input beam and this angle is read from the scale of the rotation stage. The grating angle is the difference of both values. This measurement process is fraught with measurement errors. Reading values from a scale has an error of half a scale gradation. The applied rotation stage (*M-UTR80, Newport Inc.*) has a scale graduation of 1 arc minute. Since two measurements are necessary in order to determine the angle, the uncertainty of this angle is estimated as 1 arc minute or 290 μrad. This error is important to set up the compressor at the same angle as the stretcher. The gratings inside the compressor can be made parallel to few ten μrad with pulse-front tilt measurements like [83, 85, 106].

In the following, the effects of small AOI deviations and changes in the grating separation on the dispersion are analyzed. For Figure 4.11 (a) the influence of the angle γ on the dispersion terms is calculated with a constant grating separation of $D = 6.2255\,\mathrm{m}$ with Equation 2.55-2.57. Even small variations of 0.02° (or $\approx 340\,\mu$rad) cause significant differences of $2 \cdot 10^6\,\mathrm{fs}^2$ in the GDD and $1 \cdot 10^8\,\mathrm{fs}^3$in the TOD (compare Table 2.1). As a consequence, the compressor AOI has to be set up with very high accuracy in order to match the stretcher dispersion.

In Figure 4.11 (b), the dispersion terms are plotted as function of the grating separation for a fixed compressor angle $\gamma = 58.5^\circ$. In this length scan, 10 mm change cause $1 \cdot 10^6\,\mathrm{fs}^2$ in the GDD and $3 \cdot 10^7\,\mathrm{fs}^3$ in the TOD. Thus, the angle and the grating separation provide two degrees of freedom to tune GDD and TOD. Nevertheless, these dispersion terms are not changing independently and an iterative approach with alternating angle scan and length scan is needed in order to optimize the compression.

The discussed configuration, where the grating AOI α is smaller than the diffraction angle β, is chosen due to the higher dispersion provided (compare Figure 4.4

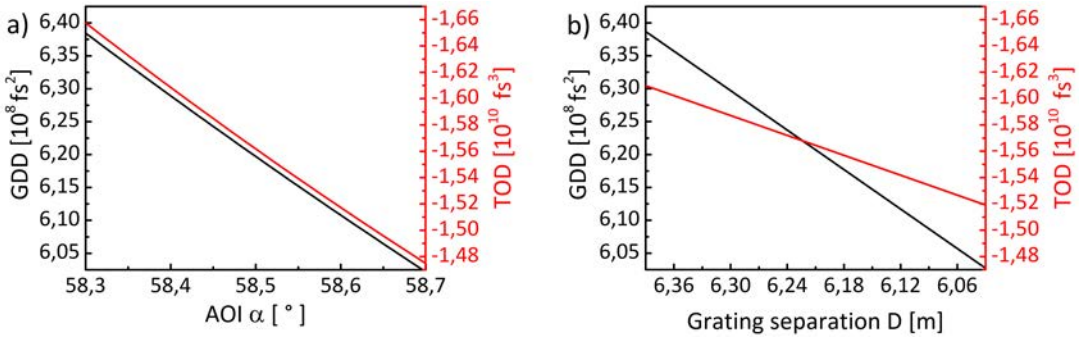

Figure 4.11: Variation of the GDD and TOD in the stretcher with (a) the angle of incidence γ ($D = 6.2255\,\text{m}$) and (b) the grating separation D ($\gamma = 58.5°$).

(a)). Nevertheless, this configuration is inverse to the usual arrangement in stretcher and compressor designs. For the normal geometry i.e. $\alpha = 69.97°$, $\beta = 58.5°$ the same GDD as discussed above can be obtained with approximately 14 m grating separation (instead of 6 m). Nevertheless, the introduced TOD and FOD are approximately a factor two (respectively 5.5) smaller. The sensitivity to angle changes is smaller as well: 0.02° angle change cause a factor 4 less change in GDD, factor 9 less in TOD and factor 2 less in FOD. Therefore, the normal configuration grating compressor and stretcher are less sensitive to dispersion fluctuations caused by angle changes, compared to the inverted configuration, which is probably the reason why this configuration is used more often. Nevertheless, in the PFS project the more compact configuration was preferred due to space constraints in the lab.

4.2.3 *Conclusion*

As a conclusion of this section, a Martinez stretcher design [27] was optimized for our parameters in order to provide a GDD of $6 \cdot 10^8\,\text{fs}^2$ with a rather compact footprint of 0.5 x 3.1 m. Ray tracing is performed in order to optimize the setup, to verify its feasibility and to investigate this setup regarding its aberrations. The spatio-temporal couplings in the stretcher are negligible. Nevertheless, the aberrations cause changes in the dispersion, which have to be considered for the compression. The alignment of the grating angles can be done with high enough accuracy in order to avoid additional spatio-temporal couplings. Nevertheless, the angle of incidence on the grating (γ) has a strong effect on the dispersion and has to be kept constant in very strict limits in order to provide stable compression. The compressor dispersion has to be matched to the stretcher via angle scan and length scan, which is discussed in more detail in Section 4.6, where the compressor is discussed.

4.3 THE REGENERATIVE AMPLIFIER

The stretched pulses (4 ns, 4 nm, 0.5 nJ) are amplified in the regenerative amplifier up to 200 μJ pulse energy. The gain medium in this amplifier is an Yb:glass rod with 8 mm length and $N_{Yb} = 6 \cdot 10^{20} cm^{-3}$ doping concentration. The layout of this amplifier is shown in Figure 4.12.

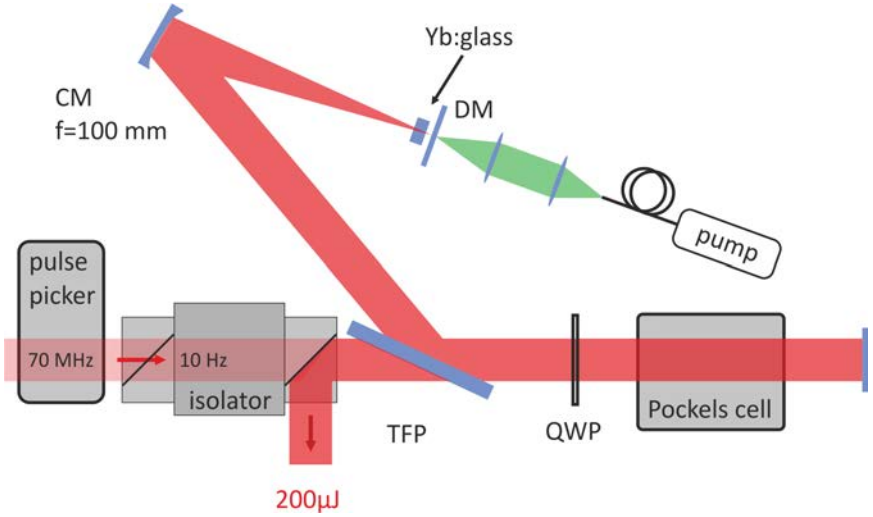

Figure 4.12: Layout of the regenerative amplifier. DM: dicroic mirror, CM: concave mirror, TFP: thin-film polarizer, QWP: quarter-wave plate.

The amplifier is pumped by a fiber-coupled diode laser with up to 5 W output power at 976 nm center wavelength. The pump light is focused to a spot diameter of 100 μm FWHM in the gain medium, through a dichroic mirror. The gain material is not cooled because the pump duration of 1.5ms and the repetition rate of 10 Hz result in a low enough average power to allow sufficient heat dissipation.

The cavity consists of two plane end mirrors and a concave mirror with a focal length of $f = 100$ mm. The dichroic end mirror is located in the focal plane of the concave mirror and the other end mirror is placed in 1.35 m distance of the concave mirror. The setup is folded by a thin-film polarizer (TFP), which works under an angle of incidence of 65°. The cavity mode is modeled with the matrix method (see Section 2.1.2). The result is a cavity mode with two waists at the end mirrors. The waist on the dichroic end mirror has a radius of 50 μm. The gain material is located in this focus region in order to reach sufficient pump intensity. The waist on the other end mirror has a radius of 1.2 mm. Therefore, the beam is large in the long arm of the cavity, where the Pockels cell is located, and nonlinearities are minimized and damage is prevented. The exact beam size depends strongly on the alignment of the distance of the dichroic mirror from the concave mirror. This alignment is used to match the cavity mode to the pump beam. The angle of incidence on the concave mirror causes astigmatism and is therefore minimized to 4°. In this case, the beam size differs by $\pm 10\%$ in the sagittal and meridional plane.

The seed is p-polarized and is transmitted through the TFP. After passing the quarter-wave plate twice (the Pockels cell is turned off at this time) the polarization is rotated by 90 degrees and the pulse is now reflected by the TFP. The Pockels cell has to be switched on with the quarter-wave voltage before the pulse passes the next time. In this way, the pulse is kept in the cavity. As soon as the Pockels cell is turned off again, the pulse is cavity-dumped and transmitted through the TFP. The in- and output pulses are separated by an optical isolator.

In Figure 4.13 (a) the pulse build up in the regenerative amplifier cavity is shown. The data is measured with a fast photodiode (*DET10A, Thorlabs*). It is shown that the

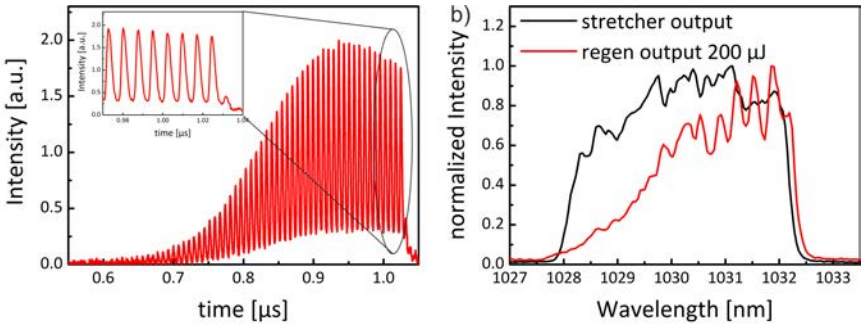

Figure 4.13: (a) The pulse build-up in the regenerative amplifier is observed with a photo diode. The pulse is amplified above the detection noise level after approximately 600 ns and runs in saturation for 950 ns round-trip time (i.e. 120 round trips). (b) The comparison of input and output spectra for the regenerative amplifier shows a red-shift for the amplified spectrum. The gain narrowing effect reduces the bandwidth from 3.9 nm FWHM to 2.3 nm.

amplifier runs in saturation at a cavity round-trip time of 950 ns which corresponds to approximately 120 round trips and an output energy of 200 μJ. At this working point, energy fluctuations in the output are minimized and account for less than 1% standard deviation. For longer round-trip times, the energy decreases again.

This amplifier utilizes Yb:glass as gain medium. Yb:glass has a much larger gain bandwidth compared to Yb:YAG, which helps to reduce gain narrowing effects in this amplifier. In Figure 4.13 (b) the effect of gain narrowing is illustrated. The FWHM bandwidth is significantly reduced from 3.9 nm to 2.3 nm due to the high amplification factor of $4 \cdot 10^5$. The following amplifiers will be based on Yb:YAG and have to provide a similar total gain. This leads to the expectation that gain narrowing in these amplifiers will be even more severe. Since the pulses are stretched, gain narrowing also reduces the stretched pulse length. Due to the reduction of the threshold fluence for laser-induced damage at shorter pulse durations, gain narrowing effects in CPA systems therefore greatly increase the risk of damage in the main amplifiers. Spectral shaping can help to to pre-compensate for the gain narrowing, as will be explained in the following section.

4.4 SPECTRAL AMPLITUDE SHAPING

The wavelength dependent emission cross section of laser media leads to a wavelength dependent gain. Since the emission cross section is (more or less) peaked, so-called gain narrowing occurs for broad seed spectra (the amplified bandwidth decreases with high amplification factors). In order to pre-compensate this effect, the spectral shape of the input spectrum can be changed in a way that the output spectrum maintains a broader bandwidth. In this section simulations of gain narrowing and spectral amplitude shaping as well as an experimental setup for the spectral amplitude shaping are introduced. The results in this section are published in [99].

4.4.1 *Simulation of gain narrowing in Yb:YAG*

The effect of gain narrowing in the Yb:YAG amplification stages, where the signal will be amplified from 200 μJ to 4×10 J (i.e. by a factor of $2 \cdot 10^5$), will be modeled in the following.

In order to do so, the amplification in Yb:YAG is simulated for different spectral components. These calculations are performed with a simple numeric model based on the rate equations.[1] Based on data for the emission and absorption cross section (see for example [107]), the inversion and spectral gain are calculated. In order to simulate CPA with normally dispersed beams, the different wavelength components are calculated iteratively, in descending order.

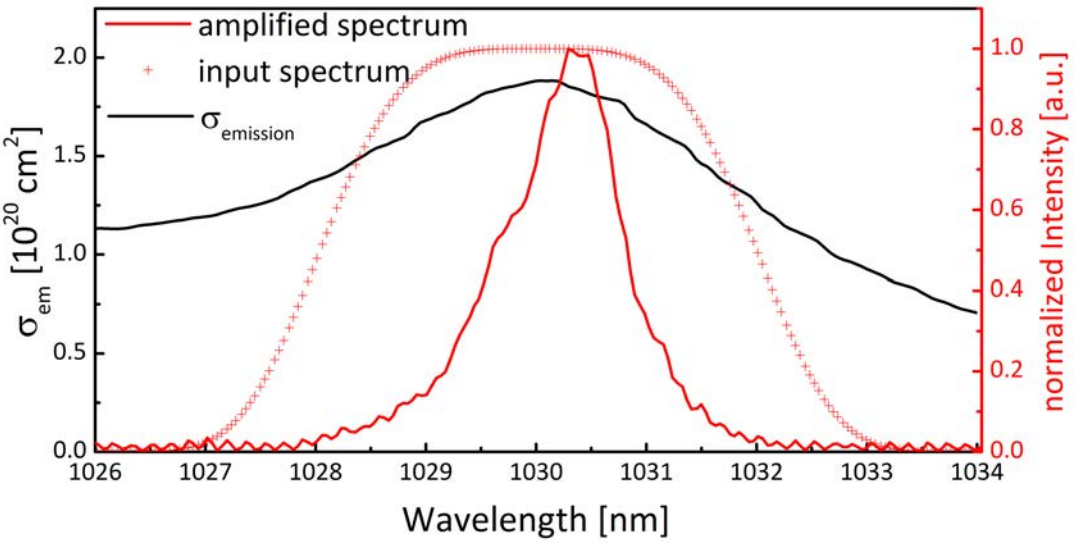

Figure 4.14: The emission cross section for Yb:YAG at room temperature is shown in black. The consequence of the peak-like structure is a reduction of bandwidth during amplification. In red the simulated spectrum for an initially 4 nm broad spectrum, amplified by a factor of $2.5 \cdot 10^4$ is shown as an example.[99]

In Figure 4.14, the emission cross section for Yb:YAG at room temperature is plotted along with a simulated spectrum for an initially 4 nm FWHM broad Supergaussian spectrum, amplified by a factor of $2.5 \cdot 10^4$. In this case, gain narrowing reduces the bandwidth to 1.4 nm FWHM. For higher amplification or lower starting bandwidth gain narrowing results in even narrower spectra. The reduced bandwidth will increase the minimum achievable pulse duration and could lead to optical damage in the amplifiers due to the reduced chirped pulse length.

The outcome of this simulation is the spectral gain curve for a certain total gain factor. This information can be used for the compensation of gain narrowing: If a certain amplified spectrum is divided by the spectral gain curve, the suitable input spectrum for the desired output spectrum under the specific amplification conditions is obtained.

This is not exactly true for chirped pulses. In this case the exact shape of the spectral gain curve depends on the spectral distribution of the input spectrum, because

1 Details about this code can be found in the PhD thesis of Christoph Wandt

the different spectral components are amplified consecutively and the amplification of the first wavelength components decrease the inversion and thus the gain for the remaining wavelengths. Therefore, the described calculation has to be applied in an iterative way in order to obtain correct predictions for the input spectrum, as shown in Figure 4.15.

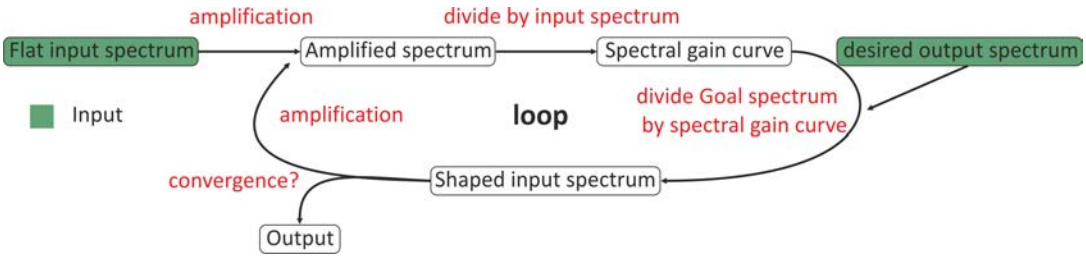

Figure 4.15: Simulation algorithm for spectral amplitude shaping. The amplification for a flat input spectrum is calculated and the spectral gain curve is obtained. Division of the desired output spectrum by the spectral gain curve gives an estimation of a needed input spectrum for the next iteration. After a few iterations, the algorithm converges and the amplitude shape of the input spectrum for the chosen output spectrum is obtained.

After a few iterations- usually less than six- the algorithm is converging. In this way, an intuitive and very general rule for the desired changes in the input spectrum is obtained: The input spectral amplitude has to be reduced for wavelengths were the gain is higher. The amount of this reduction depends on the total gain factor.

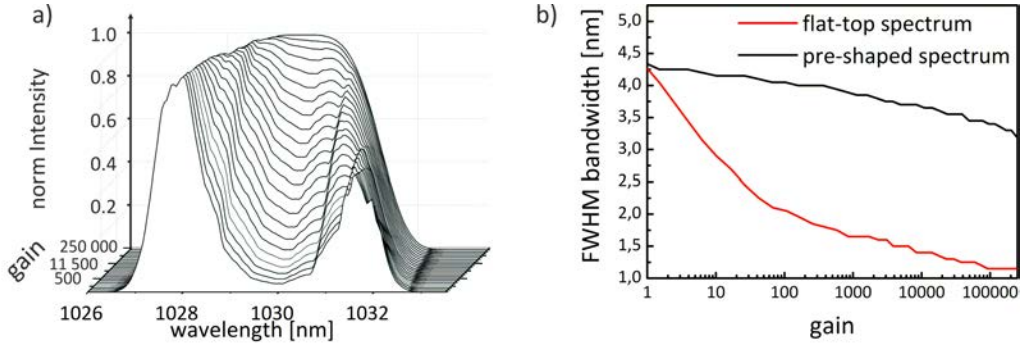

Figure 4.16: The effect of spectral shaping of the input spectrum on gain narrowing is shown. (a) The evolution of the pre-shaped input spectrum with increasing gain is shown. The input spectrum is optimized for an 3.2 nm amplified fourth-order super-Gaussian output spectrum at an amplification of $2.5 \cdot 10^5$. (b) Comparison between the gain-dependent FWHM bandwidth of an initially super-Gaussian spectrum with the pre-shaped spectrum. [99]

In Figure 4.16 (a), the calculated input spectrum is shown which results in a fourth-order super-Gaussian spectrum of 3.2 nm FWHM after amplification by a factor of $2.5 \cdot 10^5$ in Yb:YAG . During the amplification, the introduced hole around 1030 nm reduces its depth and finally a smooth spectrum is obtained. Figure 4.16 (b) shows the gain dependent FWHM bandwidth for the pre-shaped spectrum in comparison to a super-Gaussian input spectrum of same initial width. It is evident that the spectrally shaped spectrum can maintain a threefold increase in bandwidth

during this amplification compared to the super-Gaussian input spectrum. This technique helps to minimize the compressed pulse duration and increases the chirped pulse duration which reduces the risk of damage. The application of spectral amplitude shaping is therefore a key technique in order to obtain shortest pulses in combination with high pulse energy.

4.4.2 *Experimental setup for spectral shaping*

A spectral amplitude shaping stage is implemented in the experimental setup immediately before the regenerative amplifier. The main component of this spectral shaping stage is a spatial light modulator (SLM). An SLM is a linear array of nematic liquid crystals where an independent voltage can be applied. The refractive index for extra-ordinary polarized light varies with the applied voltage while the refractive index for ordinary polarized light stays constant. Therefore, this device can alter the phase or the polarization state if the light is polarized parallel to the crystal optical axes or under 45°, respectively. The latter effect can be used together with polarizers for attenuation. When an SLM is used for spectral amplitude shaping, the individual pixels have to be illuminated with different wavelength components. This is usually achieved in the focal plane of a zero-dispersion stretcher. As mentioned in Section 2.4, the net-dispersion is zero in a stretcher with the grating in the focal plane of the imaging lens. Figure 4.17 shows the setup for spectral amplitude shaping.

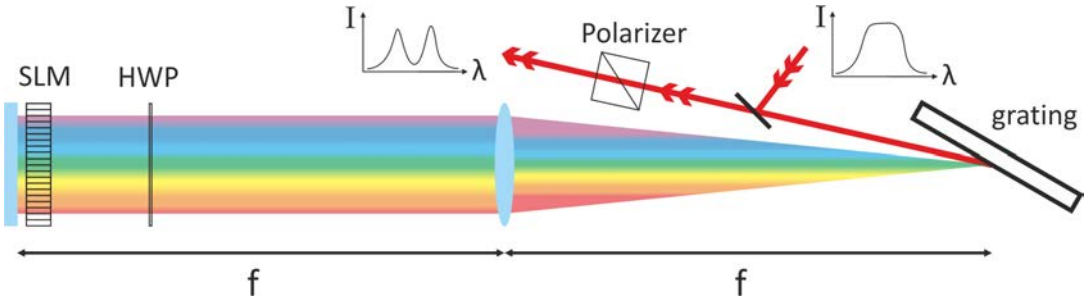

Figure 4.17: Layout of the spectral amplitude shaping stage. The SLM is placed in the focal plane of a zero-dispersion stretcher in order to attenuate different wavelength components individually. A HWP rotates the polarization of the linear polarized light 45° to the crystal axes. In this way the SLM can change the polarization state for the individual wavelengths. A polarizer after the stretcher selects the needed polarization for the output beam.

The SLM (*SLM-128-A-NM, CRI*), used in this setup, has 128 pixels and an aperture of $12.8 \times 5\,\text{mm}$. The grating in the zero dispersion stretcher has a line density of 1740 l/mm and is used under an angle of incidence of 58.5°. The focal length of the lens is $f = 400\,\text{mm}$ in order to illuminate the full aperture of the SLM with the available 4 nm bandwidth.[2]

2 The results in this chapter were obtained with the SLM shaping setup. Nevertheless, later it was replaced by an acousto-optic programmable dispersive filter (*Dazzler* HR-45-1053-board-V5-rev5, Fastlite). This device is more easy to use and has the benefit that both amplitude and phase can be shaped individually. All experiments results were reproduced after this replacement.

The drawback of spectral shaping is that a large amount of energy is wasted. In the PFS system, approximately 70% of the energy has to be cut away before the amplification (see also Figure 4.18 (b)). Nevertheless, since spectral shaping is applied before the regenerative amplifier, the energy loss can be easily compensated by a few more amplification passes.

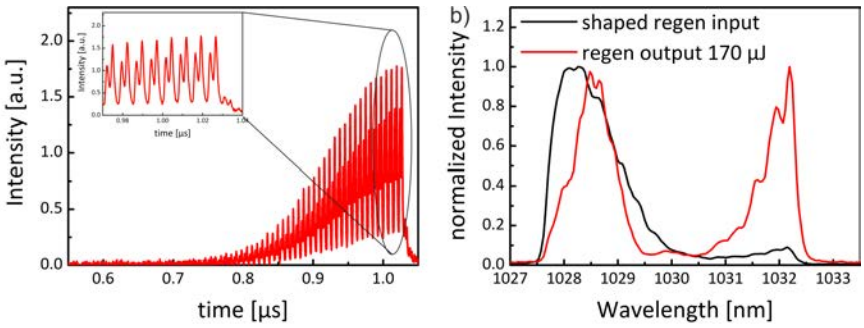

Figure 4.18: This measurement is performed with a spectrally shaped input spectrum and can be directly compared to Figure 4.13, where the input was unshaped. (a) For shaped pulses, the amplification is saturated after 140 amplification passes (i.e. 1040 ns round-trip time) instead of 100 passes for the unshaped case. The slower pulse built-up can be explained by the reduced input energy and the reduced overall gain for the broader spectrum. The photo diode can resolve the temporal shape of the pulse, which indicates the spectral shape due to the spectral chirp. (b) The input spectrum for the regenerative amplifier (black) is shaped in order to pre-compensate the redshift. The output spectrum (red) has the desired shape for further amplification in Yb:YAG (compare Figure 4.16).

As shown in Figure 4.18 (a), the shaped input pulse with reduced energy leads to saturation in the regenerative amplifier at 1040 ns (instead of 950 ns compare Figure 4.13). Output energies around 170 μJ, similar to the unshaped case, can be obtained with the shaped spectrum. This is possible due to the combination of the spectral shaping with an amplifier supporting a larger bandwidth (Yb:glass) than the rest of the amplifier chain (Yb:YAG). In other applications, where shaping is applied inside the cavity of a regenerative amplifier, the resulting spectral cavity loss reduces the achievable saturated output energy. Thus, the approach applied here has advantages in cases where the pump power in the regenerative amplifier is limited and the seed energy is sufficiently high.

Due to the lack of data for the emission cross section for the Yb:glass applied in the regenerative amplifier its gain narrowing cannot be modeled at the moment. Nevertheless, the measurements show that a spectrum with the desired shape (compare Figure 4.16) can be generated after the regenerative amplifier. The amplification of the shaped spectra in Yb:YAG is discussed in the following chapter.

4.5 THE 0.3 J MULTI-PASS AMPLIFIER

In this section, the Yb:YAG multipass amplifier stage is introduced. Experimental results for the amplification of shaped spectra are presented in addition to a discussion for the limitations of spectral amplitude shaping.

4.5.1 *Amplifier setup*

The multi-pass amplifier, depicted in Figure 4.19, amplifies the input signal by a factor of 1500, up to 300 mJ output energy. For reaching this level, an 8-pass, diode-pumped, Yb:YAG amplifier is employed.

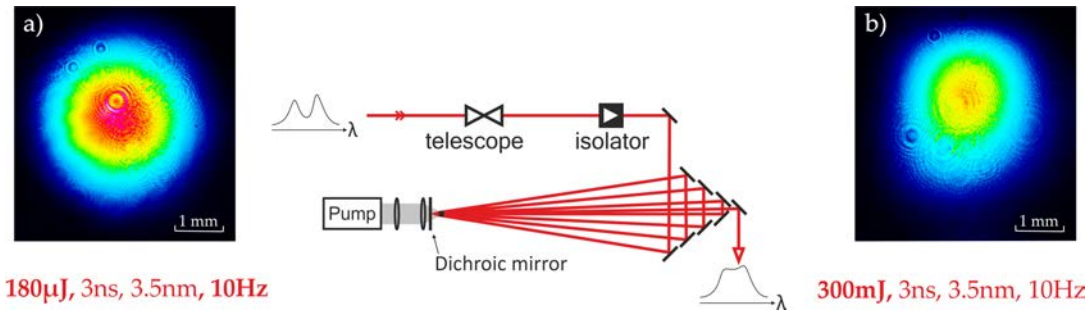

Figure 4.19: Layout of the multi-pass amplifier. The spectrally shaped output of the regenerative amplifier (180 μJ) with the beam profile shown in (a) is amplified in eight amplification passes to 300 mJ pulse energy. A high gain factor of 1500 is achieved by strong focusing of the pump light at 940 nm to an intensity of 35 kW/cm^2. The output beam profile, shown in (b), is slightly distorted mainly due to pump spot inhomogeneity. The spectral shaping of the input allows for a large bandwidth in the output beam.

The crystal in the Yb:YAG multi-pass amplifier is 8 mm long and 3 at.% doped. The 6 mm diameter rod is AR-coated on both faces and connected to a copper heat sink with indium foil via its circumference. As shown in Figure 4.20, the crystal is pumped (through a dichroic mirror) by a quasi-cw diode-laser stack (*Jenoptik Laser Diode*) with 3 kW average power (4.5 J, 1.5 ms, 10 Hz) at 940 nm central wavelength. This pump power is focused on a spot of 0.086 cm^2, leading to a pump fluence of 35 kW/cm^2 and a small-signal single-pass gain of approximately 3. The pump setup is identical to the amplifier presented in [108]. Nevertheless, two more amplification passes were added and the path lengths were changed in order to increase the output energy to 300 mJ.

The thermal management in the crystal is not optimized. Therefore, the crystal is heating up and thermal lensing is observed. The amplification passes are aligned successively: the seed is send to the crystal, amplified once and reflected from the dichroic mirror before the second amplification pass. After the double pass amplification, the beam profile is observed with propagation distance and the path length of the next pass is chosen such that a beam diameter is 2.5 mm on the crystal is reached by diffraction. In this way, an eight-pass amplifier is realized which boosts the input from 180 μJ up to 300 mJ with 3% standard deviation (amplification factor of 1500).

The drawback of this setup is that the pump power cannot be varied, because the thermal properties and the corresponding thermal lensing in the crystal would change in this case - causing different beam propagation through the system and focusing on optics. Another problem is the reduced beam quality of the output compared to the input beam. The main reason for this is a non-homogenous pump profile. These two problems, the thermal properties and pump homogeneity and the

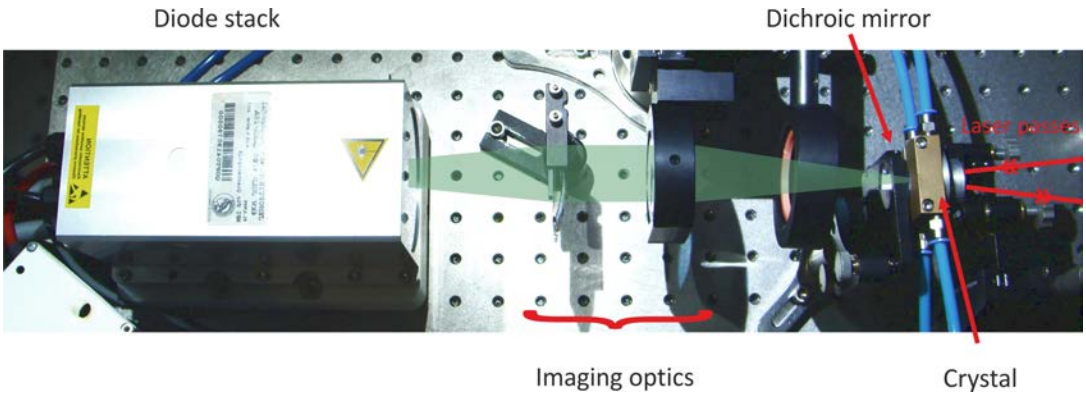

Figure 4.20: Pump setup for the multi-pass amplifier. The pump light from the 3 kW pump diode stack is collimated with a toric lens and focused with an achromatic lens through a dichroic mirror. The crystal is mounted in a water-cooled copper-heat sink.

resulting decrease of beam quality are to be avoided and therefore are key design issues of the subsequent amplifier stages, currently under development by Christoph Wandt.

4.5.2 *Amplification of shaped spectra*

The amplification of the original spectrum, without shaping, was limited to approximately 60 mJ due to optical damage resulting from gain narrowing and stretched pulse shortening in the multi-pass amplifier. Therefore, the previously mentioned spectral amplitude shaping technique was employed Spectral changes are introduced very carefully in small steps and for slowly increasing amplification factors because small changes in the input spectrum are transferred non-linearly to the output after amplification. In a first step, the output spectrum of the regenerative amplifier is shaped in order to fit to the calculated spectrum for further amplification in Yb:YAG. This input spectrum is then amplified in the Yb:YAG multi-pass amplifier after a stepwise increase of the input energy. Small corrections in the spectral shape can be applied during this procedure. For the full input energy of 180 μJ, the shaped input (shown in red in Figure 4.21 (b)) is amplified to 300 mJ with the spectrum shown in black.

For comparison, the input spectrum for 3.5 nm FWHM top-hat output profile was calculated, as shown in Figure 4.21 (a). Its major feature is a dip at 1030 nm. Compared to the spectrum predicted by our model, the real input spectrum (Figure 4.21 (b)) has narrower wings due to clipping in the stretcher. Additionally, a broader dip was chosen—in such a way that the output spectrum is still suppressed in the center and further amplification without significant gain narrowing is possible. This fact can also be seen in Figure 4.16 (a). Hence, the applied technique is applicable for higher energies and for the full amplification in the PFS system.

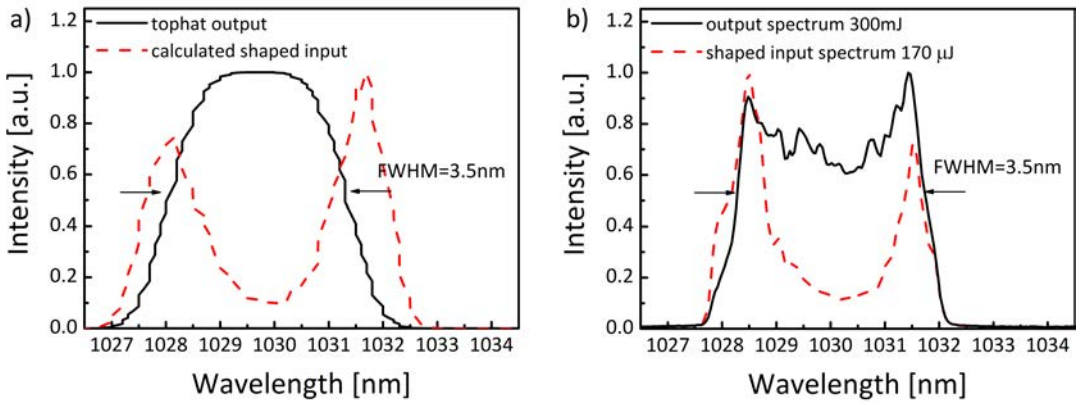

Figure 4.21: Comparison of the calculated spectral shaping and measured spectra. (a) The input spectrum (red, dashed) which supports a broad flattop spectrum (black, solid) after amplification is calculated. In (b) the measured spectra for the maximum amplification are shown. The amplified spectrum (black, solid) is still suppressed in the center, showing that further amplification is possible without significant gain narrowing. [99]

4.5.3 *Limitations of the spectral shaping technique*

The limitations of the spectral shaping technique for the bandwidth can be inferred from the spectral gain curve. In Figure 4.22 (a) the normalized spectral gain is plotted for an overall amplification factor of 3×10^5 in Yb:YAG at room temperature.

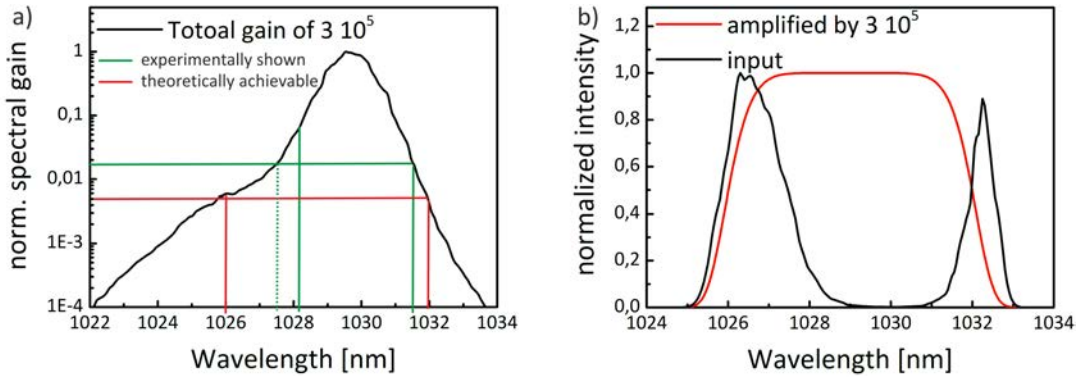

Figure 4.22: (a) Spectral gain curve for an amplification factor of 3×10^5 in Yb:YAG at room temperature. The currently achieved bandwidth is marked in green. The dotted green line shows that a broader bandwidth is achievable theoretically. Nevertheless, this is prevented by clipping in the current stretcher setup (with 58.5° AOI). The wavelengths with a factor 200 less amplification compared to the peak are marked in red and are considered as achievable bandwidth for the simulations in (b). (b) Simulated maximum obtainable spectral width for spectral shaping at an amplification factor of 3×10^5 in Yb:YAG at room temperature under the assumption that a suppression to 0.5% is still feasible.

Figure 4.22 (a) shows the difference in gain for the individual spectral components for the desired total gain level in the PFS system. For lower total gain, the differences in the spectral gain will be decreased. As marked in green a bandwidth of 3.5 nm (i.e. between 1028.25 and 1031.75 nm) is preserved at a gain factor of 1500, and from

simulations (compare Figure 4.16) it can be expected that a similar bandwidth can be preserved for the full laser system. Theoretically, an even broader bandwidth would be achievable in the current amplification experiment (green, dashed) but is prevented by clipping in the stretcher.

For an even larger bandwidth, higher suppression is necessary. This raises technical challenges: the polarization rotation has to be applied with extremely high accuracy and the polarizers have to have high extinction ratio. Apart from this, the signal to noise ratio will become a problem for suppressed wavelength components because of amplified spontaneous emission during the amplification. This could also lead to poor contrast in the compressed pulse. Due to these reasons, a suppression to less than 0.5% seems impractical. When this limitation is considered, the maximum attainable spectral width at a gain of 3×10^5 is about 6 nm FWHM, as can be inferred from the red marks in Figure 4.22 (a).

Due to the asymmetric shape of the spectral gain curve (Figure 4.22(a)), it is preferable to center the spectrum around 1029 nm for the use of extreme bandwidths. The calculated amplified spectrum and the shaped input spectrum for extreme suppression down to 0.5% are shown in Figure 4.22 (b). The amplified spectrum in this case is a super-Gaussian of order 4 with 6 nm bandwidth. This spectrum would support Fourier-limited pulses with 460 fs pulse duration.

These large bandwidths cannot be verified in the PFS pump laser setup at the moment, since the spectrum is limited to 4.2 nm by clipping in the stretcher. For a larger bandwidth, a redesign in the stretcher would be necessary to provide a bandwidth of at least 8 nm without clipping. Additionally the much shorter compressed pulses are not beneficial for the application in short-pulse pumped OPCPA, since timing jitter and B-integral problems are enhanced. These issues will be discussed in more detail later.

4.5.4 *Conclusion*

In this section, experimental results for amplification in Yb:YAG at a repetition rate of 10 Hz up to 300 mJ with an unprecedented spectral bandwidth of 3.5 nm were presented. An essential ingredient to reach this result is spectral amplitude shaping. This is a well-known technique but is usually not applied to this extent because the loss modulation significantly reduces the input energy before the amplification. Thus, a higher gain (accompanied with higher gain narrowing) is needed for the shaped spectrum which limits the useful extent of spectral amplitude shaping. The combination of spectral shaping followed by a broad-band amplification stage (the regenerative amplifier) compensates for this major drawback in our case.

A significant bandwidth increase from 1.3 nm to 3.5 nm could be demonstrated. This does not only reduce the Fourier-limited pulse length but also helps to increase the efficiency in the Yb:YAG amplifier system. In Yb:YAG, the saturation fluence ($10\,\mathrm{J/cm^2}$) lies above the damage threshold fluence for short pulses, but efficient energy extraction is not possible below the saturation fluence. In this context, the increased bandwidth also increases the chirped pulse duration and at the same time the damage threshold. Therefore, a more efficient energy extraction can be expected.

The drawback of the extended spectrum is that the gain in the Yb:YAG amplifiers is reduced compared to the narrow spectrum. Therefore, more amplification passes have to be applied in order to reach the same output energy. This is probably acceptable in many cases, when a shorter pulse duration is needed, but could be a limiting factor for large scale systems.

4.6 THE COMPRESSOR

The first compressor layout was developed by Izhar Ahmad in his PhD thesis. The design is presented here for completeness. In this work, a ray-tracing analysis is performed and design-related problems for the experimental realization and alignment of the compressor are pointed out.

The compressor design is of the Treacy type [26]. The same gratings as in the stretcher ($N = 1740\,\text{lines/mm}$) are used under an identical angle of incidence ($\alpha = 58.5°$) and grating separation ($D = 6.2255\,\text{m}$). The special feature of the PFS pump compressor is the requirement to compress two (and later maybe up to four) identical beams in a single setup.

This is achieved using a common large-size second grating with $800\,\text{mm} \times 400\,\text{mm}$ in combination with individual first gratings for each beam and a common tilted folding mirror. The setup is illustrated in Figure 4.23 for a top and side view, where the path of a single beam is illustrated to avoid confusion.

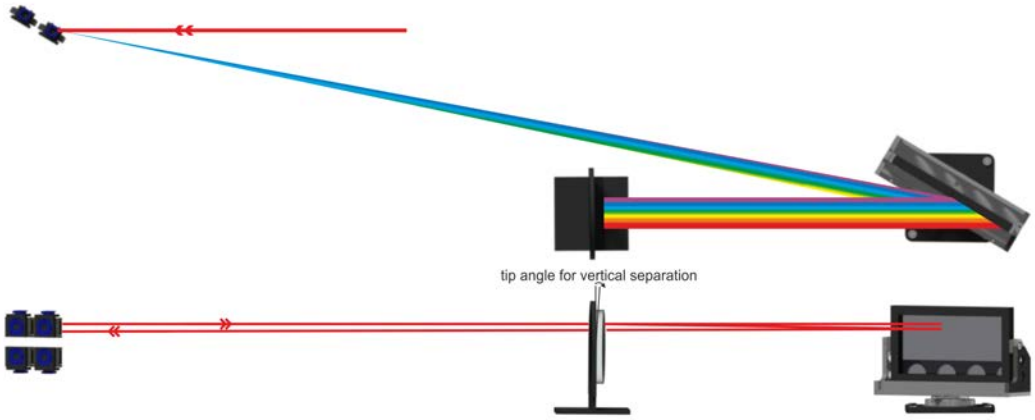

Figure 4.23: Setup for the four beam Treacy compressor. The gratings have a line density of $N = 1740\,\text{lines/mm}$ and are used under an angle of incidence of $\alpha = 58.5°$, with a grating separation of $D = 6.2255\,\text{m}$. The beam path for a single beam is illustrated. The vertical separation of the incoming and outgoing beam is achieved with a small tip angle of the folding mirror. The 4 beams are stacked in a 2×2 array.

Due to the long stretched pulse duration of $3 - 4\,\text{ns}$, the compressor has to provide the necessary delay between opposite ends of the relatively narrow laser pulse spectrum. This necessitates the use of large gratings in the dispersion plane, which in addition have to have high diffraction efficiency and damage thresholds. All these requirements can be fulfilled by multilayer dielectric gratings [109]. The big advantage of this kind of gratings compared to conventional metallic gratings is the en-

hanced damage threshold. In [110] it is shown that the damage threshold of these kind of gratings can exceed $3.5\,J/cm^2$ for 500 fs pulses at 72.5° where gold gratings have $0.67\,J/cm^2$ under the same conditions. Due to this fivefold increase in the damage threshold, the beam size in the compressor can be decreased. Together with a grating size of 800 mm × 400 mm, this enables the stacking of four individual beams in a single compressor in the PFS compressor system.

The necessary beam size depends on the pulse parameters. For the PFS system, the final beams will have an energy of 10 J in $\Delta t = 1$ ps. At this stage, it is not yet clear whether the beam will be Gaussian or super-Gaussian of some higher order. A top-hat ($I = const for r < R$) profile is ideal for pumping OPCPA stages because of the constant intensity (and therefore constant gain) over the transverse position. The disadvantage of the top-hat is that the steep edges will create diffraction patterns with local intensity peaks during propagation. More realistically, the beam profile could be described by a super-Gaussian profile of low order. Nevertheless, the top-hat profile will be considered as limiting case. The peak intensity and fluence is calculated for top-hat and for Gaussian profiles of different sizes with formulas from Section A.2. The results are summarized in Table 4.3.

Gaussian FWHM	w_0	I_0 [$\frac{W}{cm^2}$]	F_0 [$\frac{J}{cm^2}$]
2 cm	1.69 cm	$2.1 \cdot 10^{12}$	2.20
3 cm	2.56 cm	$9.2 \cdot 10^{11}$	0.98
4 cm	3.41 cm	$5.2 \cdot 10^{11}$	0.55
5 cm	4.27 cm	$3.3 \cdot 10^{11}$	0.35
6 cm	5.12 cm	$2.1 \cdot 10^{11}$	0.22
top-hat diameter	I_0 [$\frac{W}{cm^2}$]	F_0 [$\frac{J}{cm^2}$]	
3 cm	$1.4 \cdot 10^{12}$	1.41	
4 cm	$7.4 \cdot 10^{11}$	0.79	
5 cm	$4.8 \cdot 10^{11}$	0.51	
6 cm	$3.3 \cdot 10^{11}$	0.35	

Table 4.3: Peak intensity and fluence for different beam sizes of a Gaussian and a top-hat profile for pulses with 10 J energy in $\Delta t = 1$ ps.

The previously mentioned damage fluence of $3.5\,J/cm^2$ is the highest fluence with zero damage probability. In the design of a laser system one should keep a certain safety margin in order to prevent damage even in cases of locally enhanced intensities like from beam clipping.

Another constraint is the size of the first grating (200 × 100 mm). These gratings were purchased at a very early stage of the project planning, before the start of this PhD work. Under an AOI of 58.5°, the aperture is approximately 10 × 10 cm. Moreover, two beams have to fit onto a single grating: the input beam and the

output beam which are vertically offset due to a small angle at the folding mirror (9 m away). For example, an vertical angle of 0.11° corresponds to a vertical offset of 2 cm. This offset should be large in order to avoid an additional long propagation to separate the in- and out-going beam.

Siegman [69], shows that Gaussian beams transmitted through circular aperture with diameter πw_0 cause 1% power loss, but ±17% intensity ripples in the near field according to 17% intensity reduction on axis in the far field. An aperture of $4.6\, w_0$ reduces these effects to less than 1%. Two Gaussian beams on a single grating with 2 cm vertical separation, can fulfill this constraint up to a size of 2 cm FWHM ($w_0 = 1.69$ cm). Together with the envisioned pulse energy of 10 J, the peak fluence of 2.2 J/cm^2 (compare Table 4.3) is only a factor 1.6 below the damage fluence. A lower fluence can be realized with a spatial super-Gaussian beam with a more flat profile in the center and less wings. A reasonable compromise for this kind of beam profile would be a diameter of approximately 4 cm, which corresponds to a fluence 4.4 times below the damage threshold. A vertical offset of 2 cm on the grating (i.e. 0.11° tip angle between the in and out-coupled beam) is possible without clipping. Nevertheless, a long propagation after the compressor is necessary in order to separate both beams spatially.

The horizontal spread of the beam inside the compressor is determined via ray tracing. For wavelength of 1030 ± 2 nm, the size is 41 cm and 24 cm on the large grating and on the folding mirror, respectively. The tip angle of 0.11° on the end mirror introduces a vertical spatial chirp 0.3 mm/nm in the output beam. This spatial chirp is tolerable for the 4 nm bandwidth. In effect the extreme wavelengths are vertically separated by 1.2 mm (in a 4 cm large beam) which results in a narrower bandwidth and longer pulse length in the outermost beam positions. Another aspect should be considered for the alignment of the compressor: as mentioned in Section 2.3, a pulse-front tilt introduced by an angular chirp (misaligned grating parallelism) could be inadvertently compensated by a combination of the spatial chirp and a certain temporal chirp. Therefore, special care should be taken in the characterization of the compressed pulse.

Fitting of four beams in this compressor is done by stacking four small gratings, as shown in Figure 4.23. The horizontal distance is 22 cm and the vertical distance 20 cm. This ensures enough separation to individually align the four beams and is small enough to prevent clipping in the compressor if the folding mirror has a diameter of 50 cm. There are alignment constraints for the PFS compressor due to the fact that four beams are using a common second grating and folding mirror. The four compressors have to be aligned individually i.e. second grating and folding mirror always stay fixed. Photographs of the compressor components are shown in Figure 4.24. The mounts for the large optical components (second grating, end mirror) were build in the institute workshop. Due to reasons of robustness, simplicity and cost, these mounts lack provisions for translatory motion and only feature tip and rotation control. The alignment of the compressor length is therefore performed with the small grating. For accurate grating parallelism, the pulse-front tilt or angular chirp in the output beam have to be measured and removed with fine alignment of the first grating after each grating movement. In order to find the shortest compressed pulse, fine angle tuning with few 100 μrad is necessary. These small angles

can be changed when the input beam is steered with the last turning mirror before the grating. At the same time the angle has to be observed with high resolution (for the zero order reflection) in order to make the angle scan reproducible. The compressor can then be aligned with an iterative angle and length scan.

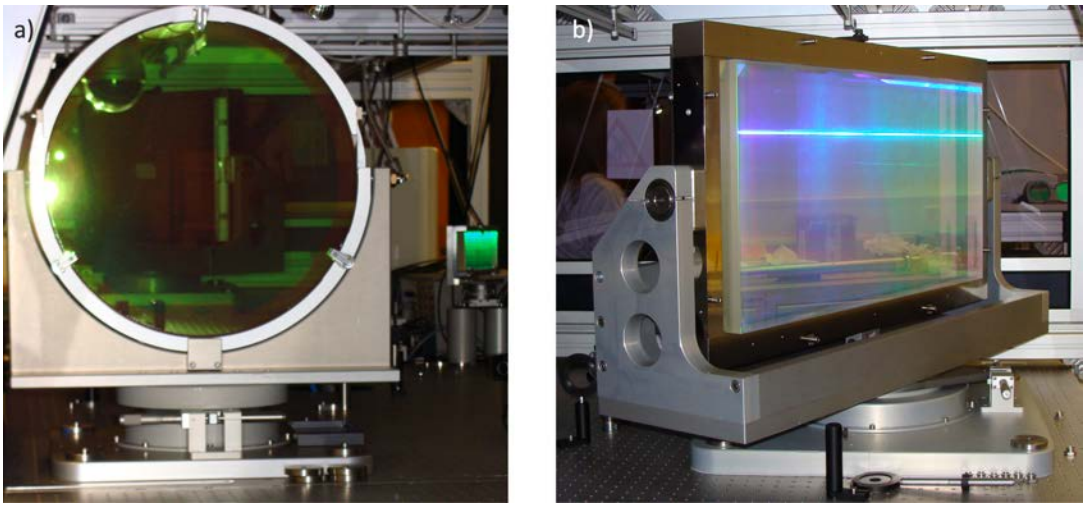

Figure 4.24: Photographs of the compressor components (compare Figure 4.23). (a) The plane end-mirror with 500 mm diameter and the first grating are shown. (b) Shows the 400 × 800 mm large grating.

At the current state, the compressor is set up and aligned for a single beam (i.e. with a single small grating). For the first compression experiment, the beam size in the compressor is chosen to be 2 cm (Gaussian profile). This is large enough to compress the available pulses with an energy of 300 mJ without the risk of damage.

4.6.1 *Simulation of the compression*

Simulations are carried out in order to find the sensibility of the compressor alignment for the pulse compression under consideration of a certain stretcher setting. The stretcher dispersion terms are obtained from ray-tracing (compare Table 4.1) for an AOI of 58.5° and a grating separation of 6.2255 m. The dispersion orders calculated by the ray-tracing include effects from aberrations in the stretcher. The dispersion terms for the compressor are calculated with Eqs. 2.55-2.57. The effect of the remaining spectral phase after stretching and compression is evaluated for the measured spectrum with 3.5 nm FWHM (compare Figure 4.21). The pulse width in the following graphs is normalized to the Fourier limited pulse width of 890 fs.

In Figure 4.25 the calculated compressed pulse length is shown as function of the compressor grating dispersion for different fixed angles. This situation represents a compressor length scan, as is typically performed in the lab. If the compressor angle is 0.1° smaller than the stretcher angle, the needed compressor grating separation is 10 cm shorter than expected for compression (see Figure 4.25(b)) and the minimum pulse length is 10% above the transform limit. Additionally, in this misaligned case the pulse length is less sensitive to a few mm length de-tuning around the pulse length minimum. Without changing the compressor length, a slightly different com-

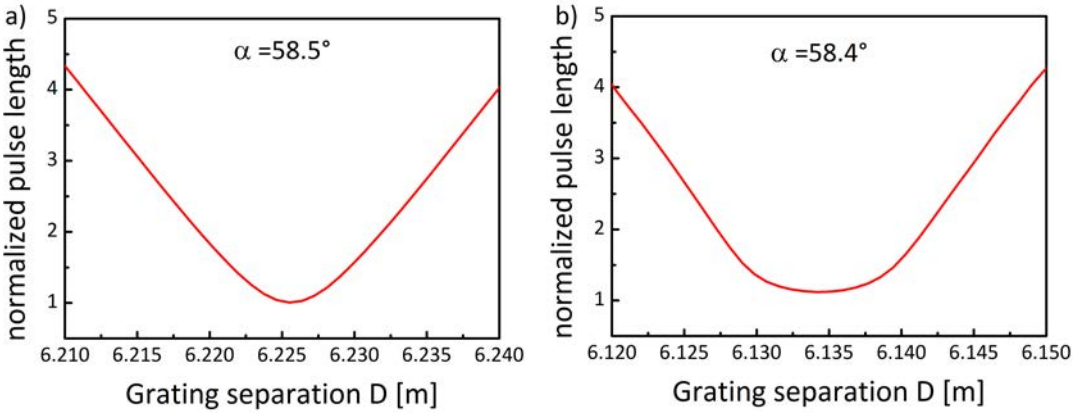

Figure 4.25: The effect of a compressor lengths scan on the pulse length is shown for the optimum angle (a) and for a slightly misaligned angle (b).

pressor angle setting of $\pm 0.01°$ (including the perpendicular fold mirror) can cause a $\pm 10\,\%$ pulse-length increase due to the changed dispersion.

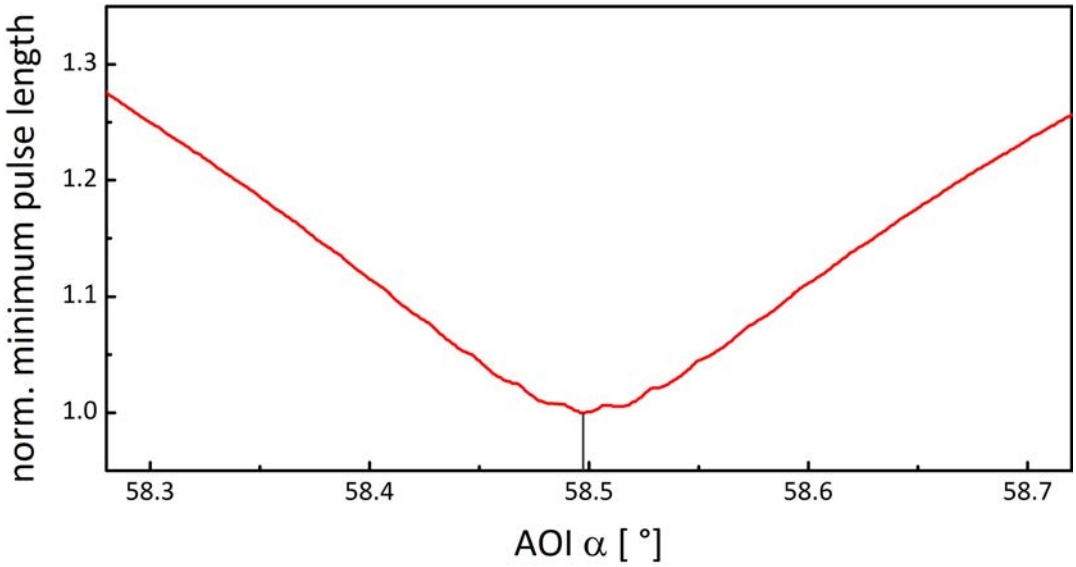

Figure 4.26: Dependence of the minimum pulse length on the compressor angle. In this graph, the compressor grating separation is varied for each angle.

Curves like in Figure 4.25 are calculated for a variety of angles. The minimum pulse length is extracted for each curve and the the dependence of the minimum pulse length on the compressor angle is shown in Figure 4.26. The ripples in the curve around the minimum are artifacts caused by the discrete gridsize of 0.5 mm and $5 \cdot 10^{-4}$degree. The absolute minimum of this curve is close to the design angle of 58.5°. The small deviation from this value comes from the aberrations in the stretcher. This curve gives some hints for the practical alignment: if the shortest pulse length (obtained with a length scan and constant angle) is 10 % above the transform limit, then the compressor angle is de-tuned by 0.1°. The direction can be found by the measured compressor grating separation: if larger than expected- the angle was to large.

In order to find the optimum compression conditions and the sensitivity of the angle and length alignment, the dispersion terms and the corresponding pulse length are shown in Figure 4.27 for a range of $\pm 0.02°$ and $\pm 2\,\mathrm{cm}$. The remaining dispersion for a stretched and re-compressed pulse is calculated for this range of angles and grating separations (compare Figure 4.27 (b)-(d)). The effect of these dispersion terms on the pulse length is shown in Figure 4.27 (a).

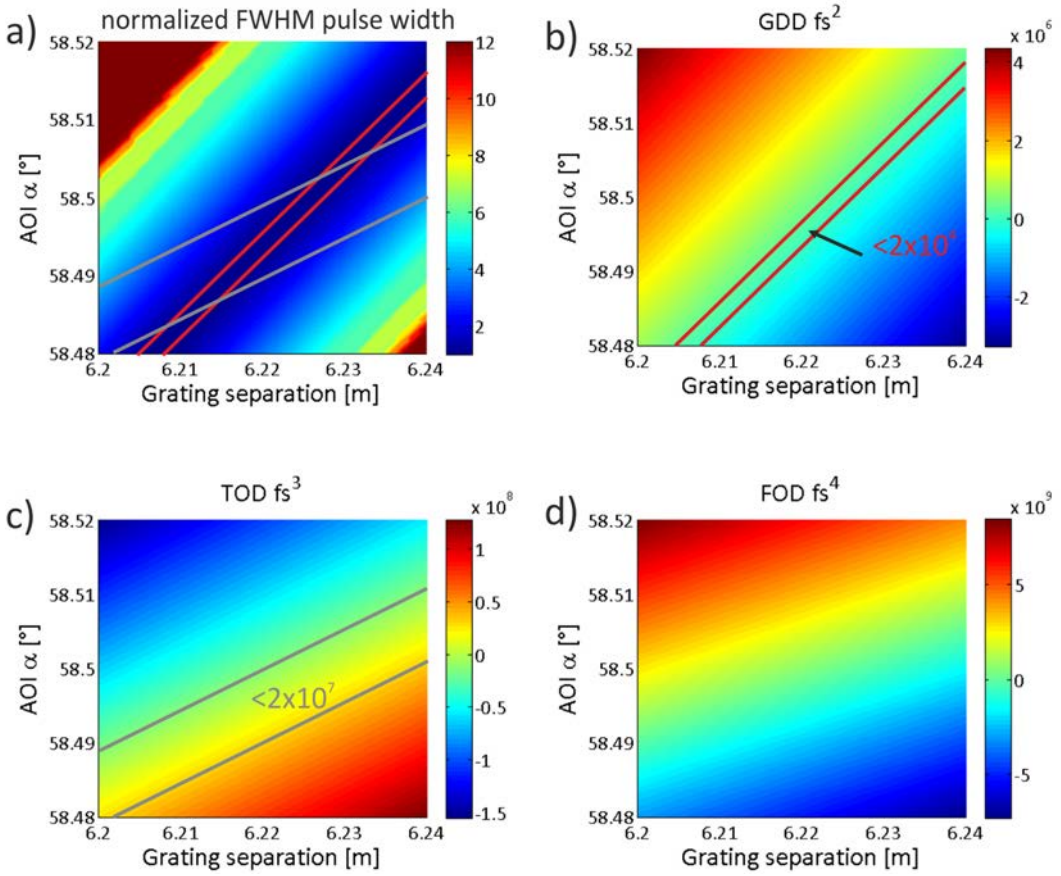

Figure 4.27: The difference of the dispersion terms for a certain stretcher ($\alpha = 58.5°$, $D = 6.2255\,\mathrm{m}$, dispersion terms obtained by ray tracing including aberration effects) and a range of compressor angles and grating separations is shown in (b)- (d). The effect of these dispersion terms on a pulse with the amplified spectrum (compare Figure 4.21) is shown in (a). The pulse width is normalized by the Fourier limited pulse width. The region of negligible dispersion (compare Table 2.1) is marked in the pictures: red for GDD, gray for TOD, the FOD is negligible for the FWHM pulse width in the range displayed here.

In Section 2.2, the effect of the different dispersion orders on the pulse shape was discussed. A simulation showed the magnitude of the dispersion orders, which have negligible effect on the pulse FWHM. These values were summarized inTable 2.1. In Figure 4.27 this negligible GDD and TOD is marked in red and gray, respectively. The effect of the forth order in Figure 4.27 (d) is negligible for the pulse FWHM duration in the whole plotted range. In Figure 4.27 (a) the regions with low GDD and TOD are marked, as well. In the region, where both GDD and TOD are small the pulse can be considered to be compressed. If the compressor angle is set correctly in a range

of $58.495 \pm 0.012^\circ$, the beam can be compressed easily with a compressor grating separation scan without a need of an additional angle scan.

In the previous passage it is assumed that the fold mirror is tuned to be perpendicular when the AOI is changed. The situation is different when the effect of beam pointing at the compressor input on the dispersion is considered. In this case, the fold mirror is aligned to be perpendicular for the design angle. A slightly larger input angle (i.e. from pointing fluctuations) will be reflected at the fixed fold mirror under non-perpendicular incidence and cause a slightly smaller angle on the back propagation through the compressor. Therefore, the sensitivity of the compressor setup with fold mirror on beam pointing is reduced. Even $\pm 0.2^\circ$ (or $\pm 3.5\,\mathrm{mrad}$) AOI fluctuations (with fixed separation and fold mirror) cause only $\pm 10\,\%$ pulse-length fluctuations.

As a conclusion of this section, the design for a compressor with four individual beams is presented. The introduced spatial chirp introduced by the tip angle of the folding mirror can be considered to be small. Alignment sensitivities for the angle and grating separation are calculated. For the angle alignment, a rotation scale gradation with 1/60 degree is sufficient to get a reasonable compression result. The compressor length has to be exact to less than a mm.

Part III

EXPERIMENTS

5

PULSE COMPRESSION

5.1 BEAM POINTING MONITORING

An accurate online beam angle monitor with data analysis at the stretcher and compressor input is a necessary tool for the alignment of the compression. The relative angle change of a laser-beam direction can be measured as focus position in the focal plane of a lens and the angle in μrad is then the difference in the focus position divided by the focal length. A *Labview* program was developed, which reads out cameras and determines the beam centroid. In the stretcher, this program is used together with a *Basler ACE640-100gm* camera and a lens with 1 m focal length. The camera pixel size is 5.6 μm which results in a resolution of at least 5.6 μrad. The determination of the beam centroid can be done with sub-pixel resolution which further improves the measurement accuracy. For the camera setup used in the stretcher, the error due to pixel noise is around 2 μm (2 μrad) standard deviation.

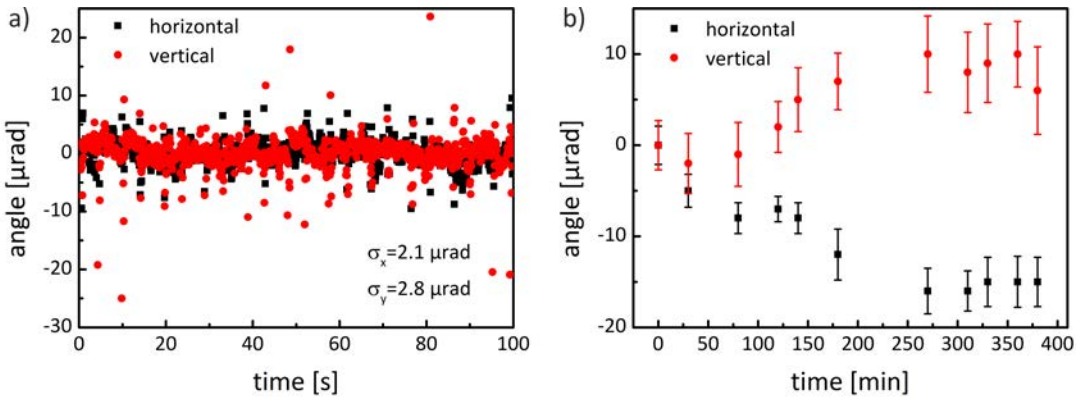

Figure 5.1: The beam pointing direction is measured at the stretcher input for 1000 measurements on a shot-to-shot basis (a) and as a fluctuation over several hours (b). Each point in this graph represents the mean of 100 measurements with the corresponding standard deviation as error-bar.

In Figure 5.1 the measured relative beam pointing direction into the stretcher is shown on a short time scale (a) and over one day (b). In the former case (1000 measurements), the standard deviation of the angle is below 3 μrad in the vertical and horizontal direction. These values are close to the resolution limit of the used camera setup. During a four-hours warm-up period, the pointing changes by less than 20 μrad and stays constant within a few μrad afterwards. For the compressor, these beam pointing fluctuations are even smaller, since the beam profile is magnified (by factor 50) compared to the stretcher which demagnifies the angles by the same amount. With two of these cameras, the beam position (near field) and the direction (far field) are observed for the zeroth order diffraction of the input beam off the grating. In the previous chapter it was discussed that 3.5 mrad pointing fluctuation

cause 10% pulse length fluctuations. This 20 μrad long-term drift is therefore negligible and does not change the compressed pulse length significantly. In the future, the cameras may be used to control motorized mirrors for automatic alignment and compensation of the slow drift.

5.2 COMPRESSION RESULTS

The compressor was aligned using the strategy outlined in Section 4.6. The gratings are aligned parallel by minimizing the pulse-front tilt in both dimensions in a interferometric inverted field autocorrelator (compare [83]).

As shown in Figure 4.1, an acousto-optic programmable dispersive filter (*Dazzler HR-45-1053-board-V5-rev5, Fastlite*) is implemented for shaping the spectral phase [111]. In this device an acoustic wave with time dependent frequency is generated in a crystal. The incident (ordinary) light wave is scattered into the extraordinary wave by acousto-optic coupling. Locally there is only one acoustic frequency present forming an acoustic grating. Thus, only one light frequency is scattered at the corresponding position, while the intensity of the acoustic wave determines the scatter efficiency. In this way, the device can shape both the spectral amplitude and phase in a very simple setup. (The spectral amplitude shaping stage, described earlier, was replaced by the *Dazzler* in the final compression experiments, which allows control over both spectral amplitude and phase.)

The *Dazzler* used in the experiment has a 45 mm crystal and can alter the spectral phase to an amount that corresponds to a time window of 14 ps. For 4 nm bandwidth, this translates to a maximum change of either the $GDD = \pm 6 \cdot 10^5\,\mathrm{fs}^2$, the $TOD = \pm 2.5 \cdot 10^8\,\mathrm{fs}^3$ or the $FOD = \pm 4 \cdot 10^{10}\,\mathrm{fs}^4$.

In a first attempt, compression to 115% of the Fourier limit was achieved. In order to improve the compression, a parameter-scan for a non-shaped (1.5 *nm*) broad spectrum at low power) was performed. In a first step, the expected width of the autocorrelation trace was calculated for different values of the GDD and TOD. The results are illustrated in Figure 5.2.

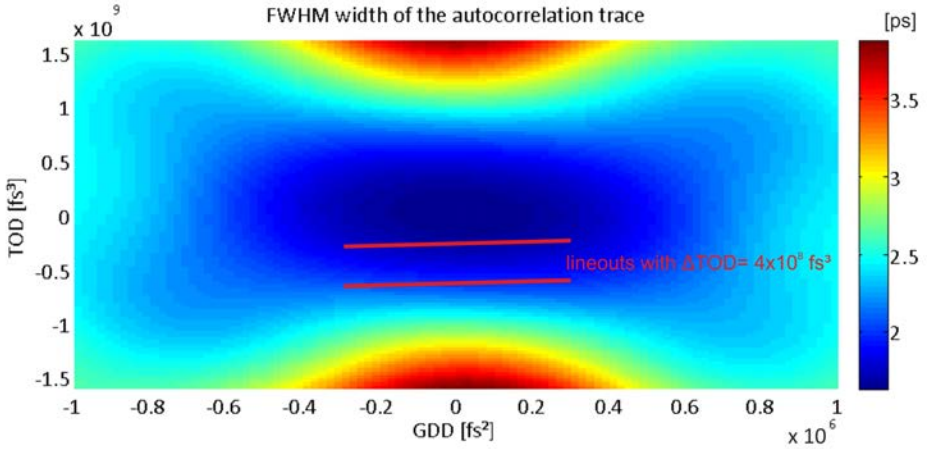

Figure 5.2: The auto-correlation width is plotted color-coded as function of GDD and TOD. The red lines mark the line-outs that best match the measured curves in Figure 5.3 a) and b).

The goal is to find the remaining GDD and TOD values for a given setting of the stretcher and compressor in order to improve the compression. When the pulse-length is minimized with a compressor length scan, the GDD is close to zero and the remaining TOD has to be determined. When the TOD value is known, the compressor angle and length can be changed in a straight -forward way.

In order to determine the TOD, two different length scans in the compressor are performed for a TOD of either $+2 \cdot 10^8\,\mathrm{fs}^3$ or $-2 \cdot 10^8\,\mathrm{fs}^3$ introduced by the *Dazzler*. In both cases, the compressor length is scanned by 13 mm with a 10 μm-resolution delay stage. The difference in GDD and TOD is calculated for each length. Since the TOD is slowly changing for a length scan of few mm, the two measured curves correspond to (nearly) horizontal line-outs in Figure 5.2. The measured line-outs have a known offset of $4 \cdot 10^8\,\mathrm{fs}^3$ in TOD direction, but the absolute position is unknown. The remaining TOD value can be found, by shifting both measured line-outs simultaneously (in the TOD direction) to fit to the calculated surface. Two measurements are used, because the sign of the TOD cannot be obtained by a single measurement since Figure 5.2 is symmetric.

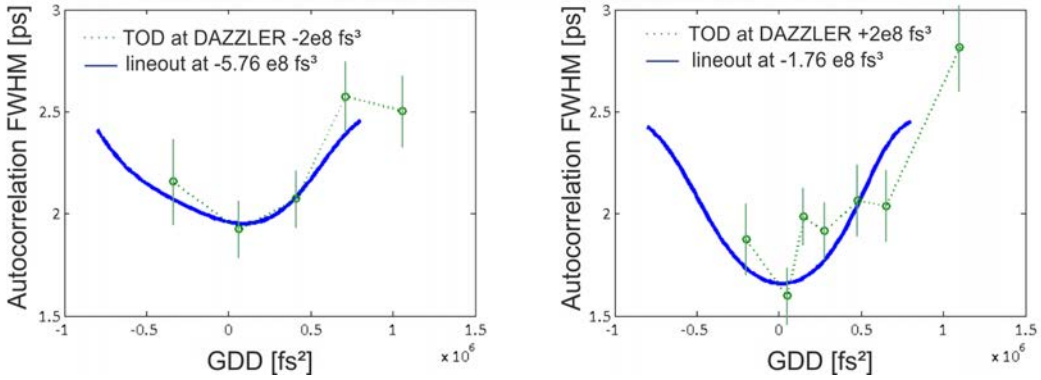

Figure 5.3: Estimation of the remaining TOD in the compressor. Data from compressor length scans with a known amount of TOD introduced by the DAZZLLER is compared with the calculated values of Figure 5.2. The remaining TOD in the compressor is obtained from this comparison.

In Figure 5.3, the measured autocorrelation widths are shown for both cases in comparison to the best fitting curves from the calculation. The TOD values of the calculated curves are $-5.76 \cdot 10^8\,\mathrm{fs}^3$ and $-1.76 \cdot 10^8\,\mathrm{fs}^3$. Hence, the remaining TOD of the compressor without adding TOD with the *Dazzler* was $-3.76 \cdot 10^8\,\mathrm{fs}^3$. This value cannot be compensated by the *Dazzler* but can be compensated by an angle reduction about 0.1° in combination with a length reduction about 12 cm. With this procedure, it was possible to obtain nearly optimum compression. Once this alignment is found, small changes can be also compensated by the *Dazzler* settings.

As shown in Figure 5.4, the spectrally shaped amplified pulses were compressed to 900 fs, close to transform limit (884 fs) with 200 mJ [99]. The transmission efficiency of 66% includes the losses of a spatial filter after the compressor. Spatial filtering of the beam is performed in order to remove high-frequency modulations of the beam profile imprinted by the gratings.

The compressed pulse duration is measured by a home-built single-shot second-order autocorrelator with a tuning window of 6 ps and a pixel resolution of 22 fs. This device is designed to measure 700 fs pulses with 6% accuracy. The measured autocorrelation trace is shown in Figure 5.4.

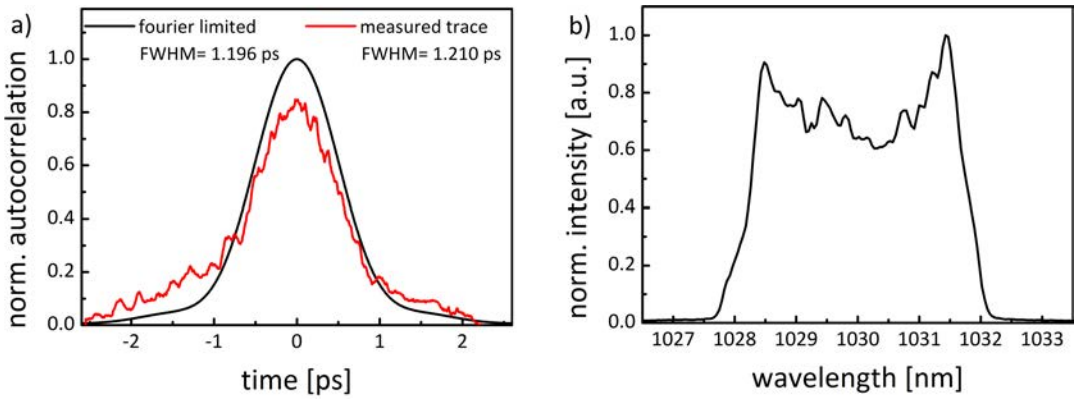

Figure 5.4: (a) The calculated autocorrelation trace for the Fourier-limited pulse (black) and measured autocorrelation trace (red) [99]. The measured trace is normalized to enclose the same area as the calculated autocorrelation trace. The corresponding pulse length is 884 fs and 895 fs, respectively. (b) The corresponding spectrum.

The autocorrelation traces are averaged over 1000 shots, resulting in a mean width is 1.21 ps with a standard deviation of 0.04 ps. The Fourier limited pulse shape and the corresponding autocorrelation trace are calculated from the measured spectrum. From this, a deconvolution factor between the pulse duration and the width of the autocorrelation trace of 1.3518 can be inferred for this particular case. Using this factor, an estimate for the compressed pulse duration of 895 fs (transform limit 884 fs) with a measurement uncertainty of 40 fs was obtained. The existence of side wings in the Fourier-limited trace results from the steep edges in the spectrum (compare Figure 5.4(b)), which are caused by clipping in the stretcher. As can be seen in Figure 5.4 (a) the autocorrelation trace is slightly asymmetric, which is most likely caused by an imperfect beam profile in the autocorrelator. Although the main pulse is close to the Fourier-limited FWHM, there are large side wings which could be explained by uncompensated higher order dispersion. Another possibility could be spatio-temporal coupling caused by B-integral issues when the compressed pulse propagates in several meters air after the last grating. In the latter case, the problem will be solved by a vacuum chamber for the compressor, which is currently under construction.

5.3 REFINED DISPERSION MANAGEMENT

During the experimental realization of the CPA pump laser, it was shown that a significantly broader bandwidth (3.5 nm top-hat) than the initially assumed 1.5 nm Gaussian spectrum can be amplified. The modifications in the dispersion management in order to respond to the different situation are described in the following.

5.3.1 *Stretcher modifications*

As explained in more detail in Chapter 6, the stretcher had to be rebuilt on a new breadboard and inside an air-tight box in order to provide a better timing jitter stability. During this reconstruction, the stretcher AOI was changed from 58.5° to 60° due to the following reasons:

A broader amplified spectrum than initially considered was observed in the experiment—leading to a shorter compressed pulse duration and a longer stretched pulse duration than estimated in Section 2.4. Therefore, the stretcher dispersion can be reduced while the stretched pulse duration stays constant. For example for 700 fs compressed pulse duration (instead of 1 ps) the needed GDD reduces from $6 \cdot 10^8$ fs^2 to $5 \cdot 10^8$ fs^2. The reduced dispersion in the stretcher can be achieved for example by reducing the grating separation from approximately 6 m to 5 m (with a fixed angle of 58.5°) or by increasing the angle from 58.5° to 60° (with a fixed grating separation of 6 m). The latter one was preferred because of the higher diffraction efficiency of the gratings for the increased angle (compare Figure 4.4) which increases the compressor transmission by approximately 4 %.

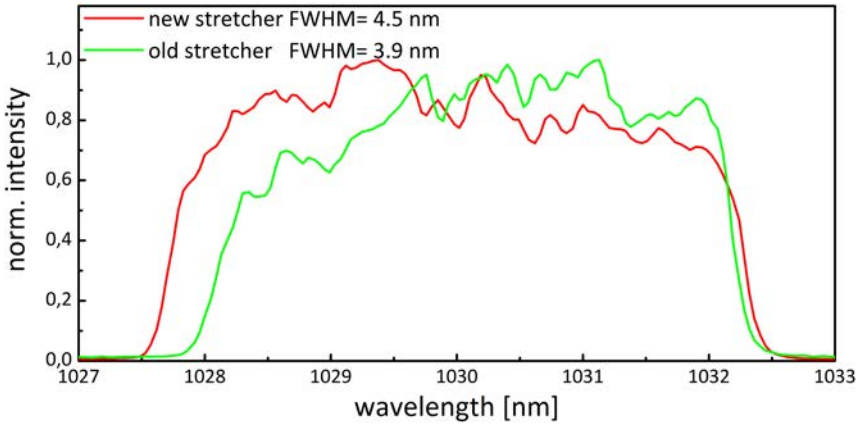

Figure 5.5: The transmitted bandwidth for the old stretcher with 58.5° is compared to the new stretcher 60°. The bandwidth is increased by 0.6nm allowing for a shorter pulse length after compression.

Increasing the angle also increases the transmitted spectral bandwidth in the stretcher (compare Figure 5.5), because of the decreased grating dispersion and the increased effective grating aperture in dispersion direction. The Fourier-limited pulse duration of the thereby broadened stretcher output spectrum (compare Figure 5.5 green) is reduced to 660 fs and fits to the bandwidth theoretically predicted in Figure 4.22. Together with the increased bandwidth, the sensitivity of the compression on dispersion orders is increased, as shown in Table 5.1 for the current case with 700 fs and the extreme case (predicted in Figure 4.22) with 500 fs.

For the current case with 700 fs, the stretcher angle was increased to 60° from 58.5° which decreased the total dispersion. Simultaneously, the sensitivity of the dispersion terms on small angle changes is reduced (e.g. 0.2° angle fluctuation cause a change of $3 \cdot 10^5$ instead of $6 \cdot 10^5$fs^2 in the GDD) while the pulse duration reacts more sensitive on dispersion changes (compare Table 2.1 andTable 5.1). Therefore,

	$\Delta\tau_{FWHM}$	GDD [fs^2]	TOD [fs^3]	FOD [fs^4]
	+10%	$8 \cdot 10^4$		
$\tau = 700$fs	+10%		$7 \cdot 10^7$	
	+10%			$3 \cdot 10^{10}$
	+20%	$8 \cdot 10^4$	$7 \cdot 10^7$	$3 \cdot 10^{10}$
	$\Delta\tau_{FWHM}$	GDD [fs^2]	TOD [fs^3]	FOD [fs^4]
	+10%	$4.5 \cdot 10^4$		
$\tau = 500$fs	+10%		$3 \cdot 10^7$	
	+10%			$1 \cdot 10^{10}$
	+20%	$4.5 \cdot 10^4$	$3 \cdot 10^7$	$1 \cdot 10^{10}$

Table 5.1: Effect of different dispersion orders on the FWHM pulse length for 700 fs and 500 fs pulses at 1030 nm. The values can be compared to Table 2.1, where the same analysis was performed for 1 ps pulse duration.

the alignment sensitivities discussed in previous chapters are the same for 700 fs pulses as for 1 ps pulses. Nevertheless, the higher order dispersion introduced by aberrations in the stretcher starts to affect the pulse shape for the broadened spectrum and full compression cannot be achieved with the stretcher and compressor alone. The implemented *Dazzler* provides the freedom of freely adjusting the spectral phase (inside a time window of 10 ps) in order to optimize the compression. The 500 fs pulses cannot be shown in the current setup. A larger grating with 300 mm aperture in the dispersion direction is necessary in combination with an aberration free stretcher design [28] in order to prevent spatio-temporal couplings.

The same angle change as in the stretcher has to be accomplished in the compressor in order to match stretcher and compressor dispersion. Apart from this, the timing jitter analysis (Chapter 6) shows that the full compressor has to be enclosed in a vacuum chamber- in contrast to the original plan where only the last grating should have been put in a considerably smaller vacuum chamber. The current compressor would need a chamber of the size of $6.20 \times 1.50 \times 0.9\,m^3$. Vacuum chambers of this size are expensive and have considerable weight. Hence a redesign for the compressor is done in order to minimize the compressor chamber size, weight, and cost. In the following section, the modified design of the final compressor and the corresponding vacuum chamber are presented, which will be realized in future.

5.3.2 *Final compressor and vacuum chamber design*

The original compressor design (Figure 4.23) is modified in order to fit in a rather compact and light-weight vacuum chamber. Instead of two parallel gratings in combination with a plane fold mirror, a single grating is applied with two roof mirrors- one for a horizontal offset and one for a vertical offset [112]. The new setup is shown in Figure 5.6.

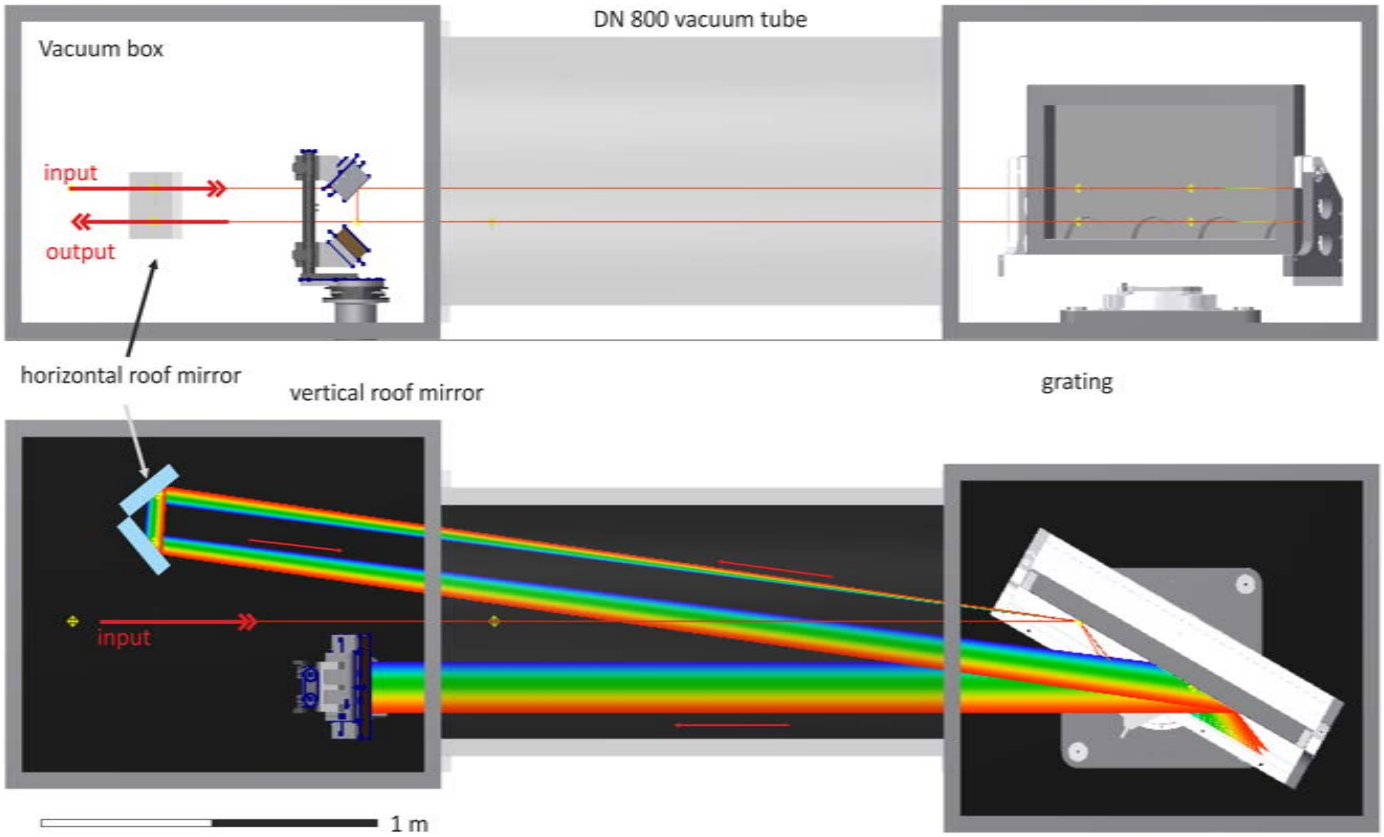

Figure 5.6: The new compressor consists of a single grating, a horizontal roof mirror and a vertical roof mirror. The input beam is diffracted from the grating propagates to the horizontal roof mirror where a horizontal offset is introduced before the second diffraction off the grating. From there, the beam is directed to the vertical roof mirror which sends the beam back over the previous optics but with a vertical offset. In this way, the input and output beam are parallel but well separated in height. The horizontal roof mirror is placed at half the original grating separation and therefore folds the setup. Both roof mirrors can be placed close together. In this scheme, it is possible to use a vacuum tube in the center of the setup where no components are placed. The grating and the two roof mirrors are placed in identical vacuum chambers of approximately $1\,m^3$. This chamber design is compact, cost effective and light-weight.

After the first diffraction off the grating, the beam is horizontally offset by the first roof mirror and redirected to the grating. In this way, the compressor is folded and the width of the grating is effectively used. Subsequently, the beam is offset vertically by the second roof mirror and performs the third diffraction off the grating, the second reflection of the horizontal roof mirror and the fourth diffraction on the grating. The output beam is parallel to the input, but vertically offset. In this way, the problem of the separation of input and output beam and the remaining spatial chirp from the angled fold mirror is removed (compare Section 4.6). Additionally, the use of a single grating will significantly simplify the compressor alignment.

The components of the compressor will be shifted in such a way that two identical (relative small) compressor chambers (ca. $1\,m^3$) and a connecting vacuum tube can be used instead of a large chamber. The increased AOI (from 58.5° to 60°) helps to decrease the angle between incident and diffracted beam and therefore allows for a compact design with only 800 mm inner diameter for the tube.

The implementation of the tube saves weight and costs and the total setup has a footprint of only $4 \times 1\,m^2$. Compared to the original design with $6.5 \times 1.5\,m^2$ the size will be significantly reduced, but only two beams can be used in the new compressor setup instead of up to four beams in the original design. Nevertheless, in the new design the aperture of 10 cm (from stacking 2×2 passes on 40 cm aperture of the large grating) is used by a single beam (instead of two beams in the former design) which enables the use of a larger beam size and pulse energy. Alternatively, the compressor has to be duplicated for the use of 4 beams. The chamber is ordered and will be delivered in the next months. In the development phase of this compressor chamber, intermediate compressor design modifications were performed in order to achieve further progress in the PFS project.

5.3.3 *Intermediate compressor design and latest compression results*

The OPCPA stages require a high pump intensity (above $100\,GW/cm^2$) which leads to nonlinear effects like self-focusing in the several meter propagation in air. The so called B-integral is frequently used to estimate when nonlinear effects become important. When the B-integral is kept below 1, nonlinearities are considered to be marginal (see Section A.3). In the described case, the B-integral for the (frequency doubled) OPCPA pump is on the order of 0.3 per meter air or per mm fused silica (the nonlinear refractive index of fused silica is well known and can be used as estimate for optical materials). Therefore, the whole OPCPA system has to be built in vacuum.

This requires some changes in the compressor, as well. In the intermediate solution, the compressor should be used with a single beam with up to 1 J pulse energy without a vacuum chamber. In order to minimize the B-integral, the beam size is chosen to fill the maximum single-beam aperture in the compressor of 3 cm FWHM. Additionally, the vacuum should start as close as possible to the compressor output. These requirements cannot be met with the initial compressor design (compare Figure 4.23) where the separation of the input and output beam was realized with a small tip angle of a plane fold mirror. Both the input and the output beam were using a single small grating (with 10 cm vertical aperture). Therefore, the beams were

partly overlapping on the first grating and had to propagate several meters more in order to be separable.

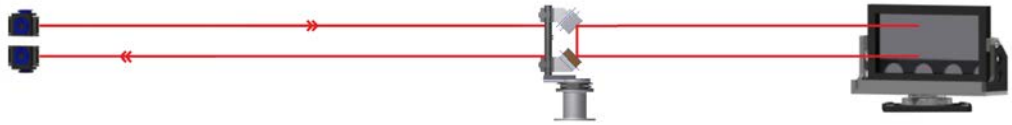

Figure 5.7: Intermediate compressor design. Compared to the original design (see Figure 4.23), two small gratings are used instead of a single one in order to create enough vertical separation between the in and out-coupled beam. A roof mirror replaces the plane fold mirror. This removes the vertical angle between in and out going beam and makes the compressor design spatial-chirp free.

In the new, intermediate compressor design, two parallel small gratings are used for in- and out coupling and the plane fold mirror is replaced by a roof mirror as shown in Figure 5.7. In this way, it is possible to start the vacuum tubing approximately 1 m after the last grating. The described changes decrease the B-integral to less than 1 (0.1 per m air or mm material- compare Section A.3).

The intermediate compressor design includes three gratings and is therefore more difficult to align. Special care has to be taken in order to align the roof mirror and the small gratings accurately. The angular chirp in the compressor was minimized by pulse-front tilt measurements with an inverted field autocorrelator [83].

The compressed pulse is analyzed by a home-built single shot frog [65]. The observation window is set to approximately 20 ps with a resolution of 45 fs per camera pixel. A double pulse with a given pulse separation can be set in the *Dazzler*. The so generated spectral fringes were used to obtain the spectral resolution of the frog of 0.205 nm per pixel. After this calibration, the frog-trace could be measured and the pulse could be compressed with fine adjustments of the *Dazzler* phase.

The measured and the retrieved frog trace are shown in Figure 5.8. The measured frog trace was obtained at compressed 200 mJ pulse energy and was rescaled with the spectral marginal in order to correct systematic measurement errors and to improve the pulse measurement [65].

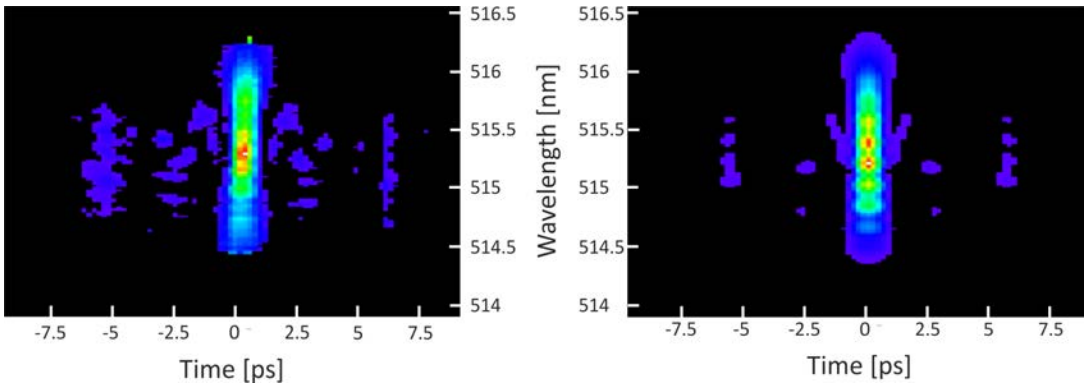

Figure 5.8: Comparison of the measured (left) and retrieved (right) frog trace. Shown are details of the 256×256 points traces. The measured trace is rescaled by the frequency marginal in order to improve the pulse measurement.

The retrieved spectrum and temporal pulse shape are compared to the measured data in Figure 5.9. The frog measurement shows that the pulse is compressed to

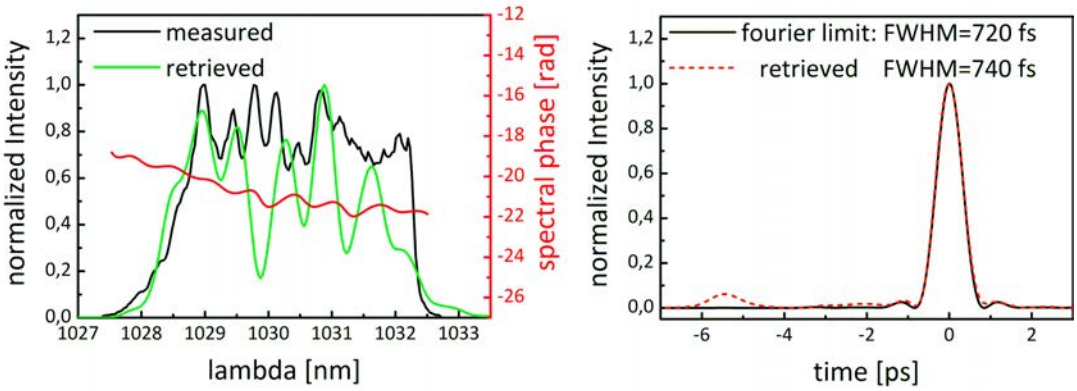

Figure 5.9: The retrieved spectrum is compared to the measured spectrum (left). The spectral width is recovered quite accurately, while the spectral shape differs considerably. The modulation in the retrieved spectrum also causes modulations in the spectral phase. On the right, the retrieved temporal pulse is compared to the Fourier limited pulse. The retrieved FWHM pulse length is 740 fs and very close to the Fourier limit 720 fs. The retrieved trace shows a pre- (or post-) pulse at 5.3 ps.

740 fs which is very close (3 %) to the Fourier limit. Both the spectrum and the phase are shaped with the *Dazzler* in order to optimize the compression for the shortest pulses.

The pedestal around the main pulse arises from the steep edges in the spectrum, which are obtained from clipping in the stretcher. The pre- (or post) pulse at 5.3 ps is present in the measured trace as well as in the retrieved trace. Its origin is unclear and a detailed investigation of the whole amplifier chain is necessary in order to eliminate this undesirable feature.

During the frog measurements it was observed that the spectrum and the phase cannot be changed independently with the *Dazzler*. This means if the phase is changed, the spectrum will change a bit as well and an iterative approach has to be applied in order to optimize the compression. In CPA it is common, that amplitude-phase coupling is present in presence of refractive index nonlinearity or saturated (nonlinear) amplification [113, 114]. This effect might explain the mentioned effect and also the presence of pre-and post pulses. Similar phenomena could also occur in the *Dazzler* RF amplifier. Although the *Dazzler* electronics are factory-set to run in a linear regime, there may be some saturation when operating with RF power close to the maximum (H. Jousselin [Fastlite inc.], personal communication, February 18, 2013). These kind of effects have to be investigated in more detail in order to improve the contrast of the compressed pulse.

5.4 CONCLUSION

In this chapter, the experimental implementation of the stretcher/compressor system for the PFS pump laser is described. A high-accuracy angle measurement is implemented for daily alignment. A compressed duration of 900 fs at an energy of

200 mJ was demonstrated in a Yb:YAG CPA system [99], which in its combination is unprecedented so far. One key ingredient for this result is the spectral amplitude shaping implemented in the pump laser front-end. With this technique it was possible to show an amplified bandwidth of 3.5 nm at this energy level where the unshaped amplification would reduce the bandwidth to less than 1.3 nm due to gain-narrowing. Simulations show that our shaping technique is efficient enough to maintain this bandwidth all the way up to the projected final pump laser energy. A modification of the stretcher (and compressor) angle resulted in a larger transmitted bandwidth in the stretcher which could also be amplified and compressed to 740 fs. Generally, a larger stretcher grating would be beneficial in order to avoid spectral clipping and the connected reduced pulse contrast. A detailed investigation of the origin of pre and post pulses on a few-ps timescale will lead to an improved contrast in future.

As summary of the dispersion management, the total amount of material in the pump laser chain is estimated: The fiber amplifier has a length of approximately 6 m (fused silica). All optics between the amplifiers i.e. lenses, polarizer cubes and vacuum windows amount to 2 m (fused silica or BK7). The Yb:glass and the Pockels cell (DKDP) in the regenerative amplifier are passed 140 times and count for 6 m material. The last components are the Yb:Yag crystals in the existing and all of the planned booster amplifiers which amount to 3 m. In total this amounts to 17 m material in the pump laser chain which results in an GDD of $5 \cdot 10^5 \text{fs}^2$, an TOD of $8 \cdot 10^5 \text{fs}^3$ and an FOD of $8 \cdot 10^5 \text{fs}^4$. The higher order Dispersion terms are negligible even for the shortest considered pulse duration of 500 fs pulses at 1030 nm (compare Table 5.1). The GDD has an significant effect, but a few-millimeter change of the grating separation in the compressor can easily compensate for this amount of GDD, simultaneously creating TOD and FOD on the order of $1 \cdot 10^7 \text{fs}^3$ and $4 \cdot 10^8 \text{fs}^4$, respectively. Generally, the compressor angle and grating separation can be used to match the second and third order dispersion, since the fourth order dispersion term is orders of magnitude below significance. Alternatively, the dispersion which can be introduced by the *Dazzler* (max. values: $GDD = \pm 6 \cdot 10^5\ \text{fs}^2$, $TOD = \pm 2.5 \cdot 10^8\ \text{fs}^3$, $FOD = \pm 4 \cdot 10^{10}\ \text{fs}^4$) can be used to compensate unmatched phase terms in order to optimize the compression.

6 TIMING JITTER

Conventional OPCPA systems work with pulse durations of several nanoseconds down to 100 picoseconds, which does not require CPA technology in the pump laser. In contrast to this, the approach applied here relies on a much shorter pulse width on the order of 1 ps. Therefore, the temporal synchronization of the pump and seed pulses also has to be accurate on orders of magnitude shorter timescales and becomes a crucial issue in the PFS system. In this chapter, measurements for the pump-seed synchronization along with actions for reducing the timing jitter are presented. These experiments are supplemented with a theoretical analysis for group delay fluctuations caused by air turbulence in a Treacy-compressor, which explains the main fraction of the measured timing jitter. This chapter is published in [115] in a modified form. An electronic reprint is appended in Appendix A.5 with the permission of OSA.

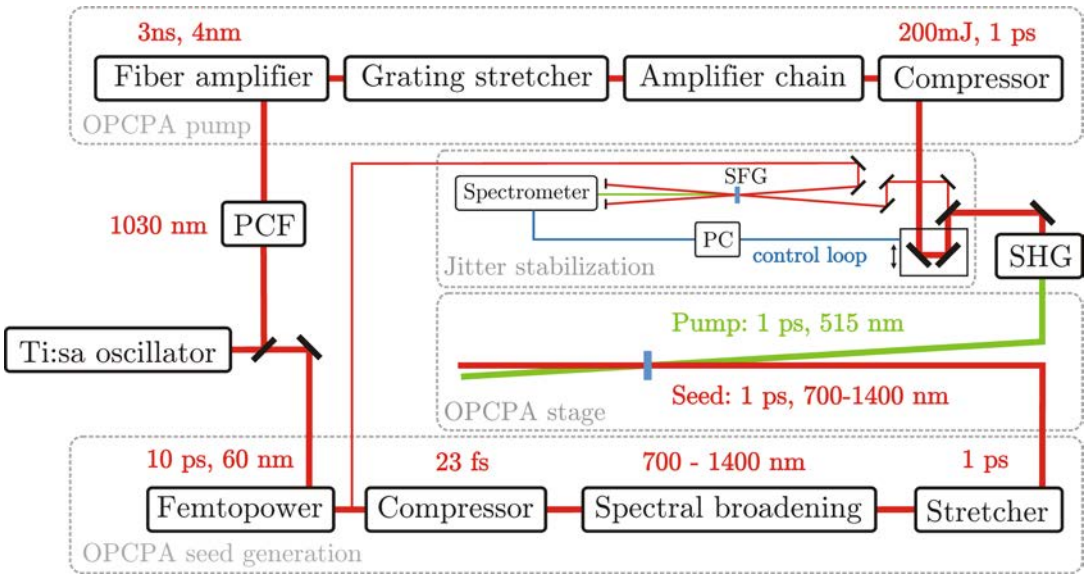

Figure 6.1: Setup of the jitter measurement. The pump and seed pulses are generated from a common oscillator in order to obtain optical synchronization between the OPCPA pump and seed pulses. In the CPA pump chain, the pulses are amplified and compressed down to 1 ps. These pulses are frequency doubled before they are used as OPCPA pump. The seed pulses are spectrally broadened to a range of $700 - 1400$ nm and stretched to approximately 1 ps. In the timing jitter stabilization stage, the timing jitter is measured and can be controlled by an optical delay stage in order to actively stabilize slow timing fluctuations.[115]

In order to recap the PFS setup, Figure 6.1 shows an overview over the system, extended by a jitter stabilization stage. The path through the CPA pump chain would result in a total optical delay of approximately 1 μs between the pump and the seed at the position of the first OPCPA stage. In order to compensate for this delay, both

pulses are selected from the master oscillator at different times. In this scheme, the sources of possible timing fluctuation between the two pulses can be the finite stability of the repetition rate of the master oscillator, temperature drifts, air turbulence and mechanical vibrations of optical components over the long optical path of the pump pulse.

All optical tables are equipped with flow boxes and are enclosed by a housing. Inside this housing, subunits such as the stretcher, regenerative amplifier, and multipass amplifier are covered in separate boxes which are not completely air-tight but provide isolation from the air turbulence caused by the flow boxes to some extent. Due to its size ($6.5 \times 1.5 \times 0.7\,\mathrm{m}^3$), the compressor is currently not separately covered.

During the first OPCPA experiments, large fluctuations in the amplified signal intensity were observed which could only be explained by timing jitter between the signal and pump pulses. Hence, a stabilization stage was implemented, which measures the timing jitter and moves a delay stage accordingly. It will be described in the following:

6.1 THE TIMING JITTER MEASUREMENT SCHEME

In order to quantify the level of synchronization in the setup described above, for each shot the relative timing between the pump and the seed pulses measured using a modified cross-correlation technique, first proposed by Miura [116]. It determines the relative timing between a compressed pulse and a linearly chirped pulse with fs resolution via sum-frequency generation (SFG), as shown in Figure 6.2. For this measurement, the compressed 1 ps long pump pulse (at 1030 nm) is used as a signal. The reference pulse is split off from the Femtopower amplifier before compression and hence has a chirped duration of 10 ps and a bandwidth of 60 nm. If the relative delay between these pulses is changing, the signal pulse creates a sum frequency signal with different parts of the chirped reference, and the centroid wavelength of the SFG signal changes accordingly.

The spectrum of the SFG signal is measured using a high-resolution spectrometer (Avantes AvaSpec-2048). The accuracy of the measurement is determined by the resolution of the spectrometer (0.06 nm) and by the chirp of the reference pulse. How the measured spectral centroid is related to the relative timing of both pulses is found with a calibration measurement, where different known delays between the pulses were introduced by a delay stage in the signal path and the corresponding centroid of the spectrum was measured. In Figure 6.2 (b), this calibration curve is shown. Each point is the mean value of 100 shots with a standard deviation on the order of 20 fs (too small to resolve the error bars in the plot). For delays larger than 1 ps one can observe a deviation from the linear fit which mirrors the higher order dispersion terms in the chirped pulse. A linear fit is applied and the calibration factor of 533 fs/nm is used in all of the following measurements for the calculation of the timing jitter from the measured spectral centroid. Nevertheless, a higher order fit would be more accurate and will be implemented in the measurement software in the future.

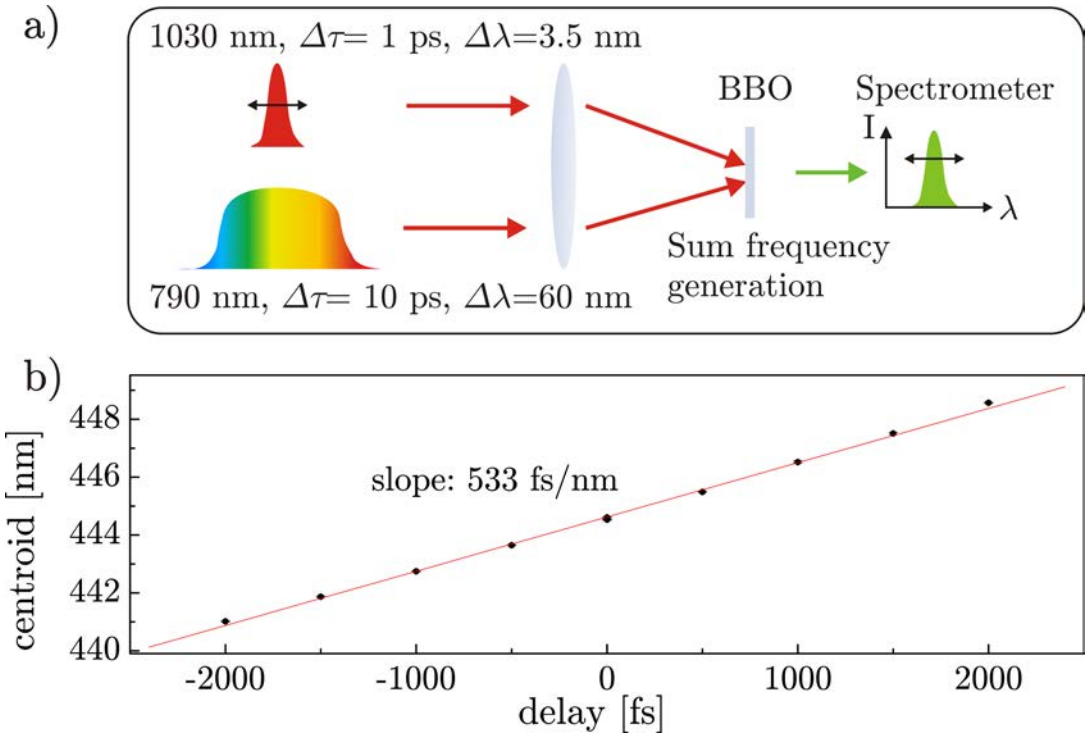

Figure 6.2: (a) Illustration of the modified cross-correlation technique for the measurement of the timing jitter. The spectrum of the sum frequency signal between the short pump pulse and a long, chirped reference pulse is measured. The relative arrival time of the pulses is transformed into a frequency change of the sum frequency signal. (b) shows the calibration curve, where the centroid of the sum frequency signal is measured at different relative delays averaged for 100 shots with a standard deviation of approx 20 fs (too small to resolve the error bars in the plot) [115]

Using this calibration factor, the resolution of the spectrometer can be translated in time resolution to 32 fs. Nevertheless, the estimation of a centroid can be done with sub-pixel resolution (e.g. [117]) but the exact improvement in accuracy depends on the width of the spectral distribution, the signal-to noise ratio and the region of interest used for the calculation. An estimation gives an accuracy of approximately 10 fs.

6.2 SOURCES OF TIMING JITTER

The first jitter characterization was made for the laser system in its original state, The pump beam was stretched, fully amplified in the regenerative and multipass amplifiers and subsequently compressed. All flow boxes were running. The fluctuation of the relative timing between pump and seed is shown in Figure 6.3 a). It amounts to 400 fs rms and $>$ 2 ps peak to peak which is unacceptable for ps OPCPA experiments.

These large temporal fluctuations between the pump and the seed pulses were not expected, since both pulses are originating from the same oscillator and thus are optically synchronized. The most probable source of these fluctuations is the long

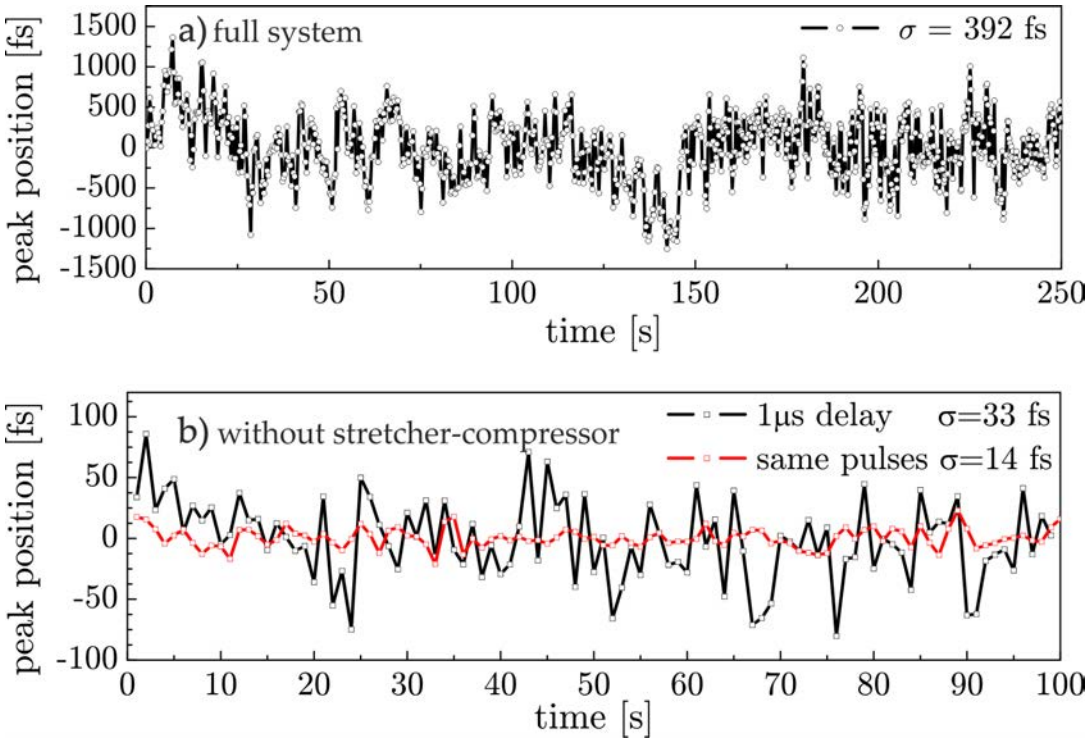

Figure 6.3: Results of timing jitter measurements with a measurement accuracy of ca. 10 fs. a) Pump pulse passes through the entire CPA chain: ±400 fs timing jitter. b) Timing jitter when stretcher/compressor are bypassed: ±14 fs when identical pulses from the master oscillator seed the signal and reference chain; ±33 fs with 1 μs delay. [115]

optical path in the pump chain (corresponds to approximately 1 μs delay) which could be fraught with jitter. Another source may be the repetition rate stability of the oscillator pulse train since the pulses for the pump and seed chain are selected at different instances in time in order to compensate for the long optical path in the pump chain.

In order to determine the source of this unexpectedly large temporal jitter and to exclude the influence of mechanical stability of in the pump chain, the timing jitter was studied with a reduced pump-laser chain. To this end, the stretcher-compressor setup was bypassed and attenuated, unstretched pulses (ca. 4 ps) were amplified in the regenerative amplifier to a low power level. The relative timing was then measured between the reference and the pulses amplified in the regenerative amplifier. In this scheme, two different measurements were performed:

Firstly, the same pulse is selected from the oscillator for the pump and seed chain. In this case the delay in the regenerative amplifier is minimized by reducing the amplification passes and the temporal overlap is found with a delay stage. As depicted in Figure 6.3 b) (red curve), the timing jitter then is measured with a standard deviation as low as 14 fs. This jitter is hardly above the resolution of the measurement system, but it leads to the following conclusion: when the optical delay is minimized and both pulses are selected at the same time, the optical synchronization scheme works and the timing jitter is minimized.

In a second measurement (Figure 6.3 b) (black curve), an optical delay of 1 μs is introduced in the regenerative amplifier by increasing the number of round trips. The pulses for the pump chain are selected from the master oscillator 1 μs later than the seed pulses in order to find the temporal overlap. The 1 μs delay in the regen is the same as for the full pump chain including stretcher, compressor and booster amplifier. In this case (black curve) one expects different sources of jitter: On one hand, the repetition rate instability of the master oscillator may introduce a jitter between the two pulses selected at different times. On the other hand, also the regenerative amplifier introduces optical delay fraught with jitter. Although both sources cannot be distinguished by this technique, together they account for a few-10 femtosecond jitter. This is close to the resolution limit of the measurement setup, and is clearly well below the tolerable limit for the short-pulse pumped OPCPA. This means that the optical delay inside the regenerative amplifier has much less influence on the timing fluctuations compared to the same optical delay generated inside the full system including the stretcher-compressor setup. It can therefore be concluded that the large timing oscillations, shown in Figure 6.3 a) arise from the stretcher-compressor setup. Most likely, mechanical vibrations of opto-mechanical components and air fluctuations along the long propagation distance dominante this timing instability. This assumption is supported by a theoretical investigation of the influence of angular deviations on the timing inside a compressor setup which is presented in the following section.

6.3 THEORETICAL INVESTIGATION OF TIMING JITTER IN A TREACY COMPRESSOR.

The experiments indicate that the optical delay inside the stretcher/compressor setup is fraught with a much larger timing jitter than expected. In this section, the effect of turbulent air flow on optical path length differences will be discussed theoretically. In the following, turbulent air flow is represented by small angular deviations in the beam pointing. Turbulent air means a statistical distribution of pockets of air with slightly different temperature (and therefore different refractive index) over the propagation distance. Whenever a light beam hits a boundary layer between air with different temperatures under non-zero incidence, it will be refracted with a slightly different angle.

This effect can be calculated: from [118], the refractive index of dry air can be obtained as function of temperature and pressure. In Figure 6.4 (left) the refractive-index change is calculated for small temperature changes around 22 °C at norm pressure.

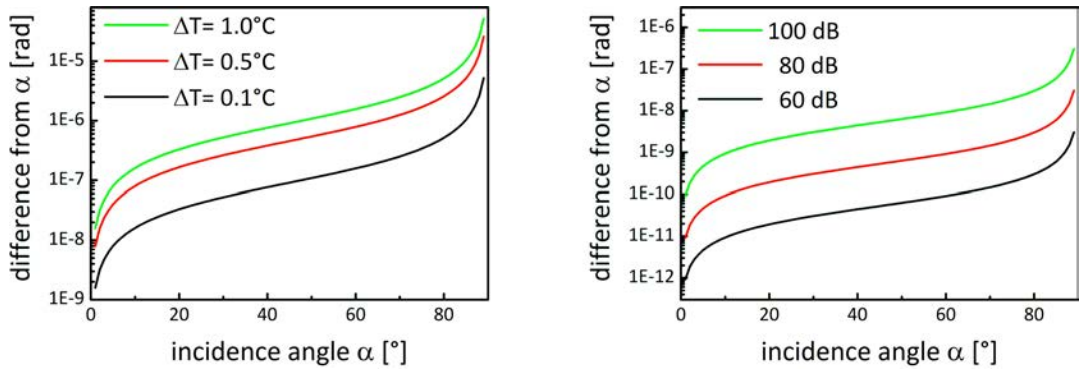

Figure 6.4: (Left) Angle change from refraction on a boundary of air with 22 °C and increased temperature ΔT. Even for ΔT=0.1 °C, the beam is diffracted by $1 \cdot 10^{-6}$rad for gracing incidence. (Right) Refraction for air with different pressure caused by acoustic waves (with reference pressure $20 \cdot 10^{-6}$Pa. The refraction from acoustic-wave induced refractive index changes in air is negligible.

It shows that refraction about 1μrad occurs for ΔT=0.1°C at large angles. For higher temperature differences, the refraction angle is increased. In Figure 6.4 (right), the dependence of the refraction on the sound pressure level of acoustic waves is shown for a constant temperature. The sound pressure level in *dB* is calculated relative to the reference pressure of 20μPa, which is usually considered as threshold of human hearing. Even the effect of sound pressure levels of 100 dB can be neglected.

This short estimate shows that a single refraction event on air with different temperatures can reach magnitudes of 1μrad. In a realistic situation, many such events are randomly distributed over the propagation path. For simplicity only a single (mean) refraction event at an average position will be considered for the whole path through turbulent air in the following.

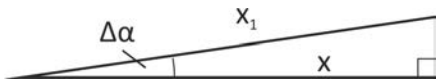

Figure 6.5: Schematic picture for calculating the timing difference of light traveling along the paths x and x_1. [115]

6.3.1 *Timing jitter from angle deviations in free space propagation*

The timing difference for a free-space propagation with the speed of light c over the distance x compared to a distance x_1 with a small angle $\Delta\alpha$ (compare Figure 6.5) can be calculated as:

$$\Delta\tau = \frac{x_1 - x}{c} = \frac{x}{c}\left(\frac{1}{cos(\Delta\alpha)} - 1\right) \approx \frac{x \cdot \Delta\alpha^2}{2c} \tag{6.1}$$

For values $x = 100\,\mathrm{m}$ and $\Delta\alpha = 10\,\mu\mathrm{rad}$ one obtains $\Delta\tau = 0.017\,\mathrm{fs}$ and can therefore neglect this timing change for probably all experimentally relevant cases in the laboratory. This estimation is also true when turning mirrors are included in the optical pass as in optical amplifiers.

6.3.2 *Timing jitter from angle deviations in a compressor setup*

In the following, the influence of beam pointing fluctuations on the optical path length inside a compressor is discussed. An analytical expression is derived for the path length difference as a function of the angle deviation $\Delta\beta$ and the distance d, relative to the first grating of this angle change inside the compressor. Additionally, the special case of an angle deviation of few μrad before the compressor input is discussed. These findings were made in close collaboration with Izhar Ahmad and a first treatment of the effect can be found in his thesis [90]. In the current work, his results haven been refined and the equations have been rearranged and approximations were introduced, where useful, in order to provide the compact formulae for the timing jitter in its current form. Additionally, terms for angle deviations on the back propagation were added in order to describe a physically relevant situation.

In most ultra-short pulse laser systems, the compressor is located in vacuum in order to avoid nonlinearities in air. (For PFS, due to the comparatively long 1 ps pulses it was not clear whether a vacuum vessel would be necessary. However, experience with first experiments shows that this cannot be avoided in the future.) Therefore, the stretcher will be the most likely source of perturbations by air fluctuations. Nevertheless, in the following a compressor will be analyzed, because the optical path is easier to explain. These considerations are also valid for the stretcher setup, as the stretcher provides the same amount of dispersion but with opposite sign. However, the additional imaging system increases the optical path compared to the compressor, making the stretcher even more sensitive to air turbulence.

The grating compressor has the remarkable property that the group delay equals the phase delay [119]. Thus, it is justified to calculate the delay in a compressor as the optical path divided by the speed of light. In general systems including dispersive material, this simple rule cannot be applied.

In the following, the influence of a perturbation of the angle inside the compressor is analyzed. Figure 6.6 shows a double-grating double-pass Treacy compressor setup with a grating separation L_1, aligned for an angle of incidence (AOI) α. The optical path of a ray with wavelength λ_0 and AOI of α is shown in red. The diffraction angle from the first grating is given by the grating equation

$$\beta = \arcsin(mN\lambda_0 - \sin\alpha), \tag{6.2}$$

where N is the line density, λ_0 is the center wavelength and m is the diffraction order. As the AOI on the second, parallel and identical grating is β, the beam diffracts at an angle α and impinges perpendicularly on the end mirror from where it takes the same path back through the compressor.

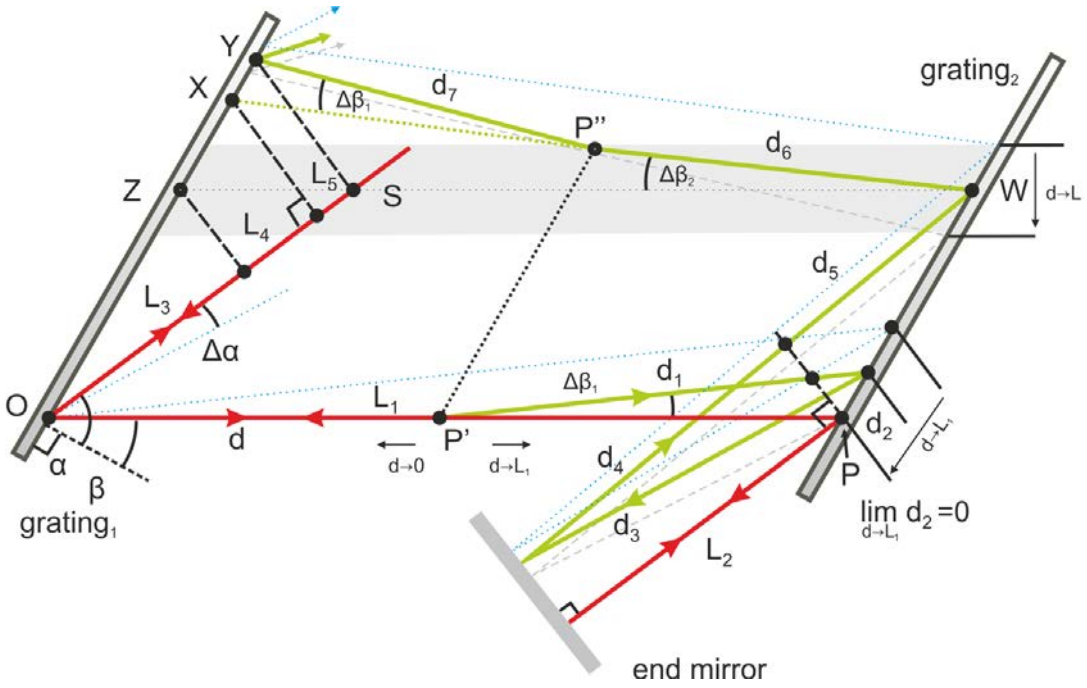

Figure 6.6: Ray diagram illustrating the change in the optical path inside the grating compressor for the center wavelength λ_0. The red ray shows the undisturbed case with an AOI of α. The green curve depicts the beam path of the pulse for the case when it is distorted at an angle $\beta + \Delta\beta_1$ at a distance d from the first grating. The blue, dotted and the gray, dashed traces show the extreme cases $d = 0$ and $d = L_1$, respectively. The case $d = 0$ corresponds to a different AOI of $\alpha - \Delta\alpha$ at the compressor input. For detailed explanation see main text. [115]

A shot-to-shot pointing fluctuation inside the dispersion plane of the compressor can be described as a deviation $\Delta\beta_1$ from the design angle β which leads to a non-zero AOI on the end mirror of $\Delta\alpha$. This in turn results in a different path (and angle) for the first pass ($\beta + \Delta\beta_1$) and the return pass through the compressor ($\beta - \Delta\beta_2$), as shown in Figure 6.6 (green). The location where the angle change takes place is parameterized with the parameter d. The extreme case $d = 0$ represents a beam pointing deviation at the compressor input O (or a pointing deviation with $\Delta\alpha$ outside the compressor), and $d = L_1$ stands for fluctuations at the position of the second grating. The angle change represents air fluctuations, which can be

considered static on the time scale of a propagating light pulse. In Figure 6.6 the angle deviations are magnified to better distinguish the different paths. In reality the points P' and P'' are closely adjacent. Therefore, the same deviation as on point P' is present on the way back through the system at point P''. (In the case when $d = 0$, P'' is on the first grating and would result in a small angle change of the outgoing beam. As described in Section 6.3.1, this effect is not relevant for the timing and is therefore neglected.)

The optical path lengths between point O and plane YS for the reference and the slightly perturbed case are given by

$$p(\beta) = L_1 + L_2 + L_2 + L_1 + L_3 + L_4 + L_5 \text{ , and} \tag{6.3}$$

$$p(\beta + \Delta\beta_1) = d + d_1 + d_2 + d_3 + d_4 + d_5 + d_6 + d_7 \text{ , respectively.} \tag{6.4}$$

The timing difference can then be calculated by $\Delta\tau = (p(\beta) - p(\beta + \Delta\beta_1))/c$. The paths L_1 and L_2 are given by the compressor design, d is a parameter and the other path lengths can be obtained from general trigonometric relations in Figure 6.6:

$$d_1 = (L_1 - d)\frac{\cos\beta}{\cos(\beta + \Delta\beta_1)} \tag{6.5}$$

$$d_2 = (L_1 - d)\frac{\sin(\Delta\beta_1)}{\cos(\beta + \Delta\beta_1)}\frac{\sin\alpha}{\cos(\Delta\alpha)} = a_1\frac{\sin\alpha}{\cos(\Delta\alpha)} \tag{6.6}$$

$$d_3 = d_4 = \frac{L_2}{\cos(\Delta\alpha)} \tag{6.7}$$

$$d_5 = (d_2 + d_3)\frac{\cos(\alpha - \Delta\alpha)}{\cos(\alpha + \Delta\alpha)} - d_4 \tag{6.8}$$

$$d_6 = (L_1 - d)\frac{\cos\beta}{\cos(\beta - \Delta\beta_2)} \tag{6.9}$$

$$d_7 = d\frac{\cos\beta}{\cos(\beta - \Delta\beta_1 - \Delta\beta_2)} \tag{6.10}$$

$$L_3 = d_5\cos(\Delta\alpha) \tag{6.11}$$

$$L_4 = L_1\frac{\sin(\Delta\beta_2)}{\cos(\beta - \Delta\beta_2)}\sin\alpha = a_2\sin\alpha \tag{6.12}$$

$$L_5 = d\frac{\cos\beta}{\cos(\beta - \Delta\beta)} \cdot \frac{\sin(\Delta\beta_1)}{\cos(\beta - \Delta\beta_1 - \Delta\beta_2)}\sin\alpha \tag{6.13}$$

The contribution to the timing difference from $2L_2 - d_3 - d_4$ has the same form as in the free space case, discussed above (Equation 6.1), and can therefore be neglected. In this approximation, the timing difference is independent of the distance of the end mirror to the second grating L_2. For the same reason $L_3 - d_5$, which accounts for

a parallel offset of plane $\overline{OP}$ and $\overline{WZ}$, has a negligible effect on the timing difference. The total timing difference can then be written:

$$\begin{aligned}\Delta\tau &= \frac{1}{c}(2L_1 - d - d_1 - d_6 + L_4 - d_2 + L_5 - d_7) \qquad (6.14)\\ &= \frac{L_1}{c}\left(2 - \frac{\cos\beta + \sin(\Delta\beta_1)\sin\alpha}{\cos(\beta+\Delta\beta_1)} - \frac{\cos\beta - \sin(\Delta\beta_2)\sin\alpha}{\cos(\beta-\Delta\beta_2)}\right)\\ &+ \frac{d}{c}\left(\frac{\cos\beta + \sin(\Delta\beta_1)\sin\alpha}{\cos(\beta+\Delta\beta_1)} - 1\right)\\ &+ \frac{d}{c}\left(\frac{\cos\beta}{\cos(\beta-\Delta\beta_2)}\left[1 - \frac{\cos(\beta-\Delta\beta_2) - \sin(\Delta\beta_1)\sin\alpha}{\cos(\beta-\Delta\beta_1-\Delta\beta_2)}\right]\right) \qquad (6.15)\end{aligned}$$

With the help of the grating equation (Equation 6.2), $\sin\alpha$ can be expressed in terms of $\sin\beta$. For small angles $\Delta\beta$, the approximations $\sin(\Delta\beta) \approx \Delta\beta$ and $\cos(\Delta\beta) \approx 1$ are justified. Under this approximation it follows that $\cos(\beta \pm \Delta\beta) \approx \cos\beta \mp \Delta\beta\sin\beta$. Equation 6.15 can then be approximated as

$$\begin{aligned}\Delta\tau &\approx \frac{L_1\, m\, N\, \lambda_0}{c}\left(\frac{\Delta\beta_2}{\cos(\beta-\Delta\beta_2)} - \frac{\Delta\beta_1}{\cos(\beta+\Delta\beta_1)}\right)\\ &+ \frac{d\, m\, N\, \lambda_0}{c}\left(\frac{\Delta\beta_1}{\cos(\beta+\Delta\beta_1)}\right)\\ &+ \frac{d\, m\, N\, \lambda_0}{c}\frac{\cos\beta}{\cos(\beta-\Delta\beta_2)}\left(\frac{\Delta\beta_1}{\cos(\beta-\Delta\beta_1-\Delta\beta_2)}\right). \qquad (6.16)\end{aligned}$$

The following calculations are done for the approximated expression (Eq. 6.16) as well as for the formula without approximations (Equation 6.15) with the following parameters: $N = 1740\text{lines/mm}$, $\lambda_0 = 1030\,\text{nm}$, $m = 1$, $L_1 = 6\,\text{m}$, $L_2 = 3\,\text{m}$ and $\alpha = 58.5°$, as in the experimental setup. It should be noted that only small angle changes (few μrad) are considered which may affect the optical path length but do not change the pulse length or angular chirp [83] in a significant way.

In these formulae all terms are proportional to $1/\cos\beta$ ($\beta \pm \Delta\beta \approx \beta$ for large β and small $\Delta\beta$) and it can be seen that smaller angles β are favorable in terms of timing difference. Nevertheless, in order to compare the jitter for different angles one has to take into account that the dispersion is also decreasing with decreasing β. Hence, the compressor length must be adapted to compare compressors with the same dispersion. Additionally, the choice of angles is restricted to some extent by the grating reflectivity.

For example, the PFS pump compressor is designed in a reverse configuration where $\alpha < \beta$ ($\alpha = 58.5°$, $\beta = 69.98°$) because in this case the necessary dispersion can be achieved with only $L_1 = 6\,\text{m}$ grating separation. Another option would be the normal configuration with $\alpha = 69.98°$, $\beta = 58.5°$ where a grating separation of $L_1 = 14\,\text{m}$ is needed. Therefore, both configurations will be compared in the following sections.

6.3.3 *Angle fluctuations at the compressor input*

The special case $d = 0$ corresponds to the situation with a certain beam pointing fluctuation $\Delta\alpha$ at the compressor input. This change translates to a fluctuation $\Delta\beta_1$

to the diffracted beam at point O on the first grating. No source of angle fluctuation inside the compressor is considered. For $d = 0$, the last two terms in Equation 6.15 and Equation 6.16 vanish and Equation 6.16 takes the form

$$\Delta\tau = \frac{1}{c}(2L_1 - d_1 - d_6 + L_4 - d_2) \tag{6.17}$$

$$= \frac{L_1\, m\, N\, \lambda_0}{c}\left(\frac{\Delta\beta_2}{\cos(\beta - \Delta\beta_2)} - \frac{\Delta\beta_1}{\cos(\beta + \Delta\beta_1)}\right) \tag{6.18}$$

The effect of angular deviation outside the compressor on the timing is very small because d_1 is a bit longer than L_1 but d_6 is a bit shorter and together they nearly cancel out each other, i.e. $d_1 + d_6 \approx 2L_1$. Additionally d_2 and L_4 compensate each other, i.e. $d_2 \approx L_4$ (compare Figure 6.6, Equation 6.5-6.13). From Equation 6.18 it can be seen that the remaining difference occurs because $\Delta\beta_1 \neq \Delta\beta_2$. This is due to the fact that the angle $\beta + \Delta\beta$ is transferred to $\beta - \Delta\beta$ after reflection off the end mirror.

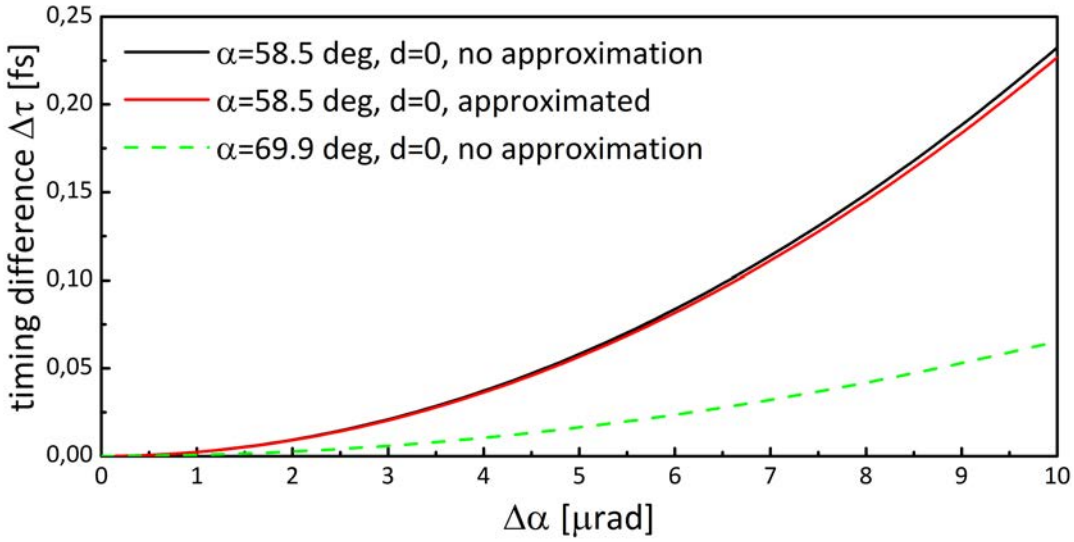

Figure 6.7: Timing difference for a small change $\Delta\alpha$ of the AOI α at the compressor input (d=0). The correct (black) formula (Equation 6.15) is compared to the approximated (red) formula (Equation 6.18). The approximation is well justified for the PFS parameters. Larger angle α (smaller angle β) is advantageous in terms of jitter (green, dashed) even though the grating separation is more than doubled to achieve the same dispersion. [115]

In Figure 6.7 the calculated timing jitter due to pointing fluctuations at the compressor input is shown. For pointing fluctuations up to 10 μrad the timing jitter is less than 0.25 fs which was also confirmed by ray tracing. The beam pointing at the compressor input was measured to be less than 1 μrad which corresponds to a negligible jitter of 0.0025 fs. Nevertheless, it should be noted that this timing jitter from angular deviations outside the compressor is two orders of magnitude larger than the effect of the same angle deviation in a freely propagating beam over the same distance (compare Equation 6.1) and that the compressor configuration with $\alpha > \beta$ would have advantages in terms of jitter, even though the grating separation is 14 m (instead of 6 m for the reverse configuration) to achieve the same dispersion.

6.3.4 *Angle fluctuations inside the grating compressor*

In the previous paragraph it was shown that angle fluctuations at the compressor input are negligible because all path length differences almost completely compensate each other. In this section, the influence of angle fluctuations originating inside the compressor will be investigated. From Figure 6.6 it can be understood what happens when d is increased, the distances on the way to the end mirror (d_1, d_2) are decreasing and cannot compensate for the distances during the back propagation (d_7, L_4, L_5) and the timing difference is drastically increased compared to the case with $d = 0$.

In Equations 6.15 and 6.16, the first term can be neglected as shown in the previous paragraph. It turns out that the second and the third term in Equation 6.16 both have the same weight. When approximating $\cos(\beta + \Delta\beta) \approx \cos\beta$, Equation 6.16 can further be simplified to:

$$\Delta\tau \approx \frac{2\,m\,N\,\lambda_0}{c\,\cos\beta}\,\Delta\beta_1 \cdot d \tag{6.19}$$

Figure 6.8 shows that the approximations for Equation 6.19 are well justified, because deviations from the non-approximated curve are negligible. As predicted by Equation 6.19, the linear character in d and $\Delta\beta$ shows clearly in the graphs. Compared to the case with $d = 0$, the jitter is up to 4 orders of magnitude higher (for $d = L_1$). Corresponding to Equation 2.55, the grating separation scales $\sim \cos^2\beta$ for constant GDD. Therefore, $\Delta\tau$ scales $\sim \cos\beta$ and the configuration with smaller β (larger α) and constant GDD is more sensitive to jitter.[1]

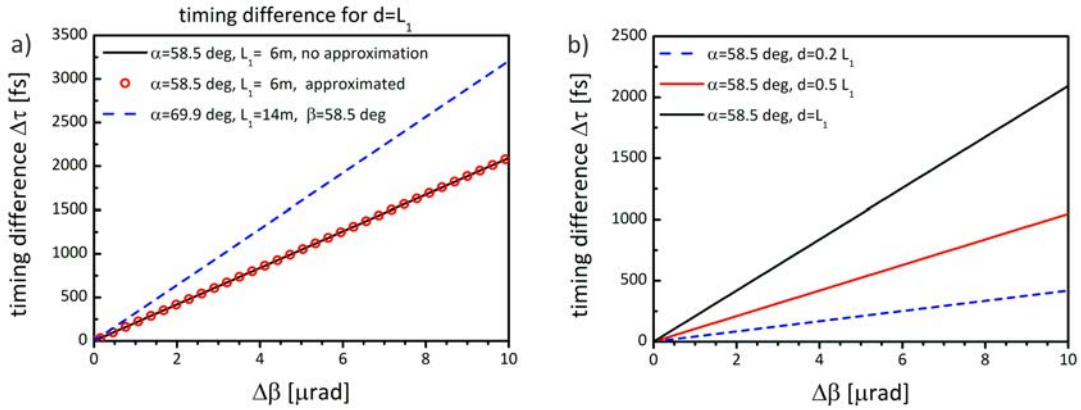

Figure 6.8: a) Timing difference for $d = L_1$: the approximations in Equation 6.19 are well justified in the considered range. The configuration with increased AOI α (or decreased β) shows reduced timing differences. b) Timing difference for different values of d. [115]

This calculation shows the effect of beam pointing fluctuations, introduced by air turbulence or mechanical instabilities. Generally a larger angle β is preferable in

1 Note, that the graphs with $\alpha = 58.5°$ and $\alpha = 69.9°$ in Figure 6.8 (a) were erroneously switched in [115].

terms of jitter. As mentioned earlier the effect of turbulent air is modeled by assuming an average angular deviation at an intermediate position. Since the mean position is most likely located at $d = 0.5\,L_1$, the corresponding curve in Figure 6.8 (b) is most suitable to reflect the effect of air turbulence. As a result of this analysis it can be stated that a Treacy-type compressor introduces a timing jitter when a beam pointing fluctuation is considered. Beam pointing fluctuations at the compressor input are orders of magnitude less critical than those occurring inside the compressor, especially close to the second grating.

6.4 TIMING JITTER MEASUREMENTS WITH REDUCED AIR TURBULENCE

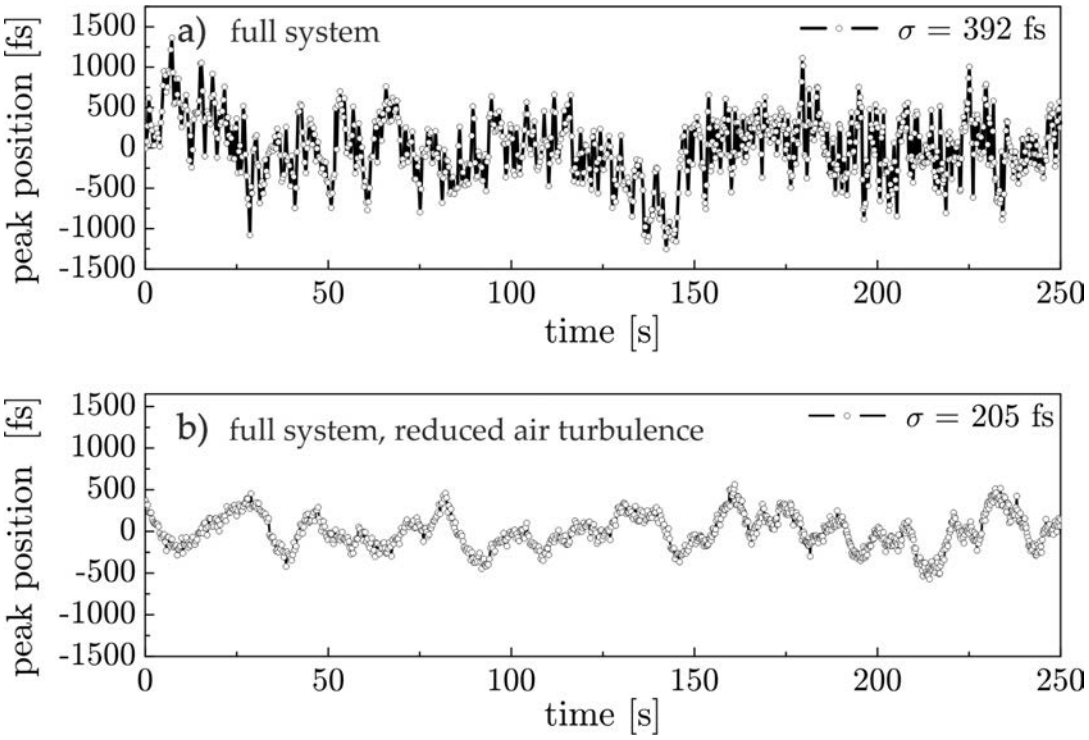

Figure 6.9: Results of timing jitter measurements a) Pump pulse passes through the entire CPA chain: ±400 fs timing jitter with no precautions to reduce air turbulence. b) Same path but with reduced air turbulence (stretcher box sealed, beam tubes in the compressor and flow-box turned off): Improved timing jitter consists of ±70 fs shot-to-shot fluctuation and ±200 fs slow oscillations.

In order to support the theoretical findings, the jitter measurement from Section 6.2 is repeated but this time with precautions taken to reduce air turbulence (see Figure 6.9 b): the flow boxes are turned off, the stretcher box is sealed more carefully and beam tubes are installed inside the compressor. This measurement can be directly compared to Figure 6.9 a) (which was presented earlier in Section 6.2) and shows a significantly improved timing jitter. The reduced jitter uncovers two separate components to the remaining timing jitter: an rms shot-to-shot variation of ±70 fs superimposed on a slow temporal drift of ±200 fs rms.

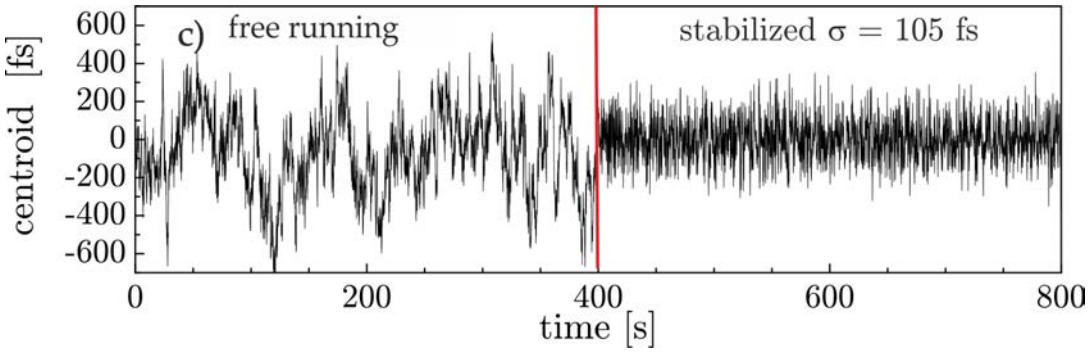

Figure 6.10: Active stabilization of slow timing fluctuations. With the improved timing jitter, it is possible to remove the slow timing fluctuations from Figure 6.9 b) with an active stabilization system. When the active stabilization is activated, the timing jitter can be reduced to 100 fs std. [115]

An active stabilization system can easily correct for this large amplitude, slow fluctuation. In the active stabilization scheme, the centroid wavelength of the SFG spectra is taken on every shot, the difference to a reference wavelength is calculated and a delay stage (in the pump-chain cf. Figure 6.1) is moved to return to the reference position in cases when the difference exceeds a certain value. This threshold is a parameter to optimize the active stabilization. If the threshold is too close to the shot-to-shot noise level, the delay stage will move on nearly every shot and the feedback loop will become unstable. In the experiment, it was shown that the stabilization currently works best with this limit set to 100 fs. In this case the jitter was stabilized to 105 fs std, as shown in Figure 6.10). This level of timing jitter is sufficiently low for carrying out the first proof-of-principle OPCPA experiments, but has to be further reduced for the final PFS system.

6.5 BEAM POINTING MEASUREMENTS IN THE STRETCHER AND COMPRESSOR

As described in Section 6.3, small angle changes in the stretcher/compressor can lead to timing jitter. In order to find sources for such angle changes (i.e. air turbulence or unstable mechanical components) beam pointing measurements were conducted at different positions in the laser system.

The beam pointing fluctuation is measured with a lens ($f = 750$ mm) and a camera (Basler ACE acA640-100gm with 5.6 μm pixel size) in the focal plane of the lens. Additionally, a folding mirror is used in order to fit this setup on a 40 cm square breadboard. The centroid of the beam profile in the Fourier plane of the lens is calculated for each shot and can be transformed to the beam pointing deviation for a known focal length of the lens. Measurement errors are minimized when the noise background is recorded and subtracted, the region of interest is minimized and the laser beam is attenuated in such a way that the full dynamic range of the CCD is used.

The setup is tested with a laser pointer where a beam pointing in horizontal and vertical direction of 1.4 ± 0.25 μrad can be measured. This number represents the accuracy of the measurement where the instability of the optical assembly and

noise of the camera are the limiting factors. In each of the following measurements, the beam pointing fluctuation is determined for 1000 shots and the mean and error are determined as rms of five of such measurements. The results are summarized in Table 6.1.

position	horizontal [μrad]	vertical [μrad]
Stretcher input	1.73 ± 0.31	1.55 ± 0.30
Stretcher output	1.40 ± 0.29	3.84 ± 0.31
Stretcher output box open	1.95 ± 0.32	5.62 ± 0.33
Compressor input	2.35 ± 0.33	3.85 ± 0.36
Compressor output	4.10 ± 0.37	4.72 ± 0.44

Table 6.1: Beam pointing measurements for the stretcher and compressor. The measured beam pointing error at the stretcher input is in the range of the measurement accuracy and therefore cannot be used for further conclusions. The output beam of the stretcher has an increased pointing error, predominantly in vertical direction. The compressor output, shows an increased beam pointing error in both directions.

When several contributions to a measurement have a statistical distribution with mean and standard deviation and are independent (in this case: input pointing fluctuation, mechanical instability, air turbulence, camera noise, etc.), the expected measured value is obtained by the root of the squared sum of the individual contributions. The difference between two measurements is thus obtained by the root of the difference of the squared contributions. Hence, the input beam to the stretcher has a $1.02 \pm 0.18\,\mu$rad and $0.66 \pm 0.16\,\mu$rad larger beam pointing error than the test laser pointer ($1.4 \pm 0.25\,\mu$rad) in the horizontal and vertical direction, respectively. This first measurement is not significantly above the measurement accuracy.

From the measurements at the stretcher output with the closed and opened stretcher box, important information can be extracted: Firstly, the beam pointing fluctuation is increased more in vertical direction, than in horizontal direction. This asymmetry points to a mechanical vibration mode, since air turbulence is expected to cause an increased beam pointing fluctuation in both directions. Nevertheless, only a horizontal beam pointing fluctuation has to be considered for the timing jitter, since the gratings work as a mirror in the vertical direction and the corresponding effect of a beam pointing change on timing jitter is negligible.

Secondly, the beam pointing error for the open compared to the closed box increases by $1.36 \pm 0.11\,\mu$rad in the horizontal direction at the stretcher output. In both situations (box open, box closed) the timing jitter was measured, as well. The additional timing jitter caused by opening the stretcher box is determined to be 256 ± 56 fs. This data set can be compared to the theory presented in Section 6.3. The additional pointing error in the stretcher from opening the box and the corresponding measured timing jitter fits best to the theoretical curve with $d = L_1$ i.e. to the theoretical case where the angle fluctuation occurs on the second grating (compare Figure 6.8 (b)). This is reasonable, since the stretcher grating is situated

approximately in the center of the box where the average beam pointing change due to air turbulence takes place.

Measurements in the grating compressor show that the beam pointing error is increased by $3.35 \pm 0.17\,\mu$rad or $2.73 \pm 0.25\,\mu$rad in the horizontal and vertical direction, respectively. The nearly isotropic increase in beam pointing error is a hint that turbulent air is the dominant factor in the compressor. A ventilator was installed close to the second grating in order to measure the increase in the beam pointing fluctuation along with the timing jitter. An increased timing jitter by 100 fs was measured, but the increase in the beam pointing error could not be measured. From the theory it can be predicted that 100 fs timing jitter is introduced by approx. $0.5\,\mu$rad beam pointing fluctuation at the second grating. This small value is not measurable in the presence of a $3\,\mu$rad beam pointing fluctuation, because in that case the total pointing error is $3.04 (= \sqrt{3^2 + 0.5^2})$ which is indistinguishable from $3\,\mu$rad within the error of the measurement.

In order to find mechanical instabilities in the compressor, the different components (first grating, second grating, fold mirror) were tested individually: on each component, the beam pointing fluctuation of a laser pointer was compared to the beam pointing fluctuation of the laser pointer when reflected on the optical component under test. For the second grating and the fold mirror, both input and output pointing deviation were not distinguishable (approx. $1.4 \pm 0.2\,\mu$rad) within the measurement error. This leads to the conclusion that both components increase the pointing error less than $0.7\,\mu$rad. Nevertheless, for the first grating (also used in the stretcher) an increase of $1.67 \pm 0.29\,\mu$rad and $2.01 \pm 0.25\,\mu$rad in the horizontal and vertical direction were measured, respectively. With this measurement, the unstable mechanical mount was identified and replaced. In the compressor, the unstable optical component is the first grating and thus instabilities cause no significant timing jitter, as shown in theory (Section 6.3.3). Nevertheless, an identical grating mount is used in the stretcher and since the beam hits this particular optic 8 times and the grating acts also as second grating, the theory predicts an influence for the timing jitter in this case. Therefore, the stretcher grating mount was replaced.

The initial design and the new design of the grating mount are compared in Figure 6.11. The tip angle in the initial grating mount design is aligned based on a commercial gimbal mirror mount with an adapter for the grating. In this design, a large weight load is hanging outside the rotation center and therefore puts load on the springs of the mirror mount. This is suboptimal and causes instabilities mainly in the vertical direction. This mirror mount is replaced in the new design by a tilting platform, which provides higher stability for the tip angle. Additionally, the previously used mirror mount had an unused degree of freedom for the tilt angle. Therefore, a source of vibration in the horizontal direction is removed by the replacement of this mirror mount.

In a next step, an completely air-tight box was built around the stretcher in order to minimize air turbulence, as depicted in Figure 6.12. If this action proves to be insufficient in future, enclosing the stretcher in vacuum for ultimate timing stability is considered.

For the installation of the box, the stretcher had to be dismantled and rebuilt on a new breadboard. In conjunction with this construction work, the stretcher angle

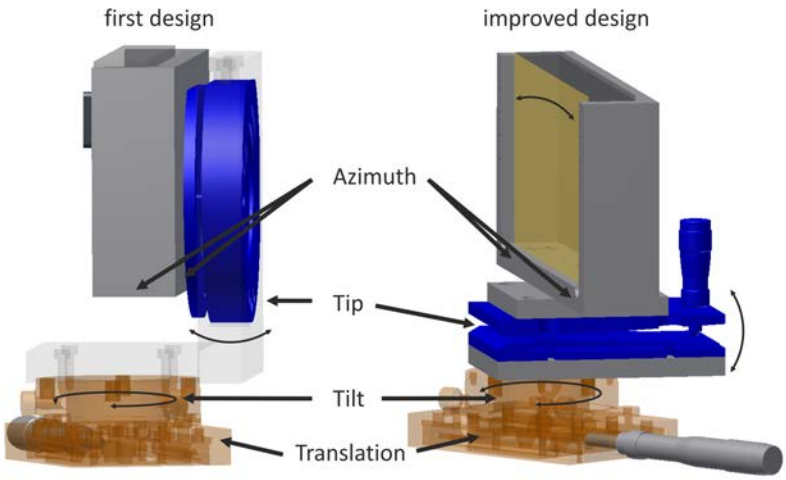

Figure 6.11: Redesigned stretcher grating mount (right side) in comparison with the initial design (left side). In the initial design, a commercial mirror mount (blue) is used to realize the alignment degree of freedom for the tip angle. The heavy frame and the grating were mounted to the front of this mirror mount. This puts load on the springs of the mirror mount and causes instabilities. In the new design (right), this mirror mount is replaced by a tilt-stage which provides higher stability.

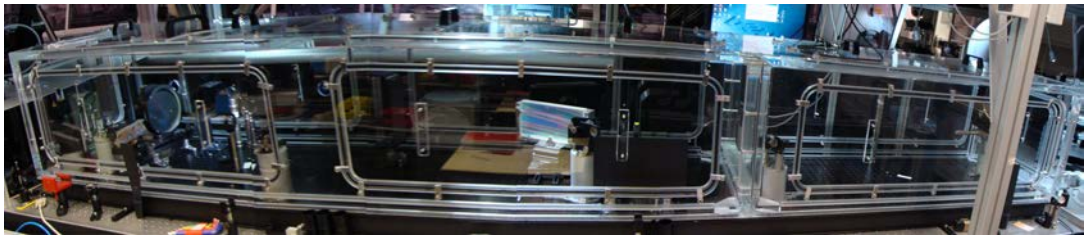

Figure 6.12: The new, air-tight box for the stretcher has all windows sealed with o-rings and is $320 \times 60 \times 50\,\mathrm{cm}^3$ in size.

was changed from 58.5° to 60°. This has some advantages for the grating reflectivity (compare Figure 4.4 (b)) and increases the compressor transmission by 4 %. Additionally, the larger input angle corresponds to a smaller diffraction angle, which helps to reduce the timing jitter by 5% (compare Equation 6.19).

The timing fluctuations in the modified setup are compared to the previous measurements in Figure 6.13. In the free-running mode, the peak-to-peak and rms fluctuations are reduced for the modified setup. Nevertheless, the average shot-to-shot timing change is increased (from 75 fs to 130 fs rms) and therefore the improvement in the stabilized timing jitter is small.

The changed grating angle in the stretcher requires the same change in the compressor. For this, the previously installed beam tubes in the compressor had to be removed, which could explain the increased shot-to-shot fluctuations. Nevertheless, even without these tubing in the compressor the synchronization could be stabilized to 99.8 fs standard deviation. This may seem a minor improvement compared to the previous value of 105 fs at first, but even with increased air turbulence in the compressor an improvement for the stabilization was possible due to the improvements

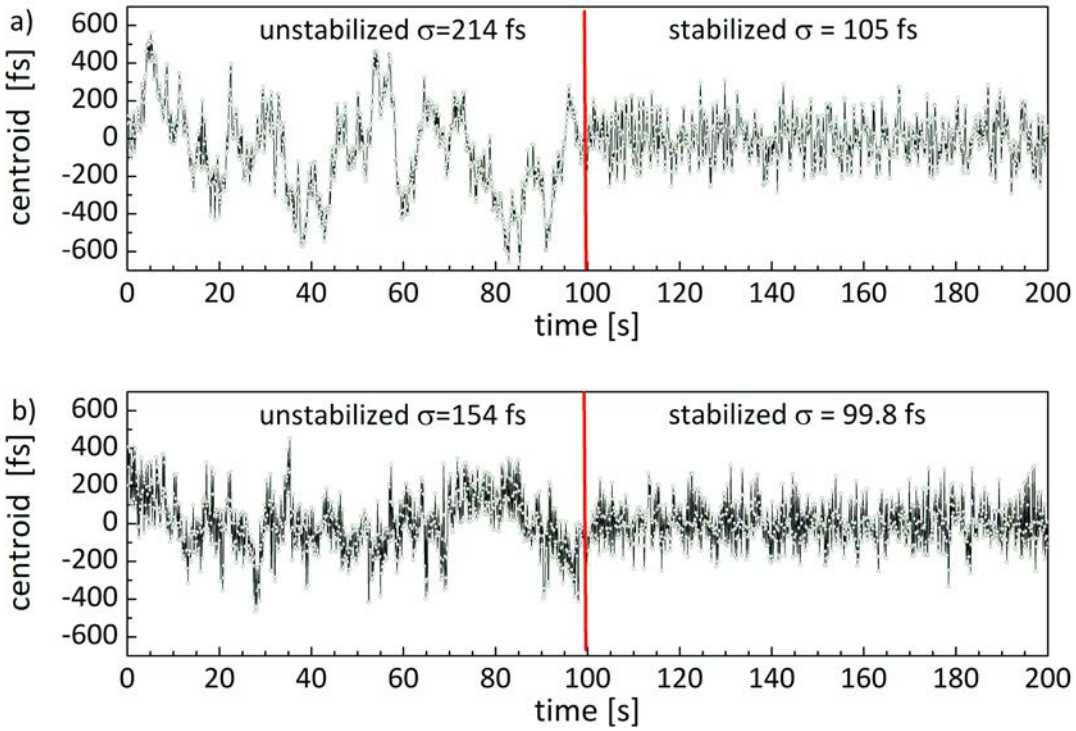

Figure 6.13: Comparison the timing jitter before (a) and after the stretcher modifications (b). In the improved setup, the slow fluctuations in the free-running mode are reduced. Nevertheless, the shot-to-shot fluctuations are increased, resulting in minor improvements for the stabilized timing jitter.

in the stretcher. This gives reason to assume that the installation of the compressor vacuum chamber (compare Section 5.3.2) leads to a major improvement for the timing fluctuations.

6.6 CONCLUSION

In this section, the pump-seed timing fluctuations for the OPCPA system are investigated in detail. An accurate timing measurement is applied and a series of measurements leads to the conclusion that the stretcher/compressor setup in the pump laser chain is the main source of timing fluctuations. This was not expected in the beginning, but could be explained by a novel theory about group delay fluctuations in a compressor introduced by small angle changes. Finally, it was shown by measurements that indeed the beam pointing fluctuation in the stretcher/compressor is increased by few μrad accompanied by an increased timing jitter. It was found that the grating mount of the stretcher grating is mechanically unstable. This mount was replaced by a more stable one and additionally the stretcher box was replaced by a completely air tight box. These actions help to further reduce the timing jitter in the stretcher and the timing could be stabilized to 100 fs rms. This level of timing jitter is sufficiently low for carrying out the first proof-of-principle OPCPA experiments. Nevertheless, further jitter improvement is expected when the vacuum compressor introduced in Section 5.3.2 will be implemented.

7 SECOND HARMONIC GENERATION AND OPCPA

As a proof of the functionality of this new pump laser concept, this chapter illustrates the first use of the pump pulses to drive a dual-stage OPCPA chain.

7.1 SECOND HARMONIC GENERATION

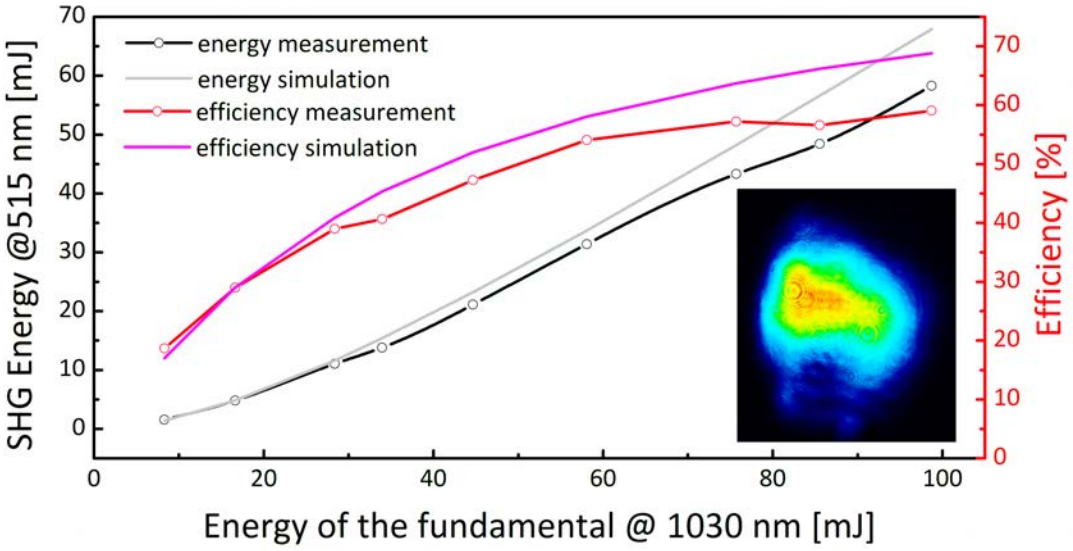

Figure 7.1: The SHG energy and efficiency as function of the input energy. The simulation shows that higher efficiency is expected. The deviation from the theory increases with higher energy which could be a hint that B-integral issues start to distort the wavefront. The inset shows the beam profile at the first OPCPA stage.

In order to be used as pump beam for the PFS OPCPA stages, the output of the compressor (200 mJ, 900 fs at 1030 nm) has to be frequency doubled to 515 nm. The second harmonic generation is performed in a 5 mm thick type-2 DKDP crystal with a transverse size of 28×28 mm. Figure 7.1 shows the efficiency and the frequency doubled output pulse energy for different input energies. The theoretical curves in Figure 7.1 are generated with *SNLO*—a freeware for nonlinear modeling from *Sandia National Laboratories*. Gaussian pulses with a radius of $w = 16$ mm and a temporal width of 900 fs are modeled in a 5 mm tick type-2 DKDP crystal. The phase and group velocities and walk-off angles are obtained from the software and a nonlinear index of $3 \cdot 10^{-16}$ cm^2/W is assumed for both wavelengths. The deviation of the measured data from the theoretical curve increases with increasing energy. The overall efficiency is strongly dependent on the exact beam profile and deviations from the modeled Gaussian beam profile could explain this discrepancy. Another reason might arise from nonlinearities before the doubling crystal (in 1 m air and a few-mm vacuum window of the spatial filter) which can distort the wavefront

and therefore reduce the doubling efficiency. A maximum efficiency of 59% was achieved resulting in pulses with 58 mJ at a wavelength of 515 nm.

The limited aperture of the available doubling crystal (28 × 28mm) in this experiment limits the applicable pulse energy. A beam size of $w = 16$ mm is necessary in order to optimize the doubling at high energies, approximately 15% of the input beam energy is clipped by the limited aperture of the crystal (28 × 28mm). The input energy in Figure 7.1 is calibrated accordingly. Nonlinear effects in the doubling crystal and during the propagation through air to the OPCPA stage result in local filamentation for a smaller beam size or higher input energies. The beam profile for the frequency doubled beam at the position of the first OPCPA stage is shown as inset in Figure 7.1. The beam size ($2w$) for the main axes is 2 and 2.5 mm respectively. Up to 50 mJ, no filamentation is observed and the energy for the first OPCPA experiment was limited to this energy level.

For the application as OPCPA pump, the second-harmonic generation (SHG) signal with up to 50 mJ is separated from the fundamental beam by dichroic beam splitters and split into two beams by a 70/30 beam splitter. All-reflective telescopes scale the beam size down for the individual OPCPA stages. In this way, pump beams for a two-stage OPCPA test are provided.

7.1.1 *Optimization of the SHG*

The doubling efficiency is generally increasing for higher intensities because shorter crystals can be used—minimizing the phase-matching error. This behavior is also shown in Figure 7.2 (left), where the maximum doubling efficiency is simulated for a 10 mm Gaussian beam with 900 fs duration in type-2 DKDP. For each data point, the energy is scaled and the optimum crystal thickness was found. It shows that the consideration of the nonlinear refractive index (gray) in the simulation with *SNLO* has a significant effect: The expected maximum efficiency is reduced compared to the case without nonlinearities (black). The nonlinearities in the crystal for high intensities are large enough to affect the phase on the length scale of the crystal, which reduces the efficiency. The B-integral (red) is calculated under the assumption of a constant beam diameter and increases above 1 for intensities above 50 GW/cm^2.

The B-integral has to be minimized in a reliable doubling stage design. The B-integral generally scales linear with the length and intensity (I) and the question arises, how the thickness of the doubling crystal scales with the applied intensity. Or in other words, is it beneficial, in therms of B-integral, to use a thicker doubling crystal with less Intensity or a thinner crystal with higher Intensity. Figure 7.2 (right) is dedicated to this question.

In Figure 7.2 (right), the minimum crystal length for a fixed doubling efficiency of 62.4% is simulated, including nonlinear effects. This particular value is the maximum achievable efficiency for the lowest intensity simulated. The minimum length to achieve this efficiency (black) scales slower as 1/I (green). Therefore, the B-integral increases for high intensities. As tradeoff between high efficiency and low B-integral, intensities around 50 GW/cm^2 will be used. Lower intensities will give less efficiency but less nonlinearity, as well.

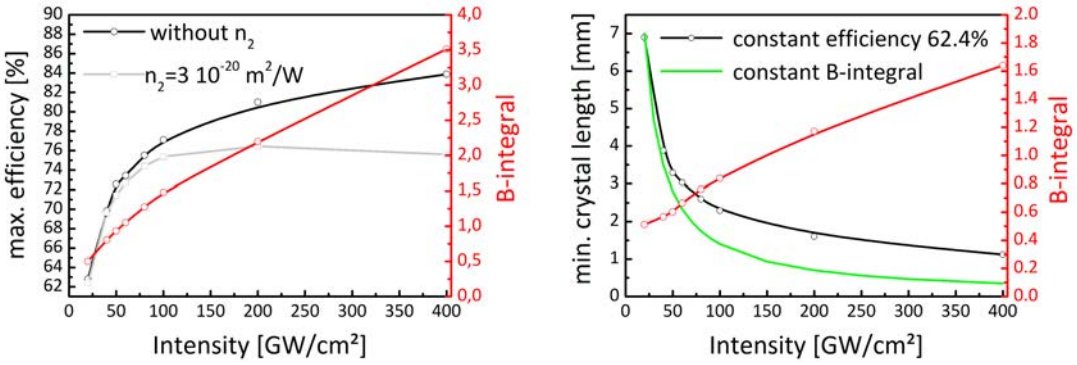

Figure 7.2: (Left) The maximum doubling efficiency is plotted for various pump intensities, taking into account the optimum crystal thickness at each intensity. When the nonlinear refractive index is included in the simulation, the efficiency drops for high intensities where the B-integral (shown in red) becomes greater than unity. (Right) The crystal thickness is modeled for a constant doubling efficiency. The B-integral increases for high intensities because the minimum crystal length does not scale as $1/I$ (green curve).

The future doubling stages will work with approximately 70% efficiency at an intensity of $50\,\mathrm{GW/cm^2}$. For the final doubling stages for infrared pulses with 10 J with 1 ps duration, a Gaussian beam profile will result in impractical large apertures for the doubling crystal. Therefore, beam shaping and imaging has to be implemented in the high energy amplifiers in order to provide a super-Gaussian beam profile. This kind of profile will also help to further increase the doubling efficiency.

7.2 PROOF OF PRINCIPLE OPCPA EXPERIMENTS

The OPCPA experiments are conducted by Christoph Skrobol and a detailed description will be found in his PhD-thesis. He developed a Fourier-split-step, pseudo-3D simulation code, which includes dispersion effects and spatial walk off. This code enables a more realistic modeling compared to the initial 1D approach (see Chapter 3). A comparison of the simulation with first OPCPA experiments in DKDP [120] shows good agreement and the new simulation largely confirms the 1D simulation results.

An improved PFS design is proposed based on these simulations (compared to Figure 3.2), where the number of OPCPA stages can be decreased from 8 to 5 due to the use of LBO as nonlinear medium for the first stages.

In a first OPCPA experiment with LBO, a total pump energy of 50 mJ (at 515 nm) was used in a double stage OPCPA experiment with a 4 and 2 mm thick LBO crystal in the first and second stage, respectively. The seed and the amplified spectra are shown in Figure 7.4 a). At the maximum amplified energy of 3 mJ, the amplified spectrum supports a Fourier-limited pulse duration of 5.4 fs, as shown in Figure 7.4 b). First attempts of compression in bulk calcium fluorite lead to approximately 10 fs pulses for the spectral parts from $900 - 1300$ nm but the spectral parts from $700 - 900$ nm had a remaining group delay which could not be compressed at this time. A new design of chirped mirrors is necessary in order to compress the full spectrum.

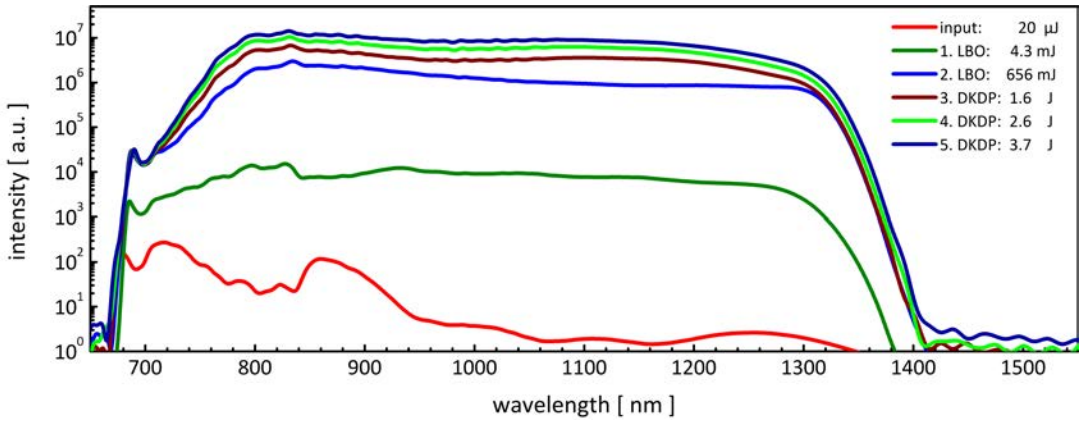

Figure 7.3: Based on simulations, an improved design for the OPCPA stages is proposed (compared to Figure 3.2). The number of amplifier stages can be reduced to 5 due to the use of LBO in the first stages. (by courtesy of C. Skrbol)

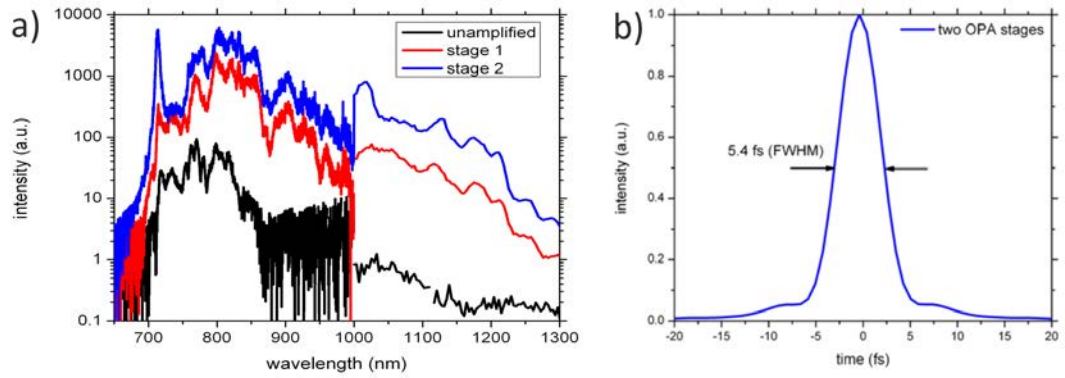

Figure 7.4: Results of the first OPCPA experiments. (a) Shows the seed spectrum and the amplified spectrum at both amplifier stages. In the seed spectrum, the red part (around 1150 nm) has orders of magnitude less energy compared to the blue part (around 800 nm). In the amplified spectra, this energy difference can be reduced and the bandwidth would support a Fourier limited pulse length of 5.4 fs.(by courtesy of C. Skrbol)

7.3 CONCLUSION

Currently, up to 50 mJ are available as pump for the first two OPCPA stages, limited by B-integral problems in the air compressor and beam transport line. For the achievement of higher pump energies, major modifications to the compressor are necessary: The compressor has to be placed in vacuum in order to reduce the B-integral. This will be also beneficial for further reduction of the timing jitter. Furthermore, all OPCPA stages work with high pump intensities above 100 GW/cm^2 and therefore have to be enclosed in vacuum, as well. This requires additional two vacuum chambers of ($6.5 \times 1.5 \times 1$ m) for the full system. The first OPCPA experiments were not optimized for efficiency, but the first results for the amplified bandwidth and compression are very promising for the future high energy OPCPA stages and demonstrate the feasibility of the PFS scheme. The vacuum design for the OPCPA stages is ongoing, as well as the development of the Joule class pump laser amplifiers. The implementation of both will enable high energy broad-band OPCPA in the near future.

Part IV

SUMMARY AND OUTLOOK

8

SUMMARY

Over the last decade, OPCPA gained increased interest for the generation of short pulses due to the broad amplification bandwidth. The OPCPA process is intrinsically free of heat generation and can provide high single-pass gain. These properties make OPCPA the preferred choice for high average power and high energy applications. So far, broad-band amplification (to low energy) and amplification to several Joules energy (with $\approx 100\,\mathrm{fs}$ pulse duration) could be demonstrated independently. The PFS aims at combining these achievements in order to produce few-cycle pulses with several Joule of energy. The high-power pan-European project ELI [3] relies on the PFS technique as prototype for its front end, because these unique pulse parameters have the potential to trigger a major advance in attosecond physics. It allows the generation of XUV attosecond pulses via the relativistic oscillating mirror mechanism. In contrast to the current gas harmonic generation, it has no limitation to the input intensity and is expected to yield a two to three orders of magnitude higher efficiency.

In order to achieve the broad bandwidth and the high gain in the PFS system, thin OPCPA crystals are used in combination with high intensity pumping. The latter one is achieved by a one picosecond pulse duration, which is significantly reduced compared to typically applied 100 ps or nanosecond pulses. The described scaling theoretically allows the amplification of octave-spanning spectra to high energies and the task of the PFS project is to demonstrate the generation of few-cycle pulses with relativistic intensities for the first time. The main challenges—besides the optimization of the OPCPA chain—are the generation of the broad-band signal pulses, the generation of suitable pump pulses and the synchronization of both. In particular, the two latter issues are in the focus of this thesis.

PUMP LASER The design of the full PFS OPCPA chain requires 1 ps pump pulses at 515 nm delivered in four beams with 5 J each. The green wavelength is obtained by frequency doubling of four individual infrared laser beams with 10 J pulse energy (for a conservative conversion efficiency of 50%). The pump laser described in Chapter 4 therefore aims at becoming a 10 TW laser system based on CPA in Yb:YAG. Such systems are not commercially available and a large part of the work for the PFS development is absorbed by the development of this pump laser system. In the past, high energy infrared lasers were mostly based on Neodymium-doped gain materials. Nevertheless, Neodymium is not applicable in the PFS system, because it does not provide sufficient bandwidth for 1 ps pulse duration. Instead, this work was focused on Yb-doped materials with broader bandwidth, their longer upper state lifetime and low quantum defect. In particular, Yb:YAG offers a good combination of its lasing parameters and its thermal and mechanical properties [121] and therefore was chosen for this work. Yb-doped materials can be efficiently pumped by diode lasers at 940 nm or 980 nm. Thus, the development of Yb:YAG oscillators

[100] and amplifiers [122] was closely connected to the development of high power diode lasers arrays [47]. Nevertheless, high energy amplification above 50 mJ [123] was not demonstrated when the PFS project started.

Within the PFS project, a record amplification up to 300 mJ in the first Yb:YAG multi-pass amplifier could be shown. The weak points in this particular amplifier showed that an advanced thermal management and superior pump laser homogeneity are crucial for building amplification stages with high beam quality. Currently, work is ongoing on the 1 J amplification stage in order to provide a scalable design for the final 10 J amplifier. The design and characterization of this amplifier will be presented by Christoph Wandt in his PhD thesis. In close collaboration with industry partners, a prototype pump source with a very homogenous profile was developed. The crystal of this amplifier will be used as active mirror and glued on a heat sink for improved thermal management.

The dispersion management for this pump laser system is the main aspect of this thesis and the design of a compact double-pass pulse stretcher and a compressor are presented in Chapter 4. The narrow bandwidth of Yb:YAG requires a dispersion two orders of magnitude larger compared to commonly used Ti:sapphire CPA systems. A large grating separation is necessary in order to meet the design parameters. Compression of 200 mJ pulses from 4 ns down to to 900 fs [99] was demonstrated in Chapter 5, which has been the most powerful pulse created in Yb:YAG at the time published. This record was possible due to the use of spectral shaping (Section 4.4), where the input spectrum of a broad-band amplification stage (Yb:glass regenerative amplifier) is manipulated to pre-compensate the wavelength-dependent gain curve. Therefore, a broader spectral bandwidth and thus shorter pulses are obtained.

Later changes in the stretcher setup reduced spectral clipping and increased the supported bandwidth. Thus, the compressed pulse duration was further reduced to 740 fs. An estimate for the limits of this spectral shaping technique shows that sub-500 fs pulse duration are theoretically feasible in a Yb:YAG CPA system with several Joule pulse energy. Nevertheless, these pulse durations cannot be demonstrated in our current setup because changed stretcher design with larger optics would be necessary for the experimental realization.

Such kind of lasers are interesting also for other applications, especially for the highly efficient generation of high energy THz pulses. Fülöp [124] predicts that an optimum efficiency ($> 10\%$) for THz generation by optical rectification is achieved at a fourier limited pulse duration of 500 fs and at cryogenic temperatures, which could enable efficient THz pulse generation on the 10 mJ-level. An Yb:YAG CPA system would therefore be an ideal source for this application and diode-pumping in principle allows for high repetition rate operation. The pulses of the PFS pump laser (with 70 mJ and 1.3 ps at that time) were used in [125] in order to support this theory and a record pulse energy of 125 μJ and efficiency (0.25%) for THz pulse generation was demonstrated.

SYNCHRONIZATION In the very first OPCPA trials for PFS, a huge instability in the amplified signal was observed and identified as fluctuation of the relative arrival time of the pump and signal pulses. This jitter was unexpected, since both the signal and the pump pulse are generated from the same oscillator and are thus

supposed to be optically synchronized. The realization of a jitter measurement with 10 fs accurracy based on sum frequency generation enabled tracing the source of this jitter as explained in Chapter 6. Experiments showed that the stretcher/compressor setup is the main source of timing jitter. A theoretical analysis revealed that the optical path length in a stretcher or compressor setup is much more fraught with jitter than a comparable optical path in an amplifier. The detailed analysis of this effect led to a quantitative model for timing jitter in stretcher/compressor setups originating from small angle changes. These angle changes may be caused by air turbulence or mechanical instability of optical components. A simple analytic expression for the jitter is obtained in approximation. The jitter increases linearly with the introduced angle change and with the position where the angle change occurs: If the angle change is introduced at the position of the first grating, the symmetry of the parallel grating setup compensates the additional optical path and the timing difference is negligible. When the angle change takes place at the second grating, this compensation is not working anymore and a large additional optical delay is introduced—resulting in a delayed pulse arrival time. In between these extreme positions, the jitter increases linearly with distance from the first grating.

Attempts to reduce the air turbulence without implementing a full vacuum box around the stretcher supports this theory. For removing the remaining slow fluctuations, an active stabilization system was successfully applied and stabilized the jitter to 100 fs rms. This jitter level is sufficiently low for first OPCPA experiments. Nevertheless, the output energy and spectrum will still exhibit noticeable fluctuations originating from the remaining jitter. Therefore, more work is necessary in order to further reduce the jitter. First steps in this direction were taken: an improved stretcher box, the replaced stretcher-grating mount and the increased stretcher input angle. Due to these efforts in the stretcher only, the jitter for the otherwise open system could be reduced to a level where the both compressor and stretcher were boxed. Further improvement in the jitter is expected when the compressor is enclosed in a vacuum box, as proposed in Section 5.3.2.

FREQUENCY DOUBLING In Chapter 4, the development of a novel multi-100 mJ CPA laser with sub-ps pulse duration at 1030 nm was described. For the application as OPCPA pump in PFS, these pulses have to be frequency doubled. Currently, up to 100 mJ of the available output energy were frequency doubled with up to 60% efficiency and 60 mJ at 515 nm can be used in the first OPCPA experiments. The output energy was limited so far by the crystal size (28 mm) and by nonlinearities in the crystal and air. Simulations for the final doubling stage show that a low intensity (i.e 50 GW/cm^2) in combination with 7 mm long crystals should be preferred over higher intensities with shorter doubling crystals in order to minimize the B-integral. In the future, larger aperture crystals will be used and the doubling stage and all OPCPA stages will be built in vacuum in order to apply a higher pump energy.

OPCPA EXPERIMENTS The pump-seed synchronization was stabilized to 100 fs due to the efforts described in this thesis. This enabled us to conduct first OPCPA experiments in DKDP [120] and lately with two LBO OPCPA stages (see Section 7.2). By these experiments, an amplified bandwidth supporting 5.4 fs Fourier-limited pulses

was verified. In the very first compression experiments with CaF_2 bulk material, the spectral part from 900 − 1400 nm was compressed to approximately 10 fs. The spectral components below 900 nm were not compressed at this time but the group delay curve for the full spectrum was measured and chirped mirrors are designed in order to compensate the remaining dispersion. These proof-of-principle experiments therefore show the feasibility of the PFS strategy for the generation of few-cycle pulses with relativistic intensity.

8.1 OUTLOOK

Further progress in the PFS project will be made when higher pump energy for the OPCPA is available. As mentioned earlier, the application of higher pump energy requires all OPCPA stages to be built in vacuum. Similar to the compressor of the pump laser, these chambers will have to be large and the design and ordering delays the project. Therefore, Christoph Skrobol developed an intermediate vacuum setup for two OPCPA stages, consisting of available smaller chambers and standard vacuum tubes. This setup is currently set up in the lab and is ready for operation. Together with the intermediate compressor (Section 5.3.3), a pump energy of up to 1 J (at 1030 nm) can be applied as soon as it is available in two consecutive OPCPA stages. Simultaneously, the vacuum chamber and the setup for the final OPCPA stages are planned.

Christoph Wandt has designed and built the 1 J amplifier for the pump laser. Currently he is aligning and optimizing this amplifier- especially the crystal cooling. So far, up to 1.2 J of pulse energy could be shown at 1 Hz repetition rate. At higher repetition rates, the crystal cooling has to be optimized in order to handle the increased heat load.

In the middle of 2013 the PFS project will be working in the described mode and amplified pulses in the range of 50 mJ can be expected with a spectrum supporting 5 fs pulse duration. The compression of these pulses will be achieved with bulk material (CaF_2) and higher order dispersion is compensated with a matched design of chirped mirrors. Once these pulses are compressed, the PFS system will be a high power light source with unique properties: multi-TW peak power in a CEO-phase stabilized few-cycle pulse. At this stage in the project, the first experiments for single-attosecond-pulse generation may become possible, testing the expected high temporal contrast of the PFS concept.

After this first step, the pump laser will be upgraded in energy. The next amplifier stage will deliver 10 J and is an up-scaled version of the well-designed 1 J stage. Simultaneously, the compressor chamber and the chamber for the third OPCPA stage will be installed. When the third OPCPA stage is in operation, the energy of the few cycle pulses can be boosted to the J-level and the jitter is expected to remain at the few-ten femtosecond level. An option for the last amplifier is cryogenic cooling of the Yb:YAG crystal in order to increases the efficiency, because Yb:YAG changes from a quasi-three-level to a four-level system. In this case, the bandwidth of the emission cross section will be reduced [126], resulting in pulse durations of 1 − 2 ps.

In a final step, the main amplifiers of the pump laser will be multiplexed together with further OPCPA stages, which will further increase the energy to the final energy of several Joule.

The work presented in this thesis addresses major issues in the framework of the PFS project on the way towards Joule-scale few-cycle pulse generation with the short-pulse pumped OPCPA scheme. After the completion of the PFS laser, the unique pulses will be used to study new regimes of relativistic light-electron interactions and to scale attosecond pulses to higher pulse and photon energy into the hard X-ray regime.

The inherent advantages of the PFS concept (energy-scalable, high-contrast, few-cycle pulses) have sparked widespread interest in the laser community and led to a number of similar projects using the same principle, even though PFS itself is not yet operational. At MPQ, a follow-up project dubbed PFS-pro aims to combine multi-kHz, picosecond CPA thin-disk pump laser technology with the PFS-OPCPA ansatz. It makes use of the low absorption in nonlinear crystals to scale the average power of a PFS-like system to 100's of Watts. On an international level, PFS/PFS-pro has had a major impact on the Extreme Light Infrastructure (ELI), a pan-European initiative to construct 3 major research laser facilities in , Romania, Czech Republic and Hungary. The latter two installations will use PFS technology to power their frontend laser systems up to the kHz and Joule level. According to its website, one important aspect of ELI "is the possibility to produce ultra-short pulses of high energy photons, electrons, protons, neutrons, muons and neutrinos in the attosecond and possibly zeptosecond (10^{-21} sec.) regimes on demand."[3] Therefore, the presented work might also affect the broad range of fundamental and applied research planned for ELI.

Part V

APPENDIX

A

USEFUL CALCULATIONS

A.1 TRANSFORMATION FROM FREQUENCY TO WAVELENGTH

Since calculations (including the Fourier transform) use the frequency but experimental devices (spectrometers) usually use the wavelength, it is important to transform these quantities between wavelength and frequency.

$$\varphi_\lambda(\lambda) = \varphi_\omega(2\pi c/\lambda) \tag{A.1}$$

$$S_\lambda(\lambda) = S_\omega(2\pi c/\lambda)\,\frac{2\pi c}{\lambda^2} \tag{A.2}$$

Transformation from frequency to wavelength is not linear (i.e. $\omega = 2\pi c/\lambda$). Therefore the phase looks different when plotted over the different domains. The spectrum has to be rescaled by $\omega = 2\pi c/\lambda^2$ because the spectral energy (i.e. the integral over the spectrum) should be independent of the choice of variables. The consequence is, that a symmetric spectrum or a linear phase in frequency space look deformed in the wavelength space, as illustrated in Figure A.1.

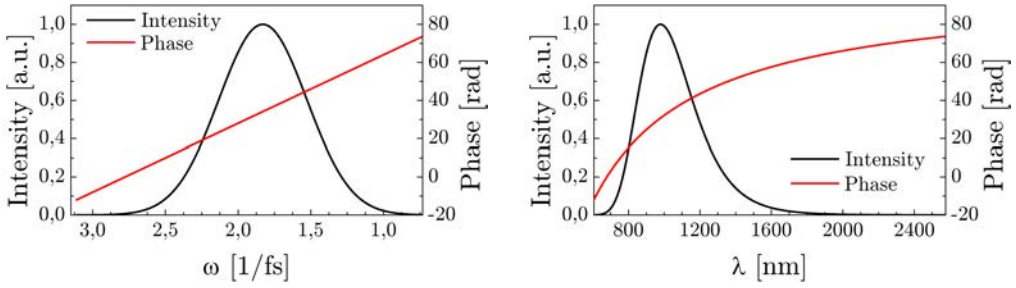

Figure A.1: A Gaussian spectrum with linear phase (as function of ω) (left) is transformed to wavelength space (right). The rescaling during this transformation changes the shape of the spectrum and phase.

A.2 PEAK INTENSITY OF A GAUSSIAN FUNCTION

A laser pulse is often described by a Gaussian intensity distribution.

$$I = I_0\, e^{-4\,ln2\left(\frac{x-x_0}{\Delta x}\right)^2} \tag{A.3}$$

Where I_0 is the peak intensity and Δx is the full-width half maximum (FWHM) of the distribution. The integration of A.3 gives:

$$\int_\infty^\infty I_0 e^{-4\,ln2\left(\frac{x-x_0}{\Delta x}\right)^2} = I_0\,\Delta x\sqrt{\frac{\pi}{4\,ln2}} \tag{A.4}$$

A laser pulse is usually described as Gaussian function in the transverse space dimensions and in time. The pulse energy can then be expressed as:

$$E = \int_{-\infty}^{\infty}\int_{-\infty}^{\infty}\int_{-\infty}^{\infty} I\,dx\,dy\,dt = I_0\,\Delta x\,\Delta y\,\Delta t\left(\frac{\pi}{4\,ln2}\right)^{\frac{3}{2}} \tag{A.5}$$

Similar relations follow for the Fluence $F = \int I\,dt$ and the Power $P = \int\int I\,dx\,dy$. The measured variable in the lab is usually the energy. The peak intensity, peak fluence or the peak power have to be calculated for different applications. When $\Delta x = \Delta y$ is used, the important equations can be written:

$$I_0 = \frac{E}{\Delta x^2\,\Delta t}\left(\frac{4\,ln2}{\pi}\right)^{\frac{3}{2}} \tag{A.6}$$

$$F_0 = \frac{E}{\Delta x^2}\frac{4\,ln2}{\pi} \tag{A.7}$$

$$P_0 = \frac{E}{\Delta t}\left(\frac{4\,ln2}{\pi}\right)^{\frac{1}{2}} \tag{A.8}$$

A.3 B-INTEGRAL

The B integral describes the accumulated nonlinear phase shift on the optical axes (z) and is defined as:

$$B = \frac{2\pi}{\lambda}\int dz\,n_2\,I_0(z) \tag{A.9}$$

where $I(z)$ is the optical intensity along the beam axis, and n_2 the nonlinear index. For fused silica, the $n_2 = 3\cdot 10^{-20}\,\frac{m^2}{W}$ and for air a factor of thousand less. A simple estimation (considering I_0 =constant) for the pumping of the OPCPA stages ($\lambda = 515\,\text{nm}$, $I_0 = 100\,\text{GW/cm}^2$) gives a B-integral of 0.38 for a propagation of 1 mm in fused silica (or 1 m in air). An other example (for the intermediate compressor) with $\lambda = 1030\,\text{nm}$, $E = 1\,\text{J}$, $\tau = 1\,\text{ps}$, $FWHM = 4\,\text{cm}$ gives an intensity of $I_0 = 5.2\cdot 10^{14}\,\text{W/m}^2$.The resulting B-integral is 0.093 per mm fused silica or per meter air.

A.4 FOURIER TRANSFORM OF A LINEARLY CHIRPED PULSE

A pulse with Gaussian amplitude and quadratic temporal phase $\phi(t) = -bt^2$ has the form:

$$E(t) = E_0\,e^{-at^2}\,e^{ibt^2} = E_0\,e^{-(a-ib)t^2}, \tag{A.10}$$

where E_0 is a constant and b is the chirp parameter. The spectrum of this pulse can be found via Fourier transform:

$$\tilde{E}(\omega) = \int_{-\infty}^{\infty} dt\,E(t)\,e^{-i\omega t} \tag{A.11}$$

$$= \int_{-\infty}^{\infty} dt\,E_0\,e^{-[(a-ib)t^2+i\omega t]} \tag{A.12}$$

The integral is simplified by completing the square in the exponent, so that:

$$(a-ib)t^2 + i\omega t + \beta^2 - \beta^2 = \alpha^2 t^2 + 2\alpha\beta t + \beta^2 = (\alpha t + \beta)^2 - \beta^2, \tag{A.13}$$

where the coefficients are $\alpha = \sqrt{a-ib}$ and $\beta = i\omega/(2\sqrt{a-ib})$. Equation A.12 can be rewritten:

$$\tilde{E}(\omega) = E_0\, e^{-\omega^2/4(a-ib)} \int_{-\infty}^{\infty} dt\, e^{-[\sqrt{a-ib}t + i\omega/(2\sqrt{a-ib})]^2}. \tag{A.14}$$

The change of variables in the integral $u = \sqrt{a-ib}t + i\omega/(2\sqrt{a-ib})$ gives $du/dt = \sqrt{a-ib}$ and

$$\tilde{E}(\omega) = E_0\, e^{-\omega^2/(4(a-ib)} \int_{-\infty - Im[\omega/(2\sqrt{a-ib})]}^{\infty - Im[\omega/(2\sqrt{a-ib})]} e^{-u^2} \frac{du}{\sqrt{a-ib}}. \tag{A.15}$$

Cauchy's theorem (e.g. [127]) states that the integral of a complex, analytic function over a closed contour C is 0: $\oint_C f(z)dz = 0$. Since e^{-u^2} is analytic, Cauchy's theorem can be applied and we can trace a box:

$$\oint_C du\, e^{-u^2} = \int_{-p}^{p} du\, e^{-u^2} + \int_{p}^{p+iq} du\, e^{-u^2} + \int_{p+iq}^{-p+iq} du\, e^{-u^2} + \int_{-p+iq}^{-p} du\, e^{-u^2} = 0, \tag{A.16}$$

where p and q are real. Applying the substitution $u = p + iz$ and $du/dz = i$, the second integral becomes

$$\int_{p}^{p+iq} du\, e^{-u^2} = \int_0^q dz\, ie^{-(p+iz)^2} = i\int_0^q dz\, e^{-p^2} e^{-2ipz} e^{z^2} \tag{A.17}$$

The limit as p goes to infinity of the integrand is

$$\lim_{p\to\infty} e^{-p^2} e^{-2ipz} e^{z^2} = 0, \tag{A.18}$$

because the first term goes to zero, while the second and third term are finite. Similarly, it can be shown that $\lim_{p\to\infty} \int_{p+iq}^{-p+iq} du\, e^{-u^2} = 0$. Therefore, Equation A.16 simplifies to

$$\int_{-\infty+iq}^{\infty+iq} du\, e^{-u^2} = \int_{-\infty}^{\infty} du\, e^{-u^2} \tag{A.19}$$

and the Integral in Equation A.15 can be substituted by the integral on the real axis $\int_{-\infty}^{\infty} du\, e^{-u^2}$. It can be shown that the integral of a Gaussian function from $-\infty$ to ∞ is $\sqrt{\pi}$. Therefore, the electric field spectrum (Equation A.15) can be rewritten

$$\tilde{E}(\omega) = \frac{\sqrt{\pi}\, E_0}{\sqrt{a-ib}}\, exp\left[-\frac{\omega^2}{4(a-ib)}\right]. \tag{A.20}$$

A.5 GENERAL THEORY FOR FIRST ORDER SPATIO-TEMPORAL DISTORTIONS

Following Akturk [76], this theory is presented as overview rather than exact calculations in order to demonstrate the ideas and to find all possible spatio-temporal couplings. The E field is in the following written as

$$E(x,t) \propto exp\left[Q_{xx}\,x^2 + 2Q_{xt}\,xt - Q_{tt}\,t^2\right], \tag{A.21}$$

where the transformation to the previously used form in Equation 2.41 can be made with:

$$Q = i\frac{\lambda}{\pi}\begin{pmatrix} Q_{xx} & Q_{xt} \\ -Q_{xt} & Q_{tt} \end{pmatrix}^{-1} \tag{A.22}$$

The pulse-front tilt in this notation is:

$$PFT = \frac{Re\{Q_{xt}\}}{Re\{Q_{tt}\}}. \tag{A.23}$$

The beam is fully described by 6 different quantities: In the (x,t)-domain these are the real and imaginary part of Q_{xx}, Q_{xt} and Q_{tt}. The diagonal elements describe the Gaussian beam parameters in space and time, whereas the off diagonal element describes the coupling terms. The real part of the coupling term Q_{xt} yields a position time coupling of the intensity. The arrival time of the maximum intensity varies across the transversal coordinate. This effect is called pulse-front tilt. The imaginary part of Q_{xt} is a phase term, which is time and space dependent. This phase distortion causes the wave front of the pulse to rotate in time and is therefore called wave-front rotation. This distortion is not commonly known and was first considered by Akturk [76].

In order to find all possible coupling terms, the electric field (Eq.2.41) can be Fourier-transformed in 4 different domains. A Fourier transform to the (x,ω)-domain yields

$$E(x,\omega) \propto exp\left[R_{xx}\,x^2 + 2R_{x\omega}\,x\omega - R_{\omega\omega}\,\omega^2\right], \tag{A.24}$$

with a R matrix which is related to the Q matrix by:

$$R_{xx} = Q_{xx} + \frac{Q_{xt}^2}{Q_{tt}} \qquad R_{x\omega} = -\frac{i}{2}\frac{Q_{xt}}{Q_{tt}} \qquad R_{\omega\omega} = \frac{1}{4Q_{tt}}. \tag{A.25}$$

The real part of the coupling term $R_{x\omega}$ is connected to a space-frequency coupling in the intensity—the so called spatial chirp (SPC), which is given by:

$$SPC = \frac{Re[R_{x\omega}]}{Re[R_{xx}]} \tag{A.26}$$

The phase coupling in this domain is related to the imaginary part and is called wave-front-tilt dispersion.

An analog approach gives for the (k,ω) domain:

$$E(k,\omega) \propto exp\left[S_{kk}\,x^2 + 2S_{k\omega}\,k\omega - S_{\omega\omega}\,\omega^2\right], \tag{A.27}$$

with

$$S_{kk} = \frac{1}{4R_{xx}} \qquad S_{k\omega} = \frac{i}{2}\frac{R_{x\omega}}{R_{xx}} \qquad S_{\omega\omega} = R_{\omega\omega} + \frac{R_{x\omega}^2}{R_{xx}} \tag{A.28}$$

and for the (k,t) domain:

$$E(k,t) \propto exp\left[P_{kk}\,x^2 + 2P_{kt}\,kt - P_{tt}\,t^2\right], \tag{A.29}$$

with

$$P_{kk} = S_{kk} + \frac{S_{k\omega}^2}{S_{\omega\omega}} \qquad P_{k\omega} = \frac{i}{2}\frac{S_{k\omega}}{S_{\omega\omega}} \qquad P_{\omega\omega} = \frac{1}{4S_{\omega\omega}}. \tag{A.30}$$

The corresponding couplings are angular dispersion

$$AGD = \frac{\partial\theta}{\partial\omega} = \frac{k\partial\theta}{k\partial\omega} = \frac{\partial k}{k\partial\omega} = \frac{\lambda}{2\pi}\frac{Re[S_{k\omega}]}{Re[S_{kk}]} \tag{A.31}$$

and angular spectral chirp ($\rightarrow Im[S_{k\omega}]$) in the (k,ω)-domain. Furthermore, time versus angle (TVA)

$$TVA = \frac{\partial\theta}{\partial t} = \frac{\partial k}{k\partial t} = \frac{\lambda}{2\pi}\frac{Re[P_{kt}]}{Re[P_{tt}]} \tag{A.32}$$

and angular temporal chirp ($\rightarrow Im[P_{kt}]$) in the (k,t)-domain.

In each of these domains there exists a different matrix with a coupling term, i.e. 8 couplings over all. Fortunately, all these terms are connected via Fourier transforms and are therefore not independent. This is one reason, why the phase couplings are not calculated explicitly: It is enough to know two couplings (and four parameters of Gaussian beams) in order to fully characterize a pulse. All other terms can be calculated from these values. Since phase couplings are not very intuitive and hard to measure it is more useful to calculate two of the known couplings: PFT, AGD, SPC or the less known TVA.

The connection between coupling terms can be easily calculated. Similar to Equation A.25 it can be shown that

$$Q_{xt} = -\frac{i}{2}\frac{R_{xt}}{R_{\omega\omega}} \tag{A.33}$$

The pulse-front tilt (proportional to $Re[Q_{xt}]$ normalized by the local pulse width) is then:

$$PFT \propto Re[Q_{xt}] = Re[\frac{i}{2}\frac{R_{x\omega}}{R_{\omega\omega}}] \tag{A.34}$$

$$= \frac{1}{2\left|R_{\omega\omega}\right|^2}\left(Re[R_{x\omega}]Im[R_{\omega\omega}] - Im[R_{x\omega}]Re[R_{\omega\omega}]\right), \tag{A.35}$$

where the frequency chirp is $FCH \propto Im[R_{\omega\omega}]$, the spatial chirp is $SPC \propto Re[R_{x\omega}]$ and the spectral bandwidth $\propto Re[R_{\omega\omega}]$. One can then write:

$$PFT \propto SPC \times FCH + Im[R_{x\omega}]\Delta\omega. \tag{A.36}$$

Similar it follows that

$$AGD \propto Re[S_{k\omega}] = Re[\frac{i}{2}\frac{R_{x\omega}}{R_{xx}}] \tag{A.37}$$

$$= \frac{1}{2\left|R_{\omega\omega}\right|^2}\left(Re[R_{x\omega}]Im[R_{xx}] - Im[R_{x\omega}]Re[R_{xx}]\right) \tag{A.38}$$

For a collimated beam i.e. $Re[R_{xx}] = 0$, the angular dispersion can be connected with $Im[R_{x\omega}]$

$$Im[R_{x\omega}] \propto AGD. \tag{A.39}$$

The combination of Equation A.36 and Equation A.39 results in the useful relation:

$$PFT \propto SPC \times FCH + AGD, \tag{A.40}$$

HIGH ENERGY PICOSECOND YB:YAG CPA SYSTEM AT 10 HZ REPETITION RATE FOR PUMPING OPTICAL PARAMETRIC AMPLIFIERS

High energy picosecond Yb:YAG CPA system at 10 Hz repetition rate for pumping optical parametric amplifiers

Sandro Klingebiel,[1,*] **Christoph Wandt,**[1] **Christoph Skrobol,**[1] **Izhar Ahmad,**[1] **Sergei A. Trushin,**[1] **Zsuzsanna Major,**[1,2] **Ferenc Krausz**[1,2] **and Stefan Karsch**[1,2]

[1]*Max-Planck-Institut für Quantenoptik, Hans-Kopfermann-Str. 1, D-85748 Garching, Germany*

[2]*Department für Physik, Ludwig-Maximilians-Universität München, Am Coulombwall 1, D-85748 Garching, Germany*

[*]*sandro.klingebiel@mpq.mpg.de*

Abstract: We present a chirped pulse amplification (CPA) system based on diode-pumped Yb:YAG. The stretched ns-pulses are amplified and have been compressed to less than 900 fs with an energy of 200 mJ and a repetition rate of 10 Hz. This system is optically synchronized with a broadband seed laser and therefore ideally suited for pumping optical parametric chirped pulse amplification (OPCPA) stages on a ps-timescale.

OCIS codes: (140.3615) Lasers, ytterbium; (140.3480) Lasers, diode-pumped; (320.5520) Pulse compression.

References and links

1. J. Faure, Y. Glinec, A. Pukhov, S. Kiselev, S. Gordienko, E. Lefebvre, J.-P. Rousseau, F. Burgy, and V. Malka, "A laser-plasma accelerator producing monoenergetic electron beams," Nature **431**, 541–544 (2004).
2. Y. Nomura, R. Horlein, P. Tzallas, B. Dromey, S. Rykovanov, Zs. Major, J. Osterhoff, S. Karsch, L. Veisz, M. Zepf, D. Charalambidis, F. Krausz, and G. D. Tsakiris, "Attosecond phase locking of harmonics emitted from laser-produced plasmas," Nat Phys **5**, 124–128 (2009).
3. M. Geissler, J. Schreiber, and J. M. ter Vehn, "Bubble acceleration of electrons with few-cycle laser pulses," New J. Phys. **8**, 186 (2006).
4. G. D. Tsakiris, K. Eidmann, J. M. ter Vehn, and F. Krausz, "Route to intense single attosecond pulses," New J. Phys. **8**, 19 (2006).
5. P. Dietrich, F. Krausz, and P. B. Corkum, "Determining the absolute carrier phase of a few-cycle laser pulse," Opt. Lett. **25**, 16–18 (2000).
6. Zs. Major, S. Trushin, I. Ahmad, M. Siebold, Chr. Wandt, S. Klingebiel, T. Wang, J. A. Fülöp, A. Henig, S. Kruber, R. Weingartner, A. Popp, J. Osterhoff, R. Hörlein, J. Hein, V. Pervak, A. Apolonski, F. Krausz, and S. Karsch, "Basic concepts and current status of the petawatt field synthesizer-a new approach to ultrahigh field generation," Review of Laser Engineering **37**, 431–436 (2009).
7. I. Ahmad, S. Trushin, Zs. Major, C. Wandt, S. Klingebiel, T.-J. Wang, V. Pervak, A. Popp, M. Siebold, F. Krausz, and S. Karsch, "Frontend light source for short-pulse pumped opcpa system," Appl. Phys. B: Lasers and Optics **97**, 529–536 (2009).
8. O. V. Chekhlov, J. L. Collier, I. N. Ross, P. K. Bates, M. Notley, C. Hernandez-Gomez, W. Shaikh, C. N. Danson, D. Neely, P. Matousek, S. Hancock, and L. Cardoso, "35 j broadband femtosecond optical parametric chirped pulse amplification system," Opt. Lett. **31**, 3665–3667 (2006).
9. V. V. Lozhkarev, G. I. Freidman, V. N. Ginzburg, E. V. Katin, E. A. Khazanov, A. V. Kirsanov, G. A. Luchinin, A. N. Mal'shakov, M. A. Martyanov, O. V. Palashov, A. K. Poteomkin, A. M. Sergeev, A. A. Shaykin, and I. V. Yakovlev, "Compact 0.56 Petawatt laser system based on optical parametric chirped pulse amplification in KD*P crystals," Laser Phys. Lett. **4**, 421–427 (2007).

#138831 - $15.00 USD Received 30 Nov 2010; revised 14 Jan 2011; accepted 17 Jan 2011; published 7 Mar 2011

10. D. Herrmann, L. Veisz, R. Tautz, F. Tavella, K. Schmid, V. Pervak, and F. Krausz, "Generation of sub-three-cycle, 16 tw light pulses by using noncollinear optical parametric chirped-pulse amplification," Opt. Lett. **34**, 2459–2461 (2009).
11. J. Tümmler, R. Jung, H. Stiel, P. V. Nickles, and W. Sandner, "High-repetition-rate chirped-pulse-amplification thin-disk laser system with joule-level pulse energy," Opt. Lett. **34**, 1378–1380 (2009).
12. T. Metzger, A. Schwarz, C. Y. Teisset, D. Sutter, A. Killi, R. Kienberger, and F. Krausz, "High-repetition-rate picosecond pump laser based on a yb:yag disk amplifier for optical parametric amplification," Opt. Lett. **34**, 2123–2125 (2009).
13. M. Siebold, J. Hein, C. Wandt, S. Klingebiel, F. Krausz, and S. Karsch, "High-energy, diode-pumped, nanosecond Yb:YAG MOPA system," Opt. Express **16**, 3674–3679 (2008).
14. Chr. Wandt, S. Klingebiel, M. Siebold, Zs. Major, J. Hein, F. Krausz, and S. Karsch, "Generation of 220mJ nanosecond pulses at a 10Hz repetition rate with excellent beam quality in a diode-pumped Yb:YAG MOPA system," Opt. Lett. **33**, 1111–1113 (2008).
15. P. Banks, M. Perry, V. Yanovsky, S. Fochs, B. Stuart, and J. Zweiback, "Novel all-reflective stretcher for chirped-pulse amplification of ultrashort pulses," IEEE J. Quant. Electron. **36**, 268–274 (2000).
16. E. Treacy, "Optical pulse compression with diffraction gratings," IEEE J. Quant. Electron. - **5**, 454–458 (1969).

1. Introduction

High-power, few-cycle light pulses are of great interest for studying laser-matter interactions at extreme conditions. Several applications such as the generation of mono-energetic electron beams by laser-wakefield acceleration in the "bubble" regime or higher-harmonic generation from solid surfaces have been demonstrated [1, 2] and theoretical predictions call for light sources delivering ever shorter and more powerful pulses in order to drive these processes more efficiently [3, 4]. The generation of Joule-class pulse energies combined with the few-cycle duration has yet to be demonstrated.

The PFS project aims at developing a light source delivering Petawatt-scale carrier-envelope phase controlled [5] pulses with pulse energies $> 3\,\mathrm{J}$ in the few-cycle regime ($< 5\,\mathrm{fs}$, 700...1400 nm) at a repetition rate of 10 Hz [6, 7]. The concept for reaching the ambitious parameters of PFS is based on the optical parametric chirped pulse amplification (OPCPA) technology, using a modified scheme as compared to existing facilities. In the PFS design short pulses are used to pump the OPA stages, i.e. on the order of 1 ps, in contrast to 100 ps – ns pulse durations in previous systems (e.g. in [8–10]). The short-pulse-pumped OPCPA approach improves the conditions for high-power few-cycle-pulse generation as compared to long-pulse-pumped OPCPA in several ways. Firstly, the significantly increased pump power permits the use of thinner OPA crystals while keeping the same level of gain, which implies an increase of amplification bandwidth as compared with OPA driven by longer pulses. Secondly, the short pump-pulse duration reduces the necessary stretching factor for the broadband-seed pulse, thereby increasing stretching and compression fidelity and allowing the use of simple, high-throughput stretcher-compressor systems, consisting of bulk glass and chirped multilayer mirrors. Finally, the short pump-pulse duration results in a short amplification time window and hence dramatically enhanced temporal pulse contrast outside this window. However, the drawback of ps-pumped OPCPA is that it requires a very accurate and stable synchronization between the pump and seed pulses. Therefore a special, synchronized pump delivering 1-2 ps pulses with $4\times5\,\mathrm{J}$ pulse energy (frequency doubled at 515 nm) i.e. $4\times12\,\mathrm{J}$ in the fundamental beam (1030 nm) at 10 Hz repetition rate is required. Such a system is not commercially available and therefore a challenge for development in its own right.

Recently Yb:YAG based CPA systems delivering sub-2 ps pulses with energies as high as 125 mJ at 100 Hz [11], and 25 mJ at 3 kHz [12] have been demonstrated. For the PFS pump laser we aim for higher pulse energies but limit our repetition rate to 10 Hz. We have developed Yb:YAG amplifiers and have shown up to 3 J pulse energy with ns-pulses at 1 Hz repetition rate [13], and for 200 mJ pulses we raised the repetition rate to 10 Hz [14]. In this paper we present a full characterization of a high energy CPA system generating the shortest high energy

#138831 - $15.00 USD Received 30 Nov 2010; revised 14 Jan 2011; accepted 17 Jan 2011; published 7 Mar 2011

pulses in Yb:YAG and show its potential for OPCPA pumping. We implemented a spatial light modulator (SLM) for spectral amplitude shaping which counteracts gain narrowing and therefore pushes the limit for the compressed pulse length below 900 fs. Simulations show, that similar values can be reached for 50 J pulse energy.

2. Experimental setup

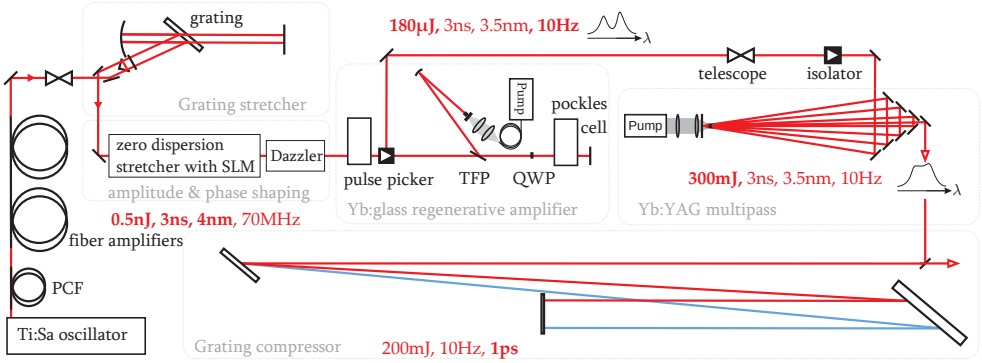

Fig. 1. Experimental setup: The seed pulses from the Ti:Sa oscillator are spectrally shifted to 1030 nm in a photonic crystal fiber (PCF), pre amplified in a double stage fiber amplifier, stretched to 3 ns and their spectral amplitude is shaped by an SLM in a zero-dispersion stretcher. The subsequent Dazzler shapes the spectral phase to improve the compression. The amplifier chain consists of a Yb:glass regenerative amplifier and a Yb:YAG multipass. After the main amplification compression is realized in a Treacy type compressor. TFP:thin film polarizer,QWP: quarter wave plate, SLM: Spatial Light Modulator.

As shown in Fig. 1(a) Ti:sapphire fs oscillator (Femtolaser rainbow) is used as front-end. The advantage of this approach is that the broadband OPCPA seed can be derived from the same oscillator and therefore will be optically synchronized. For the OPCPA pump a fraction of the oscillator output is spectrally shifted to 1030 nm in a photonic-crystal fiber. An interference filter selects a $\Delta\lambda = 10$ nm band centered at 1030 nm from the frequency spectrum with 3.4 pJ pulse energy. This output is then amplified in a two-stage Yb-doped fiber amplifier (designed by the Institute for Applied Physics, Jena, Germany) to 14 nJ pulse energy (70 MHz, 4.4 ps).

The seed pulses are temporally stretched in a compact all-reflective grating stretcher [15] to a FWHM pulse-duration of 3 ns with a spectral bandwidth of 4 nm centered at 1030 nm. It has been constructed using a 1740 lines/mm multilayer-dielectric reflection grating with an angle of incidence of 59°, a f = 2.5 m concave mirror, a flat mirror in the focal plane of the curved one, and two retroreflectors. This geometry provides a 4-times folded optical path, i.e. 8 reflections off the grating.

In Yb:YAG the bandwidth is normally limited by strong gain narrowing therefore we incorporated a spatial light modulator (SLM) which allows spectral amplitude shaping by changing the transmission for each wavelength. The SLM (CRI corporation) is located in the Fourier plane of an additional zero-dispersion stretcher, which is adapted to the aperture of the used SLM (12.8 mm × 5 mm). The losses of this setup are easily compensated by a few more round trips in the subsequent regenerative amplifier. Recently, a Dazzler (Fastlite Inc.) was implemented with the capability of simultaneously shaping the spectral phase and amplitude. Nevertheless the presented results were achieved using the SLM for spectral amplitude shaping.

#138831 - $15.00 USD Received 30 Nov 2010; revised 14 Jan 2011; accepted 17 Jan 2011; published 7 Mar 2011

The Yb:glass regenerative amplifier boosts the pulse energy to the 200 μJ-level without significant gain narrowing. The Yb:glass gain medium (8 mm long, 12 mm diameter, doping level $N_{Yb} = 6 \cdot 10^{20}\,\mathrm{cm}^{-3}$) is pumped by a fiber-coupled laser diode (5 W, 1.5 ms, 10 Hz, 976 nm) focused to a pump spot of 100 μm. Owing to the low average power, no cooling is needed and the glass is mounted in a standard mirror mount. The cavity is 1.6 m long and consists of two plane end mirrors and a focusing mirror with 200 mm focal length, which generates a focus of 100 μm diameter next to the amplifying medium on one of the end mirrors. A thin film polarizer, a quarter wave plate and a Pockels-cell are used for coupling the beam in and out of the cavity. After approximately 100 round trips this amplifier reaches saturation. Seed-energy fluctuations cause only a small variation in output energy and lead to a very stable output (1% standard deviation) with a nearly diffraction limited beam profile ($M^2 = 1.2$) as shown in Fig. 2(a).

For reaching the final output energy, we apply an 8-pass, diode-pumped, Yb:YAG amplifier, which is an upgraded version of the amplifier presented in [14]. The AR-coated Yb:YAG crystal rod (8 mm long, 6mm diameter, 3 at.% -doped) is connected to a copper heat sink with indium foil over its lateral area and is pumped by a diode-laser stack (Jenoptik Laserdiode GmbH) with an output power of 3 kW (1.5 ms, 10 Hz) at a center wavelength of 940 nm. In order to provide a small signal single pass gain of approximately 3 a pump intensity of 35 kW/cm^2 is needed and the pump is focused to an area of 0.086 cm^2. For a fixed pump power, the length of the individual passes in this non-imaging amplifier setup can be chosen in such a way that the beam size on the crystal stays 2.5 mm for all passes. This amplifier boosts the energy from 180 μJ to 300 mJ (3% standard deviation) with the beam profile shown in Fig. 2(b). In order to quantify the beam quality, we measured the strehl ratio of the compressed 1030 nm beam. The beam profile is measured in the near- and far field. Additionally the far field distribution for a perfect gaussian beam with the same size in the near field is simulated. Thereafter, the encircled energy on the area of $\pi\omega_0^2$ was calculated for the calculated focus and compared to the encircled energy on the same area for the measured focus. With this method the strehl ratio was measured to be 0.82 ± 0.05.

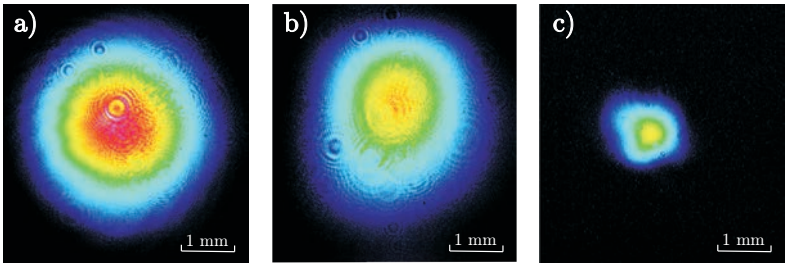

Fig. 2. Measured beam profiles: a) output beam profile of the regenerative amplifier (2.5mm diameter), b) output beam profile of the 8-pass amplifier (2.5mm diameter) and c) beam profile of the frequency doubled beam down collimated to 1.3 mm diameter at the position of the first OPA stage. The diffraction rings originate from dust on the filters in front of the camera.

3. Results and discussion

The high gain of 1500 in the main amplifier would lead to a gain-narrowed bandwidth of 1.5 nm (cf. Figure 4 a) and thus to a shortened pulse duration for stretched pulses which would increase the risk of optical damage significantly. In order to counteract this effect and to preserve the maximum bandwidth we applied spectral amplitude shaping. The final output spectrum and the

#138831 - $15.00 USD Received 30 Nov 2010; revised 14 Jan 2011; accepted 17 Jan 2011; published 7 Mar 2011

corresponding shaped input spectrum are shown in Fig. 3(b).

We also investigated the effect of gain narrowing numerically. The calculations used a simple model based on the rate equations as described in [14]. There it was shown, that the simulation of the amplification in Yb:YAG fits well to the experimental data. For spectral shaping we carry out the reverse calculation, in order to find a suitable input spectrum for the desired output spectrum.

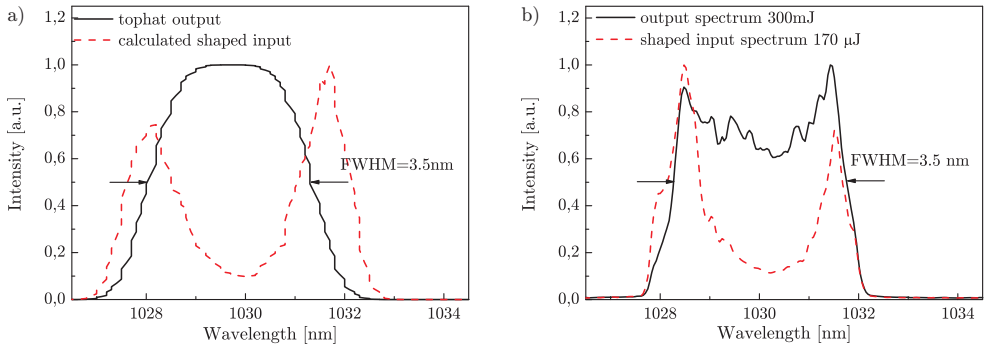

Fig. 3. (a) The input spectrum (red, dashed) which supports a broad flattop spectrum (black, solid) after amplification is calculated. In b) measured spectra for the maximum amplification are shown. The amplified spectrum (black, solid) is still suppressed in the center, showing that further amplification is possible without significant gain narrowing.

As an example, we calculated the input spectrum for 3.5 nm FWHM top-hat output profile, as shown in Fig. 3(a). The major feature is the dip at 1030 nm. Compared to the spectrum predicted by our model, the real input spectrum (Fig. 3(b) has narrower wings due to clipping in the stretcher, and we choose it in such a way, that the output spectrum is still suppressed in the center to enable further amplification without significant gain narrowing.

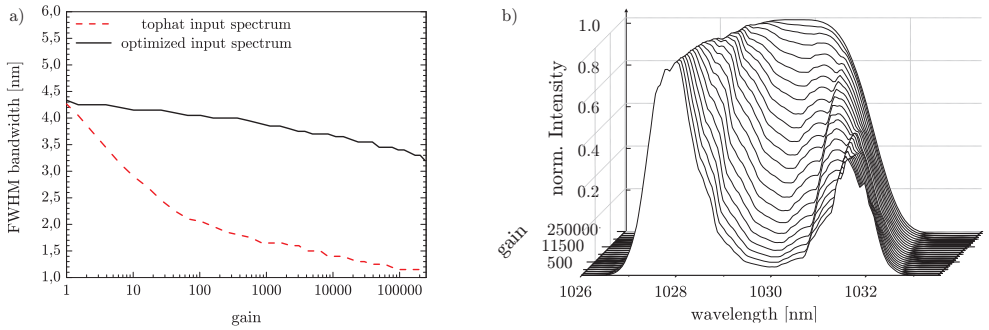

Fig. 4. Results of the simulation: a) gain narrowing for a top-hat input spectrum (red), and the reduced effect for the spectrally shaped spectrum (black). Figure b) shows the normalized spectra at different amplification levels for shaped pulses and illustrates, how the input spectrum with a dip in the center evolves to a tophat spectrum during amplification while the bandwidth is preserved large.

Furthermore the bandwidth for our final gain factor of $2.5 \cdot 10^5$ was simulated by subsequently raising the pump power. The results are shown in Fig. 4(a), which illustrates the change of the FWHM bandwidth of the shaped input spectrum with overall gain. Compared to a top-hat shaped input spectrum our calculation predicts a threefold increase in bandwidth. Fig. 4(b)

#138831 - $15.00 USD Received 30 Nov 2010; revised 14 Jan 2011; accepted 17 Jan 2011; published 7 Mar 2011

shows the calculated spectral shape and illustrates how this shape evolves into a smooth top-hat spectrum with increasing gain.

We succeeded in compressing these spectrally shaped, amplified pulses with 66 % efficiency to 900 fs with 200 mJ. In a Treacy type grating compressor [16] with 6 m grating separation, gratings with the same grating period as in the stretcher are utilized. As shown in Fig. 1 we use a reverse configuration, meaning that the incident beam has a smaller angle to the grating normal than the diffracted one. The grating angles were optimized for shortest pulses and the implemented Dazzler enables us to correct for higher order phases.

The compressed pulse duration is measured by a home-built single-shot second-order autocorrelator with a tuning window of 6 ps and a pixel resolution of 22 fs. This device is designed to measure 700 fs pulses with 6 % accuracy. For 1000 shots the autocorrelation traces are measured the mean width is 1.21 ps with a standard deviation of 0.04ps. The measured autocorrelation trace is shown in Fig. 5.

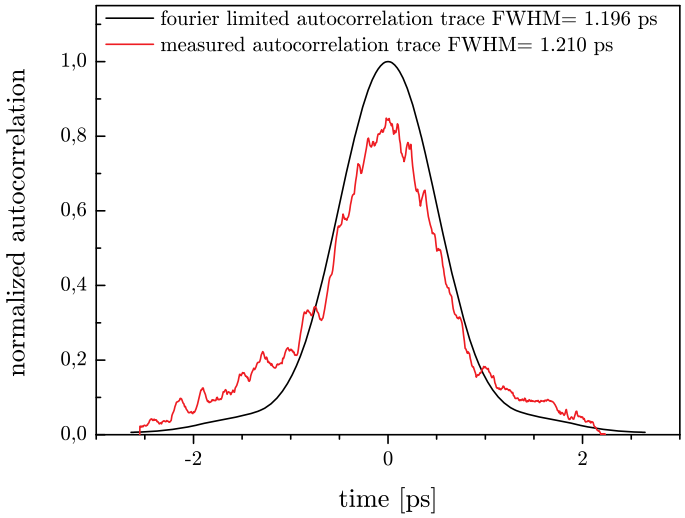

Fig. 5. Calculated autocorrelation trace for the Fourier-limited pulse (black) and measured autocorrelation trace (red). The latter one is normalized to to enclose the same area as the calculated autocorrelation trace. The corresponding pulse length is 884 fs and 895 ps, respectively.

The fourier limited pulse shape and the corresponding autocorrelation trace are calculated from the measured spectrum. From this we have inferred a deconvolution factor between the pulse duration and the width of the autocorrelation trace of 1.3518 for this particular case. Using this factor we can obtain a realistic estimate for our compressed pulse duration which turns out to be 895 fs (transform limit 884 fs) with a measurement uncertainty of 40 fs. As can be seen in Fig. 5 the autocorrelation trace is slightly asymmetric, which is most likely caused by an imperfect beam profile in the autocorrelator. Although the main pulse is close to fourier limited FWHM, there are large side wings which could be explained by uncompensated higher order dispersion. Another possibility could be spatio-temporal coupling caused by B-integral issues when the compressed pulse propagates in several meters air after the last grating. This problem will be solved by a vacuum chamber for the compressor, which is currently under construction.

In a 5 mm type 2 DKDP crystal frequency doubling with 40% conversion efficiency is achieved so far. We therefore have 80 mJ pulse energy in the green, which is sufficient for pumping the first two to three OPA stages. The beam profile of the frequency doubled beam at

#138831 - $15.00 USD Received 30 Nov 2010; revised 14 Jan 2011; accepted 17 Jan 2011; published 7 Mar 2011

the position of the first OPA stage is shown in Fig. 2(c).

Another important aspect for short pulse pumped OPCPA is the timing jitter between pump and seed pulses. In our case the pulse length is 1ps and therefore a timing jitter at least 100 fs is desired for reliable operation of the OPCPA process. We measured the timing jitter in a single-shot cross-correlation experiment between the 30 fs, 800 nm pulse (representing the timing of the OPCPA seed) and the compressed pulses (1030 nm) in a 1 mm BBO crystal. The relative position of the correlation traces on the camera can be converted to a relative timing between the pulses. On a 10 s timescale, a jitter of 273 fs standard deviation was measured. We believe, these timing fluctuations mainly originate from air turbulences, and the mechanical instability of different optical components in the pump laser chain. A more extensive analysis of the jitter is under way in order to find out where exactly this jitter originates from. Preliminary results show, that active stabilization allows for a timing jitter of less than 100fs.

4. Summary

In summary we showed amplification in Yb:YAG up to 300 mJ pulse energy at 10 Hz repetition rate with an unprecedented spectral bandwidth of 3.5 nm. This was realized by spectral amplitude shaping using a SLM to counteract gain narrowing. In our system we demonstrated the operation of a sub-ps CPA laser system based on Yb:YAG at an energy level of up to 200 mJ for the first time. We have therefore demonstrated, to our knowledge, the highest-peakpower pulses ($\approx$160GW) generated in a Yb:YAG laser to date. From a gain-narrowing point-of-view, these results can be scaled to the 50 J-level, as predicted by our simulations. In order to obtain the best possible efficiency for the frequency doubling stage and therefore the highest possible pulse energy in the green, some additional optimization will have to be performed. The laser system described in this manuscript fulfills the requirements and is currently being used to drive the next important step in the PFS-project, namely the development of the first OPA-stage.

Acknowledgments

The authors appreciate the support of the Max-Planck Society.

#138831 - $15.00 USD Received 30 Nov 2010; revised 14 Jan 2011; accepted 17 Jan 2011; published 7 Mar 2011

EXPERIMENTAL AND THEORETICAL INVESTIGATION OF TIMING JITTER INSIDE A STRETCHER-COMPRESSOR SETUP

Experimental and theoretical investigation of timing jitter inside a stretcher-compressor setup

Sandro Klingebiel,[1,5,*] **Izhar Ahmad,**[1,3,4,5] **Christoph Wandt,**[1] **Christoph Skrobol,**[1] **Sergei A. Trushin,**[1] **Zsuzsanna Major,**[1,2] **Ferenc Krausz,**[1,2] **and Stefan Karsch**[1,2]

[1]*Max-Planck-Institut für Quantenoptik, Hans-Kopfermann-Str. 1, D-85748 Garching, Germany*
[2]*Department für Physik, Ludwig-Maximilians-Universität München, Am Coulombwall 1, D-85748 Garching, Germany*
[3]*Optics Laboratories, PO 1021, Nilore, Islamabad, Pakistan*
[4] *izhar916@yahoo.com*
[5]*These authors contributed equally to this work*
[*]*sandro.klingebiel@mpq.mpg.de*

Abstract: In an optically synchronized short-pulse optical-parametric chirped-pulse amplification (OPCPA) system, we observe a few-100 fs-scale timing jitter. With an active timing stabilization system slow fluctuations are removed and the timing jitter can be reduced to 100 fs standard deviation (Std). As the main source for the timing fluctuations we could identify air turbulence in the stretcher-compressor setup inside the chirped pulse amplification (CPA) pump chain. This observation is supported by theoretical investigation of group delay changes for angular deviations occurring between the parallel gratings of a compressor or stretcher, as they can be introduced by air turbulence.

OCIS codes: (320.7120) Ultrafast phenomena; (320.5520) Pulse compression; (190.4970) Parametric oscillators and amplifiers; (140.3615) Lasers, ytterbium.

References and links

1. O. V. Chekhlov, J. L. Collier, I. N. Ross, P. K. Bates, M. Notley, C. Hernandez-Gomez, W. Shaikh, C. N. Dan-son, D. Neely, P. Matousek, S. Hancock, and L. Cardoso, "35 J broadband femtosecond optical parametric chirped pulse amplification system," Opt. Lett. **31**, 3665–3667 (2006).
2. V. V. Lozhkarev, G. I. Freidman, V. N. Ginzburg, E. V. Katin, E. A. Khazanov, A. V. Kirsanov, G. A. Luchinin, A. N. Malshakov, M. A. Martyanov, O. V. Palashov, A. K. Poteomkin, A. M. Sergeev, A. A. Shaykin, and I. V. Yakovlev, "Compact 0.56 petawatt laser system based on optical parametric chirped pulse amplification in KD*P crystals," Laser Phys. Lett. **4**, 421–427 (2007).
3. D. Herrmann, L. Veisz, R. Tautz, F. Tavella, K. Schmid, V. Pervak, and F. Krausz, "Generation of sub-threecycle, 16 TW light pulses by using noncollinear optical parametric chirped-pulse amplification," Opt. Lett. **34**, 2459–2461 (2009).
4. P. Dietrich, F. Krausz, and P. B. Corkum, "Determining the absolute carrier phase of a few-cycle laser pulse," Opt. Lett. **25**, 16–18 (2000).
5. S. Karsch, Zs. Major, J. Fülöp, I. Ahmad, T. Wang, A. Henig, S. Kruber, R. Weingartner, M. Siebold, J. Hein, Chr. Wandt, S. Klingebiel, J. Osterhoff, R. Hörlein, and F. Krausz, "The petawatt field synthesizer: a new approach to ultrahigh field generation," in Advanced Solid-State Photonics, OSA Technical Digest Series (CD) (Optical Society of America, 2008), paper WF1.
6. Zs. Major, S. A. Trushin, I. Ahmad, M. Siebold, Chr. Wandt, S. Klingebiel, T.-J. Wang, J. A. Fülöp, A. Henig, S. Kruber, R. Weingartner, A. Popp, J. Osterhoff, R. Hörlein, J. Hein, V. Pervak, A. Apolonski, F. Krausz, and

#157597 - $15.00 USD Received 3 Nov 2011; revised 2 Dec 2011; accepted 3 Dec 2011; published 30 Jan 2012

S. Karsch, "Basic concepts and current status of the petawatt field synthesizer-a new approach to ultrahigh field generation," Rev. Laser Eng. **37**, 431–436 (2009).
7. I. Ahmad, S. A. Trushin, Zs. Major, Chr.Wandt, S. Klingebiel, T.-J. Wang, V. Pervak, A. Popp, M. Siebold, F. Krausz, and S. Karsch, "Frontend light source for short-pulse pumped OPCPA system," Appl. Phys. B **97**, 529–536 (2009).
8. D. Strickland and G. Mourou, "Compression of amplified chirped optical pulses," Opt. Commun. **55**, 447–449 (1985).
9. S. Klingebiel, Chr. Wandt, C. Skrobol, I. Ahmad, S. A. Trushin, Zs. Major, F. Krausz, and S. Karsch, "High energy picosecond Yb:YAG CPA system at 10 Hz repetition rate for pumping optical parametric amplifiers," Opt. Express **19**, 5357–5363 (2011).
10. N. Ishii, L. Turi, V. S. Yakovlev, T. Fuji, F. Krausz, A. Baltuska, R. Butkus, G. Veitas, V. Smilgevicius, R. Danielius, and A. Piskarskas, "Multimillijoule chirped parametric amplification of few-cycle pulses," Opt. Lett. **30**(5), 567–569 (2005).
11. C. P. Hauri, P. Schlup, G. Arisholm, J. Biegert, and U. Keller, "Phase-preserving chirped-pulse optical parametric amplification to 17.3 fs directly from a Ti:sapphire oscillator," Opt. Lett. **29**(12), 1369–1371 (2004).
12. D. Yoshitomi, X. Zhou, Y. Kobayashi, H. Takada, and K. Torizuka, "Long-term stable passive synchronization of 50 μJ femtosecond Yb-doped fiber chirped-pulse amplifier with a mode-locked Ti:sapphire laser," Opt. Express **18**, 26027–26036 (2010).
13. C. Y. Teisset, N. Ishii, T. Fuji, T. Metzger, S. Köhler, R. Holzwarth, A. Baltuska, A. M. Zheltikov, and F. Krausz, "Soliton-based pump-seed synchronization for few-cycle OPCPA," Opt. Express **13**(17), 6550–6557 (2005).
14. E. Treacy, "Optical pulse compression with diffraction gratings," IEEE J. Quantum Electron. **5**, 454–458 (1969).
15. I. Ahmad, L Berge, Zs. Major, F. Krausz, S. Karsch, and S. A. Trushin, "Redshift of few-cycle infrared pulses in the filamentation regime," New J. Phys. **13**, 093005 (2011).
16. P. S. Banks, M. D. Perry, V. Yanovsky, S. N. Fochs, B. C. Stuart, and J. Zweiback, "Novel all-reflective stretcher for chirped-pulse amplification of ultrashort pulses," IEEE J. Quantum Electron. **36**, 268–274 (2000).
17. T. Miura, K. Kobayashi, K. Takasago, Z. Zhang, K. Torizuka, and F. Kannari, "Timing jitter in a kilohertz regenerative amplifier of a femtosecond-pulse Ti:Al2O3 laser," Opt. Lett. **25**, 1795–1797 (2000).
18. G. Pretzler, A. Kasper, and K. J. Witte, "Angular chirp and tilted light pulses in CPA lasers," Appl. Phys. B **70**, 1–9 (2000).
19. O. E. Martinez, "3000 times grating compressor with positive group velocity dispersion: application to fiber compensation in $1.3-1.6\,\mu m$ region," IEEE J. Quantum Electron. **23**, 59–64 (1987).
20. F. Adler, A. Sell, F. Sotier, R. Huber, and A. Leitenstorfer, "Attosecond relative timing jitter and 13 fs tunable pulses from a two-branch Er:fiber laser," Opt. Lett. **32**, 3504–3506 (2007).
21. Q. Hao, W. Li, and H. Zeng, "High-power Yb-doped fiber amplification synchronized with a few-cycle Ti:sapphire laser," Opt. Express **17**, 5815–5821 (2009).

1. Introduction

State-of-the-art high-energy optical parametric chirped pulse amplification (OPCPA) systems are usually operated with stretched pulse durations in the range of 100 ps - ns (cf. Ref. [1–3]). In contrast to that the short-pulse OPCPA scheme uses much shorter pulses on the order of 1 ps. This significantly increases the pump power and permits the use of thinner OPA crystals while keeping the same level of gain, which implies an increase of amplification bandwidth as compared with OPA driven by longer pulses. Additionally the short pump-pulse duration reduces the necessary stretching factor for the broadband-seed pulse, thereby increasing stretching and compression fidelity and allowing the use of simple, high-throughput stretcher-compressor systems, consisting of bulk glass and chirped multilayer mirrors. Furthermore, the technique of few-ps OPCPA possesses immense potential for generating high contrast pulses due to the short, ps-scale time window for the parametric fluorescence. Nevertheless the high-energy pump laser is not commercially available and therefore needs to be developed.

The Petawatt Field Synthesizer (PFS) is based on the above introduced short-pulse OPCPA scheme. The PFS project aims at developing a petawatt-scale carrier-envelope phase [4] controlled light source to deliver pulses with energies of > 3 J in the few-cycle regime (< 5 fs, $700-1400$ nm) at a repetition rate of 10 Hz [5–7]. The PFS design with several OPCPA stages requires a special, synchronized pump delivering $1-2$ ps pulses with 4×5 J pulse energy (frequency doubled at 515 nm), i.e. 4×12 Joule in the fundamental beam (1030 nm) at 10 Hz repetition rate. The pump source with these specifications is based on the chirped-pulse ampli-

#157597 - $15.00 USD Received 3 Nov 2011; revised 2 Dec 2011; accepted 3 Dec 2011; published 30 Jan 2012

fication (CPA) principle [8] using Yb:YAG as the amplification medium pumped by high power laser diodes. At present, this source is capable of delivering 200 mJ pulses at 1030 nm with a compressed pulse duration of ≈ 1 ps [9].

Precise synchronization between pump and seed pulse is a prerequisite for stable amplification in the OPCPA stages, since the pulses are only 1 ps long. Simulations of the OPCPA amplification show, that 150fs timing jitter could result in significant spectral changes in the amplified signal, while the Fourier-limited pulse length changes only by 4%. Therefore we consider 150 fs as a tolerable upper limit for the timing jitter in a 1 ps OPCPA stage.

Different active, e.g Ref. [10], and passive optical synchronization schemes such as direct seeding [11], injection seeding [12] and frequency shifting using a photonic crystal fiber (PCF) [13] have already been developed, which allow for few-fs jitter between different amplifier chains. We apply the latter technique to derive both pump and seed pulses from the same oscillator. The initially synchronized pump beam has to be amplified prior to the OPCPA stage. In these amplifiers the pulse propagates along a significantly longer path than the seed pulses. This additional optical path amounts to several 100m in our case and makes the setup highly sensitive to mechanical vibrations and air fluctuations as sources of timing jitter. Therefore it is important to check the temporal synchronization at the position of the OPCPA stages.

In this paper we present the results of single-shot measurements of the relative timing between the pump and the seed pulses at 10 Hz repetition rate in order to quantify the level of synchronization in our experimental setup. Additionally we applied an active stabilization stage to reduce the jitter to 100 fs. We could identify air turbulence inside the stretcher-compressor setup of the CPA pump laser as the main source of the timing jitter by performing several measurements at different stages in the CPA pump laser chain. In order to investigate the influence of air fluctuations inside the stretcher/compressor on the timing of the pulse theoretically, we performed calculations for the optical path length with a small perturbation of the beam pointing inside a Treacy-type compressor [14].

2. Experimental setup

The schematic layout of our system is shown in Fig. 1. In order to achieve optical synchronization, both seed and pump pulses are derived from a common Ti:sapphire oscillator (*Rainbow, Femtolasers GmbH*), which serves as the master oscillator. For the generation of the OPCPA seed, a fraction of the oscillator output is amplified in a commercial Ti:sa amplifier (*Femtopower Compact-Pro, Femtolasers GmbH*) and subsequentially compressed in a hybrid pulse compressor (HPC). The output of the HPC is used for generating a broadband supercontinuum by a two-stage spectral broadening technique. Details about the OPCPA seed generation are described in [7, 15]. The near-infrared spectral part (700 nm to 1400 nm) of this supercontinuum is then stretched to approximately 1 ps for seeding the first stage of the main OPCPA chain, which is under construction. For the OPCPA pump generation, a part of the oscillator output is spectrally shifted to 1030 nm in a PCF and amplified in a two-stage fiber amplifier to 1 W. In order to stretch the narrow bandwidth (ca. 4nm) pulses to 3ns we apply an all reflective stretcher [16] in a double-pass configuration (i.e. 8 reflections off the grating). After stretching, the amplification takes place in an Yb:glass regenerative amplifier (regen) followed by a multi-pass amplifier based on Yb:YAG, both of which are diode-pumped. The compression is realized with a Treacy-type compressor [14] with a large grating separation of 6 m, using the same gratings as in the stretcher (1740 lines/mm). After compression an energy of 200 mJ is delivered within 1 ps pulse duration. A more detailed description of the setup can be found in [9].

The path through the CPA pump chain would result in a total optical delay of $\approx 1\,\mu$s between the OPCPA pump and the seed at the position of the first OPCPA stage. In order to compensate

#157597 - $15.00 USD Received 3 Nov 2011; revised 2 Dec 2011; accepted 3 Dec 2011; published 30 Jan 2012

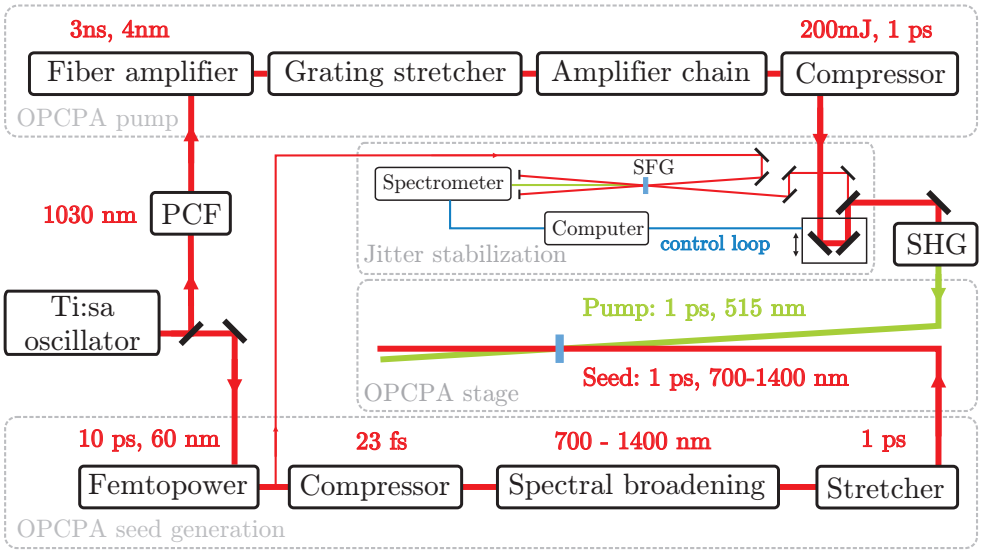

Fig. 1. (Color online) Schematic layout for the generation of the broadband seed and the synchronized pump for the broadband short-pulse OPCPA. PCF: photonic crystal fiber; SHG: second harmonic generation; SFG: sum frequency generation; Femtopower: Ti:sa amplifier (Femtolasers GmbH).

for this delay, the pulses for the pump and the seed chains are selected from the master oscillator at different times. In this scheme, the sources of possible timing fluctuation between the two pulses can be the finite stability of the repetition rate of the master oscillator, temperature drifts, air turbulences and mechanical vibrations of optical components over this rather long optical path of the pump pulse.

It should be noted, that all our optical tables are equipped with flow boxes and are enclosed by a housing. Inside this housing subunits such as the stretcher, regen, multipass amplifier are covered in separate boxes, which are not air-tight, but provide isolation from the ambient air turbulences to some extent. Due to its size ($6.5 \times 1.5 \times 0.7$ m^3), the compressor is currently not separately covered.

3. Measurement of the timing jitter

In order to quantify the level of synchronization in the above described setup we performed single-shot measurements of the relative timing between the pump and the seed pulses. For this purpose we apply a modified cross-correlation technique (cf.2 a), first proposed by Miura [17]. Using this technique, the relative timing between a compressed pulse and a linearly chirped pulse can be measured with fs resolution via sum frequency generation (SFG). For this we use the compressed 1 ps long pump pulse before it is frequency doubled, i.e. at 1030 nm. The reference pulse is split off from the Femtopower amplifier before compression and hence has a duration of 10 ps and a bandwidth of 60 nm (cf. Fig 1).

The spectrum of the SFG signal is measured using a high-resolution spectrometer (*Avantes AvaSpec-2048*). The accuracy of the measurement is determined by the resolution of the spectrometer (0.06 nm) and by the chirp of the reference pulse. Determination of the centroid wavelength can be done with sub-pixel resolution resulting in an improved accuracy of approximately 10 fs in our case. In order to calibrate the measurement, we set different known delays

#157597 - $15.00 USD Received 3 Nov 2011; revised 2 Dec 2011; accepted 3 Dec 2011; published 30 Jan 2012

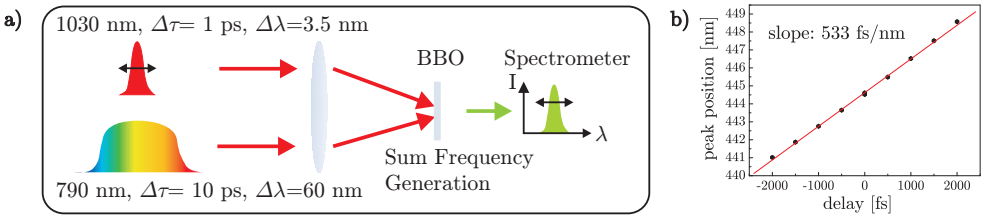

Fig. 2. a) Schematic picture of the modified cross-correlation technique [17]. The spectrum of the sum frequency signal between the short pump pulse and a long, chirped reference pulse is measured. The relative arrival time of the pulses is transformed into a frequency change of the sum frequency signal. b) Calibration curve for the used setup. The centroid of the sum frequency signal is measured at different relative delays.

between the pulses and measured the centroid of the spectrum. In Fig. 2(b) the calibration curve for the lowest jitter pulses (compare Fig. 3(b)) is shown. Each point is the mean value of 100 shots and the standard deviation is too small to resolve the error bars in the plot. For delays larger than 1 ps one can observe a deviation from the linear fit, which could be explained by higher order dispersion in the chirped pulse. In this delay range, a higher order fit would be more accurate. Nevertheless in the central part ($\pm$1 ps), where we work, the linear fit is sufficiently accurate and no correction is needed. The calibration factor of 533 fs/nm of the linear fit is used for all of the following measurements.

4. Experimental results and discussion

Our findings are summarized in Fig. 3. The measured fluctuation of the relative timing between pump and seed are shown in Fig. 3(a). Here the pump pulse is stretched, fully amplified in the regenerative and multipass amplifiers and subsequently compressed. For this measurement no precautions were taken to reduce air fluctuations, i.e. the flowboxes were running. We find that the timing jitter has a standard deviation of 400 fs, which would be unacceptable for proceeding with the short-pulse pumped OPCPA experiments.

In order to determine the source of this measured rather large temporal oscillation, we studied the effect of the different components of the CPA pump-laser chain. First, we bypassed the stretcher-compressor setup and amplified the unstretched pulses (ca. 4 ps) in the regen to a low power level. The relative timing was then measured between the reference and the pulses amplified in the regen in case when i) the same pulses, and ii) different pulses with approximately 1 μs delay (this delay is expected for the full amplifier chain including stretcher and compressor) were selected from the master oscillator for both chains. The appropriate optical delay is achieved by adjusting the number of round trips in the regen.

As depicted in Fig. 3(b), when the same pulses were selected for amplification in pump- and seed-chains (red curve), the jitter is hardly above the resolution of our measurement system. In the case with 1 μs delay (black curve) one could expect different sources of jitter. On the one hand the repetition rate instability of the master oscillator introduces a jitter between the two selected pulses. Although the oscillator repetition rate is not stabilized, a low temporal jitter can be expected on a s timescale since the main causes for the change of the repetition rate, acoustic noise (1kHz-100Hz) and thermal fluctuations (1 Hz and below) act on a much slower timescale. On the other hand also the regen introduces optical delay fraught with jitter. Although both sources can not be distinguished by the described measurement, together they account for a few-10 femtosecond jitter. This is close to the resolution limit of our measurement setup, and is clearly well below our tolerable limit for the short-pulse pumped OPCPA. This

#157597 - $15.00 USD Received 3 Nov 2011; revised 2 Dec 2011; accepted 3 Dec 2011; published 30 Jan 2012

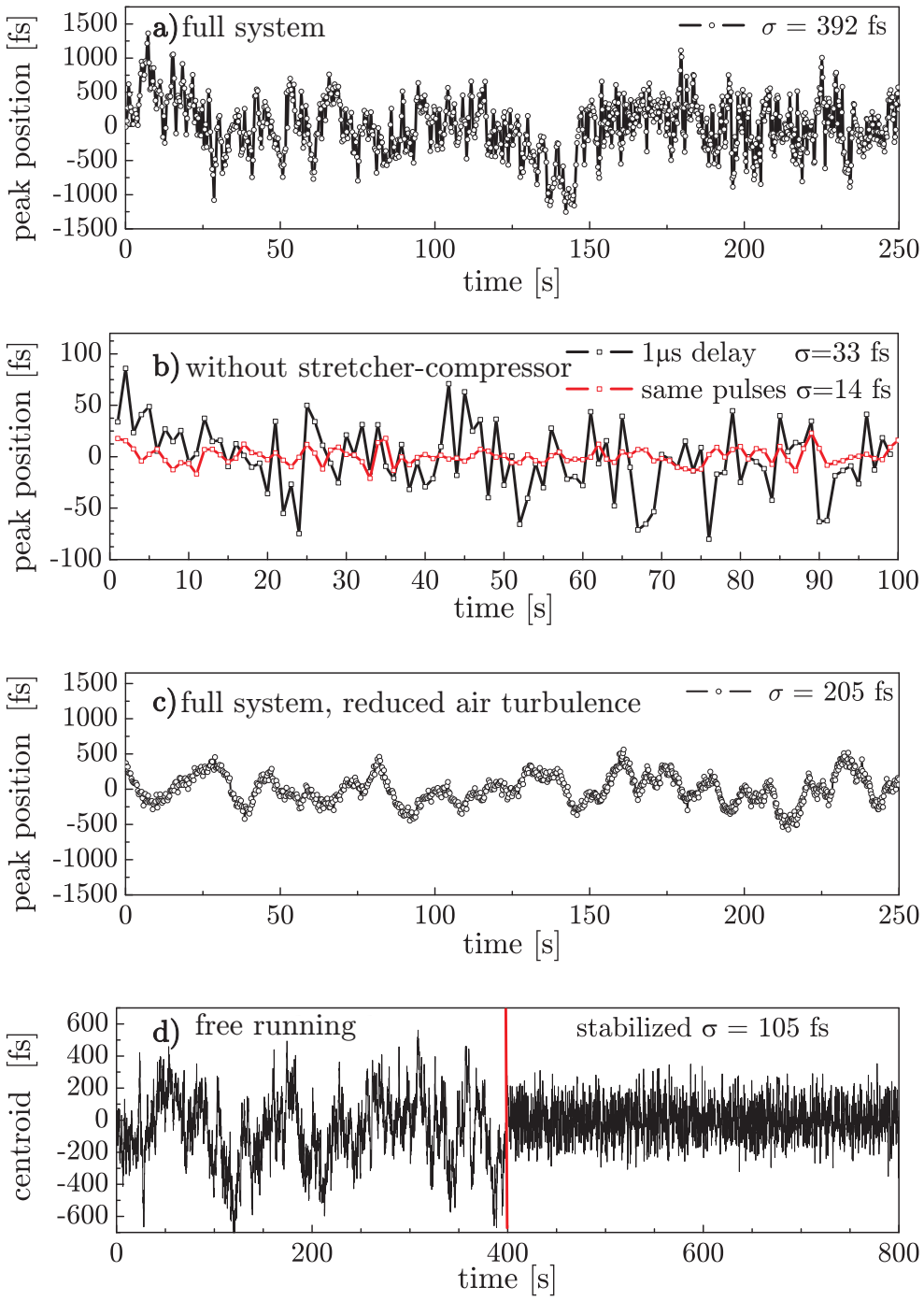

Fig. 3. Results of timing jitter measurements a) Pump pulse passes through the entire CPA chain: ±400 fs timing jitter. b) Timing jitter when stretcher/compressor are bypassed: ±14 fs when the same pulses are used from the master oscillator; ±33 fs with 1 μs delay. c) Pump pulse passes through entire CPA chain with precautions to reduce air turbulence: timing jitter consists of ±70 fs shot-to-shot fluctuation and ±200 fs slow oscillations. d) comparison between free running (left) and actively stabilized timing jitter (right).

#157597 - $15.00 USD Received 3 Nov 2011; revised 2 Dec 2011; accepted 3 Dec 2011; published 30 Jan 2012

means that the optical delay inside the regenerative amplifier has much less influence on the timing fluctuations compared to the same optical delay generated inside a stretcher-compressor setup. We can therefore conclude that the large timing oscillations, shown in Fig. 3(a) arise from the stretcher-compressor setup. We believe that the mechanical instabilities of different optomechanical components and air fluctuations along the long propagation distance contribute strongly to this timing instability. This argument is supported by Fig. 3(c), which shows again the pass through the whole pump-laser chain. But this time with precautions taken to reduce air turbulences: the flowboxes are turned off, the stretcher box is sealed more carefully and beam tubes are installed inside the compressor. This measurement can be directly compared to Fig. 3(a) and shows a significantly improved timing jitter. The reduced jitter enables us to see two separate components to the remaining timing jitter: a shot-to-shot variation of ± 70 fs superimposed on a slow temporal drift of ± 200 fs.

An active stabilization system can easily correct for this large amplitude, slow fluctuation. In our active stabilization scheme we take the centroid wavelength of the SFG spectra on every shot, calculate the difference to a reference wavelength and move a delay stage (in the pump-chain cf. Fig. 1) to return to the reference position in cases, when the difference exceeds a certain value. This threshold is a parameter to optimize the active stabilization. If the threshold is too close to the shot to shot noise level, the delay stage will move on nearly every shot and the stabilization will become unstable. In the experiment, it was shown that the stabilization currently works best with this limit set to 100 fs. In this case we can stabilize the jitter to 105 fs Std, as shown in Fig. 3(d). This is sufficiently low for carrying out the first OPCPA experiments.

5. Theoretical considerations for optical path length inside a stretcher/compressor

The experiments indicated that the optical delay inside the stretcher-compressor setup is fraught with a much larger timing jitter compared to the same optical delay inside the regenerative amplifier. Furthermore it was shown that reducing the air turbulence resulted in a significant decrease of the timing jitter. In this section we will discuss the effect of turbulent air flow on the optical path length differences theoretically. The main feature of turbulent air is an inhomogeneous density which causes local refractive index gradients. A passing light beam will be refracted on such a refractive index step and is slightly deflected. For example a simulation for dry air at constant pressure shows, that a temperature change of 0.1K at room temperature can cause deflections in the range of μrad, if grazing incidence is considered. As many of these inhomogeneities are distributed randomly over the entire path length, we model the effect of turbulent air by assuming a mean angular deviation occurring at a mean position throughout the following analysis

At first let us consider a free-space propagation with the speed of light c over the distance x and a distance x_1 with a small angle difference $\Delta\alpha$ (compare Fig. 4). The timing difference can be calculated as

$$\Delta\tau = \frac{x_1 - x}{c} = \frac{x}{c}\left(\frac{1}{cos(\Delta\alpha)} - 1\right) \approx \frac{x \cdot \Delta\alpha^2}{2c} \tag{1}$$

For relatively large values $x = 100$ m and $\Delta\alpha = 10\,\mu$rad one obtains $\Delta\tau = 0.017$ fs and can therefore neglect this timing change for probably all experimentally relevant cases in the laboratory.

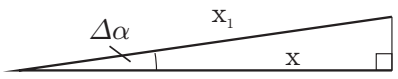

Fig. 4. Schematic picture for calculating the timing difference of light traveling along the paths x and x_1.

#157597 - $15.00 USD Received 3 Nov 2011; revised 2 Dec 2011; accepted 3 Dec 2011; published 30 Jan 2012

In the following we will discuss the influence of beam pointing fluctuations on the optical path length inside a compressor. We derive the analytical expression for the path length difference as a function of the angle deviation $\Delta\beta$ and the location of this angle change d for the general case, with a few μrad angle deviation originating inside the compressor. Additionally, the special case of beam pointing of few μrad at the compressor input is discussed.

In most systems, the compressor is located in vacuum in order to avoid nonlinearities in air (our compressor is not vacuum sealed, yet). Therefore, the stretcher will be the most likely source of perturbations by air fluctuations. Nevertheless, we will analyze a compressor because the optical path is more easy to explain. These considerations are also valid for the stretcher setup, as the stretcher provides the same amount of dispersion but with opposite sign. However, the additional imaging system increases the optical path compared to the compressor, making the stretcher even more sensitive to air turbulence.

In the following we investigate the influence of a perturbation of the angle inside the compressor. Fig. 5 shows a double-grating double-pass Treacy compressor setup with a grating separation L_1, aligned for an angle of incidence (AOI) α. The optical path of a ray with wavelength λ_0 and AOI of α is shown in red. The diffraction from the first grating is given by the grating equation

$$\beta = \arcsin(mN\lambda_0 - \sin\alpha). \tag{2}$$

where N is the line density, λ_0 is the center wavelength and m is the diffraction order. As the AOI on the second grating is β the beam diffracts at an angle α and impinges perpendicular on the end mirror from where it takes the same path back through the compressor.

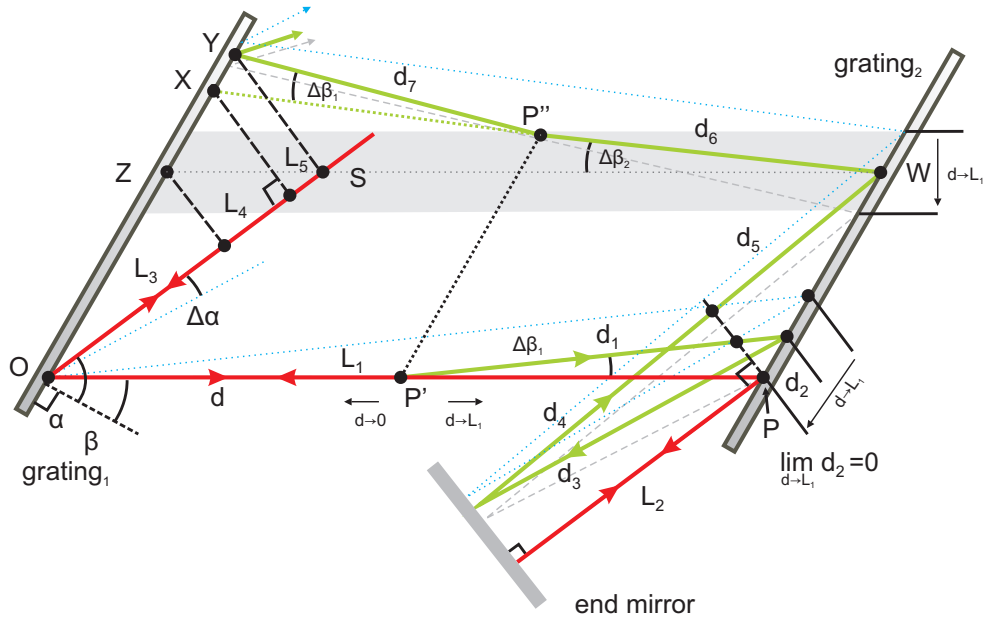

Fig. 5. Ray diagram illustrating the change in the optical path inside the grating compressor for the center wavelength λ_0. The red ray shows the undisturbed case with an AOI of α. The green curve depicts the beam path of the pulse for the case when it is distorted at an angle $\beta + \Delta\beta_1$ at a distance d from the first grating. The blue, dotted and the gray, dashed traces show the extreme cases $d = 0$ and $d = L_1$, respectively. The case $d = 0$ corresponds to a different AOI of $\alpha - \Delta\alpha$ at the compressor input. For detailed explanation see main text.

#157597 - $15.00 USD Received 3 Nov 2011; revised 2 Dec 2011; accepted 3 Dec 2011; published 30 Jan 2012

A shot-to-shot pointing fluctuation inside the dispersion plane of the compressor can be described as a deviation $\Delta\beta_1$ from the design angle β which leads to a non-zero AOI on the end mirror of $\Delta\alpha$. This in turn results in a different path (and angle) for the first pass ($\beta + \Delta\beta_1$) and the return pass through the compressor ($\beta - \Delta\beta_2$), as shown in Fig. 5 (green). The location where the angle change takes place is parametrized with the parameter d. The extreme case $d = 0$ represents beam pointing at the compressor input O (or pointing with $\Delta\alpha$ outside the compressor), and $d = L_1$ stands for fluctuations at the position of the second grating. The angle change represents air fluctuations, which can be considered static on the time scale of a propagating light pulse. In Fig. 5 the angle deviations are magnified to better distinguish the different paths. In reality the points P' and P'' are closely adjacent. Therefore the same deviation as on point P' is present on the way back through the system at point P''. (In the case when $d = 0$, P'' is on the first grating and would result in a small angle change of the outgoing beam. This effect is not relevant for the timing and is therefore neglected.)

The optical path lengths between point O and plane YS for the aligned and the slightly perturbed case are given by

$$p(\beta) = L_1 + L_2 + L_2 + L_1 + L_3 + L_4 + L_5 \text{ , and} \tag{3}$$

$$p(\beta + \Delta\beta_1) = d + d_1 + d_2 + d_3 + d_4 + d_5 + d_6 + d_7 \text{ , respectively.} \tag{4}$$

The timing difference can then be calculated by $\Delta\tau = (p(\beta) - p(\beta + \Delta\beta_1))/c$. The paths L_1 and L_2 are given by the compressor design, d is a parameter and the other path lengths can be obtained from general trigonometric relations in Fig. 5:

$$d_1 = (L_1 - d)\frac{\cos\beta}{\cos(\beta + \Delta\beta_1)} \tag{5}$$

$$d_2 = (L_1 - d)\frac{\sin(\Delta\beta_1)}{\cos(\beta + \Delta\beta_1)}\frac{\sin\alpha}{\cos(\Delta\alpha)} \tag{6}$$

$$d_3 = d_4 = \frac{L_2}{\cos(\Delta\alpha)} \tag{7}$$

$$d_5 = (d_2 + d_3)\frac{\cos(\alpha - \Delta\alpha)}{\cos(\alpha + \Delta\alpha)} - d_4 \tag{8}$$

$$d_6 = (L_1 - d)\frac{\cos\beta}{\cos(\beta - \Delta\beta_2)} \tag{9}$$

$$d_7 = d\frac{\cos\beta}{\cos(\beta - \Delta\beta_1 - \Delta\beta_2)} \tag{10}$$

$$L_3 = d_5\cos(\Delta\alpha) \tag{11}$$

$$L_4 = L_1\frac{\sin(\Delta\beta_2)}{\cos(\beta - \Delta\beta_2)}\sin\alpha \tag{12}$$

$$L_5 = d\frac{\cos\beta}{\cos(\beta - \Delta\beta_2)} \cdot \frac{\sin(\Delta\beta_1)}{\cos(\beta - \Delta\beta_1 - \Delta\beta_2)}\sin\alpha \tag{13}$$

The contribution to the timing difference from $2L_2 - d_3 - d_4$ has the same form as in the free space case, discussed above (Eq. (1)), and can therefore be neglected. In this approximation, the timing difference is independent of the distance of the end mirror to the second grating L_2. For the same reason $L_3 - d_5$, which accounts for a parallel offset of plane $\overline{OP}$ and $\overline{WZ}$, has a

#157597 - $15.00 USD Received 3 Nov 2011; revised 2 Dec 2011; accepted 3 Dec 2011; published 30 Jan 2012

negligible effect on the timing difference. The total timing difference can then be written:

$$\begin{aligned}\Delta\tau &= \frac{1}{c}(2L_1 - d - d_1 - d_6 + L_4 - d_2 + L_5 - d_7) \quad (14)\\ &= \frac{L_1}{c}\left(2 - \frac{\cos\beta + \sin(\Delta\beta_1)\sin\alpha}{\cos(\beta+\Delta\beta_1)} - \frac{\cos\beta - \sin(\Delta\beta_2)\sin\alpha}{\cos(\beta-\Delta\beta_2)}\right)\\ &+ \frac{d}{c}\left(\frac{\cos\beta + \sin(\Delta\beta_1)\sin\alpha}{\cos(\beta+\Delta\beta_1)} - 1\right)\\ &+ \frac{d}{c}\left(\frac{\cos\beta}{\cos(\beta-\Delta\beta_2)}\left[1 - \frac{\cos(\beta-\Delta\beta_2) - \sin(\Delta\beta_1)\sin\alpha}{\cos(\beta-\Delta\beta_1-\Delta\beta_2)}\right]\right) \quad (15)\end{aligned}$$

With the help of the grating equation (Eq. (2)) we can write $\sin\alpha$ in terms of $\sin\beta$. For small angles $\Delta\beta$ we can approximate $\sin(\Delta\beta) \approx \Delta\beta$ and $\cos(\Delta\beta) \approx 1$. Under this approximation it follows that $\cos(\beta \pm \Delta\beta) \approx \cos\beta \mp \Delta\beta\sin\beta$. Equation (15) can then be approximated as

$$\begin{aligned}\Delta\tau &\approx \frac{L_1 m N \lambda_0}{c}\left(\frac{\Delta\beta_2}{\cos(\beta-\Delta\beta_2)} - \frac{\Delta\beta_1}{\cos(\beta+\Delta\beta_1)}\right)\\ &+ \frac{d m N \lambda_0}{c}\left(\frac{\Delta\beta_1}{\cos(\beta+\Delta\beta_1)}\right)\\ &+ \frac{d m N \lambda_0}{c}\frac{\cos\beta}{\cos(\beta-\Delta\beta_2)}\left(\frac{\Delta\beta_1}{\cos(\beta-\Delta\beta_1-\Delta\beta_2)}\right). \quad (16)\end{aligned}$$

The following calculations are done for the approximated expression (Eq. (16)) as well as for the formula without approximations (Eq. (15)) with the following parameters: $N =$ 1740lines/mm, $\lambda_0 = 1030\,\text{nm}$, $m = 1$, $L_1 = 6\,\text{m}$, $L_2 = 3\,\text{m}$ and $\alpha = 58.5^\circ$, as in the experimental setup. It should be noted, that we are interested in small angle changes (few μrad) which may affect the optical path length, but do not change the pulse length or angular chirp [18] in a significant way.

In these formulae it can be seen, that smaller angles β are favorable in terms of timing difference. Nevertheless, in order to compare the jitter for different angles one has to take into account that the dispersion is also decreasing with decreasing β. Therefore the compressor length should be adapted to compare compressors with the same dispersion. For example our compressor is designed in a reverse configuration where $\alpha < \beta$ ($\alpha = 58.5^\circ$, $\beta = 69.98^\circ$) because in this case the necessary dispersion can be achieved with only $L_1 = 6\,\text{m}$ grating separation. Another option would be the normal configuration with $\alpha = 69.98^\circ$, $\beta = 58.5^\circ$ where a grating separation of $L_1 = 14\,\text{m}$ is needed. This configuration is also considered in the following paragraphs.

5.1. Angle fluctuations at the compressor input

The special case $d = 0$ corresponds to the situation, when there is a certain beam pointing fluctuation $\Delta\alpha$ at the compressor input. This change translates to a fluctuation $\Delta\beta_1$ to the diffracted beam at point O on the first grating. No source of angle fluctuation inside the compressor is considered. For $d = 0$, the last two terms in Eq. (15) and Eq. (16) vanish and Eq. (16) takes the form

$$\begin{aligned}\Delta\tau &= \frac{1}{c}(2L_1 - d_1 - d_6 + L_4 - d_2) \quad (17)\\ &= \frac{L_1 m N \lambda_0}{c}\left(\frac{\Delta\beta_2}{\cos(\beta-\Delta\beta_2)} - \frac{\Delta\beta_1}{\cos(\beta+\Delta\beta_1)}\right) \quad (18)\end{aligned}$$

The effect of angular deviation outside the compressor on the timing is very small because d_1 is a bit longer than L_1 but d_6 is a bit shorter and together they nearly cancel out each other,

#157597 - $15.00 USD Received 3 Nov 2011; revised 2 Dec 2011; accepted 3 Dec 2011; published 30 Jan 2012

i.e. $d_1 + d_6 \approx 2L_1$. Additionally d_2 and L_4 compensate each other, i.e. $d_2 \approx L_4$ (compare Fig. 5, Eqs. (5)–(13)). From Eq. (18) it can be seen that the remaining difference occurs because $\Delta\beta_1 \neq \Delta\beta_2$. This is due to the fact, that the angle $\beta + \Delta\beta$ is transfered to $\beta - \Delta\beta$ after reflection off the end mirror. Thus the effect of angular deviation taking place outside the compressor on the timing is very small.

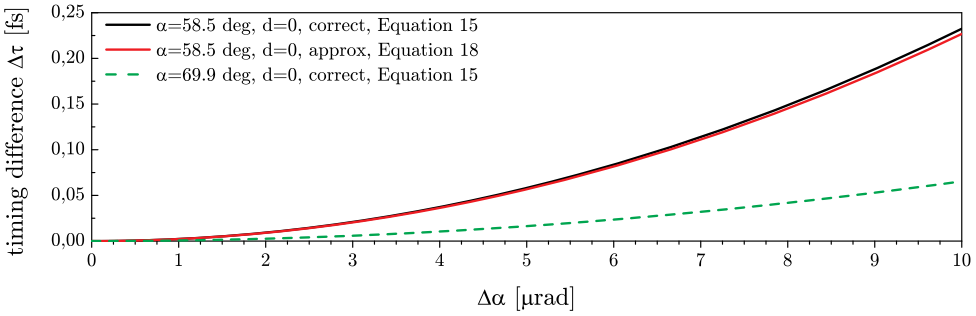

Fig. 6. Timing difference for a small change $\Delta\alpha$ of the AOI α at the compressor input (d=0). Larger angle α (smaller angle β) is advantageous in terms of jitter.

In Fig. 6 the calculated timing jitter due to pointing fluctuations at the compressor input is shown. For pointing fluctuations up to $10\,\mu$rad the timing jitter is less than $0.25\,$fs, which was also checked via ray tracing. We measured the beam pointing at the compressor input to be less than $1\,\mu$rad which corresponds to $0.0025\,$fs jitter. This jitter is negligible in our case. Nevertheless, it should be noted that this timing jitter from angular deviations outside the compressor is two orders of magnitude larger than the effect of the same angle deviation in a freely propagating beam over the same distance (compare Eq. (1)) and that the compressor configuration with $\alpha > \beta$ would have advantages in terms of jitter, even though the grating separation is more than doubled to achieve the same dispersion.

5.2. Angle fluctuations inside the grating compressor

In the previous paragraph we have shown, that angle fluctuations at the compressor input are negligible because all path lengths compensate each other to a large extent. So we will have a look at the influence of angle fluctuations originating inside the compressor. From Fig. 5 one can understand what happens when d is increased, the distances on the way to the end mirror (d_1, d_2) are decreasing and can not compensate for the distances during the back propagation (d_7, L_4, L_5) and the timing difference is drastically increased.

In Eqs. (15) and (16) we can neglect the first term as shown in the previous paragraph. It turns out, that the second and the third term in Eq. (16) both have the same weight. When approximating $\cos(\beta + \Delta\beta) \approx \cos\beta$ we can further simplify Eq. (16) to:

$$\Delta\tau \approx \frac{2\,m\,N\,\lambda_0}{c\,\cos\beta}\,\Delta\beta_1 \cdot d \tag{19}$$

Figure 7(a) shows that the approximations for Eq. (19) are well justified, because deviations from the non-approximated curve are negligible. As predicted by Eq. (19), the linear character in d and $\Delta\beta$ shows clearly in the graphs. Compared to the case with $d = 0$ the jitter is up to 4 orders of magnitude higher (for $d = L_1$) and again the normal configuration with smaller β (larger α) has advantages in terms of sensitivity to timing jitter. Figure 7(b) shows the timing jitter for different positions d. As mentioned earlier the effect of turbulent air is modeled by assuming

#157597 - $15.00 USD Received 3 Nov 2011; revised 2 Dec 2011; accepted 3 Dec 2011; published 30 Jan 2012

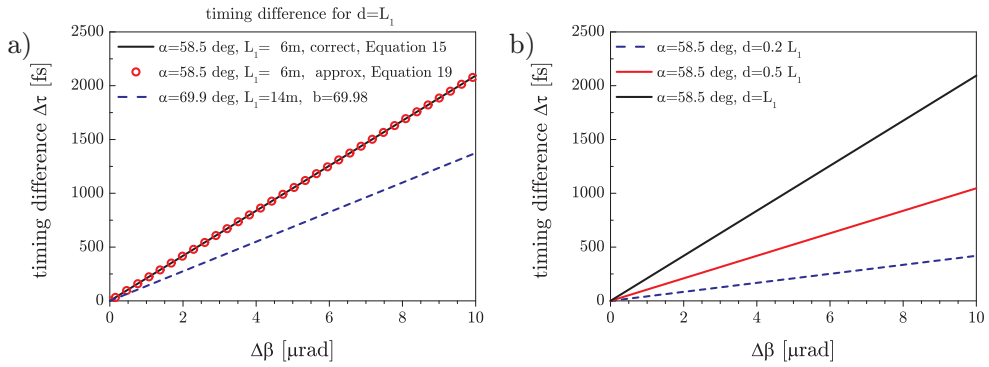

Fig. 7. a) Timing difference for $d = L_1$: the approximations in Eq. (19) are well justified in the considered range. The configuration with increased AOI α (or decreased β) shows reduced timing differences. b) Timing difference for different values of d.

a mean angular deviation at a mean position. Since the mean position is most likely located at $d = 0.5L_1$, the corresponding curve in most suitable to reflect the effect of air turbulence.

As a result of this analysis we can state that a Treacy-type compressor introduces a timing jitter, when a beam pointing is considered. Beam pointing fluctuations at the compressor input are orders of magnitude less critical than those occurring inside the compressor, especially close to the second grating. With this calculation we can explain the effect of beam pointing fluctuations, as could be introduced by air turbulence or mechanical instabilities of optical elements like gratings, mirror or imaging optics (in case of a stretcher). Generally a smaller angle β is preferable in terms of jitter even if a longer path is needed to get the necessary dispersion.

6. Summary

In conclusion, we have quantitatively investigated the level of timing synchronization between the pump and seed pulses of the PFS system, which is currently under development. Additionally an active stabilization system is applied which eliminates the slow drift and reduces the jitter to 100 fs Std. This will enable the first short-pulse pumped OPCPA experiments with our system.

Using the spectral gating technique we succeeded in demonstrating experimentally that the air fluctuations inside the stretcher-compressor setup are the main source of the pump-seed timing jitter. In addition we have provided a theory on timing difference due to angular deviations inside a stretcher/compressor. As the main result the beam pointing fluctuation at the stretcher/compressor input accounts only for less than 0.2 fs jitter whereas angle fluctuations of the same magnitude originating inside the stretcher/compressor can result in up to four orders of magnitude larger jitter, depending on where this perturbation is located inside the compressor. This theory provides a simple formula (Eq. (19)) and can perfectly explain the experimental observations. Although the grating stretcher and compressor were extensively investigated in the past (e.g. [14, 16, 18, 19]), to the best of our knowledge a sensitivity of these components for absolute timing jitter has not been reported up to now. Most probably because timing sensitive applications such as our CPA pumped ps OPCPA have been emerging in the past few years (c.f.: [12, 20, 21]). All these systems are quite different, but have one thing in common: An increased timing jitter after compression at the final stage is measured, compared to an early stage of the setup. With the presented theory it is now possible to explain a major part of the

#157597 - $15.00 USD Received 3 Nov 2011; revised 2 Dec 2011; accepted 3 Dec 2011; published 30 Jan 2012

observed increase in the timing jitter.

Air fluctuations inside a compressor are not relevant in most CPA systems, since usually compressors are situated in vacuum in order to avoid nonlinearities in air. Nevertheless the calculations are also valid for the stretcher. Therefore any air fluctuations or vibrations inside the stretcher should be avoided, if low temporal jitter is required. This means, ideally the stretcher would also be in a vacuum environment for such cases.

As a consequence of our findings we plan to enclose the stretcher in an air-tight container. If this proves to be insufficient in the future, we might even go to vacuum. For the compressor a large vacuum tank will be constructed (ca. $4.5 \times 1.5 \times 1$ m^3), in contrast to the original plan, where only the last grating should be placed in a considerably smaller chamber. These improvements will help in eliminating the air fluctuations and hence the large timing instabilities altogether.

Acknowledgments

This work was funded by the Max-Planck Society through the PFS grant. Financial support from the Extreme Light Infrastructure and the DFG Cluster of Excellence, Munich Centre for Advanced Photonics, is also acknowledged.

#157597 - $15.00 USD Received 3 Nov 2011; revised 2 Dec 2011; accepted 3 Dec 2011; published 30 Jan 2012

BIBLIOGRAPHY

[1] G. D. Tsakiris, K. Eidmann, J. Meyer-ter-Vehn, and F. Krausz. Route to intense single attosecond pulses. *New Journal of Physics*, 8(1):19, 2006. URL http://stacks.iop.org/1367-2630/8/i=1/a=019.

[2] F. Krausz and M. Ivanov. Attosecond physics. *Rev. Mod. Phys.*, 81:163–234, Feb 2009. doi: 10.1103/RevModPhys.81.163. URL http://link.aps.org/doi/10.1103/RevModPhys.81.163.

[3] Extreme light infrastructure european project, 2013. URL http://www.extreme-light-infrastructure.eu.

[4] Extreme light infrastructure proposal, 2013. URL http://www.extreme-light-infrastructure.eu/pictures/ELI-scientific-case-id17.pdf.

[5] A. Einstein. Strahlungs-emission und -absorption nach der quantentheorie. *Verhandlungen der Deutschen Physikalischen Gesellschaft*, 18:318–323, 1916.

[6] A. Einstein. On the quantum theory of radiation. *Physikalische Zeitschrift*, 18: 121–128, 1917.

[7] A. L. Schawlow and C. H. Townes. Infraread and optical masers. *Physical Review*, 112(6):1940–1949, 1958.

[8] T. H. Maiman. Stimulated optical radiation in ruby. *Nature*, 187:493–494, 1960.

[9] B Edlen. *The Nobel Prize in Physics 1964 Charles H. Townes, Nicolay G. Basov, Aleksandr M. Prokhorov*. Elsevier Publishing Company, Amsterdam, 1972.

[10] F. J. McClung and R. W. Hellwarth. Giant optical pulsations from ruby. *J. Appl. Phys.*, 33:828, 1962.

[11] A. Szabo and R. A. Stein. Theory of laser giant pulsing by a saturable absorber. *Journal of Applied Physics*, 36(5):1562–1566, 1965. doi: 10.1063/1.1703087. URL http://link.aip.org/link/?JAP/36/1562/1.

[12] W. E. Lamb. Theory of an optical maser. *Phys. Rev.*, 134:A1429–A1450, Jun 1964. doi: 10.1103/PhysRev.134.A1429. URL http://link.aps.org/doi/10.1103/PhysRev.134.A1429.

[13] E. P. Ippen, C. V. Shank, and Dienes A. Passive mode locking of the cw dye laser. *Applied Physics Letters*, 21:348–350, 1972.

[14] U. Keller. *Ultrafast solid-state lasers*, volume 46 of *Progress in Optics*. Elsevier, 2004. doi: 10.1016/S0079-6638(03)46001-0. URL http://www.sciencedirect.com/science/article/pii/S0079663803460010.

[15] P. Franken, A. Hill, C. Peters, and G. Weinreich. Generation of optical harmonics. *Physical Review Letters*, 7:118, 1961.

[16] N. Bloembergen. The stimulated raman effect. *Am. J. Phys.*, 35:989, 1967.

[17] R. Y. et al Chiao. Stimulated brillouin scattering and coherent generation of intense hypersonic waves. *Phys. Rev. Lett.*, 12:592, 1964.

[18] R. L. et al. Carman. Observation of degenerate stimulated four-photon interaction and four-wave parametric amplification. *Phys. Rev. Lett.*, 17:1281, 1966.

[19] R. H. Stolen. Phase-matched-stimulated four-photon mixing in silica-fiber waveguides. *IEEE J. Quantum Electron*, 11:100, 1975.

[20] R. Y. Chiao, E. Garmire, and C. H. Townes. Self-trapping of optical beams. *Phys. Rev. Lett.*, 13:479, 1964.

[21] Y. R. Shen. Self-focusing: experimental. *Prog. Quantum Electron.*, 4:1, 1975.

[22] B. E. A. Saleh and M. C. Teich. *Fundamentals of Photonics*, chapter 19. Nonlinear optics, page 751 ff. Wiley, 1991.

[23] R. L. Sutherland. *Handbook of nonlinear optics*, chapter 6. E Self focusing. Marcel Dekker, Inc, 2 edition, 2003.

[24] D. Strickland and G. Mourou. Compression of amplified chirped optical pulses. *Optics Comm.*, 56:219, 1985.

[25] M. Pessot, P. Maine, and G. Mourou. 1000 times expansion/compression of optical pulses for chirped pulse amplification. *Optics Comm.*, 62:419, 1987.

[26] E. B. Treacy. Optical pulse compression with diffraction gratings. *IEEE J. Quantum Electron.*, QE-5:454, 1969. URL http://ieeexplore.ieee.org/stamp/stamp.jsp?arnumber=01076303.

[27] o. E. Martinez. 3000 times grating compressor with positive group velocity dispersion: application to fiber compensation in 1.3-1.6-μm region. *IEEE J. Quantum Electron.*, QE-23:59–64, 1987. URL http://ieeexplore.ieee.org/stamp/stamp.jsp?arnumber=01073201.

[28] G. Cheriaux, P. Rousseau, F. Salin, J. P. Chambaret, Barry Walker, and L. F. Dimauro. Aberration-free stretcher design for ultrashort-pulse amplification. *Opt. Lett.*, 21(6):414–416, Mar 1996. doi: 10.1364/OL.21.000414. URL http://ol.osa.org/abstract.cfm?URI=ol-21-6-414.

[29] F. J. Duarte and J. A. Piper. Dispersion theory of multiple-prism beam expander for pulsed dye lasers. *Opt. Commun.*, 43:303–307, 1982.

[30] R. L. Fork, O. E. Martinez, and J. P. Gordon. Negative dispersion using pairs of prisms. *Opt. Lett.*, 9(5):150–152, May 1984. doi: 10.1364/OL.9.000150. URL http://ol.osa.org/abstract.cfm?URI=ol-9-5-150.

[31] Z. Cheng, F. Krausz, and Ch. Spielmann. Compression of 2 mJ kilohertz laser pulses to 17.5 fs by pairing double-prism compressor: analysis and performance. *Optics Communications*, 201:145 – 155, 2002. ISSN 0030-4018. doi: 10.1016/S0030-4018(01)01675-3. URL http://www.sciencedirect.com/science/article/pii/S0030401801016753.

[32] A. Ricci, A. Jullien, N. Forget, V. Crozatier, P. Tournois, and R. Lopez-Martens. Grism compressor for carrier-envelope phase-stable millijoule-energy chirped pulse amplifier lasers featuring bulk material stretcher. *Opt. Lett.*, 37(7): 1196–1198, Apr 2012. doi: 10.1364/OL.37.001196. URL http://ol.osa.org/abstract.cfm?URI=ol-37-7-1196.

[33] V. Pervak, C. Teisset, A. Sugita, S. Naumov, F. Krausz, and A. Apolonski. High-dispersive mirrors for femtosecond lasers. *Opt. Express*, 16(14):10220–10233, Jul 2008. doi: 10.1364/OE.16.010220. URL http://www.opticsexpress.org/abstract.cfm?URI=oe-16-14-10220.

[34] V. Pervak, I. Ahmad, S. A. Trushin, Zs. Major, A. Apolonski, S. Karsch, and F. Krausz. Chirped-pulse amplification of laser pulses with dispersive mirrors. *Opt. Express*, 17(21):19204–19212, Oct 2009. doi: 10.1364/OE.17.019204. URL http://www.opticsexpress.org/abstract.cfm?URI=oe-17-21-19204.

[35] F. Tavella, K. Schmid, N. Ishii, A. Marcinkevicius, L. Veisz, and F. Krausz. High-dynamic range pulse-contrast measurements of a broadband optical parametric chirped-pulse amplifier. *Applied Physics B: Lasers and Optics*, 81:753–756, 2005. ISSN 0946-2171. URL http://dx.doi.org/10.1007/s00340-005-1966-3. 10.1007/s00340-005-1966-3.

[36] F. Tavella, Y. Nomura, L. Veisz, V. Pervak, A. Marcinkevicius, and F. Krausz. Dispersion management for a sub-10-fs, 10 TW optical parametric chirped-pulse amplifier. *Opt. Lett.*, 32(15):2227–2229, Aug 2007. doi: 10.1364/OL.32.002227. URL http://ol.osa.org/abstract.cfm?URI=ol-32-15-2227.

[37] S. Rubenchik, A.and Witkowski. *Physics of laser plasma*. Elsevier Science Pub. Co., Inc., 1991.

[38] P. Sprangle, E. Esarey, and A. Ting. Nonlinear theory of intense laser-plasma interactions. *Phys. Rev. Lett.*, 64:2011–2014, Apr 1990. doi: 10.1103/PhysRevLett.64.2011. URL http://link.aps.org/doi/10.1103/PhysRevLett.64.2011.

[39] G. A. Mourou, T. Tajima, and S. V. Bulanov. Optics in the relativistic regime. *Mourou, G. A., Tajima, T., and Bulanov, S. V.*, 78:1, 2006.

[40] G. Mourou. The exawatt laser: from relativistic to ultra relativistic optics. In *Lasers and Electro-Optics, 2007 and the International Quantum Electronics Conference. CLEOE-IQEC 2007. European Conference on*, pages 1 –2, june 2007. doi: 10.1109/CLEOE-IQEC.2007.4387077.

[41] M. Perry. Crossing the petawatt threshold. *Sci. Tech. Rev.*, 12:4–11, 1996.

[42] M. D. Perry, D. Pennington, B. C. Stuart, G. Tietbohl, J. A. Britten, C. Brown, S. Herman, B. Golick, M. Kartz, J. Miller, H. T. Powell, M. Vergino, and V. Yanovsky. Petawatt laser pulses. *Opt. Lett.*, 24(3):160–162, Feb 1999. doi: 10.1364/OL.24.000160. URL http://ol.osa.org/abstract.cfm?URI=ol-24-3-160.

[43] C. Danson, P. Brummitt, R. Clarke, J. Collier, B. Fell, A. Frackiewicz, S. Hancock, S. Hawkes, C. Hernandez-Gomez, P. Holligan, M. Hutchinson, A. Kidd, W. Lester, I. Musgrave, D. Neely, D. Neville, P. Norreys, D. Pepler, C. Reason, W. Shaikh, T. Winstone, R. Wyatt, and B. Wyborn. Vulcan petawatt - an ultra-high-intensity interaction facility. *Nuclear Fusion*, 44:239, 2004.

[44] H. Kitagawa, Y.and Fujita, R. Kodama, H. Yoshida, S. Matsuo, T. Jitsuno, T. Kawasaki, H. Kitamura, T. Kanabe, S. Sakabe, K. Shigemori, N. Miyanaga, and Y. Izawa. Prepulse-free petawatt laser for a fast ignitor. *IEEE Journal of Quantum Electronics*, 40:281–293, 2004.

[45] M. Aoyama, K. Yamakawa, Y. Akahane, J. Ma, N. Inoue, H. Ueda, and H. Kiriyama. 0.85-PW, 33-fs Ti:sapphire laser. *Opt. Lett.*, 28(17):1594–1596, Sep 2003. doi: 10.1364/OL.28.001594. URL http://ol.osa.org/abstract.cfm?URI=ol-28-17-1594.

[46] J. H. Sung, S. K. Lee, T. J. Yu, T. M. Jeong, and J. Lee. 0.1 hz 1.0 pw ti:sapphire laser. *Opt. Lett.*, 35(18):3021–3023, Sep 2010. doi: 10.1364/OL.35.003021. URL http://ol.osa.org/abstract.cfm?URI=ol-35-18-3021.

[47] J.G. Endriz, M. Vakili, G.S. Browder, M. DeVito, J.M. Haden, G.L. Harnagel, W.E. Plano, M. Sakamoto, D.F. Welch, S. Willing, D.P. Worland, and H.C. Yao. High power diode laser arrays. *Quantum Electronics, IEEE Journal of*, 28(4):952 –965, apr 1992. ISSN 0018-9197. doi: 10.1109/3.135214.

[48] A. Giesen, H. Hügel, A. Voss, K. Wittig, U. Brauch, and H. Opower. Scalable concept for diode-pumped high-power solid-state lasers. *Applied Physics B: Lasers and Optics*, 58:365–372, 1994. ISSN 0946-2171. URL http://dx.doi.org/10.1007/BF01081875. 10.1007/BF01081875.

[49] M. Nisoli, S. De Silvestri, and O. Svelto. Generation of high energy 10 fs pulses by a new pulse compression technique. *Applied Physics Letters*, 68(20): 2793–2795, 1996. doi: 10.1063/1.116609. URL http://link.aip.org/link/?APL/68/2793/1.

[50] R. Baumgartner and R. Byer. Optical parametric amplification. *Quantum Electronics, IEEE Journal of*, 15(6):432 – 444, jun 1979. ISSN 0018-9197. doi: 10.1109/JQE.1979.1070043.

[51] G. Cerullo and S. De Silvestri. Ultrafast optical parametric amplifiers. *Review of Scientific Instruments*, 74(1):1–18, 2003. doi: 10.1063/1.1523642. URL http://link.aip.org/link/?RSI/74/1/1.

[52] J. Moses, C. Manzoni, S.-W. Huang, G. Cerullo, and F. X. Kaertner. Temporal optimization of ultrabroadband high-energy OPCPA. *Opt. Express*, 17(7):5540–5555, Mar 2009. doi: 10.1364/OE.17.005540. URL http://www.opticsexpress.org/abstract.cfm?URI=oe-17-7-5540.

[53] D. Herrmann, L. Veisz, R. Tautz, F. Tavella, K. Schmid, V. Pervak, and F. Krausz. Generation of sub-three-cycle, 16 TW light pulses by using noncollinear optical parametric chirped-pulse amplification. *Opt. Lett.*, 34(16):2459–2461, Aug 2009. doi: 10.1364/OL.34.002459. URL http://ol.osa.org/abstract.cfm?URI=ol-34-16-2459.

[54] Z. X., X. Yang, Y. Leng, H. Lu, L. Lin, Z. Zhang, R. Li, W. Zhang, D. Yin, S. Jin, J. Peng, B. Tang, and B. Zhao. High-power output from a compact OPCPA laser system. *Chin. Opt. Lett.*, 1(1):24–27, Jan 2003. URL http://col.osa.org/abstract.cfm?URI=col-1-1-24.

[55] O. V. Chekhlov, J. L. Collier, I. N. Ross, P. K. Bates, M. Notley, C. Hernandez-Gomez, W. Shaikh, C. N. Danson, D. Neely, P. Matousek, S. Hancock, and L. Cardoso. 35 J broadband femtosecond optical parametric chirped pulse amplification system. *Opt. Lett.*, 31(24):3665–3667, Dec 2006. doi: 10.1364/OL.31.003665. URL http://ol.osa.org/abstract.cfm?URI=ol-31-24-3665.

[56] C. Hernandez-Gomez, S. P. Blake, O. Chekhlov, R. J. Clarke, A. M. Dunne, M. Galimberti, S. Hancock, R. Heathcote, P. Holligan, A. Lyachev, P. Matousek, I. O. Musgrave, D. Neely, P. A. Norreys, I. Ross, Y. Tang, T. B. Winstone, B. E. Wyborn, and J. Collier. The Vulcan 10 PW project. *Journal of Physics: Conference Series*, 244(3):032006, 2010. URL http://stacks.iop.org/1742-6596/244/i=3/a=032006.

[57] E. W. Gaul, M. Martinez, J. Blakeney, A. Jochmann, M. Ringuette, D. Hammond, T. Borger, R. Escamilla, S. Douglas, W. Henderson, G. Dyer, A. Erlandson, R. Cross, J. Caird, C. Ebbers, and T. Ditmire. Demonstration of a 1.1 petawatt laser based on a hybrid optical parametric chirped pulse amplification/mixed Nd:glass amplifier. *Appl. Opt.*, 49(9):1676–1681, Mar 2010. doi: 10.1364/AO.49.001676. URL http://ao.osa.org/abstract.cfm?URI=ao-49-9-1676.

[58] F. Giambruno, C. Radier, G. Rey, and G. Cheriaux. Design of a 10 PW (150J/15fs) peak power laser system with Ti:sapphire medium through spectral control. *Appl. Opt.*, 50(17):2617–2621, Jun 2011. doi: 10.1364/AO.50.002617. URL http://ao.osa.org/abstract.cfm?URI=ao-50-17-2617.

[59] P. B. Corkum and F. Krausz. Attosecond science. *Nature Physics*, 3:381–387, 2007. doi: 10.1038/nphys620. URL http://www.nature.com/nphys/journal/v3/n6/full/nphys620.html.

[60] S. Gordienko, A. Pukhov, O. Shorokhov, and T. Baeva. Relativistic doppler effect: Universal spectra and zeptosecond pulses. *Phys. Rev. Lett.*, 93:115002, Sep 2004. doi: 10.1103/PhysRevLett.93.115002. URL http://link.aps.org/doi/10.1103/PhysRevLett.93.115002.

[61] V.G. Dmitriev, G.G. Gurzadyan, and D.N. Nikogosyan. *Handbook of nonlinear optical crystals*. Springer series in optical sciences. Springer, 1997. ISBN 9783540612759.

[62] N. Zaitseva, J. Atherton, R. Rozsa, L. Carman, I. Smolsky, M. Runkel, R. Ryon, and L. James. Design and benefits of continuous filtration in rapid growth of large kdp and dkdp crystals. *Journal of Crystal Growth*, 197(4):911 – 920, 1999. ISSN 0022-0248. doi: 10.1016/S0022-0248(98)01095-1. URL http://www.sciencedirect.com/science/article/pii/S0022024898010951.

[63] B. C. Stuart, M. D. Feit, S. Herman, A. M. Rubenchik, B. W. Shore, and M. D. Perry. Nanosecond-to-femtosecond laser-induced breakdown in dielectrics. *Phys. Rev. B*, 53:1749–1761, Jan 1996. doi: 10.1103/PhysRevB.53.1749. URL http://link.aps.org/doi/10.1103/PhysRevB.53.1749.

[64] Zs. Major, S. Trushin, I. Ahmad, M. Siebold, Chr. Wandt, S. Klingebiel, T.-J. Wang, J. A. Fülöp, A. Henig, S. Kruber, R. Weingartner, A. Popp, J. Osterhoff, R. Hörlein, J. Hein, V. Pervak, A. Apolonski, F. Krausz, and S. Karsch. Basic concepts and current status of the petawatt field synthesizer-a new approach to ultrahigh field generation. *Review of Laser Engineering*, 37(6):431–436, june 2009.

[65] R. Trebino. *Frequency-resolved optical gating: the measurement of ultrashort laser pulses*. Kluwer academic publisher, 2000.

[66] G. A. Reider. *Photonik*, chapter 1. Licht als elektromagnetische Welle, pages 2–5. Springer, 1997.

[67] B. E. A. Saleh and M. C. Teich. *Fundamentals of Photonics*, chapter 2.2 A Complex Representation and the Helmholtz Equation, page 45 ff. Wiley, 1991.

[68] B. E. A. Saleh and M. C. Teich. *Fundamentals of Photonics*, chapter 3.1 The Gaussian beam, page 81 ff. Wiley, 1991.

[69] A. E. Siegman. *Lasers*, chapter 17.1 Gaussian beam propagation, page 666 ff. University Science Books, 1986.

[70] O. Svelto. *Principles of Lasers*, chapter 4.7. Gaussian beams, page 148 ff. Springer, fourth edition, 1998.

[71] B. E. A. Saleh and M. C. Teich. *Fundamentals of Photonics*, chapter 1.4 Matrix optics, pages 26–32. Wiley, 1991.

[72] A. E. Siegman. *Lasers*, chapter 20.2 Gaussian beams and ABCD matrices, page 783 ff. University Science Books, 1986.

[73] A. E. Siegman. *Lasers*, chapter 21.1 Complex paraxial resonator analysis, page 815 ff. University Science Books, 1986.

[74] A. E. Siegman. *Lasers*. University Science Books, 1986.

[75] Leon Cohen. *Time-frequency analysis*. Prentice Hall PTR, 1995.

[76] Selcuk Akturk, Xun Gu, Pablo Gabolde, and Rick Trebino. The general theory of first-order spatio-temporal distortions of gaussian pulses and beams. *Opt. Express*, 13(21):8642–8661, Oct 2005. doi: 10.1364/OPEX.13.008642. URL http://www.opticsexpress.org/abstract.cfm?URI=oe-13-21-8642.

[77] A.G. Kostenbauder. Ray-pulse matrices: a rational treatment for dispersive optical systems. *Quantum Electronics, IEEE Journal of*, 26(6):1148 –1157, jun 1990. ISSN 0018-9197. doi: 10.1109/3.108113.

[78] C. Palmer and E. Loewen. *Diffraction Grating Handbook*. Newport, sixth edition edition, 2005.

[79] J. Hebling. Derivation of the pulse front tilt caused by angular dispersion. *Optical and Quantum Electronics*, 28(12):1759–1763, 1996. ISSN 0306-8919. doi: 10.1007/BF00698541. URL http://dx.doi.org/10.1007/BF00698541.

[80] B. C. Platt and R Shack. History and principles of shack-hartmann wavefront sensing. *J.Refract.Surg.*, 17(5):573–577, 2001.

[81] P. O'Shea, M. Kimmel, X. Gu, and R. Trebino. Highly simplified device for ultrashort-pulse measurement. *Opt. Lett.*, 26(12):932–934, Jun 2001. doi: 10.1364/OL.26.000932. URL http://ol.osa.org/abstract.cfm?URI=ol-26-12-932.

[82] C. Iaconis and I.A. Walmsley. Spectral phase interferometry for direct electric-field reconstruction of ultrashort optical pulses. *Opt. Lett.*, 23(10):792–794, May 1998. doi: 10.1364/OL.23.000792. URL http://ol.osa.org/abstract.cfm?URI=ol-23-10-792.

[83] G. Pretzler, A. Kasper, and K.J. Witte. Angular chirp and tilted light pulses in CPA lasers. *Applied Physics B: Lasers and Optics*, 70:1–9, 2000. ISSN 0946-2171. URL http://dx.doi.org/10.1007/s003400050001.

[84] K. Varju, A.P. Kovacs, G. Kurdi, and K. Osvay. High-precision measurement of angular dispersion in a CPA laser. *Applied Physics B: Lasers and Optics*, 74:s259–s263, 2002. ISSN 0946-2171. URL http://dx.doi.org/10.1007/s00340-002-0882-z.

[85] S. Akturk, M. Kimmel, P. O'Shea, and R. Trebino. Measuring pulse-front tilt in ultrashort pulses using grenouille. *Opt. Express*, 11(5):491–501, Mar 2003. doi: 10.1364/OE.11.000491. URL http://www.opticsexpress.org/abstract.cfm?URI=oe-11-5-491.

[86] X. Gu, S. Akturk, and R. Trebino. Spatial chirp in ultrafast optics. *Optics Communications*, 242:599–604, 2004. ISSN 0030-4018. doi: 10.1016/j.optcom.2004.09.004. URL http://www.sciencedirect.com/science/article/pii/S0030401804008855.

[87] I. Walmsley, L. Waxer, and C. Dorrer. The role of dispersion in ultrafast optics. *Review of Scientific Instruments*, 72(1):1–29, 2001. doi: 10.1063/1.1330575. URL http://link.aip.org/link/?RSI/72/1/1.

[88] Schott glass catalouge, 2012. URL http://www.schott.com/advanced_optics/english/abbe_datasheets/schott_datasheet_all_english.pdf.

[89] Michael Bass, Casimer DeCusatis, Jay Enoch, Guifang Li, Virendra N. Mahajan, Eric Van Stryland, and Carolyn MacDonald. *Handbook of Optics, Optical Properties of Materials, Nonlinear Optics, Quantum Optics*, volume 4. McGraw-Hill, 3rd edition, 2009.

[90] I. Ahmad. *Development of an optically synchronized seed source for a high-power few-cycle OPCPA system.* PhD thesis, LMU München: Fakultät für Physik, 2011. URL http://edoc.ub.uni-muenchen.de/13250/.

[91] J. A. Fülöp, Zs. Major, A. Henig, S. Kruber, R. Weingartner, T. Clausnitzer, E.-B. Kley, A. Tünnermann, V. Pervak, A. Apolonski, J. Osterhoff, R. Hörlein, F. Krausz, and S. Karsch. Short-pulse optical parametric chirped-pulse amplification for the generation of high-power few-cycle pulses. *New Journal of Physics*, 9(12):438, 2007. URL http://stacks.iop.org/1367-2630/9/i=12/a=438.

[92] I. Ahmad, S. Trushin, Zs. Major, Chr. Wandt, S. Klingebiel, T.-J. Wang, V. Pervak, A. Popp, M. Siebold, F. Krausz, and S. Karsch. Frontend light source for short-pulse pumped opcpa system. *Applied Physics B: Lasers and Optics*, online first:–, 2009. URL http://dx.doi.org/10.1007/s00340-009-3599-4.

[93] N. Aközbek, S. A. Trushin, A. Baltuska, W. Fuß, E. Goulielmakis, K. Kosma, F. Krausz, S. Panja, M. Uiberacker, W. E. Schmid, A. Becker, M. Scalora, and M. Bloemer. Extending the supercontinuum spectrum down to 200 nm with few-cycle pulses. *New Journal of Physics*, 8:177, September 2006. doi: 10.1088/1367-2630/8/9/177.

[94] S. A. Trushin, K. Kosma, W. Fuß, and W. E. Schmid. Sub-10-fs supercontinuum radiation generated by filamentation of few-cycle 800 nm pulses in argon. *Optics Letters*, 32:2432, 2007. doi: 10.1364/OL.32.002432.

[95] E. Goulielmakis, S. Koehler, B. Reiter, M. Schultze, A. J. Verhoef, E. E. Serebryannikov, A. M. Zheltikov, and F. Krausz. Ultrabroadband, coherent light source based on self-channeling of few-cycle pulses in helium. *Optics Letters*, 33:1407, June 2008. doi: 10.1364/OL.33.001407.

[96] K. Kosma, S. A. Trushin, W. Fuß, and W. E. Schmid. Characterization of the supercontinuum radiation generated by self-focusing of few-cycle 800 nm pulses in argon. *Journal of Modern Optics*, 55(13):2141–2177, 2008.

[97] C. Y. Teisset, N. Ishii, T. Fuji, T. Metzger, S. Köhler, R. Holzwarth, A. Baltuška, A. M. Zheltikov, and F. Krausz. Soliton-based pump-seed synchronization for few-cycle OPCPA. *Optics Express*, 13:6550, August 2005. doi: 10.1364/OPEX.13.006550.

[98] F. Tavella, A. Marcinkevicius, and F. Krausz. 90 mJ parametric chirped pulse amplification of 10 fs pulses. *Optics Express*, 14:12822–12827, December 2006. doi: 10.1364/OE.14.012822.

[99] S. Klingebiel, Chr. Wandt, C. Skrobol, I. Ahmad, S. A. Trushin, Zs. Major, F. Krausz, and S. Karsch. High energy picosecond yb:yag cpa system at 10 hz repetition rate forpumping optical parametric amplifiers. *Opt. Express*, 19(6):5357–5363, Mar 2011. doi: 10.1364/OE.19.005357. URL http://www.opticsexpress.org/abstract.cfm?URI=oe-19-6-5357.

[100] J. Aus der Au, G. J. Spühler, T. Südmeyer, R. Paschotta, R. Hövel, M. Moser, S. Erhard, M. Karszewski, A. Giesen, and U. Keller. 16.2-w average power from a diode-pumped femtosecond yb:yag thin disk laser. *Opt. Lett.*, 25 (11):859–861, Jun 2000. doi: 10.1364/OL.25.000859. URL http://ol.osa.org/abstract.cfm?URI=ol-25-11-859.

[101] G. L. Bourdet and O. Casagrande. Theoretical comparison of ytterbium doped sesquioxydes under pulsed diode pumping. *Optics Communications*, 244:327–332, 2005.

[102] A. Lucca, G. Debourg, M. Jacquemet, F. Druon, F. Balembois, P. Georges, P. Camy, J. L. Doualan, and R. Moncorgé. High-power diode-pumped yb3+:caf2 femtosecond laser. *Opt. Lett.*, 29(23):2767–2769, Dec 2004. doi: 10.1364/OL.29.002767. URL http://ol.osa.org/abstract.cfm?URI=ol-29-23-2767.

[103] P. Camy, J.L. Doualan, A. Benayad, M. von Edlinger, V. Ménard, and R. Moncorgé. Comparative spectroscopic and laser properties of yb3+-doped caf2, srf2 and baf2 single crystals. *Applied Physics B*, 89:539–542, 2007. ISSN 0946-2171. doi: 10.1007/s00340-007-2829-x. URL http://dx.doi.org/10.1007/s00340-007-2829-x.

[104] M. Siebold, M. Hornung, R. Boedefeld, S. Podleska, S. Klingebiel, Chr. Wandt, F. Krausz, S. Karsch, R. Uecker, A. Jochmann, J. Hein, and M. C. Kaluza. Terawatt diode-pumped yb:caf2 laser. *Opt. Lett.*, 33(23):2770–2772, 2008. URL http://ol.osa.org/abstract.cfm?URI=ol-33-23-2770.

[105] M. J. Guardalben. Littrow angle method to remove alignment errors in grating pulse compressors. *Appl. Opt.*, 47(27):4959–4964, Sep 2008. doi: 10.1364/AO.47.004959. URL http://ao.osa.org/abstract.cfm?URI=ao-47-27-4959.

[106] F. Liu, X. Liu, Z. Wang, J. Ma, X. Liu, L. Zhang, J. Wang, S. Wang, X. Lin, Y. Li, L. Chen, Z. Wei, and J. Zhang. Compression grating alignment by far-field monitoring. *Applied Physics B: Lasers and Optics*, 101:587–591, 2010. ISSN 0946-2171. URL http://dx.doi.org/10.1007/s00340-010-4237-x. 10.1007/s00340-010-4237-x.

[107] L.D. DeLoach, S.A. Payne, L.L. Chase, L.K. Smith, W.L. Kway, and W.F. Krupke. Evaluation of absorption and emission properties of yb3+ doped crystals for laser applications. *Quantum Electronics, IEEE Journal of*, 29(4):1179–1191, apr 1993. ISSN 0018-9197. doi: 10.1109/3.214504.

[108] Chr. Wandt, S. Klingebiel, M. Siebold, Zs. Major, J. Hein, F. Krausz, and S. Karsch. Generation of 220mj nanosecond pulses at a 10hz repetition rate

with excellent beam quality in a diode-pumped yb:yag mopa system. *Opt. Lett.*, 33(10):1111–1113, 2008. URL http://ol.osa.org/abstract.cfm?URI=ol-33-10-1111.

[109] M. D. Perry, R. D. Boyd, J. A. Britten, D. Decker, B. W. Shore, C. Shannon, and E. Shults. High-efficiency multilayer dielectric diffraction gratings. *Opt. Lett.*, 20(8):940–942, Apr 1995. doi: 10.1364/OL.20.000940. URL http://ol.osa.org/abstract.cfm?URI=ol-20-8-940.

[110] J. Neauport, E. Lavastre, G. Razé, G. Dupuy, N. Bonod, M. Balas, G. de Villele, J. Flamand, S. Kaladgew, and F. Desserouer. Effect of electric field on laser induced damage threshold of multilayer dielectric gratings. *Opt. Express*, 15(19):12508–12522, Sep 2007. doi: 10.1364/OE.15.012508. URL http://www.opticsexpress.org/abstract.cfm?URI=oe-15-19-12508.

[111] F. Verluise, V. Laude, Z. Cheng, Ch. Spielmann, and P. Tournois. Amplitude and phase control of ultrashort pulses by use of an acousto-optic programmable dispersive filter: pulse compression and shaping. *Opt. Lett.*, 25 (8):575–577, Apr 2000. doi: 10.1364/OL.25.000575. URL http://ol.osa.org/abstract.cfm?URI=ol-25-8-575.

[112] M. Lai, S. T. Lai, and C. Swinger. Single-grating laser pulse stretcher and compressor. *Appl. Opt.*, 33(30):6985–6987, Oct 1994. doi: 10.1364/AO.33.006985. URL http://ao.osa.org/abstract.cfm?URI=ao-33-30-6985.

[113] N. V. Didenko, A. V. Konyashchenko, A. P. Lutsenko, and S. Y. Tenyakov. Contrast degradation in a chirped-pulse amplifier due to generation of prepulses by postpulses. *Opt. Express*, 16(5):3178–3190, Mar 2008. doi: 10.1364/OE.16.003178. URL http://www.opticsexpress.org/abstract.cfm?URI=oe-16-5-3178.

[114] D. N. Schimpf, E. Seise, J. Limpert, and A. Tünnermann. The impact of spectral modulations on the contrast of pulses of nonlinearchirped-pulse amplification systems. *Opt. Express*, 16(14):10664–10674, Jul 2008. doi: 10.1364/OE.16.010664. URL http://www.opticsexpress.org/abstract.cfm?URI=oe-16-14-10664.

[115] S. Klingebiel, I. Ahmad, Chr. Wandt, C. Skrobol, S. A. Trushin, Zs. Major, F. Krausz, and S. Karsch. Experimental and theoretical investigation of timing jitter inside a stretcher-compressor setup. *Opt. Express*, 20(4):3443–3455, Feb 2012. doi: 10.1364/OE.20.003443. URL http://www.opticsexpress.org/abstract.cfm?URI=oe-20-4-3443.

[116] T. Miura, K. Kobayashi, K. Takasago, Z. Zhang, K. Torizuka, and F. Kannari. Timing jitter in a kilohertz regenerative amplifier of a femtosecond-pulse ti:al2o3 laser. *Opt. Lett.*, 25(24):1795–1797, Dec 2000. doi: 10.1364/OL.25.001795. URL http://ol.osa.org/abstract.cfm?URI=ol-25-24-1795.

[117] P. G. Backes and W. H. Stevenson. A comparison of methods for accurate image centroid position determination with matrix sensors. *Journal of Laser Applications*, 2(2):33, 1990.

[118] K. P. Birch and M. J. Downs. Correction to the updated edlén equation for the refractive index of air. *Metrologia*, 31(4):315, 1994. URL http://stacks.iop.org/0026-1394/31/i=4/a=006.

[119] J.-C. Diels and W. Rudolph. *Ultrashort Laser Pulse Phenomena*, chapter 2.5.6. GVD Introduced by Gratings, pages 117–120. Academic Press, 2 edition, 2006.

[120] C. Skrobol, I. Ahmad, S. Klingebiel, Chr. Wandt, S. A. Trushin, Zs. Major, F. Krausz, and S. Karsch. Broadband amplification by picosecond opcpa in dkdp pumped at 515 nm. *Opt. Express*, 20(4):4619–4629, Feb 2012. doi: 10.1364/OE.20.004619. URL http://www.opticsexpress.org/abstract.cfm?URI=oe-20-4-4619.

[121] W.F. Krupke. Ytterbium solid-state lasers. the first decade. *Selected Topics in Quantum Electronics, IEEE Journal of*, 6(6):1287 –1296, nov.-dec. 2000. ISSN 1077-260X. doi: 10.1109/2944.902180.

[122] C. Hönninger, I. Johannsen, M. Moser, G. Zhang, A. Giesen, and U. Keller. Diode-pumped thin-disk yb:yag regenerative amplifier. *Applied Physics B: Lasers and Optics*, 65:423–426, 1997. ISSN 0946-2171. URL http://dx.doi.org/10.1007/s003400050291. 10.1007/s003400050291.

[123] E. C. Honea, R. J. Beach, S. C. Mitchell, J. A. Skidmore, M. A. Emanuel, S. B. Sutton, S. A. Payne, P. V. Avizonis, R. S. Monroe, and D. G. Harris. High-power dual-rod yb:yag laser. *Opt. Lett.*, 25(11):805–807, Jun 2000. doi: 10.1364/OL.25.000805. URL http://ol.osa.org/abstract.cfm?URI=ol-25-11-805.

[124] József András Fülöp, László Pálfalvi, Matthias C. Hoffmann, and János Hebling. Towards generation of mj-level ultrashort thz pulses by optical rectification. *Opt. Express*, 19(16):15090–15097, Aug 2011. doi: 10.1364/OE.19.015090. URL http://www.opticsexpress.org/abstract.cfm?URI=oe-19-16-15090.

[125] J. A. Fülöp, L. Pálfalvi, S. Klingebiel, G. Almási, F. Krausz, S. Karsch, and J. Hebling. Generation of sub-mj terahertz pulses by optical rectification. *Opt. Lett.*, 37(4):557–559, Feb 2012. doi: 10.1364/OL.37.000557. URL http://ol.osa.org/abstract.cfm?URI=ol-37-4-557.

[126] J. Dong, M. Bass, Y. Mao, P. Deng, and F. Gan. Dependence of the yb3+ emission cross section and lifetime on temperature and concentration in yttrium aluminum garnet. *J. Opt. Soc. Am. B*, 20(9):1975–1979, Sep 2003. doi: 10.1364/JOSAB.20.001975. URL http://josab.osa.org/abstract.cfm?URI=josab-20-9-1975.

[127] S. Lang. *Complex Analysis*. Springer, 2003.

With automatic spell checkers
running unleashed over what we compose,
our era is that of correctly spelled typos.

— Neil deGrasse Tyson

ACKNOWLEDGMENTS

It is a great pleasure to thank everyone who has contributed in one or another way to the completion of this dissertation. In particular, I would like to gratefully thank my supervisor Prof. Dr. Karsch who gave me the freedom to explore on my own, and at the same time the guidance and support, which was necessary to finish this dissertation. I am also grateful to Prof. Dr. Krausz, one of the directors of the Max-Planck-Institute for Quantum Optics and head of the attosecond physics department, for creating an outstanding scientific environment for me and many other PhD students. My gratitude is extended to Prof. Dr. Kaluza for reviewing my thesis and his interest in my work.

I want to thank all of my colleagues in the group of Prof Karsch for countless discussions, critical comments and inspiring ideas but also for a pleasant working atmosphere during countless hours in the lab. Not to forget hilarious coffee breaks and lunch-time discussions. Non of this work would have been possible without their support and collaboration.

Finally, and most importantly, I would like to show my gratitude to my wife Marion and to my family for their unconditional love, moral support, and tolerance which made the hardship of writing this thesis worthwhile.

PUBLICATIONS BY THE AUTHOR

S. Klingebiel, I. Ahmad, Chr. Wandt, C. Skrobol, S. A. Trushin, Zs. Major, F. Krausz and S. Karsch, *Experimental and theoretical investigation of timing jitter inside a stretcher-compressor setup*, Opt. Express, 20, 3443-3455, **2012**.

C. Skrobol, I. Ahmad, **S. Klingebiel**, Chr. Wandt, S. A. Trushin, Zs. Major, F. Krausz and S. Karsch, *Broadband amplification by picosecond OPCPA in DKDP pumped at* 515 *nm*, Opt. Express, 20, 4619-4629, **2012**.

J. A. Fülöp, L. Palfalvi, **S. Klingebiel**, G. Almasi, F. Krausz, S Karsch and J. Hebling, *Generation of sub-mJ terahertz pulses by optical rectification*, Opt. Lett., 37, 557-559, **2012**.

S. Klingebiel, Chr. Wandt, C. Skrobol, I. Ahmad, S. A. Trushin, Zs. Major, F. Krausz and S. Karsch, *High energy picosecond Yb:YAG CPA system at* 10 *Hz repetition rate for pumping optical parametric amplifiers*, Opt. Express, 19, 5357-5363, **2011**.

Zs. Major, S. A. Trushin, I. Ahmad, M. Siebold, Chr. Wandt, **S. Klingebiel**, T.-J. Wang, J. A. Fülöp, A. Henig, S. Kruber, R. Weingartner, A. Popp, J. Osterhoff, R. Hörlein, J. Hein, V. Pervak, A. Apolonski, F. Krausz and S. Karsch, *Basic Concepts and Current Status of the Petawatt Field Synthesizer-A New Approach to Ultrahigh Field Generation*, Review of Laser Engineering, 37, 431-436, **2009**.

I. Ahmad, S. A. Trushin, Zs. Major, Chr. Wandt, **S. Klingebiel**, T.-J. Wang, V. Pervak, A. Popp, M. Siebold, F. Krausz and S. Karsch, *Frontend light source for short-pulse pumped OPCPA system*, Applied Physics B: Lasers and Optics,97(3), 529-536, **2009**.

Chr. Wandt, **S. Klingebiel**, M. Siebold, Zs. Major, J. Hein, F. Krausz and S. Karsch, *Generation of* 220 *mJ nanosecond pulses at a* 10 *Hz repetition rate with excellent beam quality in a diode-pumped Yb:YAG MOPA system*, Opt. Lett., 33, 1111-1113, **2008**.

M. Siebold, M. Hornung, R. Boedefeld, S. Podleska, **S. Klingebiel**, Chr. Wandt, F. Krausz, S. Karsch, R. Uecker, A. Jochmann, J. Hein and M. C. Kaluza, *Terawatt diode-pumped Yb:CaF2 laser* Opt. Lett., 33, 2770-2772, **2008**.

M. Siebold, J. Hein, Chr. Wandt, **S. Klingebiel**, F. Krausz and S. Karsch, *High-energy, diode-pumped, nanosecond Yb:YAG MOPA system*, Opt. Express, 16, 3674-3679, **2008**.

DATA ARCHIVING

The experimental raw data, the simulation files, evaluation files and the figures can be found on the data-archive sever of the Laboratory for Attosecond Physics at the Max Planck Institute of Quantum Optics. The data file paths are self-explanatory: In folders for each chapter, the data is organized in sub-folders, named as the corresponding figure or table. Each of these folders contains the figure file as png, the raw data, a readme.txt and all evaluation files, which were necessary to produce the final figure. The data analysis and processing steps are explained in corresponding text document.

COLOPHON

This document was typeset using the typographical look-and-feel `classicthesis` developed by André Miede. The style was inspired by Robert Bringhurst's seminal book on typography "*The Elements of Typographic Style*". `classicthesis` is available for both LaTeX and LyX:

http://code.google.com/p/classicthesis/

Final Version as of July 19, 2013 (`classicthesis` version 0.1).